Harnessing Plasmon-Enhanced Spectroscopy for Ultra-Sensitive Analyte Detection and Theranostics

THESIS

Submitted in partial fulfilment

of the requirements for the degree of

DOCTOR OF PHILOSOPHY

by

KAJA SRAVANI

ID. No. 2018PHXF0011H

Under the Supervision of

Prof. Amit Nag

BIRLA INSTITUTE OF TECHNOLOGY AND SCIENCE, PILANI

2024

BIRLA INSTITUTE OF TECHNOLOGY AND SCIENCE, PILANI

CERTIFICATE

This is to certify that the thesis entitled **"Harnessing Plasmon-Enhanced Spectroscopy for Ultra-Sensitive Analyte Detection and Theranostics"** submitted by **Kaja Sravani,** ID. No **2018PHXF0011H** for the award of Ph.D. from the institute embodies original work done by her under my supervision.

Signature of the Supervisor: 

Name: **Prof. Amit Nag**

Designation: **Professor**

Department of Chemistry

BITS Pilani-Hyderabad Campus.

Date: 27.02.2024

BIRLA INSTITUTE OF TECHNOLOGY AND SCIENCE, PILANI

DECLARATION

I hereby declare that the research work embodied in the thesis entitled **"Harnessing Plasmon-Enhanced Spectroscopy for Ultra-Sensitive Analyte Detection and Theranostics"** has been carried out under the supervision of Prof. Amit Nag, Department of chemistry, BITS-Pilani Hyderabad, India. The work is original and has not been submitted in part or full for any degree for this or to any other university.

Sravani Kaja

Acknowledgments

This thesis becomes a reality with the kind support and help of many individuals. I would like to thank some of those who were with me from the beginning, some who joined me at some stage during the journey, whose rally round kindness, love, and blessings have brought me to this day. I wish to thank each one of them with all my heart.

Foremost, I give my heart full thanks to my parents ***Mrs. Krishna Veni Kaja*** and ***Mr. Venkateswar Rao Kaja*** for all their support, for all the sacrifices they made on my behalf, and who longed to see this achievement come true. I also thank my grandmother ***Mrs. Vasundhara Devi Kaja*** for the constant love and caring. I thank God for giving me strength and good health throughout this journey.

I want to express my sincere gratitude to my supervisor ***Prof. Amit Nag,*** for his guidance, patience, continuous support, and suggestions that have contributed immensely to the evolution of ideas on the subject. I heartfully thank him for motivating me at every stage during this entire journey. His valuable guidance helped me in all the time of my research and writing of this thesis. This thesis would not have been possible without his support.

I sincerely acknowledge my DAC (doctoral advisory committee) members, ***Prof. Manab Chakravarty,*** for his immense support and encouragement, and ***Prof. Ramakrishnan Ganesan*** for their support and valuable scientific suggestions from time to time. I am thankful to the Head of the Department (HOD), DRC convenor, and entire chemistry department faculty members for their help, valuable interaction, and discussions throughout the journey.

I owe my sincere gratitude to ***Prof. V. Ramagopal Rao*** **(**Vice-Chancellor of BITS), ***Prof. Souvik Bhattacharya*** (former Vice-Chancellor of BITS), and ***Prof. G Sundar*** (Director BITS Pilani Hyderabad Campus) for permitting me to carry out my doctoral work on this campus. I would like to express my sincere thanks to the Academic-Graduate Studies and Research Division (AGSRD, Ph.D. Programme), Associate Dean, ***Prof. V. V. Vamshi Krishna,*** for their continuous support and

encouragement during my research work. I extend my thanks to ***Mr. Praveen,*** AGSRD, for his help and information to complete the course formalities in time.

A heartful thanks to my besties ***Mr. Pavan Garlapati, Dr. Deepthi Priyanka Damera,*** and ***Dr. Banchhanidhi Prusti*** for their much-needed care and support both personally and professionally. I would also thank my past and present lab mates **Ashin *Varghese Mathews*** and ***Ronak Lazarus*** for their care and encouragement. I like to thank Ashin specially for all the COMSOL simulations presented in this thesis. I also like to thank ***Shalini Dyagala, and Rikitha Sharyl Fernandes*** for all the fun in the hostel. I would like to thank my colleagues ***Dr. Arun, Dr. Himabindu, Leela Sri,*** *and* ***Ravallika,*** for their help and motivation. I especially thank my cousin ***Mr. Praneeth Kumar Kesa*** for his unconditional love and support.

I especially thank **Dr. J. Sowmya** for guiding me after my Masters and encouraging me to pursue this Ph.D. I also want to thank my teachers ***Dr. Swaroopa Rani*** (late), ***Dr. Mamatha, Dr. Premalatha, Dr. A. Haripadmasri, Mr. Pavan Vemula, Mrs. Jyothi, and Mrs. Shailaja*** for their constant inspiration and motivation. I want to thank my friends ***Madhu, Pranathi, Swathi,*** and ***Sadath*** for being a part of this long journey.

I thank all the technicians in the Chemistry Department and Central Analytical Laboratory for their co-operation. I would like to especially thank ***Mr. Kali Suresh*** for capturing all the FE-SEM images presented in this thesis. I would also like to thank all the research scholars from the chemistry department who supported me in writing and motivating me to strive towards my goal.

Date: 27.02.2024 (Kaja Sravani)

Abstract

Nano plasmonics is making a significant transformation to our world and is key to many applications, such as surface-enhanced spectroscopy, sensing of important drugs and pollutants, light-activated cancer treatments, and the enhancement of light absorption in photovoltaics and photocatalysis. This thesis provides a detailed account of the preparation of various plasmonically active nanomaterials, their detailed characterization, and applications using fluorescence and Raman spectroscopy. This work offers a comprehensive understanding and application of different plasmon-enhanced spectroscopies, such as metal-enhanced fluorescence (MEF), metal-enhanced singlet oxygen generation (MESOG), and surface-enhanced Raman spectroscopy (SERS).

The introduction of the work is presented in **Chapter 1**. In **Chapter 2**, the technical details of different instruments, synthesis procedures, and materials used in this thesis are provided. In **chapter 3**, we report a gold nanoparticle (AuNP)-based sensor for the detection of picric acid (PA) in aqueous condition, based on MEF of poly(allylamine)hydrochloride (PAH). Notable enhancement in fluorescence intensity is observed when PAH is incubated with Au@SiO2 nanoparticles, where the silica shell controls the distance between the gold core and PAH. We have noticed almost 280-fold enhancement when PAH is incubated with 45 nm diameter Au nanoparticles. A significant reduction in excited state lifetime followed the enhancement in fluorescence intensity, identifying the mechanism to be primarily obtained from the intrinsic radiative decay rate enhancement of PAH. The MEF sensor shows excellent selectivity for the detection of PA in water, among similar electron-deficient compounds via fluorescence quenching. The detection limit of the sensor is calculated to be 79 nM, in the linear range. Detection of PA is demonstrated in simulated water samples, where matrix effects are taken into account to assess the efficacy of the sensor.

In **chapter 4**, we developed isotropic and anisotropic nano structures for exploring concurrent enhancement in fluorescence as well as singlet oxygen

generation (SOG) capacities of photosensitizers (PS) placed in the vicinity of metal nano particles (MNPs). SOG is used in photodynamic therapy (PDT) for the treatment of cancer. This chapter consists of two parts: chapters 4A and 4B. In **Chapter 4A**, driven by the need for more personalized medicine, shortened irradiation time, and treatment efficiency of PDT, a library of novel theranostic nanoparticle systems for personalized medicine in PDT of cancer is described. Ag and Au nanoparticles in a size range of 40-50 nm are prepared and used subsequently to synthesize core-shell plasmonic nanoparticles with various thicknesses, either with silica or polymer spacer. MEF and metal-enhanced singlet oxygen generation (MESOG) studies are performed for a naphthalene-linked pyridine-based neutral triarylethene as AIE-active PS molecule, by adsorbing on the Ag and Au core-shell nanoparticles. The factors that are varied during the study are the composition of the spacer and the spacer length. Notably, the enhancement in fluorescence and SOG of the adsorbed AIEgen are observed at the same distance from the metallic surface, resulting from a short-range near-field plasmonic effect for all the theranostic PS prepared with Ag/Au. The best result, 7.9-fold enhancement in fluorescence and 10.4-fold enhancement in SOG is observed on loading AIEgen on 42 nm Au nanoparticles with a polymer spacer, showing promising advancement for image-guided PDT. We later used this best system for confocal imaging of vesicles. Whereas in **chapter 4B**, we explored the role of the aspect ratio (AR) of different gold nano rods (GNRs) on the MEF and MESOG capability of a commercially available PS Eosin Y (Ey). For this, a library of GNRs with 6 different AR along with 6 different thicknesses of polymer was used. Here the polymer layers serve as a spacer between GNR and Ey. The best results were found with GNRs of length 135 nm and width 45 nm (GNR 4) having an aspect ratio of 2.95. maximum MEF and MESOG were obtained for the above-mentioned GNRs with a polymer thickness of about 12.6 nm. Further investigations along with COMSOL simulations were performed to understand the physics behind the enhancement. It is concluded that the synergistic effect of scattering (far field), near field plasmonic damping rate, and NSET plays an important role in the plasmonic enhancement.

In the surface-enhanced Raman scattering (SERS) technique, analytes are directly adsorbed on the surface of SERS substrates unlike MEF, where there should be

an optimum distance between MNP and the emitter. In **chapter 5**, we studied the role of the composition of the bimetallic alloy substrates in maximizing the SERS efficiency. In **Chapter 5A,** bimetallic Ag-Cu alloy microflowers (MFs) with tunable surface compositions were fabricated as SERS substrates with a limit of detection in the zeptomolar range for the analyte molecule Rhodamine 6G (R6G). The substrates were prepared on a glass coverslip through a bottom-up strategy by simple thermolysis of metal-alkyl ammonium halide precursors. The reaction temperature and composition of the alloy were varied sequentially to find out the maximum SERS efficiency from the substrates. While UV-Vis spectroscopy was employed to characterize the optical properties of the substrates, the bulk and surface composition of the MFs were determined using ED-XRF and XPS techniques, respectively. Also, the structural and morphological characterization of the substrates were performed by X-ray diffraction and SEM, respectively. For alloys, the ED-XRF studies confirmed that the bulk compositions matched with the feed ratio, while the surface compositions were found to be rich in copper in the form of both elementary copper and copper oxide, as revealed by XPS studies. From the efficiency studies for different compositions prepared, it was found that 10% Ag-Cu alloy MFs produced maximum SERS intensity for resonant R6G molecule as a probe. R6G evidence 50-fold enhancement in SERS spectra with 10% alloy microflowers as against pure Ag MF. Using 1, 2, 3-benzotriazole as a non-resonant Raman probe, uniform enhancement factors in the order of ~10^8 were achieved from different parts of the 10% Ag-Cu alloy MF. The same substrate showed excellent Raman response for detecting R6G at very low concentrations such as 10 zM, leading to the detection and analysis of SERS spectra from a single R6G molecule. In **chapter 5B**, bimetallic Ag-Au and Ag-Cu alloy MFs with tunable surface compositions were fabricated in the same way and used as SERS substrates for the sensitive detection of the anticancer drug Mitoxantrone (MTO). Two different laser excitation sources, 532 nm and 632.8 nm, were used to explore the possibility of SERS and Surface Enhanced Resonance Raman Scattering (SERRS). Ag-Cu substrate showed superior detection capability over Ag-Au, whereby the sensor recorded a noteworthy 'limit of detection (LOD)' value of 1 fM for MTO. Theoretical electromagnetic field maps were simulated on appropriately chosen plasmonic systems, to compare the

electromagnetic field enhancements with the experimental SERS efficiencies of the substrates. Further, using a 10% Ag-Cu substrate, efficient multiplexing detection of MTO was demonstrated with another anticancer drug Doxorubicin (DOX), in water and mouse blood plasma.

Even though, the synthesized Ag-Cu substrates demonstrated excellent SERS enhancement factors, one of the limitations of the substrate is the Cu-rich surface, leading to less favorable adsorption for the small molecule aliphatic and aromatic thiols. Therefore, in **chapter 6**, we synthesized SERS substrates with similar EF to the previously synthesized Ag-Cu substrates, but the surface was Au-rich. In the quest, we optimized trimetallic Ag-Au-Cu alloy (MFs) with various surface compositions and used them as efficient SERS substrates for the label-free detection of L-cysteine and thiophenols. MFs of different compositions were synthesized via appropriate mixing of metal-alkyl ammonium halide precursors, followed by a single-step thermolysis at 350 °C. While the Ag percentage was kept constant at 90% for all the substrates, the composition of Au and Cu was varied between 1% to 9% sequentially. The synthesized MFs were thoroughly characterized using FE-SEM, WAXS, XPS, and XRF techniques. FE-SEM studies revealed that the MFs were present throughout the substrate and the average size varied from 20 to 40 μm. XPS studies showed that the top surface of the alloy substrates was rich in either Au or Cu atoms, while Ag remained underneath. The performance of the trimetallic MFs as SERS substrates was evaluated using Rhodamine 6G as a probe molecule, which showed that the MFs with Ag-Au-Cu composition as 90-7-3 and 90-3-7 were found to be the best and of equal SERS efficiency. The SERS EF of both these MFs was found to be the same, approximately 9×10^7 when calculated using 1,2,3-benzotriazole as the probe molecule. Between the two, the trimetallic substrate with the higher Au percentage (Ag-Au-Cu as 90-7-3) was used for the sensitive SERS-based detection of L-Cysteine to exploit the strong Au-S binding interaction. The 'limit of quantification (LOQ)' value of 1 nM from the trimetallic MF substrate (Ag-Au-Cu as 90-7-3), 1 pM for thiophenol and its derivatives. We also used this substrate for ultra-sensitive detection of 4-Nitro thiophenol and the LOQ was found to be 0.1 pM. **Finally**, a summary of the work presented in the thesis and future perspective is presented at the end.

Table of Contents

List of Tables

List of Figures

List of Schemes

Abbreviations

MNP	Metal Nano Particles
LSPR	Localised surface plasmon resonance
MEF	Metal enhanced fluorescence
MESOG	Metal enhanced singlet oxygen generation
PS	Photosensitizer
ROS	Reactive oxygen species
$^1O_2$	Singlet oxygen
PDT	Photodynamic therapy
SERS	Surface enhanced Raman spectroscopy
SERRS	Surface enhanced Resonance Raman spectroscopy
SMSERS	Single molecule surface enhanced Raman spectroscopy
EF	Enhancement factor
AIE	Aggregation induced emission
Ey	Eosin Y
LBL	Layer by layer
NP-4-Py	(E)-4-(4-(2-([1,1′-biphenyl]-4-yl)-2-(naphthalen-1-yl) vinyl) phenyl) pyridine
%	Percentage
℃	Degree centigrade
eV	Electron volt
K_{sv}	Stren Volmer constant
Φ	Quantum yield
mg	milligram
µg	microgram
M	Molarity
mM	Milli molar
nM	Nano molar
pM	Picomolar
fM	femtomolar
zM	Zeptomolar
m	meter
cm	centimetre
µm	micrometre
nm	nanometre
mw	Milliwatt
ns	nanosecond
s	seconds
min	minutes
h	hours
λ	Wavelength (usually in nm)
τ	Lifetime value Tau
θ	radian Theta
R6G	Rhodamine 6G

MTO	Mitoxantrone
DOX	Doxorubicin
PAH	Poly allylamine hydrochloride
PSS	Poly styrene sulfonate
TEOS	Tetraethyl orthosilicate
L-Cys	L-Cysteine
TP	Thiophenol
ATP	2-Amino Thiophenol
BTP	4-Bromo Thiophenol
FTP	4-Fluoro Thiophenol
NTP	4-Nitro Thiophenol
S60	Span 60
L 64	Pluronic L64
DPBF	Diphenyl benzofuran
DMPO	5,5-dimethyl-1-pyrroline N-Oxide
MFs	Microflowers
TM	Trimetallic
NSET	Nanoparticle surface energy transfer
FRET	Fluorescence resonance energy transfer
J_λ	J integral values
AgNPs	Silver nanoparticles
AuNPs	Gold Nanoparticles
SiNPs	Silica nanoparticles
LOD	Limit of detection
LOQ	Limit of quantification

Chapter 1

Introduction

In this chapter, a brief introduction on light matter interactions at nanoscale are explained. We introduce the term plasmonics and various plasmon driven processes such as Metal enhanced fluorescence (MEF), Metal enhanced singlet oxygen generation (MESOG), and Surface enhanced Raman spectroscopy (SERS). Their mechanisms, factors affecting them and applications are explained.

1.1. The motivation of the work

According to the quantum theories, when light interacts with bulk matter several optical phenomena can take place such as absorption, transmission, scattering, reflection, refraction or diffraction of light as shown in **figure 1.1a**.[1-3] But when light interacts with matter at nanoscale especially with metal nano particles (MNPs) numerous interesting phenomena takes place and it was first explained by Gustav Mie in 1908. MNPs exhibit unique properties due to their conducting band electrons known as plasmons and the study of interaction of light with these plasmons is called plasmonics. When an electromagnetic (EM) light of a suitable wavelength interacts with plasmonic MNP, the electrons of conduction band get excited and oscillate coherently on their surface in distinct dipolar and multipolar modes and the phenomenon is known as localized surface plasmon resonance (LSPR) (**Figure 1.1b**).[4-7] LSPR can be observed in MNPs synthesized from Gold, Silver, Copper, Aluminium, in UV-Vis-NIR region. MNPs exhibit unique scattering, absorption and coupling properties depending on their size, structure and on composition.[8-15] They also have unique property of confining light below the subwavelength dimensions and thus acts as Plasmonic nanoantenna. When EM light is confined between the nanoscale gaps present in between adjacent particles, the fields are greatly enhanced and known as electromagnetic hotspots.[16] These hotspots serve as a platform for various near field enhancement studies such as Metal enhanced Fluorescence (MEF),[17-19] plasmonic catalysis,[20-22] Surface enhanced Raman spectroscopy (SERS),[23-25] biosensing,[26] refractive index change based sensing,[27] and colorimetric sensing[28] etc. Refractive index-based sensing in a very sensitive, common and useful process in which the change in refractive index is monitored by the change in LSPR wavelength shift. If the refractive index of the surrounding medium undergoes an increase, the plasmon resonance shifts towards longer wavelengths, and conversely, it shifts towards shorter wavelengths when the refractive index decreases[27]. Plasmonics also take part in sensors which are based on colour change known as colorimetric sensors and they are gaining important due to many features such as low cost, high sensitivity, minimal time required and due to their high accessibility. They are mainly based on the change

in the assembly state of nanomaterials and can offer detection limits even up to femto molar level.

MEF and SERS are the two major fields of plasmonics, that arises due to interaction of light with Plasmonic MNPs and either fluorescence or Raman signals are enhanced based on the arrangement of MNPs and molecules of interest. For example, if the molecule is adsorbed directly on the surface of MNP, its fluorescence gets quenched due to radiative energy transfer but its Raman signals get enhanced. On the other hand, if the molecule is at an optimum distance from the MNP surface, its fluorescence gets enhanced multiple folds as shown in the **figure 1.1 c and d**.[29-32] MEF and SERS finds applications such as super resolution imaging,[33] biosensors,[34] bacterial detection,[35] cancer diagnostics,[36] cancer theranostics,[37] and metal enhanced singlet oxygen generation (MESOG)[38] etc. MNPs also play an important role in enhancing the singlet oxygen generation capacity of photosensitizers and thereby increase the photodynamic therapy efficiency and can be used for killing harmful bacterial and cancer cells.

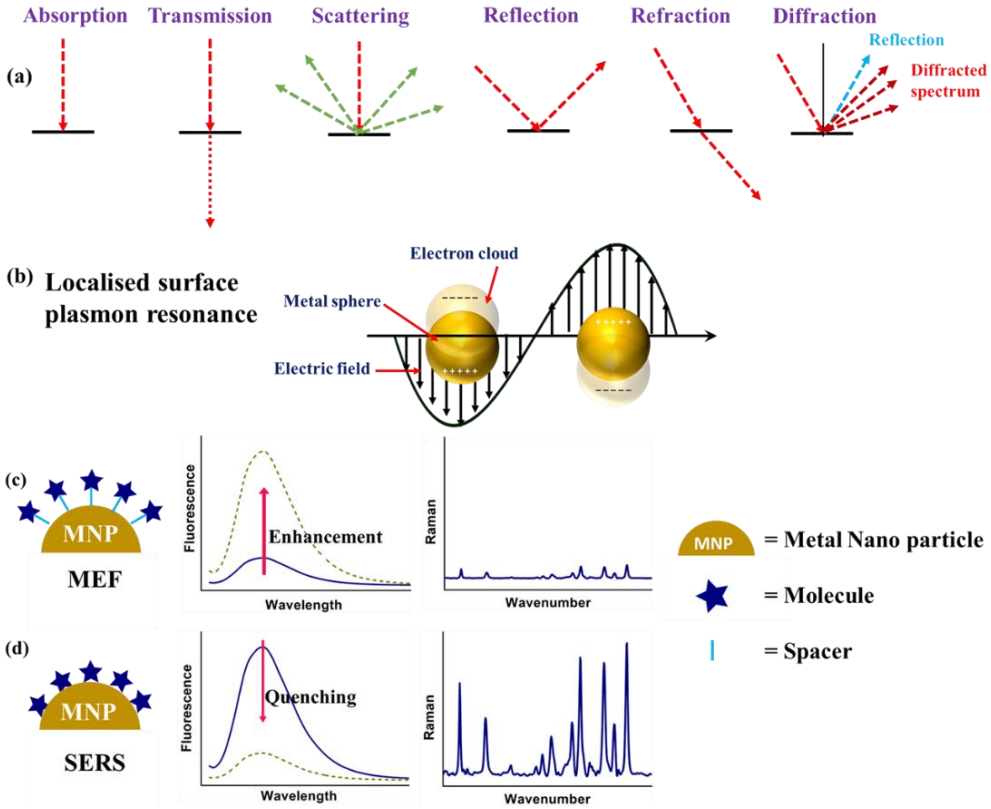

Figure 1.1. Schematic representation of (a) light matter interaction in bulk condition, (b) Localised surface plasmon observed in nano domain, (c) Metal Enhanced Fluorescence (MEF) and (d) Surface Enhanced Raman Spectroscopy (SERS).

Although there are numerous advantages, one of the most challenging task to achieve MEF is the synthesis of monodispersed spherical/anisotropic MNPs to ensure uniform hotspot formation and higher enhancement factors. Also, there are many MEF studies in solid state, there is an immediate need for devolpment of MEF systems in aqueous phase for easy biological and sensing applications. In case of MESOG systems reported in the literature, there is only enhancement of fluorescence or singlet oxygen but not both simultaneously. We found that there is need for devolopment of systems with simultaneous enhancement of fluorescence and singlet oxygen for image guided Photo Dynamic Therapy (PDT) applications. Also the major drawback associated with the synthesis of SERS substrates is the facile substrate synthesis, stablity, uniformity and reproducibility. In this thesis, we tried to address all these drawbacks for better plasmonic activities.

1.2. Background of the present thesis

This thesis provides a detailed account on the synthesis and characterization of various Nanoparticles, SERS substrates. It also describes the utilization of these substrates for plasmon enhanced spectroscopy and for their applications in ultra-sensitive detection of analytes and in theranostics.

1.2.1 Metal Enhanced Fluorescence (MEF)

When electromagnetic radiation is incident on the molecule, the chromophores present in them takes some energy from the incoming light and the process is known as absorption and occurs in ~10^{-15} s. When chromophore absorbs light which is equal or greater to the energy difference in the electronic states of the molecule, it excites to higher energy levels. The lifetime of molecule in excited state is very short and the electrons try to come back to its ground state by losing the absorbed energy in form of radiation or heat known as radiative and non-radiative relaxation respectively. Depending on the nature of the electronically excited state radiative decay can be broadly categorised into two types, fluorescence and phosphorescence. When electron combes back from singlet excited state in a spin allowed state by emitting a photon of different wavelength compared to absorbed wavelength, the phenomenon is called fluorescence and takes place in ~10^{-9} s. On the other hand, phosphorescence is a

slightly slow process and, in this electron, comes back to ground state from triplet excited energy levels in a spin forbidden state by emitting radiation. This process occurs in milli seconds time scale.

But when electromagnetic light is incident on a molecule near to MNPs, those NPs have the ability to confine and enhance the incident electric field when their LSPR is excited by electromagnetic radiation. As a result, confined electron oscillations at LSPR lead to tremendous enhancement of the local electric field, which are commonly several orders of magnitude higher than the incident field. But, the local electric field decays exponentially with increase in distance from the metallic surface (in the range of 10 nm to 30 nm). When fluorophores are placed in close proximity but to an optimum distance from the surface, the surface plasmons can enhance the fluorescence intensity of a fluorophore and the phenomenon is known as surface enhanced fluorescence (SEF) or metal-enhanced fluorescence (MEF) (**Figure 1.2**).[17-19] MEF depends on several factors such as size of MNPs, structure of MNPs, composition of MNPs and distance between fluorophore and MNP.

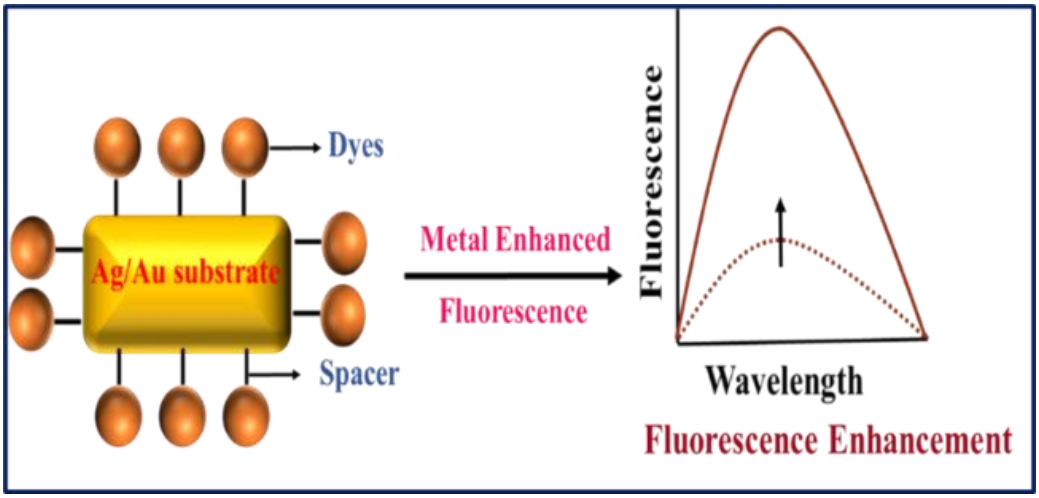

Figure 1.2. A schematic representation showing the enhancement of fluorescence of dyes in presence of MNPs at appropriate distance.

1.2.1a. Size dependence on MEF:

The size of the metal core plays an important role in MEF. Different MNPs would have different extinction spectra which is the sum of absorption and scattering cross sections of MNPs. For MNPs of radius r, the scattering scales are r^6, which grows very quickly with increasing particle size and therefore higher enhancement in fluorescence

would result from larger MNPs because they tend to scatter more. Whereas in smaller MNPs, absorption is dominant over scattering. Also, the qualification is that MEF efficiency increases with increasing core size to a point, after which the EF decreases, and that size is controlled by the quality of the dipole emission. In one of the works, Pawar et.al have shown that 33nm AuNPs exhibited maximum MEF compared to 18 or 160 nm AuNPs and they explained the possible reason in terms of scattering and absorption.[39] Nakamura et al also showed the importance of size of MNPs on the MEF. They synthesized AuNPs of sizes varying from 20 to 250 nm and found that 100 nm AuNPs gave them maximum MEF.[40]

1.2.1b. Shape dependence on MEF:

Shape of the MNP plays an important role in determining the LSPR, which in turn effects the extent of MEF. For spherical MNPs due to the symmetry, a nanosphere fundamentally displays dipolar resonance with inseparable longitudinal and transverse modes. However, in case of anisotropic NPs both transverse and longitudinal modes are seen at nanorods from these two modes. The longitudinal and transverse plasmon modes are corresponding to each resonant peak in the two plasmon modes. This concept leads to the introduction of various nanostructures of different shapes for attaining multipolar resonances. Various nanostructures such as rods,[41] plates,[42] shells,[43] cubes,[44] nano discs,[45] nano wires,[46] nano stars,[47] nano porous[48] and continuous films[49] are explored in recent years for attaining maximum MEF.

1.2.1c. Composition dependence on MEF:

The optical resonances of MNPs can be tuned over a wide spectrum of wavelengths, from UV-vis to NIR, by changing their structure and composition. Particularly, tuning the wavelengths in NIR region between 800-1200 nm is known as tissue transparency window where light can penetrate through both water and human tissues can be used for biological applications. For example, Ag has surface plasmon resonances around 400nm and on the other hand Au shows LSPR bands above 500 nm. So, synthesizing

bimetallic nanostructures can be of greater importance in facile manipulation of LSPR wavelengths. Also, few studies reported that doping of Au atoms in Ag nanoclusters has increased the efficiency of MEF.[50,51]

1.2.1d. Distance dependence on MEF:

Distance between fluorophore and MNP plays the most crucial role in determining the extent of MEF, as tuning the distance can cause fluorescence quenching to enhancement.[52-57] When fluorophore is close to the surface of MNP it can cause complete quenching of fluorescence due to energy transfer between MNP and fluorophore via Nanoparticle surface Energy Transfer (NSET).

1.2.1e. Mechanisms of MEF:

MEF is thought to be consisted of two mechanisms: (1) local electric field effect, (2) intrinsic radiative decay rate effect.[58,59] In the first mechanism, the LSPR effect produced by metal surfaces or particles can strengthen the local electric field. It is noteworthy that the lifetime and QY of fluorophores are unaffected by the local electric field effect. It was predicted that the maximum theoretical enhancement effect would be close to 140 folds. The second mechanism is that the MNPs can accelerate the fluorophore's intrinsic radiative decay rate (**Figure 1.3**). One can draw attention to the variations in the Jablonski diagram to more clearly understand this mechanism. In contrast to the local electric field effect, the intrinsic radiative decay rate effect increases QY while decreasing lifetime when fluorescence intensity is increased.

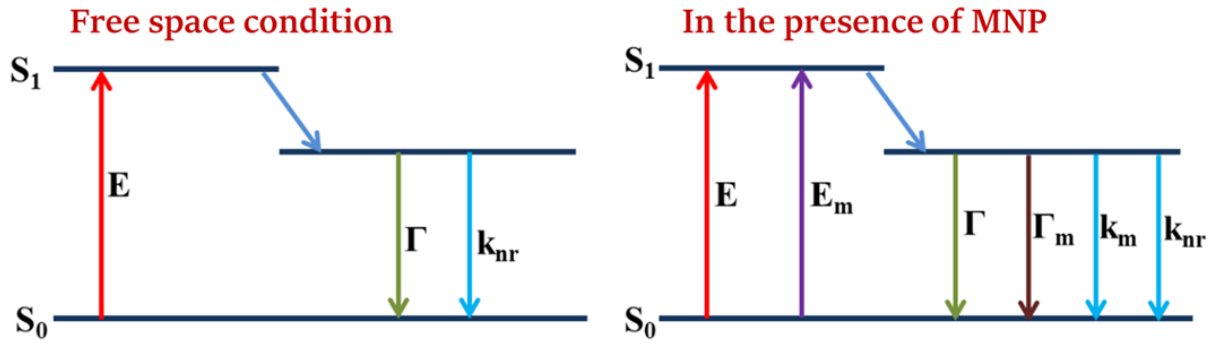

Figure 1.3. A simplified Jablonski diagram demonstrating MEF using radiative decay rate mechanism. E is Rate of excitation, E + E_m is the increase in rate of excitation in presence of metal, Γ is Radiative decay, k_{nr} is non-Radiative decay, Γ_m is the Radiative decay in presence of metal, k_m is non-Radiative decay in presence of metal.

1.2.1f. Advantages and applications of MEF:

MEF has several advantages like it offers enhanced emission, avoids photobleaching, it provides opportunities for imaging with significantly better resolutions, and also most importantly it can be used for sensitive single molecule detection. MEF exhibits multifarious applications in fields such as biotechnology,[18] biosensing,[34] bioimaging,[59] catalysis,[60] light emitting diodes,[61] biomedicine,[62] enhanced ratiometric sensing for food[63] and environmental pollutants detection[64] etc.

1.2.2. Metal Enhanced Singlet Oxygen Generation (MESOG)

Surgery, radiation and chemotherapy are the most commonly used ways in the treatment of cancers, but they possess some serious side effects. Therefore, oncologists and medical physicists came up with a novel therapy for the treatment of cancer known as photodynamic therapy (PDT).[65,66] PDT is a minimal invasive technique and basically involves the use of a photosensitizer (PS) molecules and light, to produce reactive oxygen species (ROS) which can be either used for deactivation of bacterial cells or even in killing cancer cells. One of the most crucial factors for PDT is the rate of ROS generation by PS and in this context plasmonics is efficiently used by scientists in the recent years, for enhancement of ROS generation, known as Metal enhanced singlet oxygen generation (MESOG) or metal enhanced PDT.[67-70]

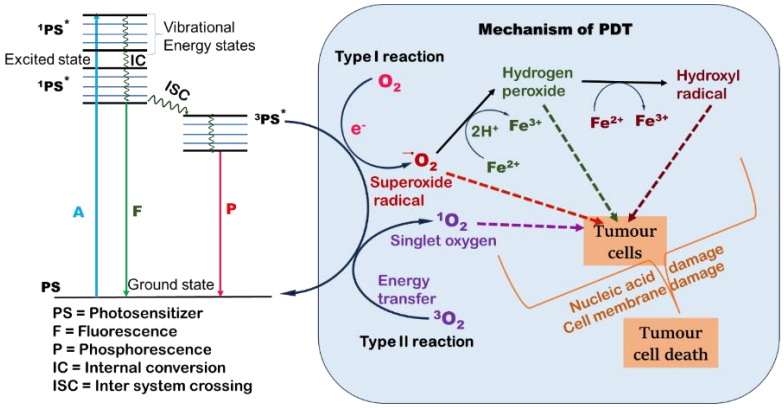

Figure 1.4. is the representation of Jablonski diagram showing the mechanism as well as types of PDT.

1.2.2a. Types of PDT

The photosensitizing process begins with the absorption of a light photon by the photosensitizer in its ground state, leading to its transition to the short-lived excited singlet state. In the presence of MNPs, there would be an enhanced absorption and this

singlet state can either return to the ground state, emitting light in the form of enhanced fluorescence, or it can convert to the more stable triplet excited state through intersystem crossing. In the triplet state, an electron in a higher orbit undergoes a spin conversion, allowing it to participate in chemical reactions. As a result, the photodynamic action primarily occurs when the photosensitizer is in the triplet state, which is long-lived enough for these reactions to take place (**Figure 1.4**). Two types of photodynamic reactions are involved in this process.[71,72] The first type, known as type I photo processes, entails electron or hydrogen transfer reactions between the triplet photosensitizer and other excited photosensitizer molecules. These reactions generate reactive intermediates, such as superoxide's, hydroperoxyls, hydroxyl radicals, and hydrogen peroxide, which can be harmful to cells. Eventually, the photosensitizer typically returns to its ground state. The second type, termed type II photo process, involves an electron spin exchange between the photosensitizer in its triplet state and ground-state triplet dioxygen. This interaction produces a cytotoxic excited singlet state of oxygen while causing the photosensitizer to revert to its ground state. Both type I and type II reactions lead to the oxidation of biomolecules in the cell, but $^1O2$ (singlet oxygen) is considered the primary mediator of phototoxicity in photodynamic therapy.

1.2.2b. Factors affecting MESOG

Choice of PS is important for improving singlet oxygen quantum yield ($^1O_2$ QY).[73] Also, a brightly fluorescent water-soluble PS would be advantageous for image guided PDT because enhanced fluorescence would lead to simultaneous visualization of tumour location.[74] Notably, conventional PS's exhibit extremely low fluorescence. Furthermore, the hypoxic tumour environment leads to a shorter lifetime of reactive oxygen species (ROS), necessitating higher PS concentrations for effective loading. However, high PS loading results in minimal production of singlet oxygen generation (SOG) and fluorescence due to the quenching effects caused by aggregation. Consequently, this procedure requires extended exposure to light, significantly restricting its practical use. Therefore, in recent years aggregation-induced emission (AIE) molecules were explored by the researchers to overcome these limitations.[75,76]

Furthermore, similar to MEF, MESOG is also affected by size, shape, composition of MNPs and the distance between MNP and PS. Many scientists have explored the roles of MNPs in SOG. Belinda Heyne and her group worked extensively on amplifying the rates of $^1O_2$ QY of Rose Bengal in the presence of AgNPs.[77] In another report, they explored the role of distance between MNP and PS and found maximum MESOG when the separation distance between them is ~20 nm.[78] In another report, they identified that anisotropic silver nano cubes produced more SOG compared to spherical NPs.[79] In other report, the group had explored the role of composition of MNP and their near field, far field effects on rates of SOG generation.[80]

1.2.2c. Applications and limitations of MESOG

MESOG plays an important role in selective organic synthesis, waste water treatment, enhanced bacterial inactivation, enhanced PDT etc. Understanding the limitations for better MESOG is important and the major drawback faced is the choice of PS, poor solubility of PS, and lack of systems which can simultaneously enhance fluorescence as well as ROS generation capacity.[81-84]

1.2.3. Raman Spectroscopy

1.2.3a. Introduction, principle and selection rules of Raman Scattering

Chandrashekar Venkata Raman in 1928 observed inelastic scattering of light experimentally and named it as Raman effect for which he was later awarded a noble price in 1930.[85] The measurement and analysis of inelastically scattering photons from matter on interaction with electromagnetic radiation, containing the useful information on the vibrational and rotational modes or electronic excitation energy is called Raman spectroscopy.[86]

The process of photon interacting with matter can be explained by showing the vibrational states associated within the electronic states as depicted in the **figure 1.5**. When light is incident on molecule, the incident photon stimulates the material system into a virtual state and it has the potential to re-emit a photon with the same energy, returning to its original vibrational ground state. This phenomenon is referred to as elastic scattering or Rayleigh scattering.[87] However, if the system is prompted to a virtual state and releases a photon with a different energy, it undergoes inelastic

scattering, known as Raman scattering. Raman scattering takes place in two ways: Stokes-Raman scattering and anti-Stokes Raman scattering.[88] In the case of Stokes-Raman scattering, the energy of the scattered photon is decreased compared to the incident photon by an amount equal to the excitation energy of one of the material's modes that the photon interacts with. Conversely, in anti-Stokes Raman scattering, the scattered photon possesses more energy than the incident photon by an amount equivalent to one of the material system's excitation modes. The probability of observing anti-Stokes Raman scattering is significantly lower than that of Stokes Raman scattering. This discrepancy is due to its dependence on the number of molecules present in the excited modes at a specific temperature, following the Boltzmann distribution.

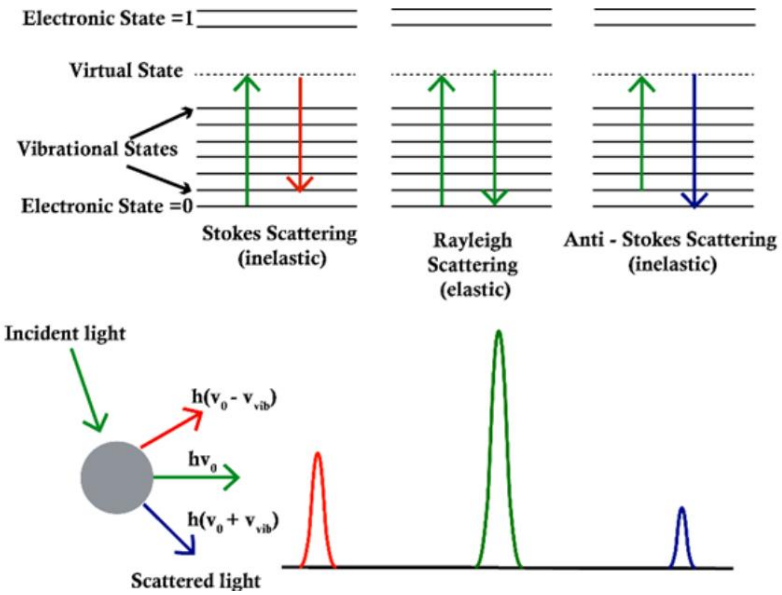

Figure 1.5. Representative description of Stokes, anti-Stokes, and Rayleigh process. (this image is taken from the chapter "Recent trends in core–shell nanostructures–based SERS substrates" from the book "Nanomaterials for Sensing and Optoelectronic Applications").

For a molecule to be Raman active there should be change in polarizability of the molecule. Polarizability α, represents the ability of an applied electric field to induce dipole moment in the atom or molecule and is represented as

$$I_{Raman} = \mu_{induced} = \alpha . E$$

where I_{Raman} is the intensity of Raman spectrum,

$\mu_{induced}$ is the induced dipole moment,

α Is the polarizability and

E is the applied electric field.

Atoms have isotropic polarizability, whereas molecules can have anisotropic polarizability depending on the symmetry of the molecule. Specific changes in a molecule's rotational or vibrational behaviour causes polarization. As a result, the molecule's electron cloud can be distorted by the oscillating electric field of electromagnetic radiation, creating what is known as an induced electric dipole moment. This induced dipole moment then emits or scatters electromagnetic radiation, which gives rise to what is called the Raman spectrum. The selection rule governing Raman transitions between different states stipulates that such transitions can only occur optically if the polarizability derivative with respect to the normal coordinate, denoted as

$$\delta\alpha/\delta Q \neq 0$$

where $\delta\alpha$ is the change in polarizability and δQ is the change in position with respect to normal coordinates

1.2.3b. Advantages and disadvantages of Raman scattering

Raman spectroscopy has several advantages compared to several other techniques. Some of the advantages are its fingerprint specificity, analysis of aqueous samples, non-destructive analysis, requires no or minimum sample pretreatment, shorter analysis times, can detect two or more samples at the same time due to their distinct and unique vibrational patterns, and can be used in wide concentration range including single molecule analysis. Although there are several advantages, there are few limitations such as inelastic scattering is inherently weak phenomenon so it requires sophisticated instruments for collecting Raman spectra of molecules and also requires long exposure to laser causing potential damage to samples. These disadvantages are overcome by integrating Raman spectra with nanoengineering techniques such as plasmonics to produce enhanced Raman signals.

1.2.3c. Types of Raman spectroscopy

Since Raman signals are inherently weak, several techniques are discovered to amplify the intensity of signal and to decrease the signal to noise ratio. Few of them are simulated Raman spectroscopy, Resonance Raman spectroscopy, Coherent Anti stokes

Raman spectroscopy, surface enhanced Raman spectroscopy and Tip enhanced Raman spectroscopy.

I. Simulated Raman Spectroscopy

This technique involves exposing the sample to a strong laser pulse, which enables the detection of a novel non-linear phenomenon in the Raman signal. It can be seen from a comparison of continuous wave lasers with an electric field of only about 10^4 V cm^{-1} and pulsed lasers with an electric field of roughly 10^9 V cm^{-1} that the latter converts a significantly greater portion of incident light into standard Raman scattering, leading to a noticeably better signal-to-noise ratio. When compared to normal Raman signals, the Stimulated Raman approach has impressively shown a Raman signal augmentation of 4-5 orders of magnitude.[89a]

II. Resonance Raman spectroscopy

Resonance Raman spectroscopy (RRS) is a specialized Raman technique where the energy of the incident photons closely matches an electronic transition within the compound or material being studied.[89b] This frequency alignment, known as resonance, results in a significant boost in the intensity of Raman scattering, enabling the analysis of chemical compounds present even at low concentration. It can enhance Raman signals in the 2-3 orders of magnitude.

III. Coherent Anti-stokes Raman spectroscopy (CARS)

In CARS, the sample is irradiated by two potent lasers that are oriented in the same direction, as opposed to the traditional single laser used in other systems. The first laser typically runs at a constant frequency, whereas the second laser's frequency can be changed to match the frequency of a particular Raman-active mode of interest.[89c] Due to careful tuning, the required Raman mode will always match to the frequency difference between the two lasers. CARS only generates one Raman peak of interest at any one time as a result of its extreme selectivity.

IV. Surface enhanced Raman spectroscopy (SERS)

In SERS technique enhancement of Raman signal of analyte molecules takes place in the presence of MNPs due to their plasmonic effects. SERS produces 10^6-10^{14} folds enhancement in the Raman signals. SERS is widely used compared to remaining other

techniques due to its easy substrate fabrication, sample preparation and less time-consuming operation.

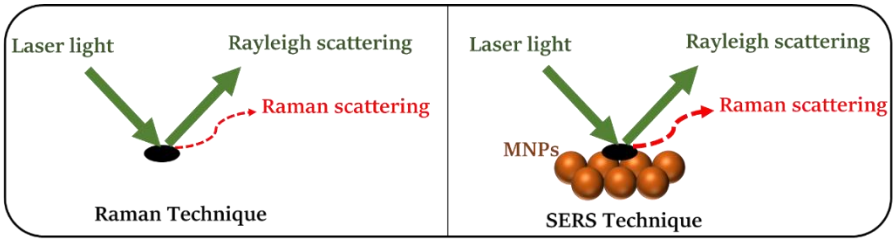

Figure 1.6. A Graphical representation of Surface Enhanced Raman Spectroscopy.

V. Tip enhanced Raman spectroscopy (TERS)

TERS is a variant of SERS that combines Raman spectroscopy with scanning probe microscopy.[89d] TERS enables the attainment of high spatial resolution chemical imaging. It has been regularly demonstrated to achieve manometer-level spatial resolution in normal laboratory conditions, and even better results can be obtained under ultralow temperatures and high pressure. The maximum resolution achievable using an optical microscope, including Raman microscopes, is constrained by the Abbe limit, which is approximately half the wavelength of the incident light. Furthermore, with SERS spectroscopy the signal obtained is the sum of a relatively large number of molecules. TERS overcomes these limitations as the Raman spectrum obtained originates primarily from the molecules within a few tens of nanometres of the tip.

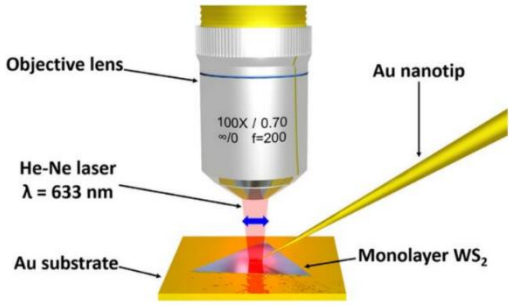

Figure 1.7. A schematic representation of Tip enhanced Raman spectroscopy. (The figure is taken from scientific reports journal "10.1038/srep40810").

1.2.3d. Surface enhanced Raman spectroscopy (SERS)

In this thesis SERS is extensively studied. So, we will discuss about the SERS phenomena in detailed starting from its discovery. In 1970s, Raman spectroscopy experienced a significant breakthrough, achieved through experiments conducted by

three distinct research groups. They discovered a remarkable improvement in Raman signals, exceeding expectations by a million times when molecules were adsorbed onto a specially prepared silver surface. Fleischmann et al. were the first to observe intense Raman scattering in 1974, from an aqueous solution of pyridine adsorbed onto a roughened silver electrode surface.[90a] Subsequently, in the late 1970s, two independent groups, Jeanmaire and Van Duyne from Northwestern University,[90b] and Albrecht and Creighton from the University of Kent,[91] attempted to explain the mechanism behind this substantial Raman signal enhancement. They recognized that the observed high intensities might not solely result from an increased number of scattering molecules. This phenomenon of enhancement of Raman signals in molecules is known as SERS (**Figure 1.7**).[23,24] SERS is an exceptionally potent, non-invasive, and highly sensitive analytical method that facilitates rapid and effortless detection of analytes, even at the level of individual molecules. In SERS, the Raman signals of polarizable molecules, when exposed to laser irradiation, are amplified by substantial local fields that are plasmonically enhanced at the surfaces or junctions of metallic nanostructures. This technique significantly broadens the scope of traditional Raman spectroscopy, as it not only provides molecule-specific chemical signatures but also achieves heightened sensitivity by overcoming the inherent weakness of Raman scattering signals. Further advancement in SERS spectroscopy is achieved by surface enhanced Resonance Raman Scattering or spectroscopy (SERRS).[92] SERRS phenomenon takes place on the substrates which have its plasmonic extinction coinciding with the laser used giving an additional enhancement to Raman signals.

a. Mechanism of SERS

The enhancement factor observed in Surface-Enhanced Raman Spectroscopy (SERS) signals from molecules adsorbed on coinage metals such as silver, gold, and copper spans an impressive range from 10^6 to 10^{14}.[23,24] This variation depends on multiple factors, including the surface's morphology, the chemical properties of the adsorbed molecules, and several other considerations. Unravelling the mechanisms behind such a substantial enhancement has been a subject of dedicated theoretical efforts ever since

SERS was discovered. Primarily, two mechanisms are proposed to account for the enhancement: a long-range classical electromagnetic enhancement and a short-range first-layer contribution that exhibits chemical specificity and vibrational selectivity. The electromagnetic effect is grounded in the concept that both the incident and scattered fields near the surface experience enhancement through surface plasmon resonance. Conversely, the other model involves a charge-transfer interaction between the adsorbed molecule and the metal surface, which is particularly favourable for molecules directly adsorbed onto the surface. In the electromagnetic enhancement mechanism, a molecule brought near the SERS-active surface of a metal becomes coupled with the localized surface plasmon, leading to enhanced Raman signals. On the other hand, in the chemical enhancement mechanism, charge transfer occurs between the adsorbed molecule and the metal surface, resulting in the observed enhancement of the Raman signal. the SERS EF was calculated by using the equation:

$$\mathbf{EF = (I_{SERS}/I_{Raman}) \times (N_{Bulk}/N_{Surface})}$$

Where I_{SERS} and I_{Raman} were the intensities of a band in SERS and normal Raman spectra of the any Raman reporter molecule and N_{Bulk} and N_{SERS} are the number of molecules in Bulk and SERS condition respectively.

b. Factors affecting SERS

From the mechanism it is clearly understood that electromagnetic enhancement plays an important role in determining the extent of enhancement of Raman signals.[93] EM enhancement of SERS substrates is affected by many parameters such as size,[94] composition[95] and shape[96] of NPs present in SERS substrate, wavelength,[97] polarisation,[98] and angle of incidence of excitation laser,[99] adsorption properties of analytes on SERS substrate,[100] and intrinsic Raman cross section of the molecule.[101] Keeping in mind all these parameters scientists tried and optimized various SERS substrates made of metal electrodes, ordered metallic nanostructures, colloidal MNPs, hybrid nanomaterials such as alloys, core shell Nano structures, Planar hybrid SERS substrates made using soft lithography. Another important factor to consider during the synthesis of SERS substrates is the reproducibility and stability of SERS substrates.

c. Applications of SERS

Due to its unique finger print patterning, sensitivity till single molecule level and multiplexing ability SERS finds its applications in a wide variety of fields such as in chemical sensing of heavy metal ions,[102] explosives sensing,[103] food,[104] and environment contaminants,[105] pesticide detection,[106] etc. it also plays a major role in biosensing of proteins,[107] amino acids,[108] target DNA identification,[109] drugs[110] and pharmaceutical adulterants[111] sensing, and even used in the detection of cancers[112] and miscarriages of pregnancy in early stages.[113] It is also used in forensic science for assessment of seized drugs.[114]

1.3. Relevance of the present study

A substantial amount of experimental data is present in the literature about the systems displaying MEF and MESOG, and SERS. In this thesis, we show the development of MEF systems in aqueous phase, as well as we attempted to synthesis hybrid plasmonic systems with photosensitizers which are useful for simultaneous enhancement of fluorescence and singlet oxygen generation for useful PDT applications. We also studied the role of anisotropic MNPs in achieving different extents of MEF and MESOG. In SERS, most of the available data in the literature are based on the mono-metallic Ag and Au substrates. Therefore, in this thesis, the role of bimetallic and trimetallic alloy SERS substrates were explored in detail for better chemical and biological sensing application. In summary, our study focuses on the outcome of the different plasmon-driven optical interaction, experienced by the emitter/analyte molecule when it is present very close to plasmonic noble metal nano particles such as Ag, Au and Cu. The findings of this work can be extended and utilized for biosensing, plasmonic catalysis, MESOG applications. In **chapter 2,** the technical details of the different instruments used for the study along with chemicals used and experimental procedures are described in detail.

In **chapter 3**, we reported the synthesis of a sensor comprising of multilayered architecture of AuNPs, a silica shell around it and finally a polymer poly(allylamine)hydrochloride (PAH) adsorbed on it. Herein we synthesized AuNPs of different sizes and also, we varied the silica shell thickness so as to maintain the

different distances between AuNP and polymer. From this study, we observed that 45 nm AuNPs showed the best MEF effect, when the distance between AuNP and PAH was ~11 nm. We then used the best MEF sensor to detect picric acid and found that picric acid caused fluorescence quenching and could be detected till 79 nm. Later, we have used the sensor in detection of picric acid in real samples.

In **chapter 4**, we studied the role of MNPs composition, MNP anisotropy, distance between MNP and Photosensitiser (PS) for producing simultaneous MEF and MESOG. In **chapter 4A**, we explored the role of Ag/Au NPs in MEF and MESOG of a neutral AIEgen NP-4-Py. For this we synthesized AgNP and AuNPs with a similar average diameter and used two different kinds of spacers like silica coating and layer by layer assembly of polymers and then adsorbed the neutral PS and studied the concurrent MEF and MESOG effects of these MNPs on PS. From the synthesized library of AIEgens we observed that AuNPs with 2 polymer layer spacer having an average thickness of ~11.2 nm showed the best MEF as well as MESOG efficiency. Later, we have successfully employed these NPs for imaging in niosomes. In **chapter 4b**, we explored the role of different AR GNRs and different spacer thickness for best MEF and MESOG effects. In this work we tried to understand the role of many radiative and non-radiative processes such as NSET, near field and far field effects on the rates of MEF and MESOG. We observed that GNRs with an aspect ratio of 2.95 gave the best MEF as well as MESOG efficiency and concluded that the observed result is due to the dominant scattering phenomenon taking place on the surface of GNR.

In **chapter 5**, we explored the role of bimetallic MFs on SERS and SERRS phenomena and used it for detecting single molecule level of Rhodamine 6G (R 6G) and also in multiplexed biosensing of anti-cancer drugs. In **chapter 5A**, we optimized the reaction temperature and synthesized bimetallic Ag-Cu MFs using a simple thermolysis method. We also synthesized MFs with different Cu compositions and carefully studied the SERS efficiency as a function of composition. We observed that MFs synthesized with 90% Ag and 10% Cu gave SERS EF of ~10^8 and could achieve single molecule sensing of R 6G and also R 6G can be detected till 10 zM concentration. In **chapter 5b**, we used two different laser lines and two different substrates like 90-

10 Ag-Au and 90-10 Ag-Cu MFs and explored various Raman phenomenon such as pre resonance Raman, Resonance Raman Scattering, SERS, and SERRS. We noticed by using 632.8 nm laser on 90-10 Ag-Cu MF substrate, we could sense anti-cancer drug Mitoxantrone (MTO) till fM concentration. We also successfully used it to perform multiplexed detection with other potential anti-cancer drug Doxorubicin (DOX) in both water and mice blood plasma.

In **chapter 6**, we synthesized trimetallic MF substrates made of Ag, Au and Cu and studied their role in SERS. We made use of superior plasmonic activity of Ag, chemical stability of Au and structural stability of Cu integrated in single structure and studied the EF as function of composition. Since our earlier studies showed best SERS EF with 90% Ag and 10% Au/Cu, we restricted ourselves to changing the % composition of Au and Cu keeping the % of Ag constant. Among all the synthesized Trimetallic MFs (TM MF), substrates with TM73 and TM37 gave similar enhancement factors compared to 90-10 Ag-Cu MFs but the only difference is former being Au rich surface and later being Cu rich according to XPS studies. We then used these MFs for sensing of important bio thiol L-Cysteine, and aromatic thiols and its derivatives and found that only Au rich TM73 could detect L-Cys in nM level, aromatics thiols in pM level. Later we also studied the adsorption of L-Cys on TM73 substrate at different pH. Finally, we could also successfully detect L-Cys using this substrate even in the presence of potential interference Glutathione and thiophenol.

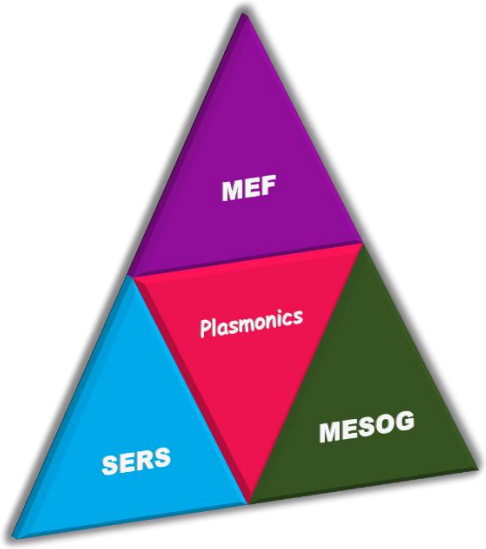

Figure 1.8. A simple representation of various plasmon driven processes studied in this thesis.

Chapter 2

Materials and characterization methods

In this chapter, we discussed about the reagents, synthesis procedures and instruments used for the experimental work carried out in this thesis.

2.1. Introduction

Various spectroscopic methods and characterization techniques are used to study the nanoparticles and synthesized SERS substrates, which will be discussed in this chapter. Most of the studies were performed using Fluorimeter and Raman spectrophotometer. Various other characterization techniques such as SEM, UV, XRD, XPS, XRF, TCSPC, DLS, FTIR, which were used to characterize the NPs as well as SERS substrates will be discussed in this chapter. A complete description of material synthesis, sample preparations used for experiments are discussed. All the list of reagents used to prepare nano materials are provided.

2.2. Materials and Reagent

2.2.1. Chapter 3A

All the chemicals obtained are commercially and are used without any purification. Gold (III) chloride trihydrate ($HAuCl_4.3H_2O$) was purchased from Sigma Aldrich. Trisodium citrate (TSC), Sodium borohydride, L- Ascorbic acid, Ammonia solution were procured from SD fine-chem limited (SDFCL). Tetra ethyl orthosilicate (TEOS) was obtained from TCI chemicals. Poly(allylamine)hydrochloride was purchased from Alfa Aesar and ethanol (HPLC grade) was bought from Pharmaco Aaper. Picric acid and all other nitro aromatics used for selectivity study were procured from Avra chemicals.

2.2.2. Chapter 4A and 4B

Silver Nitrate ($AgNO_3$), Gold (III) chloride trihydrate ($HAuCl_4.3H_2O$), Poly (sodium 4-styrene sulfonate) (PSS, MW=70000), cetyltrimethylammonium bromide (CTAB), Hydroquinone, 1,3-diphenylisobenzofuran (DPBF), Poly(ethyleneimine) 30% w/v aqueous solution (PEI, Branched MW=10000), Eosin Y, 3-aminopropyl triethoxysilane (APTES), were purchased from Sigma Aldrich. Poly (allylaminehydrochloride) (PAH) was procured from Alfa Aesar. Tannic Acid, Trisodium citrate (TSC), Poly (Vinyl Pyrrolidone) (PVP K-30 Pure), Sodium Borohydride ($NaBH_4$), Sodium chloride (NaCl), Ammonia solution (25%) were procured from SRL Chemicals. Tetraethyl orthosilicate (TEOS), and 5,5-Dimethyl-1-pyrroline-N-oxide (DMPO) was procured from TCI chemicals, India. Sodium azide was purchased from SRL, India. All chemicals are used as received without any further purification.

2.2.3. Chapter 5A, 5B and 6

Silver nitrate ($AgNO_3$), Tetra-octyl ammonium bromide (ToABr), Gold (III) chloride trihydrate ($HAuCl_4.3H_2O$), Doxorubicin hydrochloride (DOX), Rhodamine 6G were purchased from Sigma Aldrich. Mitoxantrone (MTO), and L-Cysteine was purchased from TCI chemicals India. Toluene (HPLC grade), Methanol (HPLC grade), Cupric chloride ($CuCl_2$), sodium chloride (NaCl), sodium borohydride ($NaBH_4$) was obtained from SD Fine-Chem Ltd. Coverslips (square shape 4cm^2 area) were procured from Bluestar company, India. Double distilled Millipore water was used for making all solutions. All glassware, coverslips, and silicon wafers were washed with Millipore water, acetone and dried well before use. All the solvents used are HPLC grade and are purchased from Finar Chemicals, India.

2.3. Synthesis procedures

2.3.1. Synthesis of Gold nanoparticles (AuNPs) (Chapter 3)

AuNPs were synthesized by seed growth method as reported by Ziegler *et al.*[1], with slight modification. The method involved the synthesis of gold seeds followed by their controlled growth. Seed particles were prepared by a reported method of citrate reduction.[2] Briefly, 2.5 mL of $HAuCl_4.3H_2O$ was diluted in 50 mL water and heated to boiling. To this, 2mL of 1% w/v TSC was added with vigorous stirring. The solution was kept to boiling for 5 min and later cooled to room temperature. They were used as seeds within 24 hours. The general method for growing seeds is as follows. Certain amount of seeds was diluted to 20 mL and placed in a two necked round bottomed flask. Then, to this 10 mL of solution A and B each were added separately over a period of 45 minutes under vigorous stirring. Later the mixture was kept under boiling for 30 minutes. Finally, the solution was allowed to cool down and used for further studies. Meanwhile, solution A was prepared by diluting little amount of 0.2% w/v $HAuCl_4.3H_2O$ to 10 mL. Solution B was made by diluting a mixture of 1% w/v Ascorbic acid and 1% w/v TSC stock solution to 10 mL. The comparative volume ratios for the mixing were as following: solution A: Ascorbic acid: TSC = 8:2:1. AuNPs of different sizes with little anisotropy were synthesized by varying the volume of seed used during the growth process.

2.3.2 Synthesis of Au@SiO_2 core-shell nanoparticles (Chapter 3)

To prepare the core-shell Au@SiO_2 nanoparticles, we used a procedure as reported by Graf *et al.*[3] Briefly, 1 mL of synthesized AuNPs were dispersed in 9 mL of ethanol. Then the pH was adjusted to 11 by dropwise addition of 0.1M NaOH. To this, 200 µL ammonia and various amounts of TEOS (100 µL to 1000 µL) were added and stirred for 30 minutes to obtain Au@SiO_2 core-shell nanoparticles with different silica layer thickness. They were later centrifuged at 7500 rpm for 10 minutes and the supernatant was rejected. The pellet which contained Au@SiO_2 was dispersed in 10 mL of ethanol.

2.3.3. Deposition of PAH on Au@SiO_2 (Chapter 3)

Finally, the sensor was developed after the deposition of PAH on the silica surface, by following a known procedure.[4] Briefly, to the synthesized Au@SiO_2 core shell NPs 200 µL of 1% PAH was added and stirred for 30 minutes. Later, this was centrifuged at 7000 rpm for 20 min and supernatant was discarded. The obtained pellet was dispersed in ethanol. This solution was used for all the studies and was characterized thoroughly.

2.3.4. Synthesis of Silver NPs (Chapter 4A)

AgNPs were synthesized according to a known procedure from the literature by using tannic acid (TA) and trisodium citrate (TSC) as reducing and capping agents.[5] Briefly, 22.5 mg of $AgNO_3$ (1.32 mM) was dissolved in 100 mL of water. Another 25 mL of an aqueous solution, containing 62 mg of TA (1.47 µM) and 90 mg of TSC (12.2 mM) was prepared separately. Both mixtures were heated to 60 °C. Then they were mixed under vigorous magnetic stirring and maintained at 60 °C temperature for 5 min. Later, they were brought to boiling for 20 min and cooled to room temperature. The greyish brown solution was purified by centrifugation at 13500 rpm for 20 min. The obtained pellet was re-suspended in 90 mL of water and the colloidal suspension was then mixed with 6.5 mL of aqueous PVP solution (115 mg). The solution was stirred overnight at room temperature and then purified by centrifugation at 13500 rpm for 20 min. The resulting PVP-coated AgNPs were redispersed in 90 mL of water and the process is repeated thrice and the final solution which was dispersed in 90 mL water was kept for further use.

2.3.5. Self-assembly of polyelectrolytes on AgNPs (Chapter 4A)

The 'layer by layer' (LBL) approach was used for the self-assembly of polyelectrolyte layers on the surface of AgNPs. LBL assembly was formed by depositing alternative layers of oppositely charged polymers or materials. The procedure employed for this assembly was taken from the literature and was used with slight modification in an expanded and scaled-up version.[6] Firstly, 10 mM solutions of PEI and PSS (based on monomer's molecular weight) were prepared in an aqueous 10 mM NaCl solution. Before polyelectrolyte coating, PVP-coated AgNPs were concentrated by two folds through centrifugation. Then, 30 mL of concentrated AgNPs solution was added dropwise to 37.5 mL of positively charged PEI under sonication. After sonicating for 5 min, the solution was magnetically stirred for 10 min at 600 rpm. Later this dispersion was centrifuged at 13000 rpm for 15 min and dispersed in 30 mL water. The resulting NPs were labelled as AgNP-1LBL. Further, 24 mL of AgNP-1LBL was added to 30 mL of negatively charged PSS under sonication. After sonication for 5 min and magnetic stirring for 10 min, the solution was centrifuged and dispersed in 24 mL water. The resulting dispersion was labelled as AgNP-2LBL. In the next step, AgNP-2LBL was coated with PEI following the same procedure and was labelled as AgNP-3LBL.

2.3.6. Synthesis of Ag@SiO_2 core-shell NPs (Chapter 4A)

Stober's method was employed for coating silica shells on AgNPs.[7] 1 mL of PVP stabilized AgNPs was added to 9 mL of ethanol under vigorous magnetic stirring. Various amounts of TEOS (20% v/v) varying from 5-30 µL were added to this solution. After 15 min, 0.25 mL of 25% Ammonia solution was added, and the reaction was left undisturbed for 20 hours at room temperature. After 20 hours, the solution was centrifuged at 10000 rpm for 10 min, washed with ethanol for 3 times, and redispersed in 10 mL water. Nanoparticles of different shell thicknesses (L) were synthesized by adding 6 different amounts of TEOS (5, 10, 15, 20, 25, and 30 µL), and were named as Ag@SiO_2-(1 to 6).

2.3.7. Synthesis of Gold NPs (Chapter 4A)

Synthesis of AuNPs followed a standard method as described by Turkevich and Frens, wherein, $HAuCl_4.3H_2O$ was used as a precursor for AuNPs and TSC played the role of

both reducing and capping agents.[2] Briefly, 50 mL of 0.25 mM aqueous solution of gold chloride was heated till 95 °C. To this, 0.5 mL of 1% TSC was added, and the solution was boiled for 30 min. The color of the solution changed to purplish red, indicating the formation of AuNPs. The solution was centrifuged at 10,000 rpm to remove excess or unreacted citrate and redispersed in water.

2.3.8. Self-assembly of polyelectrolytes on AuNPs (Chapter 4A)

AuNPs were stabilized using PVP, which acted as both capping and surface priming agents for further surface modifications. Briefly, 2 mL of AuNP solution was mixed with 2 mL of (1 mg /mL) aqueous PVP solution, and the reaction mixture was heated at 60 °C for 3 hours.[8] PVP-AuNPs were obtained by centrifuging the solution at 10000 rpm for 10 min. PVP stabilized AuNPs were functionalized by alternating layers of PEI and PSS, to form the layer-by-layer assembled AuNPs.[9] PEI was added to PVP-AuNPs such that the final concentration of PEI would be 0.8 mM, and the reaction mixture was stirred at 500 rpm for 24 hours. The solution was centrifuged at 12500 rpm for 20 min, and the pellet was re-suspended in water. This solution was labelled as AuNP-1LBL. 50 mL of AuNP-1LBL was taken and centrifuged again at 12500 rpm, and the pellet was re-suspended in 45 mL,10 mM NaCl solution. NaCl solution was used to minimize the repulsions between the polymers during the further reaction. To this, 5 mL of 10 mg/mL PSS solution (which was prepared in 10 mM NaCl solution) was added. The reaction mixture was stirred at 500 rpm for 4 hours and then centrifuged at 12500 rpm for 20 min and re-suspended in water. This solution was named as AuNP-2LBL. Further, 40 mL of AuNP-2LBL was centrifuged, and the pellet was suspended in 36 mL NaCl solution. Then 4 mL of 10 mg/mL PEI solution (prepared in 10 mM NaCl solution) was added to AuNP-2LBL. The reaction mixture was stirred at 500rpm for 4 hours, and the pellet was dispersed in 40 mL water. This solution was named as AuNP-3LBL.

2.3.9. Synthesis of Au@SiO_2 core-shell NPs (Chapter 4A)

For the preparation of Au@SiO_2 core-shell NPs, we employed the modified Stober's procedure described by Yang *et al.*[10] Precisely, 10 mL of AuNPs solution was centrifuged, and the pellet was dispersed in 300 µL of 0.1 mM citrate solution for the synthesis of core-shell particles. Stober's system was prepared by mixing 10 mL of

anhydrous ethanol, 150 µL NH_4OH, 375 µL water, and various TEOS amounts (2-10 µL). Immediately, 300 µL of gold colloid was added, and the reaction mixture was stirred for 12 hours at room temperature for the growth of the silica shell. Particles of different shell thicknesses were synthesized by adding 5 different amounts of TEOS (2, 4, 6, 8, and 10 µL), which were labelled as $Au@SiO_2$-(1 to 5).

2.3.10. Synthesis of silica NPs (Chapter 4A)

SiNPs were used as a control sample in MEF and ME-SOG measurements. 70 nm SiNPs were synthesized following a known procedure,[11] by hydrolysis and controlled condensation of TEOS in ethanol. Briefly, 0.02 moles of TEOS were solubilized in 100 mL of ethanol. 0.03 moles of NH_4OH and 0.1 moles of water were added to the above mixture. The reaction mixture was kept at constant stirring for 24 hours for the synthesis of SiNPs. Later they were centrifuged, and the pellet was redispersed in water. The centrifugation process is repeated thrice to ensure that the formed SiNPs are pure and are devoid of the unreacted starting materials used during the synthesis.

2.3.11. Synthesis of Span60-L64 hybrid niosomes (Chapter 4A)

Thin layer evaporation method was employed for the synthesis of Span60-L64 bilayer vesicles[12]. Span60-L64 (8 mM and 2 mM) and cholesterol (5 mM) were taken in a round bottomed flask and dissolved in 2:1 chloroform/methanol mixture. The solvent was then subjected to Rota evaporation under a vacuum of 20 Hg at 30 °C with 100 rpm to obtain a thin film in the round bottom flask. The film is then hydrated using 5 mL ultrapure water and vortexed for 5 min followed by sonication for 30 min to get final niosome suspension. Then 200 µL of this stock solution is diluted to 10 mL hybrid PS solution and used for further studies.

2.3.12. Synthesis of GNR of different Aspect ratio (Chapter 4B)

GNRs were prepared by a known procedure with a slight modification.[13] It is a two-step process which uses hydroquinone as mild reducing agent. The first step is the synthesis of seeds and the next is usage of seeds in growth solution for final GNRs preparation. The protocol for seed synthesis is as follows: 364.4 mg of CTAB was dissolved in 5 mL water under ultrasonication at 40 °C till the solution becomes clear and was then cooled to room temperature. 5 mL of 0.5 mM aqueous solution of $HAuCl_4$

was prepared separately. Once the CTAB solution had reached room temperature $HAuCl_4$ solution was added slowly under vigorous magnetic stirring. It was later followed by the addition of 600 µL of 10 mM ice cold $NaBH_4$ solution. A rapid color change was observed from yellow to brown indicating the formation of seeds. The seeds were left undisturbed for 2 hours before proceeding further. In the second step, for synthesis of different aspect ratio of GNRs, different concentrations of CTAB (10 mM, 20 mM, 35 mM, 50 mM, 75 mM and 10 mM) together with 220 mg of hydroquinone was dissolved in 50 mL water under ultrasonication at 40 °C till a clear solution was obtained and the solution was cooled to room temperature. After the solution attained room temperature 2 mL of 4 mM $AgNO_3$ solution was added and stirred for 10 min at 1200 rpm. It was then followed by the addition of 50 mL of 0.5 mM aqueous solution of $HauCl_4$. 12 µL of seeds were added immediately and stirred vigorously until the solution changed its color from yellow to dark pink. The initial color change was observed within 30 min, then the seeds were overgrown for overnight by further addition of 12 µL of seeds. Then the solution was centrifuged at 10000 rpm for 10 min and the supernatant was discarded, the pellet was again dispersed in 100 mL of Millipore water. Then solution is again subjected to centrifugation to remove excess CTAB and was then used for further studies. Then synthesized GNRs are stored at 4 °C until further use.

2.3.13. Layer By layer (LBL) Assembly on GNRs (Chapter 4B)

Self-assembly of oppositely charged polymers around GNRs was used for the coating of GNRs by LBL assembly. The synthesized GNRs were again centrifuged at 10000 rpm and redispersed in pure water to remove excess CTAB. Later, 60 mL purified GNRs were taken and added to 60 mL of negatively charged 2 mg/mL PSS in 1mM NaCl solution. The solution was stirred for 3 hours and then centrifuged at 15000 rpm for 20 minutes. The pellet containing GNR-PSS was dispersed in 60 mL Millipore water and the supernatant containing unreacted PSS was discarded. The centrifugation step was repeated three times to remove the excess unbound PSS. The solution was labelled as LBL a. In the next step, we have coated the obtained 50 mL LBL A with 50 mL positively charged 2 mg/mL PAH polymer in 1mM NaCl solution and the whole process

is repeated and the formed NRs were labelled as LBL b. like this we have coated 6 polymer layers on GNRs as shown in the scheme below and labelled as LBL a to LBL f.

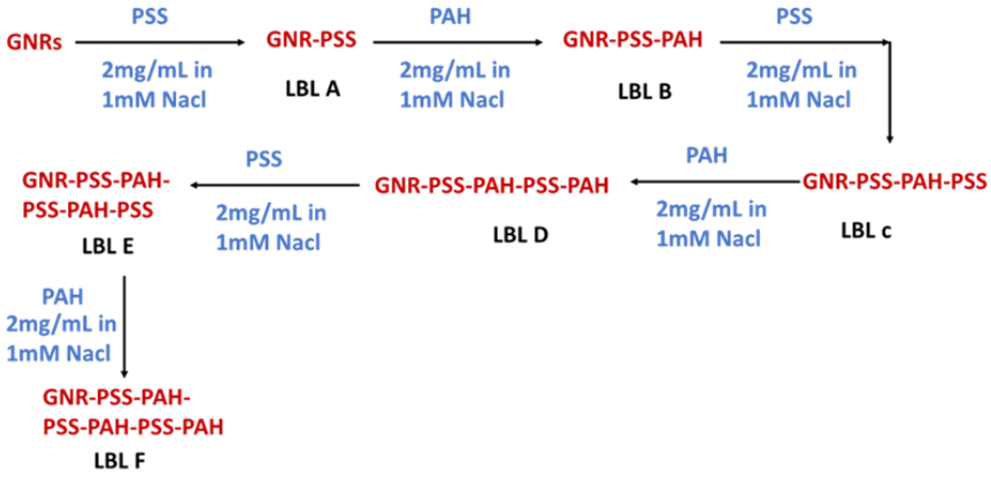

Scheme 2.1. A schematic representation of layer-by-layer (LBL) assembly of GNRs.

2.3.14. Eosin Y (Ey) Conjugation (Chapter 4B)

The optical densities (OD) values of GNR-LBL were adjusted to 0.1 by diluting it with Millipore water prior to Ey conjugation. Briefly, 10 µL of 10 mM Ey solution in ethanol was added to 10 mL of GNR-LBL solution and the reaction was allowed to proceed for 3 hours.[14] Later the solution was purified by centrifuging it at 15000 rpm for 30 min and the pellet was dispersed in water and the supernatant containing unreacted Ey was collected and stored. The UV-Visible spectra of supernatant was recorded to quantify the unbound Ey. The purification process is repeated several times until the supernatant was devoid of Ey abs peak and finally the obtained GNR-LBL-Ey conjugate was dispersed in Millipore water and used for further studies.

2.3.15. Synthesis of Amine Functionalized SiNPs (Chapter 4B)

Modified Stober's method was used for the one step synthesis of amine functionalized SiNPs.[15] This involves the simultaneous hydrolysis of TEOS and APTES ion the presence of NH_4OH and Ethanol. For the synthesis add 5 mL of TEOS, and 500 µL of APTES to solution containing 5 mL of NH_4OH, and 45 mL of ethanol. The solution was then allowed to react for 2 hours at room temperature using a magnetic stirrer. It was later centrifuged and the pellet was washed with water and ethanol to remove unreacted precursor and finally dried in an oven at 60 °C and the obtained powder is dispersed at 2 mg/mL concentration for further studies.

2.3.16. Eosin Y Conjugation on SiNP-NH_2 (Chapter 4B)

20 mg of amine functionalized SiNPs were taken and added to 10 mL of water. The solution was vortexed and sonicated for formation of uniform dispersion of SiNP-NH_2. To this solution 10 µL of 10 mM Ey solution in ethanol was added and the solution was stirred at 600 rpm for 3 hours using a magnetic stirrer. Then the solution was centrifuged and the pellet was dispersed in water. This process is repeated for at least 3 times to remove excess unbound Ey. The supernatant was collected in all the steps for quantification of amount of Ey conjugated on to NPs.

2.3.17. Synthesis of Ag-Cu MFs (Chapter 5A)

The procedure for the synthesis of MF was adapted from the earlier report.[16] To 1 mL of saturated NaCl solution, 1mL of 25 mM $AgNO_3$ solution was added under stirring to form white colloidal dispersion of silver chloride (AgCl). 2 mL of 50 mM ToABr was added to this, and the solution was shaken vigorously until AgCl was transferred to the organic phase. Subsequently, the solution was left undisturbed to allow phase separation. Then the organic phase was carefully transferred into another vial and the solution thus obtained was AgToABr. Following same procedure, CuToABr was also prepared using 25 mM $CuCl_3$ solution and 50 mM ToABr solution. Standard glass coverslips (~2 cm×2 cm) were used for the synthesis of MF substrates. For the synthesis of pure Ag MF, approximately 100 µL of AgToABr was drop cast on a clean coverslip and thermolyzed at 250 °C for two hours. Likewise, Ag-Cu alloy MFs were prepared by varying the percentage of copper (1% to 15%) by mixing appropriate quantities of AgToABr and CuToABr solutions. Beforehand, we also optimized the thermolysis temperature for Ag-CuBr formation. After thermolysis, samples were washed with toluene to remove unreacted precursors. The synthesized AgBr, and Ag-CuBr MFs were reduced to respective metals by dipping them in $NaBH_4$ (17mM) solution for 5 minutes.

2.3.18. Synthesis of Ag-Cu and Ag-Au MFs (Chapter 5B)

The synthesis procedure of the MFs was adapted from the previous reports of our group.[17,18] Briefly, metal alkyl ammonium complexes (MToABr where M= Ag, Au, and Cu) are prepared to using tetra octyl ammonium bromide as a phase transfer reagent.

At first, to 1 mL of saturated NaCl solution, 1 mL of 25 mM appropriate metal salt solution ($AgNO_3$/$HAuCl_4$/$CuCl_2$) was added. Then, 2 mL of 50 mM ToABr solution was added to this mixture, shaken vigorously, and allowed it to stand for phase separation. Then MToABr present in the organic phase was collected and used to synthesize micro flowers using further steps. Bimetallic flowers with various compositions of Ag-Au and Ag-Cu were prepared by mixing various ratios of AgToABr, AuToABr, and CuToABr (for ex, 10% Ag-Au, 10% Ag-Cu MFs and the number represents the percentage of Au/Cu). Then 40 µL of monometallic or bimetallic ToABr solution was drop cast on a 2 x 2 cm^2 coverslip and thermalized at 350^oC for 2 hours resulting in respective pristine metallic bromides. These metal bromides were then reduced to corresponding mono or bimetallic MFs by reducing them with 17 mM $NaBH_4$ solution for 5 min.

2.3.19. Synthesis of Trimetallic Ag:Au:Cu Microflowers (Chapter 6)

The procedure for the synthesis of Trimetallic MFs was adapted from the literature and used with minute modifications. Firstly, the metal (Ag, Au or Cu) salts are dissolved in water to make respective aqueous metal salt solutions of concentration 25 mM each. Then individual metal ions present in aqueous solution was transferred to organic layer by employing Tetra octyl Ammonium bromide (ToABr) as phase transfer catalyst. For this we have taken 1 mL of saturated NaCl solution and added 1 mL 25 mM aqueous metal solution under vigorous stirring. Then we have added 2 mL 50 mM ToABr in toluene and the solution was mixed thoroughly. After sometime the solution was allowed to stand still and allowed for phase separation. Later the organic layer was carefully collected and named as metal tetra octyl Ammonium bromide solution (MToABr where M= Ag/Au/Cu). Using these MToABr solutions we have synthesized 9 different sets of trimetallic flowers all with different compositions of Au and Cu. In all these flowers we have kept the amount of silver same and varied the amounts of Au and Au since our previous reports have shown that 90:10 Ag:Au and 90:10Ag:Cu gave the best SERS response. In all the sets the composition of Au has varied from 1 to 9% and copper was from 9 to 1% (ex Ag:Au:Cu = 9:1:9 to 9:9:1). For synthesis of MFs we have drop casted 40 µL of various compositions of trimetallic solutions and thermolyzed them at 350 ^oC for 2 hours. After 2 hours, the coverslips were allowed to

cool to room temperature and they are washed with toluene to remove any unreacted precursor. Then they are reduced to metallic state using 17 mM $NaBH_4$ for 2 minutes. MFs are used for SERS analysis immediately after reduction.

2.4. Sample preparation

2.4.1. Detection of PA in lab, real water samples and soil samples (Chapter 3)

In a typical experiment, 200 μL of different concentration of PA was added to 1.8 mL of sensor and mixed well. Immediately, fluorescence measurements of the solution were performed at room temperature. Pond water and lake water samples were collected from a nearby village and Shamirpet lake near BITS Pilani Hyderabad campus, respectively. All the water samples were first centrifuged and filtered through a 0.22 μm membrane. Then, 200 μL of water sample was added to 1.8 mL of sensor and fluorescence was collected. Soil samples were collected from the garden of the campus. 2 gms of ground, fine powder like soil sample was placed in five different petri dishes. Next, 10 mg, 5 mg, 2 mg and 1 mg of PA was added to four petri dishes individually and mixed well. The soil sample without PA was used as blank. Finally, 100mg soil sample from each, was added to 2 mL of sensor solution and fluorescence was collected.

2.4.2. procedure for MEF study (Chapter 4A)

Being AIEgen, **NP-4Py** molecule displayed AIE-feature with a greenish emission in the acetonitrile-water mixture when water fraction (f_w:*v/v*) was 80% (20 μL of AIEgen in dioxane (10^{-3} M) + 380 μL of acetonitrile +1600 μL of water).[19] The same concentration (10^{-5} M in 2 mL solution) of **NP-4Py** was maintained for all further fluorescence measurements. For the MEF study, we adsorbed 400 μL of AIEgen in acetonitrile to 1600 μL of polymer or silica-coated NPs solution. A blank study was performed by adsorbing the same amount of **NP-4Py** on SiNPs. All the measurements were recorded at room temperature after 5 min of adsorption. The EF for MEF was calculated as the ratio of the fluorescence intensity (FI) of AIEgen-metal nanohybrids to AIEgen-SiNPs.

$$\mathrm{EF_{MEF}} = \frac{FI_{AIEgen\ loaded\ MNPs}}{FI_{AIEgen\ loaded\ SiNPs}}$$

2.4.3. procedure for calculation of Relative Quantum yield (Chapter 4A)

We have calculated the relative quantum yields of the PS and the theranostic nanoparticles using the following equation by taking quinine sulphate as the reference.

$$\phi_S = \phi_R \frac{I_S A_R \eta_S^2}{I_R A_S \eta_R^2}$$

Where, subscripts S and R refer to sample and reference respectively; ϕ = fluorescence quantum yield; I = integrated fluorescence intensity; A = Absorbance; η = refractive index of the medium.

2.4.4. procedure for SOG measurements (Chapter 4A)

DPBF was used as an indicator of SOG measurement by the chemical trapping method. The solution containing 10^{-5} M AIE-PS adsorbed on metal NPs, and 50 μM DPBF were prepared, and then samples were irradiated by white light (35 mW cm^{-2}). Degradation of DPBF was monitored by measuring UV-Visible absorbance spectra of DPBF. The first-order kinetic model [$-\ln(A_t/A_o) = kt$] was used to determine the degradation rate of DPBF (where, A_o and A_t were initial absorbance and absorbance at time t). AIE-PS loaded on SiNPs, was used as the control sample. The SOG enhancement factor was calculated as the ratio of the SOG of AIEgen-metal nanohybrids to AIEgen-SiNPs.

$$EF_{SOG} = \frac{k_{AIEgen\ loaded\ MNPs}}{k_{AIEgen\ loaded\ SiNPs}}$$

To confirm the identity of the ROS in a separate experiment, a spin trapping probe DMPO (100 μM), selective for hydroxyl and superoxide radicals was additionally added to the solution of AIEgen loaded nanoparticles and DPBF and irradiated. Further, to confirm the involvement of $^1O_2$ as ROS, 100 μL of sodium azide (5mg/mL) was added to the solution AIEgen loaded nanoparticles and DPBF, being a selective singlet oxygen inhibitor.

2.4.5. Calibration Curve for Quantification of Conjugated Ey on GNRs (Chapter 4B)

For all our conjugation experiments, we have used 10 μL of 10 mM Ey solution to 10 mL of GNR solution. It means the final added concentration of Ey in each solution is 10 μM. Keeping this in mind we have made a calibration curve using UV-Visi spectrophotometer in the range of 0.1 μM to 10 μM. we recorded the absorbance of Ey

in all these concentration range and the OD values are noted. Then after conjugation, we recorded the absorbance of collected supernatant and the obtained pellet and then quantified the amount of Ey conjugated on GNRs.

2.4.6. Procedure for MEF and Lifetime Studies (Chapter 4B)

Before starting the experiment, all the Ey conjugated NRs solution and SiNP-NH_2-Ey solutions was adjusted to same OD value to make sure that the concentration of Ey was same in all the samples as shown in the table 1. For all the fluorescence measurements, the samples were excited at 519 nm and the emission was collected from 529 to 800 nm range. The excitation and emission slits were kept at 5 nm and the PMT voltage was set to 400. We have chosen appropriate blanks for the experiment such as GNR, GNR-LBL, SiNP-NH_2 and SiNP-NH_2-Ey samples. The MEF Enhancement Factor (EF_{MEF}) was calculated as the ratio of fluorescence intensity of Ey in presence of GNRs to Fluorescence intensity of Ey in presence of SiNPs.

$$EF_{MEF} = \frac{FI_{GNR-LBL-Ey}}{FI_{SiNP-LBL-Ey}}$$

For excited state lifetime measurements, 510 nm LED was used as source and bandpass 4 nm, peak preset 10000 counts. All these parameters were kept constant throughout the entire experiment. Instrument response function (IRF) was done using LUDOX a colloidal SiNP solution and the emission wavelength was set to the wavelength of LED used. For sample, the emission wavelength was set as 540 nm and the obtained data is fitted using a tri exponential model and the average lifetimes were calculated using the formula:

$$\tau_{Avg} = \frac{\sum \alpha_i {\tau_i}^2}{\sum \alpha_i \tau_i}$$

Where, τ_i is the lifetime of a component, α_i is considered as the contribution of that particular component and τ_{avg} is the average lifetime.

2.4.7 procedure for SOG Studies (Chapter 4B)

1,3-Diphenylisobenzofuran (DPBF) was used as a probe to indirectly monitor the production of $^1O_2$ by the Ey conjugated GNRs. On irradiation with light, DPBF undergoes a 1,4-cycloaddition to form Ortho dibenzoyl benzene which has less absorbance compared to the parent compound due to less conjugation as shown in the

figure below. This absorbance loss at 420 nm due to chemical trapping was exploited further to study the rate of production of Reactive oxygen species (ROS) by the GNR-LBL-Ey.

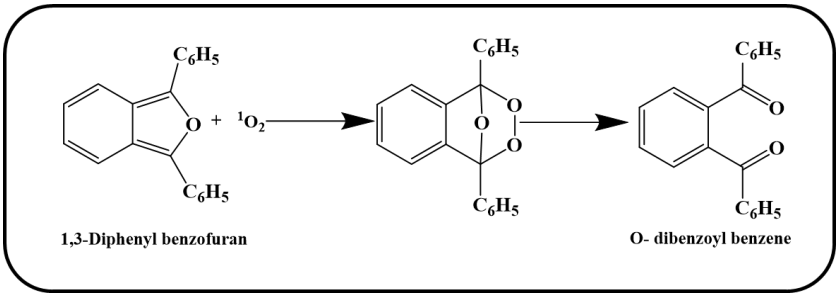

Scheme 2. Representation of Cycloaddition of DPBF in the presence of singlet oxygen.

Initially we prepared a stock of 0.1 mM DPBF in ethanol and later it was subsequently diluted in GNR solutions in water. For this experiment, we took 200 µL of 0.1 mM DPBF and added to 1.8 mL of diluted GNR-LBL-Ey solutions and irradiated it using a white light source with a power density of 35 mW/cm^2. The decrease in absorbance of DPBF at 420 nm was measured at every 2 s for 30 s using a UV-Visible spectrophotometer. Later, the decay rate of the photosensitized process was determined by plotting the natural logarithm values of DPBF absorption at 420 nm against the irradiation time. These data points were then fitted to a first-order linear least-squares model and the slopes were noted. SiNP-Ey was used as a control sample to calculate metal enhanced singlet oxygen generation (MESOG) as SiNPs are devoid of any plasmonic behaviour. The SOG EF was calculated as the ratio of slopes of DPBF degradation in the GNR-LBL-Ey to SiNP-Ey.

$$EF_{SOG} = \frac{K_{GNR-LBL-Ey}}{K_{SiNP-LBL-Ey}}$$

Separate experiments were performed to confirm the presence of $^1O_2$ in the reaction mixture by adding a spin trapping probe 0.1 mM DMPO along with the addition of DPBF and irradiated with light. DMPO selectively binds to hydroxyl and superoxide radicals but not with $^1O_2$. Additionally, sodium azide (5 mg/mL) was introduced to the GNR-LBL-Ey solution in another experiment along with DPBF to validate the involvement of singlet oxygen ($^1O_2$) as the ROS. Measurements of absorbance values on irradiation of light in either case sheds some light on the ROS generated in the experiment.

2.4.8. Experimental method for detection of Scattering (Chapter 4B)

The extinction of GNRs is the sum of scattering and absorption, and the scattering component can be determined experimentally using a integrated sphere.[20,21] When an electromagnetic radiation (I_o) is incident on NP solution, several phenomena take place such as transmittance (I_T), scattering (I_S), absorption (I_A) and reflectance of light (I_R) from cuvette walls. The light reflectance from the cuvette walls is very negligible and can be ignored.

$$I_o = I_A + I_T + I_S + I_R$$

$$I_o = I_A + I_T + I_S \text{ (because } I_R <<< I_o)$$

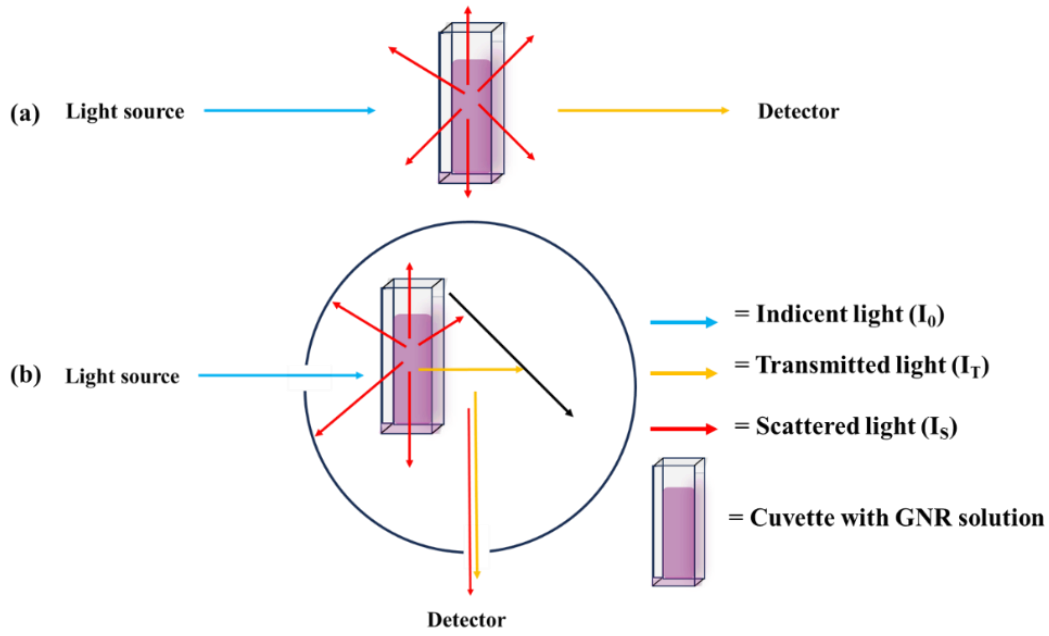

Figure 2.1. A pictorial representation of how extinction and scattering of samples was measured and (a) is the UV-Visible spectrometer used to collect the extinction of samples and (b) is the emission spectrophotometer coupled with an integrating sphere, used to measure scattering component.

While using a UV-Visible spectrophotometer, the light reaching the detector is dominated by transmittance and obtained spectra is a combination of light lost due to samples absorption and scattering. on the contrary while using an emission spectrometer coupled with an integrating sphere and placing the sample in it results in the detection of light from scattering and transmittance components implying that the light lost is mainly due to samples absorbance.

$$T_{UV\text{-}Vis} = I_T/I_o$$

$$T_{Intagrating\ sphere} = (I_T+I_S)/I_o$$

2.4.9. samples for SERS measurements (Chapter 5A, 5B and 6)

R 6G was used as the reporter molecule to understand the SERS efficiency of all the substrates used in this thesis. R 6G stock was initially prepared in ethanol and serially diluted from 1 μM to 1 zM. Then the stock solutions of MTO and DOX, 1 mM each, were prepared in methanol and serially diluted in water. 40 μL of the drug solutions of different concentrations were then drop cast onto a coverslip containing Ag-Cu and Ag-Au MFs and allowed to dry. In case of trimetallic MFs L-Cysteine solution prepared in water of known concentration was adsorbed on the MFs soon after reduction and solvent was let to evaporate before collecting the Raman spectra. All the experimental parameters were kept constant while collecting SERS spectra of different samples such as exposure time was maintained as 1 Sec, the number of accumulations was 30, and the average laser power was ~13 μW for both green and red laser. All the SERS measurements were recorded from the centre of the MFs and were collected at 10 different MFs on the same substrate (coverslip) and the average intensity value was calculated and used for further analysis.

2.5 Simulation details:

2.5.1. Details of FDTD simulations (Chapter 3)

FDTD simulations were performed by using and modifying the parameters of a model example “Fluorescence Enhancement” from the software Lumerical Solutions, Inc. (Vancouver, Canada), version 2019b.[22] Briefly, Au nanoparticle, covered with silica was considered as the antenna and a dipole emitter was placed at the top of silica shell. The dipole source was located at the emitter position and in the FDTD simulation this dipole source modelled the radiation characteristics of the emitter. Where, the ratio of γ_{dipole} to $\gamma_{radiative}$ provided an indication about the fluorescence enhancement, where γ_{dipole} and $\gamma_{radiative}$ were ‘total decay rate in presence of nanostructure’ and ‘radiative decay rate without the influence of nanostructure’ of the dipole, respectively. We calculated $\gamma_{dipole}/\gamma_{radiative}$ for the dipole as a function of distance from the spherical metallic surface. The simulations were performed at different dipole-metal distances of 7.2, 8.7, 11.2, 12.3 and 18.1 nm, matching with the experimental conditions and diameter of the gold nanoparticle was considered to be 40 nm. The dipole orientation

was considered perpendicular from the metal surface and dipole, centre of the Au nanoparticle was along the z axis (θ = 0°). Mesh step was 1 nm and mesh order was taken as 2 for all the simulations performed.

2.5.2. Details of COMSOL simulation of GNRs (Chapter 4B)

COMSOL simulation was done using the electromagnetic wave, frequency domain module (emw). All the simulation was for an incident wavelength of 519 nm and the scatter field of the GNR is observed. The propagation of the incident wave is along the x-axis with an electric field strength of 1V/m. The mesh size is set to predefined "Finer" and the properties of the materials used are obtained from the COMSOL material library. The three materials used are Gold [Au (Gold) (Windt et al. 1988: n,k 0.0024-0.1216 μm)], Water [liquid], and Silica [SiO2 (fused quartz) [solid,NIST SRM 739 - Type I]]. The parameters such as electric conductivity, relative permeability, and permittivity were added as the external parameters of the material. In order to study the scattered field after the incident electromagnetic wave interacts with the GNR, we defined a boundary condition around the GNR as a cube that has its length of one side set as 400 nm. A two-dimensional electric field map is obtained from the scattered field.

The values that are externally fed in to simulation were: Relative permeability for gold: 0.999998; Electrical conductivity for gold: 4.11e7 S/m; Relative permeability for water: 0.9999992; The relative permittivity of SiO2: 3.9; Relative permeability for SiO2: 0.9999704; Electrical conductivity for water: 5.5e-6 S/m Theoretical enhancement factor was calculated as the fourth power of ratio of difference in the maximum electric field obtained and input electric field to applied electric field. The formula used is

$$\mathrm{EF} = [E]^4 = \left[\frac{(\mathrm{E_{max}} - \mathrm{E_{min}})}{\mathrm{E_{applied}}}\right]^2$$

Where E_{max} = maximum electric field experienced by the GNR

E_{min} = minimum electric field experienced by the GNR

$E_{applied}$ = the input electric field which is 1V/m

2.5.3. Electromagnetic field simulation of Microflowers (Chapter 5B)

COMSOL Multiphysics was used to simulate the electromagnetic field distribution of the plasmonic substrates, which were formed by the interconnection and fusion of the nanoparticles. The diameter of each of the nanoparticles was considered to be 30 nm (obtained from crystallite size measurement from XRD) and accordingly, the COMSOL models were established. Keeping in mind that the MF structures were mainly composed of aggregated nanoparticles, we used three different types of models (dimer, 2D Array of NPs and random arrangement of NPs) with progressive complexity in our COMSOL simulation, to calculate the electromagnetic field enhancements for the SERS substrates of different composition. For the electrical field enhancement factor, we know that EF is the fourth power of the electric field that is experienced by the nanoparticle. For this simulation, the EF is calculated using the formula mentioned above. For the dimer and 2D array model, we used a spacing of 1 nm between the nanoparticles and interconnected nanoparticles with no spacing. Each of the contact points between nanoparticles will form a crevice or hotspot which the molecule can occupy and thereby will have an enhancement in Raman spectra when light is incident. Electromagnetic waves Frequency domain (emw) description: three-dimensional finite element-based COMSOL software was used to simulate the electric field distribution of the nanostructures. The domain of the nanoparticle was air (refractive index n = 1), and the predefined mesh size 'Finer' was used for the simulation, with incident wavelengths of 532 nm and 632.8 nm. A total of three materials were used; silver, silver-gold (Ag-Au) and silver-copper (Ag-Cu), where the alloy nanoparticles were taken in the composition of 90% silver (Ag) and 10% gold or copper. The essential values for the simulation such as electric conductivity values for the materials (values of Ag and Ag-Au) were obtained from the material library available in COMSOL (Ag from Windt[23] and Ag-Au from Rioux et.al[24] and material conductivity from ASM handbook[25] and then a two-dimensional electric field distribution map was obtained.

2.6. Instruments:

The instruments used for the development of this thesis involved both microscopic and spectroscopic techniques such as UV-Vis spectrophotometry and spectrofluorometry,

Infrared (IR) spectroscopy, Fluorescence lifetime measurement, Raman spectroscopy, confocal microscopy, X-ray photon spectroscopy (XPS), Dynamic Light Scattering (DLS), Powder- X-ray Diffraction (XRD), Small angle X-ray scattering (SAXS), X-Ray Fluorescence spectroscopy (XRF), Scanning electron microscopy (SEM).

2.6.1. UV-Vis spectrophotometry and Spectrofluorometry

Absorption spectra in solution state were recorded on Shimadzu UV-3600 plus. The extinction spectra of SERS substrates synthesized on Coverslips were recorded using Jasco V-670 UV-visible spectrophotometer, while all the Fluorescence data were recorded on Hitachi F-7000 fluorescence Spectrofluorometer the excitation and emission slit width were kept as 5 nm. The scattering measurements were performed on the Horiba Fluorolog spectrofluorometer coupled with an integrating sphere in synchronous mode from 300-800 nm range keeping an offset of 20 nm, excitation and emission slits as 1 nm each.

2.6.2. Infrared (IR) spectroscopy

FTIR spectra were measured within the range of 4000-500 cm^{-1} using JASCO FT/IR-4200 Fourier transform infrared spectrometer. 1 mg of sample of 10 µL of solution was added to 100 mg of KBr powder and the pellets were made. Background signal was recorded using KBr pellet as blank.

2.6.3. Raman spectroscopy

Surface enhanced Raman scattering experiments were performed using a Micro-Raman Spectrometer (Uniram, Korea). A continuous-wave diode pumped solid state laser working at λ = 532 nm and a He-Ne laser operating at 632.8 nm, were used as the excitation sources. A 0.55 numerical aperture and 50x air immersion objective lens were used to focus the sample and collect the backscattered Raman light. Various mirrors were used to focus the light on sample and to collect the back scattered light. Holographic notch filter is placed in the collection path to efficiently and narrowly reject the Rayleigh line from the scattered laser. This notch filter allows less than 0.5% of the backscattered laser line to pass through while transmitting over 90% of the remaining Raman scattered frequencies to the detector. The detector used in the instrument is CCD detector. A CCD is a two-dimensional array comprising silicon-

based photosensitive elements called pixels. Every pixel produces photoelectrons and retains the accumulated charges proportional to the number of incident photons on that particular pixel. These charges are subsequently gathered by a single analogue-to-digital converter (ADC), and the content of each array is measured. Currently, CCDs commonly possess a 1024 × 1024-pixel configuration, resulting in a total size of 25 mm. The spectrograph was calibrated using a standard silicon wafer at wavenumber 520 cm^{-1} or either naphthalene. All the experimental parameters were kept constant while collecting SERS spectra of different samples such as exposure time was maintained as 1s, the number of accumulations was 30, and the average laser power was ~13 μW for both green and red laser.

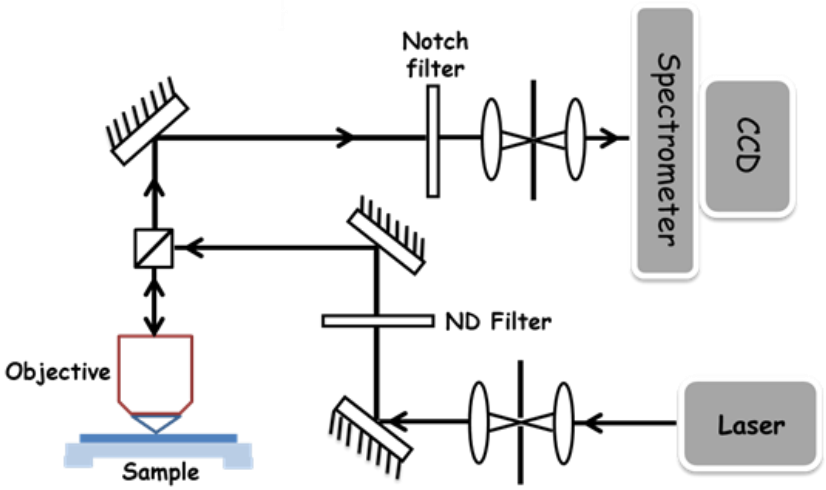

Figure2.2. A schematic representation of Raman spectrophotometer.

2.6.4. Confocal microscopy

Confocal images of the NP-4-Py loaded Span 60 vesicles were collected using Leica, TCS SP8 model having an inbuilt DMi8 microscope. 20x air immersion objective was used to collect the image. The excitation range was set to be 405 nm and the emission was collected in the range of 430-470 nm. The laser power was kept constant for all the confocal measurements.

2.6.5. X-Ray photo-electron spectroscopy (XPS)

The surface composition of MFs was recorded using Thermo scientific K-Alpha surface analysis X-ray photoelectron spectroscopy (XPS) using Aluminium Kα radiation (1486.6 eV). XPS gives the elemental composition of 1-2 nm from the surface only. The synthesized MFs were scanned to observe the presence of C, O, Ag, Au, and Cu elements

and their surface elemental composition as well as their binding states are analyzed. The obtained data was corrected using C standard peak value of 284.8 eV.

2.6.6 X-Ray fluorescence spectroscopy (XRF)

The bulk spectral composition of the MFs was analyzed using energy dispersive X-ray fluorescence (ED-XRF, Panalytical, Epsilon 1).

2.6.7. Dynamic Light Scattering (DLS)

Particle size and zeta potential of samples were analyzed by dynamic light scattering technique (DLS) using a Malvern particle size analyzer (zeta sizer nano-ZS).

2.6.8. X-ray Diffraction (XRD) and Small angle X-ray scattering (SAXS)

Crystallinity of all the synthesized MFs were determined by X-ray diffraction (XRD) technique using Rigaku Ultima IV X- ray diffractometer with Cu Kα radiation (λ = 1.54 Å) in the range of 10–80°. The scan speed and step width were of 2°/min and 0.02°, respectively. The WAXS (wide angle X-ray scattering) measurements were also performed to identify the diffraction pattern. For the WAXS measurements, the scan range and scan speed were of 0.06–3° and 0.005°/min, respectively.

2.6.9. Thermogravimetric Analysis (TGA)

The decomposition temperatures of different metal alkyl ammonium bromide solutions (MToABr where M= Ag/Au/Cu) were observed using thermogravimetric analysis (TGA). The model of the instrument used in the study was DTG-60, Shimadzu, Japan, whereas the thermal analyzer was TA-60WS, Shimadzu, Japan. To execute the TGA toluene was evaporated from the samples and then washed samples were used. All the experiments were performed on platinum pans at a heating rate of 5 °C/min in air flow in the temperature range 30 to 500 °C.

2.6.10. Scanning Electron Microscopy (SEM)

SEM was used to get the topographical morphology of the synthesized Ag, Au, Si NPs, GNRs and SERS substrates. SEM images were collected using a JEOL JSM-7600F Field Emission Scanning Electron Microscope (FE-SEM). Before imaging, the solution was drop casted on Silicon Wafer and kept it for a long time in the presence of a vacuum to make sure that it was completely dried. All the images were taken in SEI (Secondary Electron Imaging) mode. To understand about the thickness of silica layer or polymer

coating around MNP, images were also taken in STEM mode. For this 5 μL of diluted sample was drop casted on a copper grid and dried in vacuum and the images were collected in either Dark field or bright field mode.

2.4.11. Time correlated single photon counting (TCSPC)

Horiba Deltaflex Modular fluorescence lifetime system has been used for the Fluorescence Lifetime measurements. HORIBA (EZ lifetime) decay analysis software is used for fitting the raw data. Instrument response function (IRF) was measured using Ludox, a colloidal silica solution. Peak preset was kept at 10,000 counts. For AuNPs coated with PAH 340 nm Nano LED was used as the excitation source and the emission was collected at 430 nm. For MNPs coated with NP-4-Py molecule the excitation source used was 340 nm and the emission was recorded at 420 nm. In case of Ey coated AuNR, the excitation source was 510 nm Nano LED and the emission wavelength was set to be 520 nm.

2.4.12. Other Equipments used

- Analytical Balance: Sartorius Analytical Balance
- Centrifugator: R-8C laboratory centrifuge
- Water bath sonicator and vortex
- Magnetic stirrer with heating mantle
- pH meter: ELICO LI 120
- Millipore water system

Chapter 3

A metal-enhanced fluorescence sensing platform for selective detection of picric acid in aqueous medium

In this chapter, we discussed about the size of MNPs and distance between MNP and fluorophore and their effects on metal enhanced fluorescence. We then used the best MEF substrate for detection of picric acid in aqueous samples. This chapter is based on the following paper, S. Kaja, D.P. Damera and A. Nag; A metal-enhanced fluorescence sensing platform for selective detection of picric acid in aqueous medium, Analytica Chimica Acta, 2020, 1129, 12-23.

3.1. Introduction

2,4,6-Tri nitro phenol, universally known as picric acid (PA) is a hazardous chemical used in the synthesis of lethal weapons and powerful explosives. It is also extensively used in matches and leather processing, as an oxidant in rocket fuels, as a textile mordant, fireworks and also in the production of toxic eye irritant chloropicrin etc.[1-2] As a consequence of its widespread use in industries, it is polluting ground water and soil. It is reported to produce more toxicity than tri nitro toluene (TNT) and has been used extensively during world war I.[3] Even trace amount of PA present in soil or water can cause irritation to eye and skin. Over exposure to PA causes serious damage to lungs and it may also lead to threatening diseases like anaemia, cancer, and cyanosis as PA is highly soluble in water.[4] Therefore, it is highly essential to detect even low concentrations of PA in water and such practical detection of PA must take place in environments like explosion sites, wastewater treatment plant etc. In such environments, there is also a possibility of presence of other chemical explosives along with picric acid. However, selective detection of PA is a challenging task because of its similar nature to phenolic poisons and other electron withdrawing nitro aromatic compounds. A variety of sensors such as nanoparticles,[5-7] gels,[8] metal organic frame works,[9-12] organic molecules[13-21] and many analytical techniques involving X-ray diffraction, Raman spectroscopy, neutron activation,[22-24] have been explored for PA detection. Among various techniques used, fluorescence-based detection is most popular as it is highly sensitive, cost effective and also due to easy sample preparation and quick response time.[25]

On the other hand, Ag or Au nanoparticles can confine and enhance the electromagnetic radiation incident upon them, by the resonant oscillation of surface electrons which is commonly known as surface plasmon resonance (SPR). As a result, this highly localized electron oscillations at SPR enable the metal nanoparticles to behave as a new excitation source with tremendous enhancement of the local electric field. The obtained field is commonly many orders of the magnitude higher than the incident field. But the local electric field is dominant only very near to the metal surface. It decays exponentially with increase in the distance from the metallic surface,

and it becomes insignificant after ~ 30 nm. When fluorophores are positioned at an appropriate distance from the metallic surface, the surface plasmons can enhance the fluorescence intensity of a fluorophore and the phenomenon is named as metal-enhanced fluorescence (MEF).[26] MEF has gained enormous importance in recent years for its analytical applications in diverse areas like optics, molecular physics, medical diagnosis, biological research etc.[27-31] In case of MEF, frequencies emitted by fluorophore couple with the resonances of surface plasmons resulting into a radiation with enhanced intensity by the metal nanoparticle. A crucial point in MEF is the distance between the fluorophore and the metal surface, as by varying the distance it is possible to switch from fluorescence enhancement to quenching.[32] Core-shell nanostructures comprised of Au or Ag as metal core and an appropriate dielectric shell of silica or polymer, are most preferred MEF substrates to obtain a convincing result. For example, core-shell technology in MEF was successfully demonstrated by Geddes and co-workers[33] and Halas group[34,35] where they observed enhancement in molecular fluorescence of the dyes adsorbed on the silica layer (shell), at an optimum distance of few nm from the metallic Ag and Au surfaces (core), respectively. Subsequently, a range of optimum metal-emitter distances have been reported by several groups in their distance-dependence MEF studies, as the optimum distance varies with the metal and size/shape of the nanoparticles. While, the optimum distance was reported as ~ 12 nm by two different studies using Ag@SiO_2 nanoparticles[36] and Boron Nitride coated Ag film[37], another study registered 20 nm as the critical distance using SiO_2 coated nano porous gold.[38] In a separate report, 8 nm was revealed as the optimum distance where Au nanorods and polyelectrolytes were used as nanoantennae and spacer, respectively.[39] Although rare, but a study using Au nanocage@SiO_2, obtained the maximum fluorescence intensity with a very high silica thickness of 80 nm.[40] Not only the metal-emitter distance, a recent study from our group has also pointed out the crucial role, played by the diameter of the Au nanoparticle in determining the extent of MEF.[41]

In the present work, for the first time a gold nanoparticle based MEF sensor is reported for detection of PA in aqueous condition. We designed our sensor

based upon the discovery that a commercially available lab chemical poly(allylamine)hydrochloride (PAH) showed strong MEF, when placed in the propinquity of AuNPs at an optimum distance. The spacer between the metal and the fluorophore was provided by the dielectric silica layer. The silica spacer was chosen as it has many advantages like easily controllable thickness to vary the distance, protection of the metal core from unwanted chemical reactions and good dispersity.[42] While the experiments were performed with three different average sizes of ~ 22, 45 and 60 nm AuNPs prepared, we recorded the maximum enhancement in case of 45 nm. It produced maximum ~ 280-fold fluorescence enhancement for PAH and the optimum distance was found to be ~ 11 nm between AuNPs and fluorophore. Furthermore, the concomitant reduction in components of excited state lifetime along with the enhancement indicated the mechanism to be predominantly resulting from the intrinsic radiative decay rate enhancement of PAH and may be partially from the confined electric field effect. Most importantly, upon interaction with nitro aromatic molecules, this MEF sensor can selectively detect PA via fluorescence quenching method. Overall, the reported MEF based fluorescence 'turn off' sensor is low-cost, easily prepared and reproducible.

3.2. Results and discussion

3.2.1. Characterization of the AuNPs and Au@SiO_2 nanoparticles

AuNPs of three different average sizes were prepared for the study, specifically 22 nm, 45 nm and 60 nm. The synthesized AuNPs were first structurally characterized using FE-SEM technique. **Figure 3.1a-c**, show the SEM images of AuNPs and the distribution of particle size is shown in also shown in the histogram. UV-Visible spectrophotometry was used to collect the extinction spectra (**Figure 3.1d**) of the AuNPs solution. It was evident from the figure that the maxima of the plasmonic spectra of the AuNPs moved continually towards higher wavelengths with slight broadening, as the size of the AuNPs increased from 22 to 60 nm. The observed red shift in the extinction spectra indicated about the progressive increase in size for the AuNPs. The number densities of as synthesized AuNPs were calculated as follows:

Radius of 45 nm AuNPs= 22.5 nm = 22.5 x 10^{-7} cm; Density = 3.9 g/cm_3; weight of gold salt = 0.0098 g; total volume occupied by AuNPs= 2.51 x 10^{-2} cc

Volume of each particle = (4/3) πr^3 = (4/3) x 3.14 x (22.5x 10^{-7})^3 = 4.76 x 10^{-17} cc

Number of Particles = Total volume occupied by AuNPs/ volume of each particle

= (2.51 x 10^{-2}) / (4.76 x 10^{-17}) = 5 x 10^{14} in 50 ml of the solution, therefore number of particles per ml is = 1 x 10^{13}; Similarly, for 22 nm = 9 x 10^{13} and 60 nm = 4 x 10^{12}.

The number densities (per ml) of the synthesized AuNPs were 9 x 10^{13}, 1 x 10^{13} and 4 x 10^{12} for 22, 45 and 60 nm, respectively.

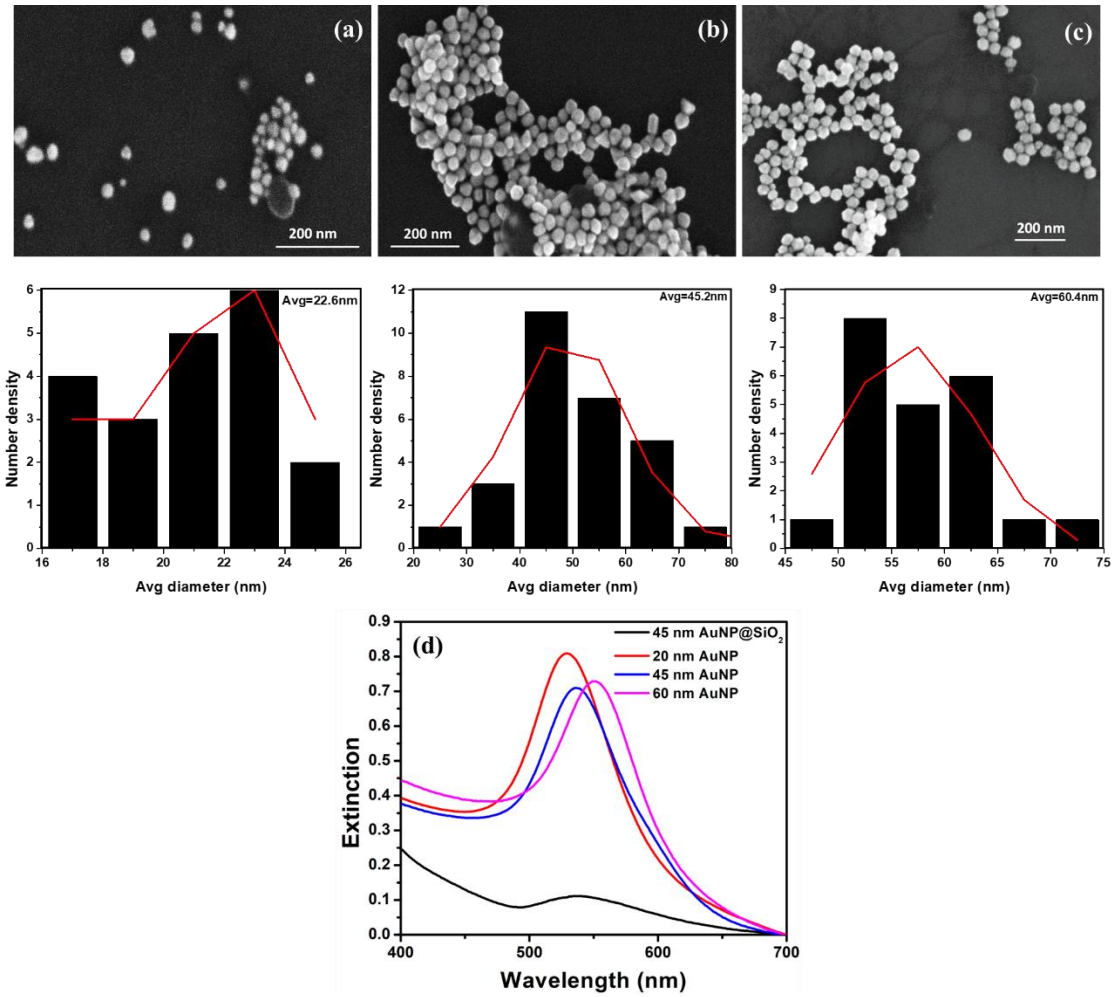

Figure 3.1. (a), (b) and (c) are FE-SEM images for 22, 45 and 60nm AuNPs and the histograms below are their corresponding average size plots respectively. and (d) is the extinction spectra of the 22, 45, 60 nm AuNPs and 45 nm silica coated core shell NPs.

After the synthesis and characterization of the AuNPs, we subsequently prepared and characterized the Au@SiO_2 core-shell nanoparticles with silica spacer. The nanoparticles with various silica shell thicknesses were synthesized through the

reported Stober method by varying the amount of TEOS added (**Figure 3.2a-e**). The extinction coefficient was found to be lower as well as red shifted for 45 nm Au@SiO_2 (11.2 nm) particles compared to the bare 45 nm AuNPs (**Figure 3.1d**), indicating the presence of silica layer. Due to the presence of the negative charge on its surface, a silica shell can offer specific binding site to bind molecules like PAH via electrostatic attraction with the positive amine groups of PAH. In fact, the zeta potential measurements (**Figure 3.3a-c.**) confirmed that the surface for both free AuNPs and Si coated AuNPs were negatively charged, whereas Au@SiO_2 surface developed positive charge after deposition of PAH. The pH of the solution was found to be 6. At this pH, alkyl amines existed predominantly as positively charged R-NH_3^+. SEM images proved that uniform silica layers of different thicknesses were grown on the surface of AuNPs. While, the change in zeta potential values and IR data have confirmed the successful PAH deposition onto the surface of core-shell nanoparticles.

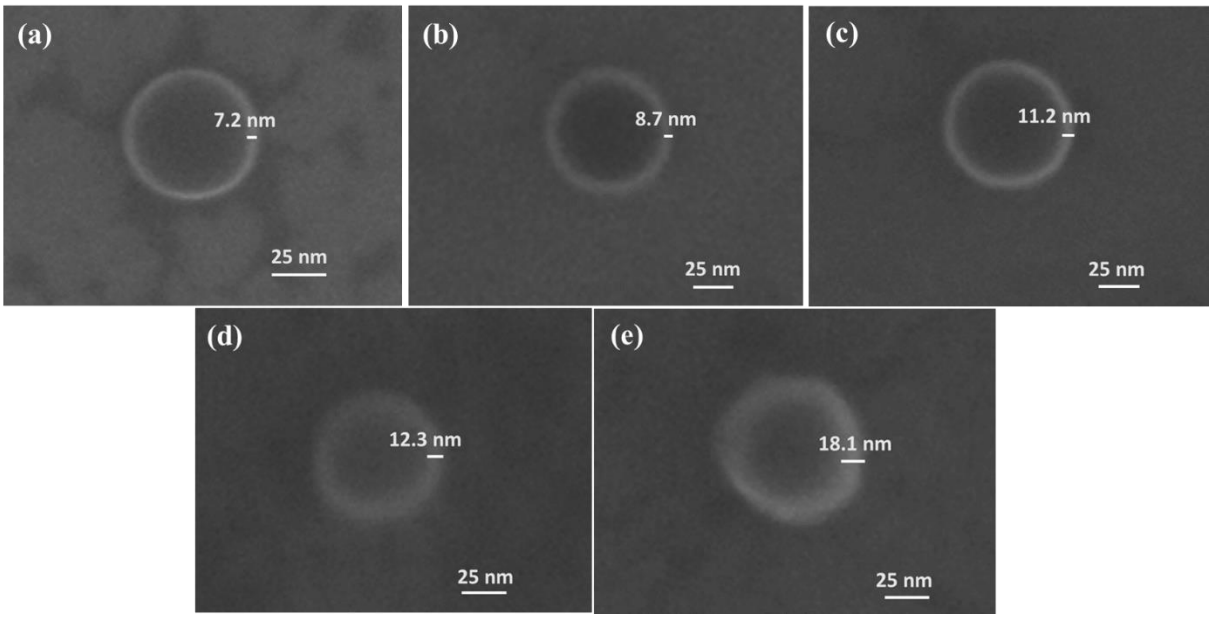

Figure 3.2. FE-SEM images of 45 nm AuNPs with (a) 100 µL (b) 200 µL (c) 400 µL (d) 500 µL and (e) 1000µL TEOS coating.

Next, FTIR spectra was recorded for PAH, AuNPs, Au@SiO_2 and Au@SiO_2-PAH to confirm the deposition of silica layer as well as PAH, as shown in **Figure 3.3d**. AuNPs showed the following peaks in IR: O-H stretch around 3437 cm^{-1}, C = O stretch around 1639 cm^{-1} and C-OH stretch around 1057 cm^{-1}.[43] The IR spectra of AuNP@SiO_2 showed a pronounced peak at 1092 cm^{-1} which can be ascribed to

asymmetric stretching of Si-O-Si. The hump at 941 cm^{-1} originated from Si-OH asymmetric vibrations.[44] The results indicated the successful formation of core shell nanoparticles. The adsorption of PAH can be confirmed by careful comparison of free PAH and Au@SiO_2-PAH. Free PAH showed two important characteristic peaks at 1612 and 1504 cm^{-1} which can be assigned as deformation vibrations of C-N str and N-H bending, respectively. Whereas in case of Au@SiO_2-PAH the peak at 1612 cm^{-1} shifted to 1629 cm^{-1} and the peak at 1504 cm^{-1} disappeared confirming the adsorption of PAH on core shell Au@SiO_2 nanoparticles.[45]

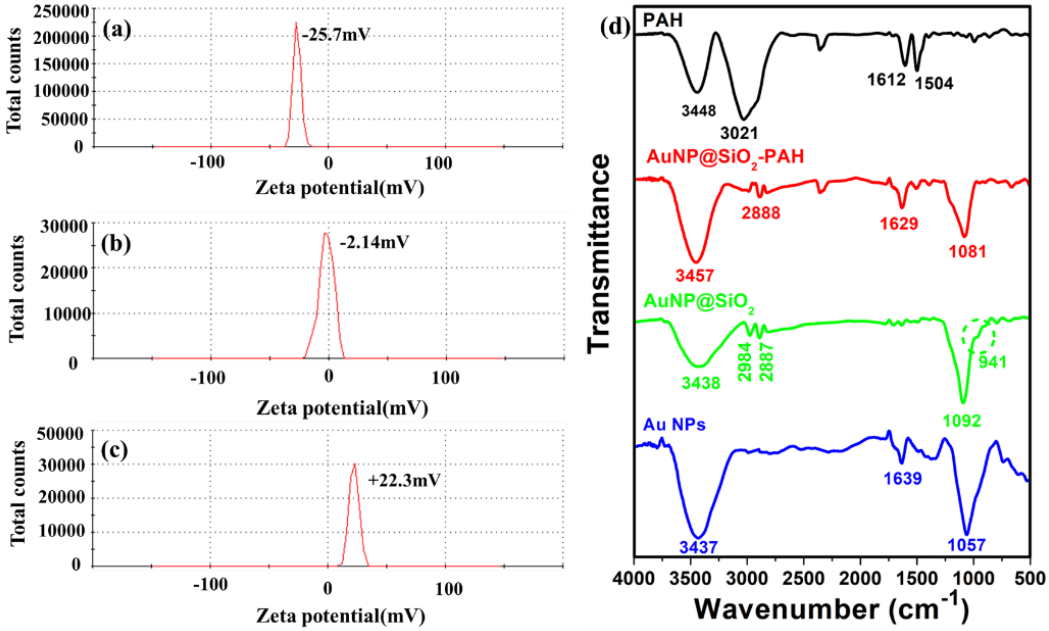

Figure 3.3. Zeta potential measurements of (a) 45 nm AuNPs, (b) Au@SiO_2 NPs, (c) PAH adsorbed Au@SiO_2 core shell NPs, and (d) FTIR spectra of AuNPs, AuNP@SiO_2, AuNP@SiO_2-PAH and free PAH.

3.2.2. MEF studies of PAH on Au@SiO_2 nanoparticles

The structure of PAH is shown in the **Figure 3.4a (inset).** The fluorescence intensity of free PAH in the bulk aqueous condition was found to be very less (**Figure 3.4a**) and can be considered as insignificant, when excited at 340 nm. We witnessed quenched fluorescence intensity when PAH was adsorbed directly on the AuNPs (**Figure 3.4a**). However, to our surprise PAH-adsorbed 45 nm Au@SiO_2 nanoparticles in ethanol showed a remarkable fluorescence enhancement compared to free PAH (**Figure 3.4b**). As a control experiment, we have also observed that Au@SiO_2 fluorescence is much less compared to Au@SiO_2-PAH indicating the insignificant role of silica in the observed fluorescence intensity (**Figure 3.4b**). This confirmed that the observed

enhancement in fluorescence of PAH with 45 nm Au@SiO_2 particles was certainly a result of MEF, imposed by the AuNPs under an appropriate core-shell arrangement. It is well-known that, for MEF the enhancement of fluorescence is highly dependent on distance between the nanostructure and fluorophore.[46,47] Earlier, Novotny and co-workers reported quenching of molecular fluorescence when molecule-gold distances were shorter than 5 nm.[48] Also, it was observed that monolayer deposition of molecules directly on silver and gold surfaces exhibited significant surface-enhanced Raman scattering with total quenching of fluorescence.[49,50] **Figure 3.5a** indicated that as we increased the thickness of Si coating, the fluorescence intensity of PAH-adsorbed 45 nm Au@SiO_2 nanoparticles also increased at the beginning, but fell off as the spacer thickness crossed an optimum value. This is again clearly understood when we plotted the enhancement factor (EF) of fluorescence, which is the ratio of the fluorescence intensity of PAH on Au@SiO_2 nanoparticles to free PAH, as a function of silica thickness (**Figure 3.5b)**. The optimum distance from the Au surface was found to be 11.2 nm, where maximum enhancement of ~ 280-fold was recorded.

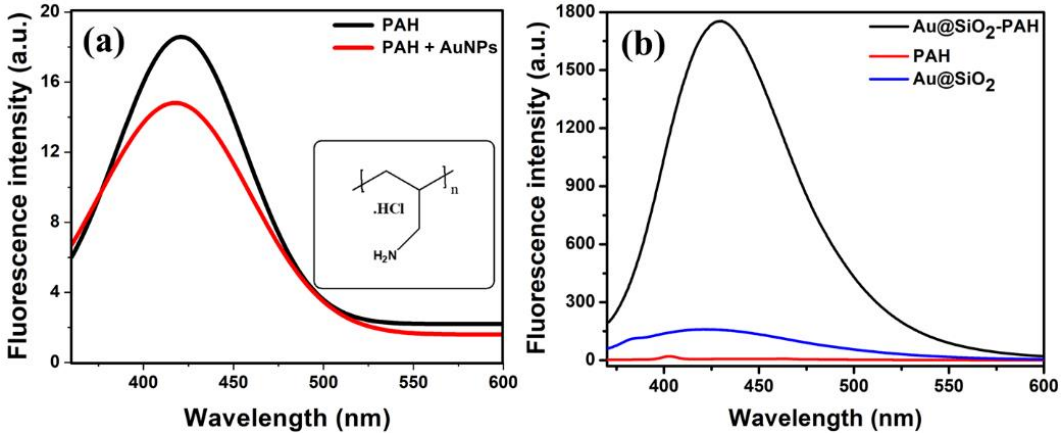

Figure 3.4. (a) are the spectra showing the quenched fluorescence intensity of PAH on direct adsorption onto 45 nm AuNPs, without silica coating, and the inset shows the structure of PAH (b) is the spectra showing the fluorescence of PAH, fluorescence of Au@SiO_2 NPs and fluorescence enhancement of PAH after adsorbing on Au@SiO_2 NPs.

The observed dependence of MEF on silica thickness compelled us to belief, that loss due to non-radiative energy transfer and near-field enhancement via plasmonic coupling must be operative as two competing processes between PAH and AuNPs. The overlap of absorption and emission spectra of PAH with plasmonic peak of 45 nm AuNPs are shown in **Figure 3.5c**. Possibly, MEF initially increases as PAH approaches

closer to Au surface, but starts to decrease once the distance becomes less than 11.2 nm due to possible non-radiative loss. The theoretical FDTD simulation results also showed very similar trend (**Figure 3.5d**), when normalized decay rate of a dipole emitter were plotted at different distances of the dipole from 40 nm AuNP surface. As can be seen in **Figure 3.5d**, the maximum enhancement in the decay rate was found at 12.3 nm and the rate dropped significantly afterwards. It must be noted here that γ_{dipole} /$\gamma_{radiative}$ was calculated as a function of wavelengths (**Figure 3.5e**), from which **Figure 3.5d** demonstrated the enhancement only at 450 nm.

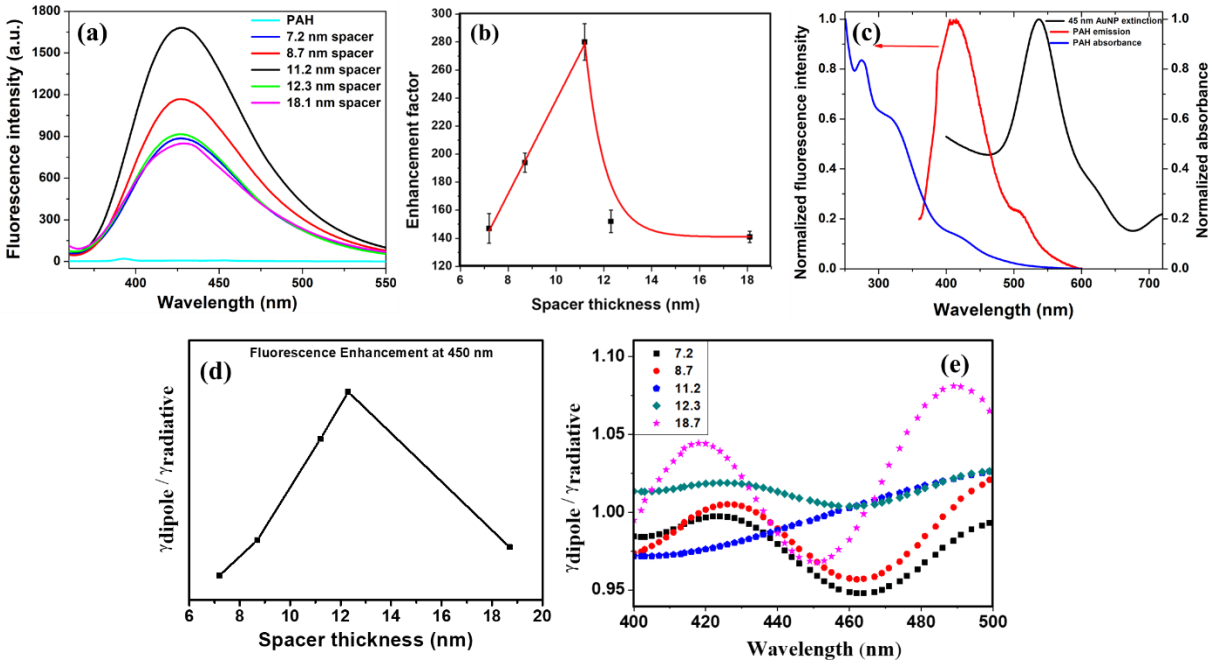

Figure 3.5. (a) Fluorescence intensity of Au@SiO_2-PAH nanoparticles as a function of spacer thickness and (b) Enhancement factor against spacer thickness, for 45 nm AuNPs. (c) Simulated decay rate enhancement of a representative 'dipole', as a function of separation from 40 nm AuNP surface, (d) is the Overlap of absorption and emission spectra of PAH with plasmonic peak of 45 nm AuNPs and (e) Calculated γ_{dipole} /$\gamma_{radiative}$ as a function of wavelengths for different spacer thickness (in nm).

3.2.3. Mechanism of MEF

At present, there are two established mechanisms for MEF, induced by near field enhancement. One mechanism is associated with the enhancement of the local electric field by the nanoparticle, in which the emitters around the metal nanoparticle can efficiently absorb more radiation. This can increase the excitation rate to enhance the fluorescence process, but without altering the lifetime and quantum yield of the fluorophores. The other mechanism states that in presence of metallic nanoparticles

the intrinsic radiative decay rate of fluorophores is strengthened, due to additional radiative channel. In contrary to the effect guided by local electric field, when enhancement in fluorescence intensity is controlled by the intrinsic radiative decay rate effect, it is accompanied by an increase in QY and an unusual decrease in the lifetime for the emitter. Therefore, fluorescence lifetime has been recognized as an important characterization tool, where a considerable decrease in lifetime with concomitant enhancement in fluorescence will predict the MEF mechanism via increase in radiative decay rate. Using a Jablonski diagram,[41] the fluorescence quantum yield (Q_o) and the decay time (τ_o) of the emitter can be expressed as following: Without metals, $Q_o = (\Gamma/ \Gamma + k_{nr} + k_q)$ and $\tau_o = (\Gamma + k_{nr} + k_q)^{-1}$, where Γ, k_{nr} and k_q are the rate constants of Radiative decay, Non-Radiative decay and quenching process, if any, respectively. Whereas, in presence of metals the modified quantum yield (Q_m) and the decay time (τ_m) become, $Q_m = (\Gamma + \Gamma_m / \Gamma + \Gamma_m + k_{nr} + k_q)$ and $\tau_m = (\Gamma + \Gamma_m + k_{nr} + k_q)^{-1}$, where Γ_m: rate constant of additional Radiative decay channel in presence of AuNPs.

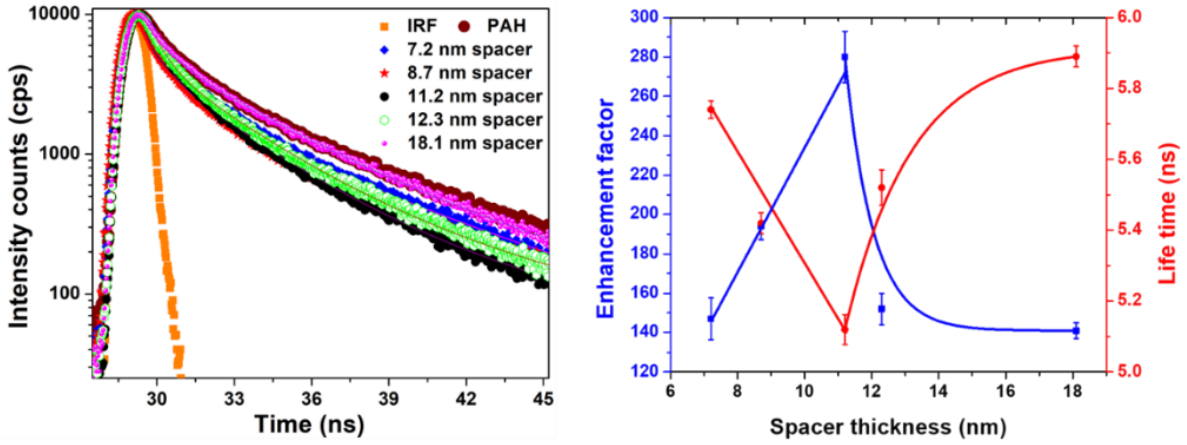

Figure 3.6. (a) Life time of 45 nm PAH-adsorbed Au@SiO_2 nanoparticles with different spacer thickness and (b) Anticorrelated behaviour of enhancement factor of PAH (blue squares) and Life time (red circles), when plotted as a function of spacer thickness.

To understand the mechanism of MEF in our study, we compared the lifetime values of free PAH with PAH-adsorbed 45 nm Au@SiO_2 nanoparticles of different thicknesses (**Figure 3.6a** & **Table 3.1**). Compared to free PAH, we observed a decrease in the slower component of the lifetime as well as in the average lifetime of PAH, when it is adsorbed on Au@SiO_2 nanoparticles. The average lifetime of the emitter was calculated using the following equation:[41]

$$\tau_f = \frac{\sum \alpha_i {\tau_i}^2}{\sum \alpha_i \tau_i}$$

Where, τ_i is the lifetime of a particular component, α_i is considered as the contribution of that particular component and τ_f is the average lifetime. However, **Table 3.1** suggests that the lifetime of PAH decreases in the beginning and then unusually increases with increase in silica spacer. But we have seen earlier in **Figure 3.5a**, that the fluorescence intensity increases initially and then decrease with spacer thickness. These results critically suggest that the enhancement of fluorescence of PAH is directly associated with the decrease of its fluorescence decay time. In fact, **Figure 3.6b** clearly showed this anticorrelated behaviour of fluorescence intensity and its corresponding lifetime, at different distances from the metallic surface. Maybe, below an optimum distance the MEF decreases due to competing NSET process at shorter distances (< 10 nm), resulting in increase in lifetime. However, it may be noted that at every thickness of the silica spacer, the lifetime of the adsorbed PAH is still less than the free PAH. The results definitely indicated that the MEF of PAH, followed the mechanism of the enhancement of intrinsic radiative decay rate.

Table 3.1. Lifetime values of free PAH with PAH-adsorbed 45 nm Au@SiO_2 nanoparticles of different thicknesses.

Sample	τ_1 (ns)	τ_2 (ns)	τ_3 (ns)	α_1 (%)	α_2 (%)	α_3 (%)	$\chi 2$	Average life time (ns)
Free PAH	0.55	3.85	10.59	21.95	55.37	33.59	1.17	6.53
With 7.2 nm spacer	1.54	3.98	9,79	26.64	31.83	41.53	1.05	5.74
With 8.7 nm spacer	1.53	2.65	9.21	22.36	31.57	46.07	1.13	5.42
With 11.2 nm spacer	1.08	2.39	9.19	20.13	35.75	44.12	1.23	**5.12**
With 12.3 nm spacer	2.69	5.77	10.87	33.12	50.7	16.18	1.20	5.52
With 18.1 nm spacer	2.97	5.89	9.76	26.73	53.04	26.73	1.24	5.89

3.2.4. Discussion on dependence of MEF on size of AuNPs using Radiating Plasmon Model

To explore how the size of the AuNPs influence the outcome of MEF, steady state fluorescence and lifetime measurements were also performed with 22 and 60 nm AuNPs and the results were compared with 45 nm case, for a fixed silica spacer. As can be seen from **Figure 3.7a**, the fluorescence enhancement is highest for 45 nm and lowest with 60 nm diameter particles. Moreover, lifetime measurements confirmed

that enhancement of fluorescence of PAH was directly connected with the decrease of its fluorescence decay time (**Figure 3.7b & Table 3.2)**, i.e., as expected we observed lowest and highest average lifetimes with 45 nm and 60 nm particles, respectively. Not only that, we also performed the MEF studies as a function of spacer thickness for 22 and 60 nm AuNPs (**Figure 3.7c-f**). We observed similar trend as 45 nm case, that with increase in fluorescence intensity of PAH, there was a concomitant lowering in the decay time for PAH (**Figure 3.7g-i**).

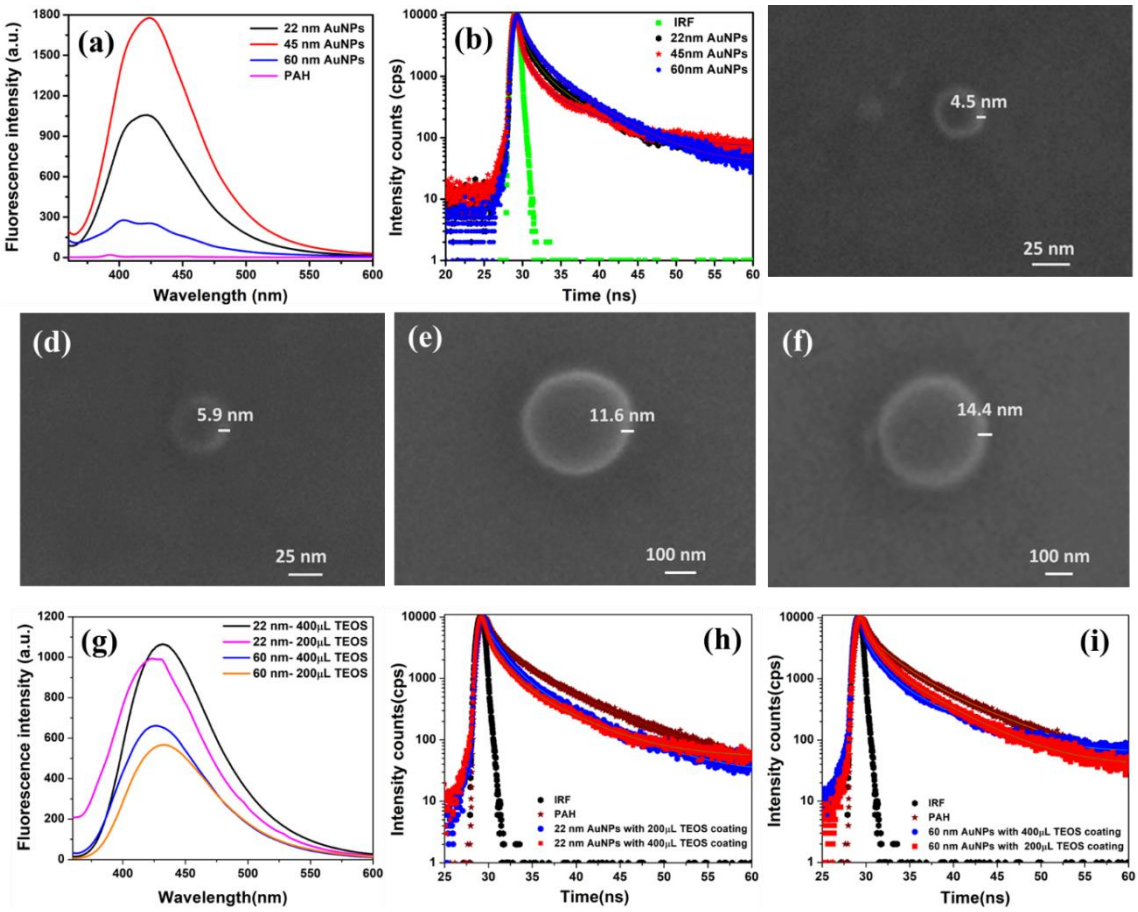

Figure 3.7. (a) Fluorescence intensity and (b) Fluorescence decay curves of PAH adsorbed onto Au@SiO_2 nanoparticles of same spacer length but different diameter of AuNPs; STEM images of 22 nm AuNPs with (c) 200 μL TEOS and (d) 400 μL TEOS coating; STEM images of 60 nm AuNPs with (e) 200 μL TEOS and (f) 400 μL TEOS coating; (g) Fluorescence intensity of PAH at two different spacer thickness for 22 nm and 60 nm AuNPs and Time resolved decay curves of PAH adsorbed at two different spacer thickness for (h)22 nm and (i) 60 nm AuNPs.

We have used the 'Radiating Plasmon'(RP) model introduced earlier by J. Lakowicz, in 2005[47] to understand the dependence of MEF on the size of AuNPs. According to RP model, due to the coupling of the emission from the excited fluorophore with the surface plasmon of the metallic nanostructure, surface plasmon coupled emission

(SPCE) is observed with enhanced intensity, at the emission wavelength of the free fluorophore. It is hypothesized that, the induced plasmons will radiate more when the scattering component of the AuNPs would be dominant compared to the absorption component of the colloid. As, the absorption cross section mainly contributes in the quenching of fluorescence. As a matter of fact, scattering efficiencies of the AuNPs are directly proportional to its diameter, so the size of the metallic nanoparticles remains as a crucial factor for observed MEF. In order to get more insight of the observed MEF effect, we have theoretically calculated (**Figure 3.8**) the absorption, scattering and extinction spectra of the used AuNPs, using MiePlot4613 software.[51] It can be clearly seen from **Figure 3.8** that the absorption component is high for smaller AuNPs, whereas scattering component increases with increase in size. We expected that with more scattering component, larger nanoparticles to be better candidates for MEF. But, as shown in **Figure 3.7a**, the actual experimental result was counterintuitive as highest enhancement was observed with 45 nm particles, while 60 nm produced the lowest enhancement. Possibly, the highest MEF was associated with 45 nm, as it possessed higher scattering efficiency and lower absorption efficiency, compared to 22 nm particles. At this point, it is also to be noted that the linewidth of the extinction band of a nanostructure is directly associated to their ability to confine and enhance the incident electromagnetic field.[52] Therefore, if the linewidth for a scattering band is found to be broad, it is challenging for the particular nanostructure to enhance the fluorescence and show desired MEF, although theoretical scattering efficiencies are still high. This was a probable reason that we observed only a modest enhancement with the 60 nm nanoparticles, as the plasmonic band was found to be broad (**Figure 3.8d & Figure 3.2f**), compared to the 22 and 45 nm particles.

Table 3.2. Lifetime values of free PAH and PAH adsorbed onto Au@SiO_2 nanoparticles of same spacer length but different diameter of AuNPs.

Sample	τ_1 (ns)	τ_2 (ns)	τ_3 (ns)	α_1 (%)	α_2 (%)	α_3 (%)	χ^2	Average life time (ns)
Free PAH	0.55	3.85	10.59	21.95	55.37	33.59	1.17	6.53
With 22 nm AuNPs	1.55	4.38	9.24	29.31	34.41	36.28	1.08	5.31
With 45 nm AuNPs	1.08	2.39	9.19	20.13	35.75	44.12	1.23	5.12
With 60 nm AuNPs	3.53	5.22	9.88	53.7	21.19	25.1	1.26	5.48

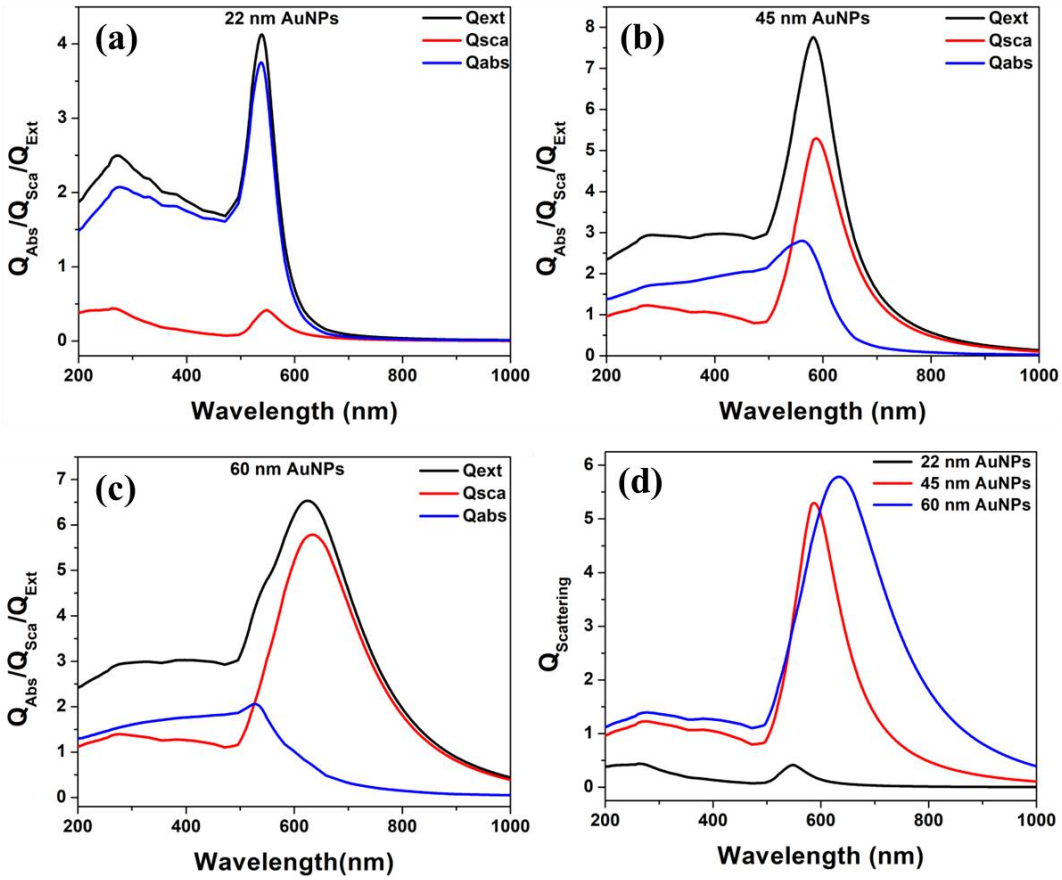

Figure 3.8. Theoretical **e**xtinction, scattering, and absorption spectra of (a) 22, (b) 45, and (c) 60 nm AuNPs in SiO_2. (d) A comparison of the scattering component of 22, 45, and 60 nm AuNPs.

3.2.5. Detection of Picric acid via fluorescence quenching of PAH-adsorbed Au@SiO_2 particles (sensor)

Generally, electron deficient molecules are inclined towards interaction with electron-rich molecules such as free amines or aryl amine groups. Based on this information, several type of sensors[53-59] has been developed for highly electron deficient nitro aromatic compounds (NACs). Thus, high fluorescence intensity of PAH as a result of MEF has encouraged us to delve into its probable application as a sensor for nitro aromatic explosives. PA is a highly electron deficient nitro aromatic molecule due to presence of three nitro groups. We observed, immediate quenching of fluorescence intensity of the 45 nm AuNP based sensor, on addition of PA. To comprehend the quenching efficacy of sensor towards PA, fluorescence titrations were performed with increasing the concentration of PA. **Figure 3.9a** demonstrated a sequential 'turn-off' behaviour of the sensor, as we observed a decrease in the emission of the sensor on addition of increasing amount of PA. The outcomes accomplished from fluorescence

titration were used to determine Stern-Volmer quenching constant between the interaction of sensor and PA. Stern-Volmer plot (I_o/I vs concentration of PA) for the sensor was presented in **Figure 3.9b**, where I and I_o are the fluorescence intensities of sensor in presence and absence of quencher (Q). The plot is obtained as linear at lower concentrations of PA and it departs from linearity at higher concentrations. The Stern-Volmer constant K_{SV} was calculated in the linear range of the graph from the relation: $\frac{I_0}{I} = 1 + K_{SV}[Q]$. The value was found to be 1.2 x 10^6 M^{-1}, comparable to earlier reported values.[14,60] It is apparent from Stern Volmer plot (**Figure 3.9b**) that the plot rises exponentially with increase in concentration of PA, demonstrating a super amplified quenching process.[61,62] The nonlinear nature of the plot suggests intensified fluorescence quenching through dynamic quenching. As shown in **Figure 3.9c**, a plot between $(I_{max} - I)/(I_{max} - I_{min})$ Vs log[PA] was obtained and the detection limit (LOD) was calculated from the X-intercept of the straight line, as per standard procedure.[63] Where, I_{max} and I_{min} were the maximum and minimum intensity in the selected range of concentrations and I was the fluorescence intensity at that particular concentration. The detection limit of this MEF sensor for PA, was found to be 79 nM.

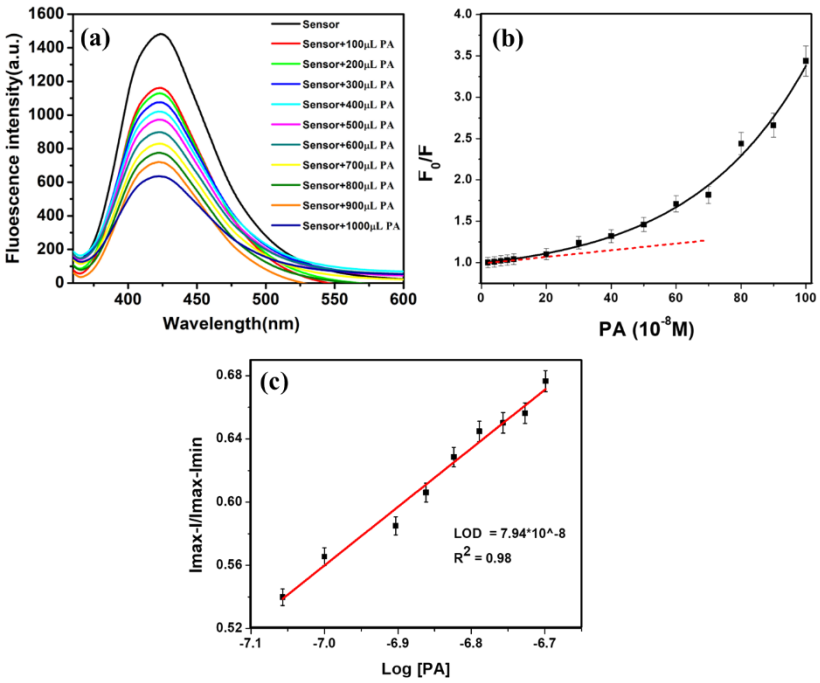

Figure 3.9. (a) Quenching of fluorescence intensity of sensor on addition of different amount of 10^{-8} M of PA in water, (b) Stern-Volmer analyses of the sensor at different concentrations of PA (the red dotted line showing the linear range) and (c) Detection limit calculation of the sensor for PA.

3.2.6. Selectivity study of the detection and discussion on the mechanism

To evaluate the selectivity of our MEF sensor for PA over other interfering analytes, fluorescence quenching studies were also performed with similar electron deficient nitro aromatics like mono nitro toluene (MNT), tri nitro toluene (TNT), phenol, 2-nitro phenol (2-NP), 4-nitro phenol (4-NP), Nitro benzene (NB), 3-Nitro acetophenone (NA) and 4-Nitro benzoic acid (NBA). The response of the sensor was recorded and plotted in **Figure 3.10a**, for all of the nitroaromatics. As expected, different extents of fluorescence quenching were observed on addition of different analytes of same concentration (10^{-6} M). For better understanding, quenching efficiency of different analytes were also calculated by using the formula $(I_0\text{-}I)/I_0*100\%$ and plotted; where I_0 and I were the corresponding fluorescence intensities of the sensor before and after the addition of different analytes (**Figure 3.10b**). As can be seen clearly, all the analytes slaked the fluorescence to little extent but picric acid has shown extremely noteworthy and sensitive fluorescence quenching efficiency of 72%. Upon varying the pH of the medium, the quenching efficiency of the sensor for PA was found to be unchanged in the acidic pH, however it slightly decreased to ~ 60% in the higher pH above 7 (**Figure 3.10c&d**).

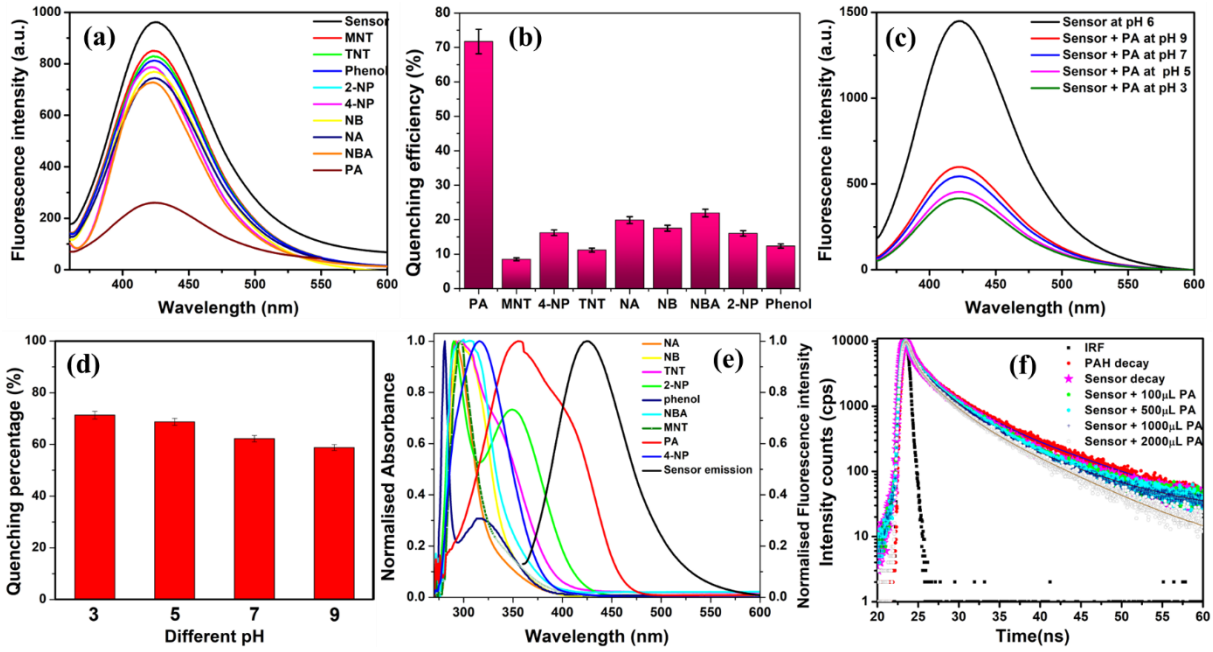

Figure 3.10. (a) Fluorescence quenching studies of sensor in presence of various analytes, 200 µL of 10^{-6} M analyte solution in water was added to 1.8 mL of sensor solution in each case; (b) Quenching efficiency plot of different analytes; (c) Absorption spectra of analytes and their overlap with emission spectra of sensor; (d) Time resolved fluorescence spectra of sensor with increasing volumes of PA.

The high selectivity of this MEF sensor towards PA and presence of curvature in the Stern- Volmer plot suggested the contribution from both static and dynamic quenching. In order to investigate if there was a possibility of fluorescence resonance energy transfer (FRET) from the sensor (donor) to NACs (acceptor), we plotted the absorption spectra of NACs along with the fluorescence spectrum of the sensor. It is known that the extent of spectral overlap between sensor's emission and quencher's absorption spectrum determines the rate of energy transfer. **Figure 3.10e** confirmed a large overlap between the fluorescence spectrum of the MEF sensor and absorption spectrum of PA which resulted in significant quenching in fluorescence, in contrast to other NACs with less or negligible overlap. To understand the extent of overlap in a quantitative way, overlap integral values (J_λ) were also calculated (**Table 3.3**). J_λ was found to be maximum for picric acid when compared to other NACs. Moreover, a comparison study of the lifetime decay curves (**Figure 3.10f**) and lifetime components (**Table 3.4**) of the sensor with increasing amount of PA clearly indicated the mechanism of the quenching process. Initially, the average lifetime of the sensor did not alter from 5.1 ns till 500 µL addition of PA, indicating a possible static quenching. However, the average lifetime dropped to 3.9 ns with further addition of 500 µL of PA to the sensor solution, suggesting dynamic quenching via FRET. This indicated that the decrease of fluorescence intensity of the sensor with PA, was an example of combined static and dynamic quenching.

Table 3.3. Overlap integral values of different analytes.

NAC	J Integral (J_λ) M^{-1} cm^{-1} nm^5
PA	69.35×10^9
MNT	0.031×10^9
TNT	1.389×10^9
Phenol	0.037×10^9
2-NP	12.117×10^9
4-NP	10.39×10^9
NB	0.055×10^9
NA	10.55×10^9
NBA	0.019×10^9

Table 3.4. Average life time values of sensor on addition of increasing volumes of PA.

Sample	τ_1 (ns)	τ_2 (ns)	τ_3 (ns)	α_1 (%)	α_2 (%)	α_3 (%)	$\chi 2$	Average life time (ns)
Free PAH	0.55	3.85	10.59	21.95	55.37	33.59	1.17	6.53
Sensor	1.08	2.39	9.19	20.13	35.75	44.12	1.33	5.13
Sensor+100 µL PA	0.55	3.29	9.09	21.55	53.52	25.05	1.32	5.13
Sensor+500 µL PA	0.57	3.35	9.09	22.2	53.35	25.55	1.33	5.10
Sensor+1000 µL PA	0.50	3.37	9.51	23.83	55.32	20.85	1.27	3.95
Sensor+2000 µL PA	0.50	2.57	7.32	25.03	51.1	35.87	1.15	3.73

3.2.7. Detection of PA in real samples

The sensor was also explored for detection of PA in aqueous samples from various sources, to assess the efficacy of the proposed method in presence of interferences from different matrix. Since, no obvious PA detection was noticed in collected water samples, we subsequently spiked each sample with three known concentrations of PA (10, 20 and 50 µM) and tested for recovery (**Figure 3.11a-d**). As shown in the **Table 3.5**, the recoveries were found to be in the range of 95-108% and the relative standard deviation of triplicates was less than 5%, proving the feasibility of sensor even in real water samples. Further, we also studied the efficacy of the sensor in competitive environment amongst possible ionic interferences in aqeous medium. We carried out the PA detection in presence of common cations and anions present in water. As shown in the **Figure 3.11e&f**, we did not observe any notable interference from metal ions or anions, indicating that the sensor could be used for detection of PA even in water samples obtained from natural sources.

Table 3.5. Detection of PA in spiked water samples.

Sample	Added (µM)	Found (µM)	Recovery (%)	RSD (%)
Tap water	10	9.54	95.4	0.2
	20	21.5	107.5	0.4
	50	52	104	0.5
Pond water	10	10.4	104	0.4
	20	19.4	97	0.2
	50	54	108	0.3
Lake water	10	10.6	106	0.3
	20	21	105	0.1
	50	51.2	102	0.2

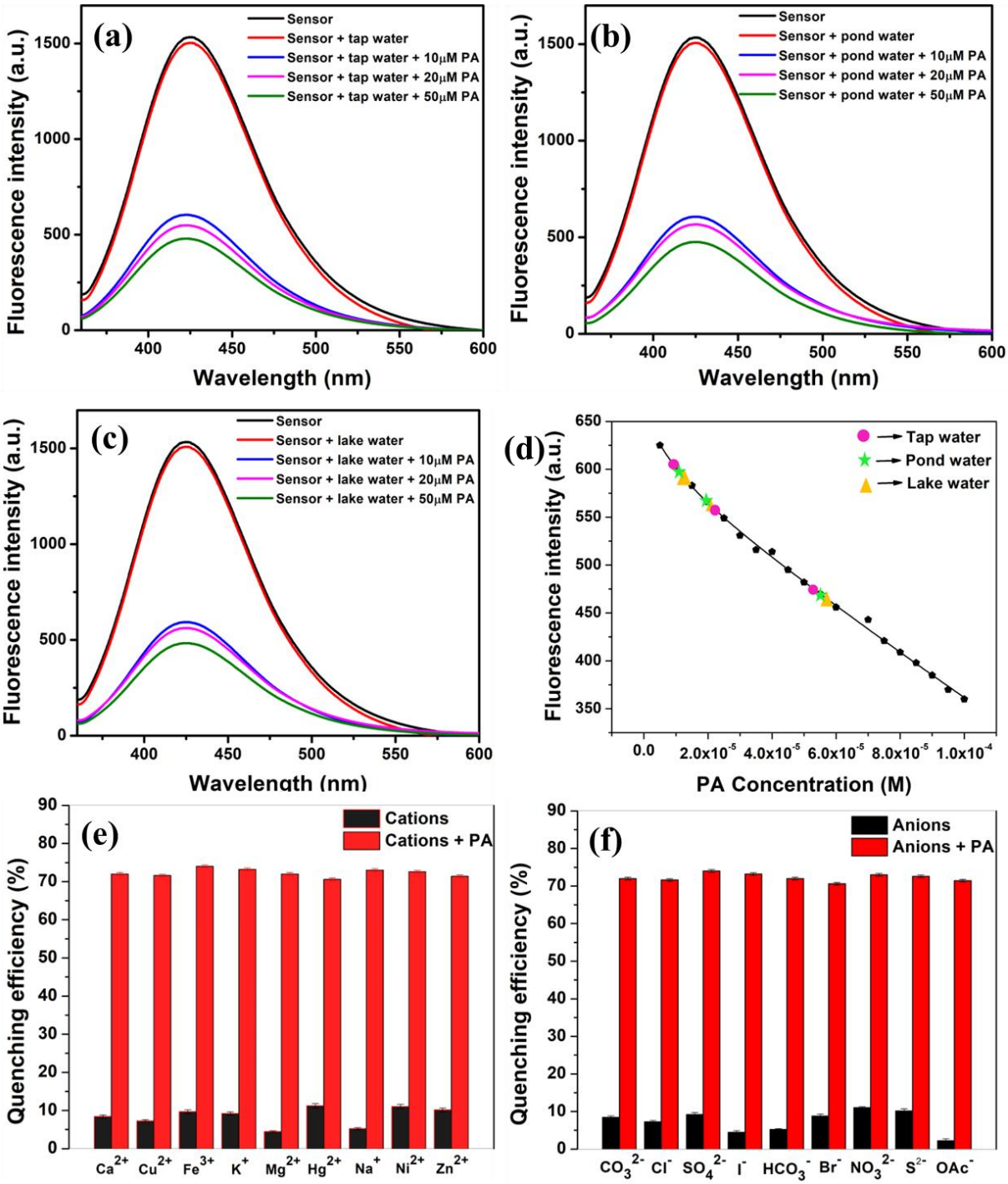

Figure 3.11. Fluorescence spectra of the sensor on addition of 200 μL of spiked sample with PA from (a) tap water, (b) pond water, (c) lake water, (d) is the calibration curve used for calculating the recovery concentrations, (e) and (f) represents the bar plot showing intact quenching efficiency of the sensor towards PA in presence of common cations and anions present in water, respectively. Black bars represent the efficiency on addition of 200 μL of 10^{-6}M respective ions to 1.8 mL of sensor, while red bars show the efficiency on subsequent addition of 200 μL of 10^{-6}M PA in the same solution.

As part of the on-site detection of PA, we extended our analysis in soil sample. As shown in **Figure 3.12**, the sensor solution with 100mg of soil but without PA, showed unchanged emission intensity under UV excitation at 365 nm. However,

addtion of same amount of soil but mixed with increasing concentration of PA, demonstrated immediate quenching of the intensity. We observed similar trend in the quenching behaviour when we recorded the fluorescence spectra of the same solutions (**Figure 3.12**). Each solution was filtered before the fluorescence spectra was obtained. It was observed, the sample containing only sensor and soil without PA, showed high fluorescence intensity (Figure 10b) indicating the applicability of the proposed method for visual detection of PA in soil.

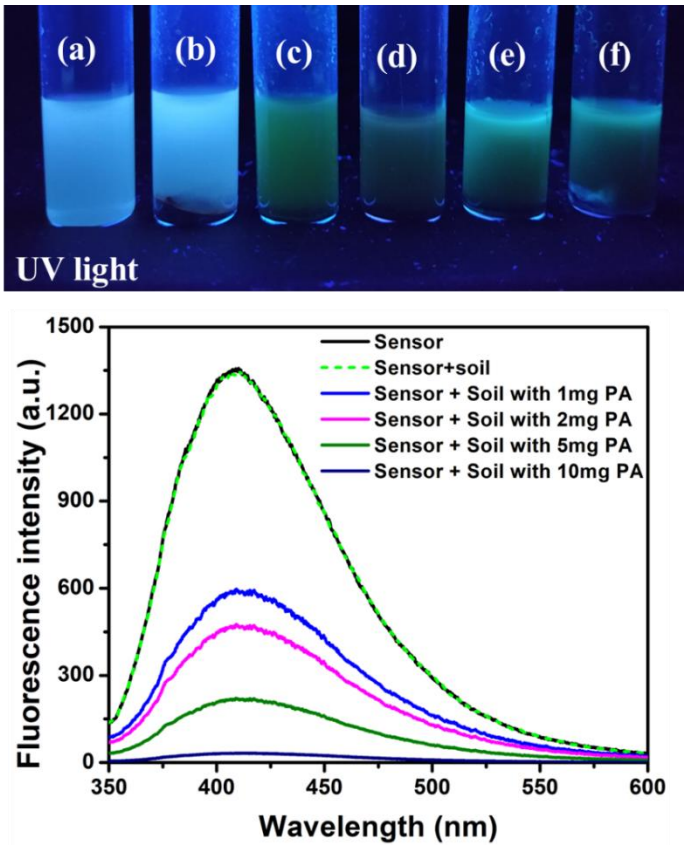

Figure 3.12. Sensing of PA in soil: (a) only sensor; (b) sensor with 100 mg of soil without PA; (c), (d), (e) and (f) sensor with 100mg of soil containing 10, 5, 2 and 1 mg of PA, respectively and the below fluorescence spectra represents the same.

3.3. Conclusions and Summary

To the best of our knowledge, first time AuNPs based MEF sensor has been used to detect picric acid in aqueous condition. The less-fluorescent reporter molecule PAH, when adsorbed on silica coated 45 nm AuNPs, was benefitted with tremendous ~280-fold fluorescence enhancement compared to free PAH in homogeneous environment. The enhancement was found to depend crucially on the distance between the metal

and the fluorophore, while ~11 nm being the optimum separation for the highest enhancement. The probable mechanism for the MEF phenomena was attributed mainly due to the enhancement of intrinsic radiative decay rate, as indicated by the reduction in the fluorophore lifetime along with enhancement. Among different AuNPs, the highest enhancement was accomplished with the average diameter of 45 nm, whereas 22 nm and 60 nm particles showed moderate and lowest enhancement, respectively. Further, the PAH adsorbed fluorescent nanoparticles were demonstrated as a selective 'turn-off' sensor for PA in water with a detection limit of 79 nm. The Stern-Volmer plot and the lifetime study of the sensor confirmed that the 'turn-off' detection process of PA was a combined case of static and dynamic quenching. Finally, the sensor was successfully applied for on-site visual detection PA in soil, in addition to the detection of PA in aqueous samples obtained from various natural source.

Chapter 4A

Development of hybrid nano theranostic systems with simultaneous MEF and MESOG using Isotropic metal nanoparticles

In this chapter, we tried to optimize and develop systems which can produce simultaneous enhancement in fluorescence as well as singlet oxygen generation. We also studied the role of MNP, role of different spacers for useful applications. This chapter is based on the following paper, S. Kaja, A. Mukherjee, M. Chakravarthy and A. Nag; Identifying high performance photosensitizer with simultaneous enhancement in fluorescence and singlet oxygen generation, from '(Ag/Au)-aggregation-induced emission-active fluorogen' theranostic nanoparticles; Colloids and Surfaces A: Physicochemical and engineering aspects, 2022, 649, 129448.

4A.1. Introduction

The increasing diversity in cancer origins and prognosis demands various treatment strategies. Photodynamic therapy (PDT), initiated by a photo-triggered reaction between photosensitizer (PS) and molecular or triplet oxygen ($^3O_2$), has the potential to replace or support the conventional radiation therapy and chemotherapy that are limited by severe adverse effects.[1-2] Moreover, there is an urgent need to develop materials that provide a therapeutic outcome with simultaneous ability to trace the disease remission/progression.[3,4] So, a PS with bright fluorescence is essential for image-guided PDT. Because, the generation of reactive oxygen species (ROS) or singlet oxygen is expected to kill the cancer cells through oxidative stress mechanism[5,6]; whereas, the enhanced fluorescence allows for simultaneous visualization of tumour location and distribution. Of note, traditional PSs are very weakly fluorescent. Moreover, the hypoxic tumoral environment, ROS's short lifetime increases the need to load higher concentrations of PS. When the loading of PS is high, the production of singlet oxygen generation (SOG) and fluorescence is very minimal due to aggregation-caused quenching effects. As a result, the procedure demands prolonged light exposure time, limiting its practical application.[7] Therefore, it is crucial to develop brightly fluorescent PS with high SOG efficiency upon light irradiation.[8]

On the other hand, plasmonic nanoparticles (NPs) made of gold and silver, have the unprecedented ability to localize and enhance their surrounding electric field and confine it into subwavelength scale due to the excitation of their surface plasmon resonance (SPR) by the incident electromagnetic field. The strong near-field effect produced by plasmon, can enhance singlet oxygen production and emission of a hybrid photosensitizer-metal nanoparticle. It has been shown from different plasmon-based optical experiments that the production of SOG by a PS or fluorescence of an emitter can be dramatically enhanced, by varying several parameters. Some of those parameters are the nanostructure morphology, size, composition and the PS/emitter-metal separation distance. It is found that the distance between the molecule and the metal is most crucial in the process of metal-induced enhancement. The considerations to which we limit this report are: the composition of the plasmonic NPs, the

composition of the spacer and the spacer length. While selecting the PS, it is advantageous to use 'aggregation-induced emission-active fluorogens (AIEgens)' as PS because they do not fluoresce in the molecular state but become brightly fluorescent in the aggregated state due to the restricted intramolecular motion, surpassing the several drawbacks of aggregation-caused quenching of traditional fluorophores.[9-11] Based on AIEgens' unique properties, a wide range of applications in the field of sensing, theranostics, optoelectronics, and bioimaging were well explored.[12-18] Moreover, recent studies on AIEgens have exhibited strong photosensitizing ability, demonstrating the suitability of AIEgens also in image-guided therapies, bacterial killing, and cancer therapies.[19,20] The typical AIE-core tetraphenylethene (TPE)-linked pyridyl salt are mostly adapted as efficient PS. The vinyl-pyridine framework facilitates lowering the singlet-triplet energy gap (ΔE_{ST}), which is vital for a molecule to become an effective photosensitizer.

The plasmonic property of silver and gold NPs, leading to metal-enhanced fluorescence (MEF) and metal-enhanced SOG (ME-SOG), contributed significantly to many technological applications in biological research, molecular physics, medical diagnosis, optical sensing, photovoltaics, etc.[21] Recently, Yen Nee Tan and his co-workers had shown a 6-fold enhancement in fluorescence and a 2-fold enhancement in SOG when their newly synthesized TPE-linked pyridyl salt as PS was electrostatically adsorbed on 85 nm AgNPs.[22] In another study, the same group reported a 10-fold enhancement in SOG when their red emissive AIEgen (similar TPE-based charged core) had been placed in the vicinity of 80 nm AgNPs.[23] Belinda Heyne and her group had studied the spacer's role in SOG and identified that maximum SOG was obtained at a thickness of spacer between 10 to 20 nm.[24,25] They also investigated the role of near- and far-field effects on SOG. They identified that the SOG of hybrid nanoparticles depended on their scattering efficiency, if they were under similar local electric fields.[26] They also demonstrated that the anisotropic shape of NPs produced more SOG due to their increased scattering efficiency and more hot spot generation.[25] Although individual reports are available on MEF and ME-SOG, only a handful of reports had indicated the simultaneous enhancement of fluorescence and SOG when PS was

coupled to metal nanoparticles. Indeed, it is challenging to improve both the SOG efficiency and brightness of fluorescence of a molecule concurrently, as both processes consume the excited state. Therefore, poor fluorescence quantum yields are generally associated with the higher SOG capability for traditional PS molecules, which is a significant drawback for image-guided PDT and warrants immediate attention and improvement.

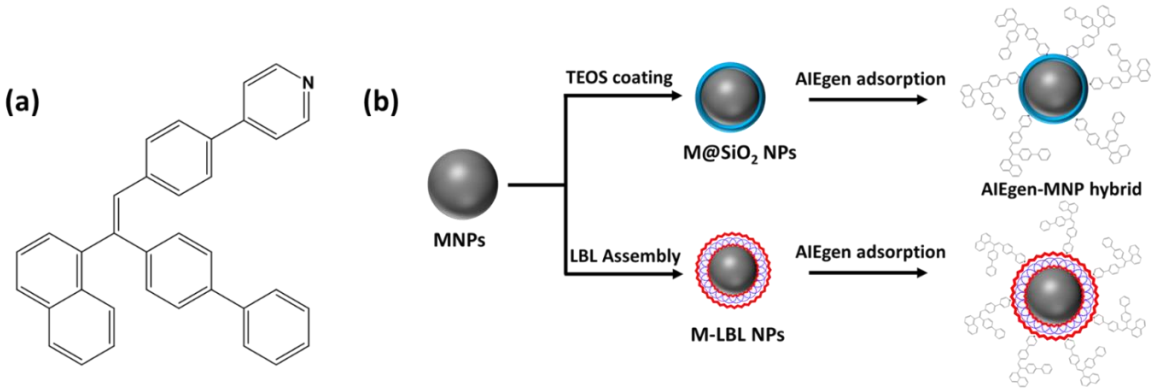

Scheme 4A.1. (a) Structure of (E)-4-(4-(2-([1,1′-biphenyl]-4-yl)-2-(naphthalen-1-yl) vinyl) phenyl) pyridine (**NP-4Py**) used as AIEgen; (b) Preparation of hybrid photosensitizer by loading of AIEgen on metal nano particles (MNPs) with a spacer.

Herein, to achieve the simultaneous MEF and ME-SOG, Ag and Au nanoparticles were selected due to their higher plasmonic efficiencies. Unlike to previous reports, we plan to explore naphthalene-biphenyl-pyridyl linked triarylethene as *neutral* and green emitting AIEgen **NP-4Py** as a new class of photosensitizer.[14] Of note, this AIEgen consists of an electron-rich platform linked with the electron poor pyridyl core, thus offering an intense electron density on the pyridyl nitrogen atom that enables binding on pure or modified Ag/Au surface.[27] A systematic investigation is performed with this new PS **NP-4Py** using two commonly-used model spacer systems: (i) a silica shell resulting in core-shell metal NPs and (ii) a polyelectrolyte coating on metal NPs by 'layer-by-layer (LBL)' self-assembly of differently charged polyelectrolytes (**Scheme 4A.1**). While, silica coating offers advantages like insulation from the surrounding medium, chemical/thermal stability, appropriateness for surface modifications, robustness and so on,[28] the LBL technique is also a simple and cost-effective method to provide binding sites for dyes or fluorophores that tightly control the thickness of the layer.[29] Using these strategies, simultaneous enhancements in fluorescence and

SOG were successfully achieved for the AIEgen loaded hybrid nanoparticle PS. The spacer length, present in between metal NPs and AIEgen, played a crucial role in controlling the extent of MEF and ME-SOG manifestation. Most importantly, upon varying the spacer length in a particular hybrid nanoparticle PS set, the highest enhancement factors in MEF and ME-SOG were witnessed at the same spacer length. The results obtained from the combined MEF and ME-SOG study of nano-hybrid PSs, could be useful for designing brightly fluorescent photosensitizers, opening up new opportunities for effective theranostic treatment in the near future. It can be hypothesized that the light activated PS metal nanoparticles will generate reactive oxygen species (ROS) causing cancer cell death, while the enhanced fluorescence intensity will allow tracking the tumour remission or progression and biodistribution of nanoparticles.

4A.2. Results

4A.2.1. Optical, morphological and DLS studies on the metal nanoparticles

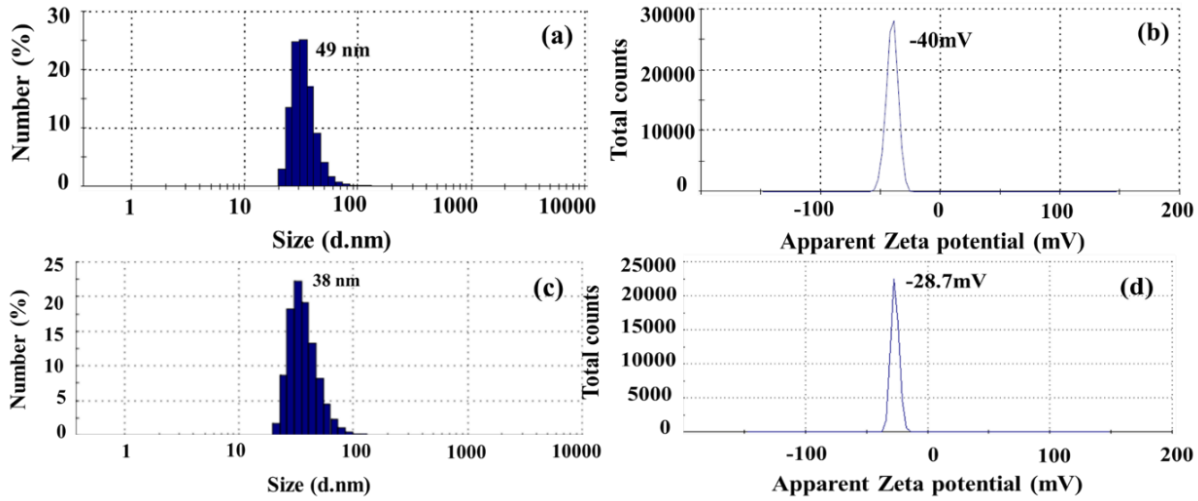

Figure 4A.1. (a) DLS and (b) Zeta potential measurements of AgNPs; (c) DLS and (d) Zeta potential measurements of AuNPs

The synthesized AgNPs and AuNPs were initially characterized by collecting their DLS spectra. The DLS measurements of AgNPs revealed the average size of particles as ~49 nm and the zeta potential as negative (-40 mV) due to the presence of tannic acid on its surface (**Figure 4A.1a & b**). In case of AuNPs the average particle

size was found to be ~38 nm and Zeta potential was -29 mV in DLS study due to the citrate capping (**Figure 4A.1c & d**). Later, we have collected the extinction spectra of NPs solutions. AgNPs and AuNPs displayed a characteristic surface plasmon resonance (SPR) maximum at 434 nm and 538 nm, respectively as shown in **Figure 4A.2a & b.** However, the final confirmation on the average size of the NPs was obtained from FE-SEM experiments (**Figure 4A.2c & d)** which revealed that AgNPs and AuNPs were found to be of uniform sizes around ~49 nm and ~42 nm, respectively and their particle size distribution plots are shown in the inset of Figures ((**Figure 4A.2c & d)**). Although the size of the metallic nanoparticles (MNPs) is a crucial factor for the plasmon-enhanced phenomena, we refrained from the size variation, as the earlier reports on MEF from our group[30] indicated that best MEF results were obtained with NPs in the diameter range of 30 nm to 50 nm. After the synthesis and characterization of Ag and Au NPs, we synthesized core-shell and LBL assembled NPs for MEF and ME-SOG studies.

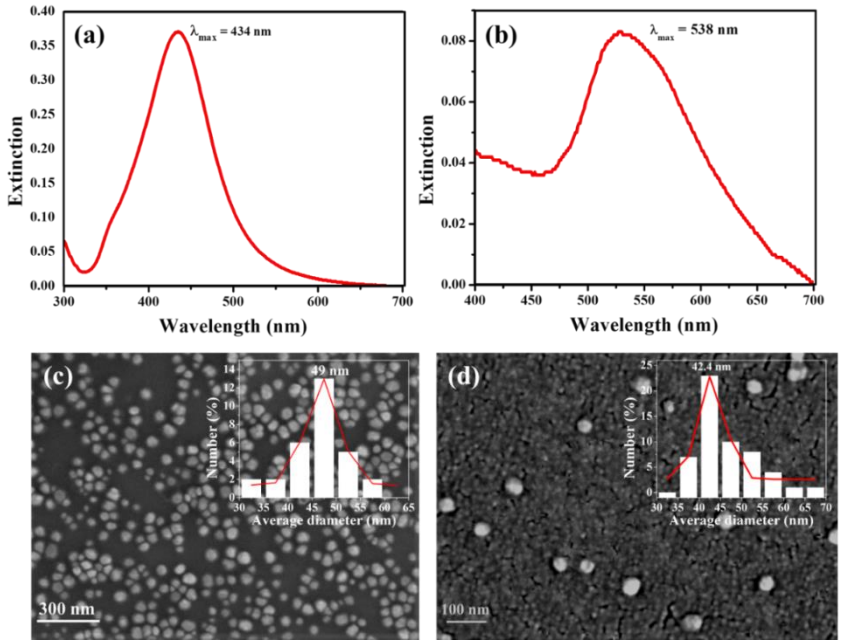

Figure 4A.2. (a), (b) are extinction spectra of AgNPs and AuNPs, respectively. (c), (d) are the FE-SEM images of AgNPs and AuNPs, respectively and the inset figures represent the average diameter plots of the same.

4A.2.2. MEF and ME-SOG studies using $Ag@SiO_2$ NPs

4A.2.2a. Characterization of $Ag@SiO_2$ NPs

$Ag@SiO_2$ core-shell NPs of 6 different silica shell thicknesses were synthesized according to Stober's protocol by changing TEOS's amount in each reaction mixture,

and characterized by recording their DLS, Zeta, FE-SEM and extinction spectra. From the DLS measurements, as shown in **Figure 4A.3,** the size of the NPs was found to be increased from 49 nm to 77 nm with an increase in the amount of silica precursor, indicating subsequent growth in thickness of silica shell. The zeta potential also decreased from -31mV to -12mV, indicating the increase in silane functional groups, which were less negatively charged than the citrate functional groups **Figure 4A.3**.[30]

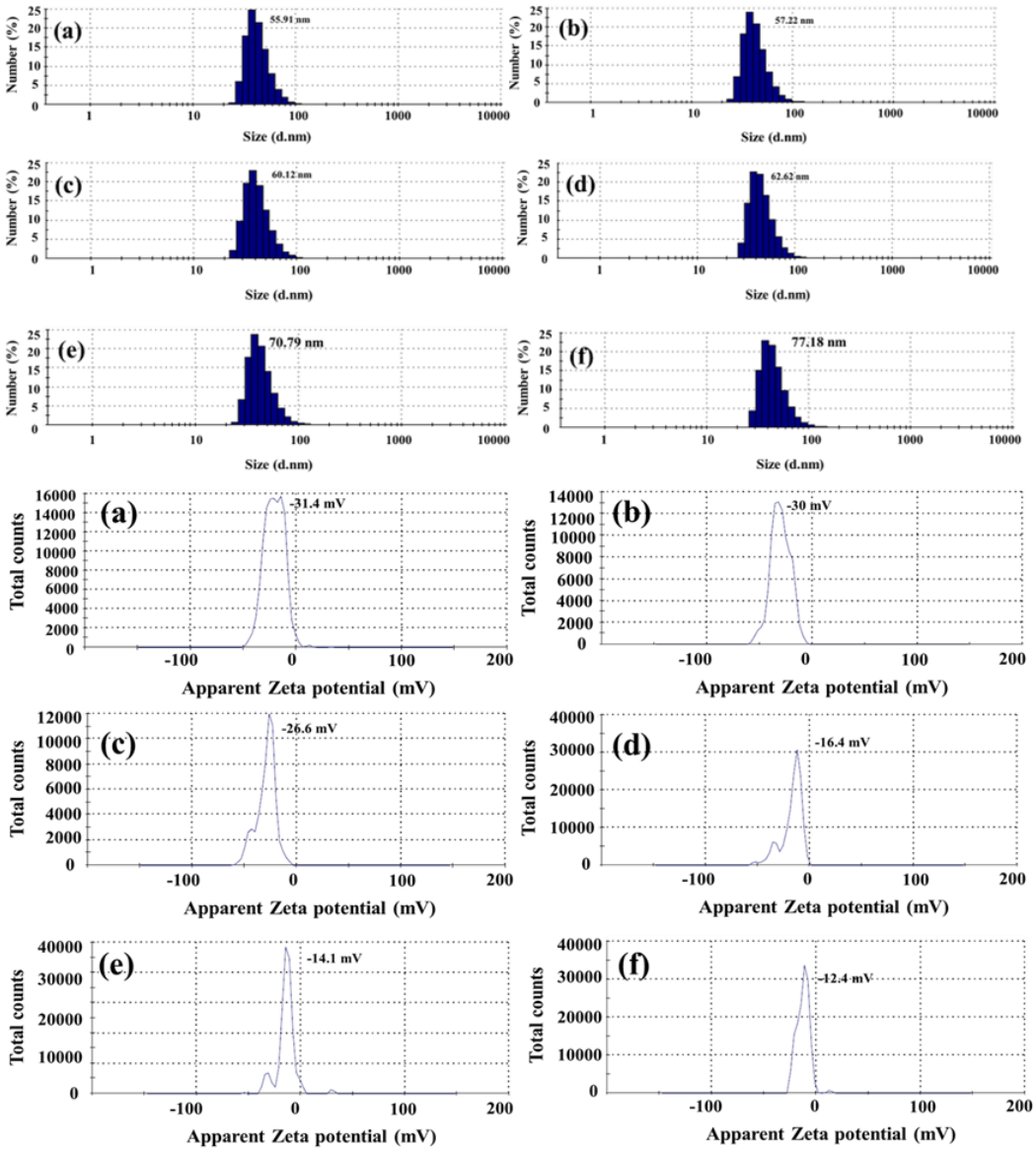

Figure 4A.3. DLS (top) and Zeta potential (bottom) measurements of $Ag@SiO_2$ NPs with increase in shell thickness from (a) to (f)

Moreover, as shown in **Figure 4A.4** the FE-SEM images of $Ag@SiO_2$ NPs revealed an increase in particle size from 47 nm to 69 nm, confirming the core-shell structure formation with an increase in silica thickness. Later, the extinction spectra of NPs were

collected and it displayed a small redshift in each case, with an increase in silica shell thickness (**Figure 4A.5a)**. This was observed due to the higher refractive index of silica compared to water.[31,32]

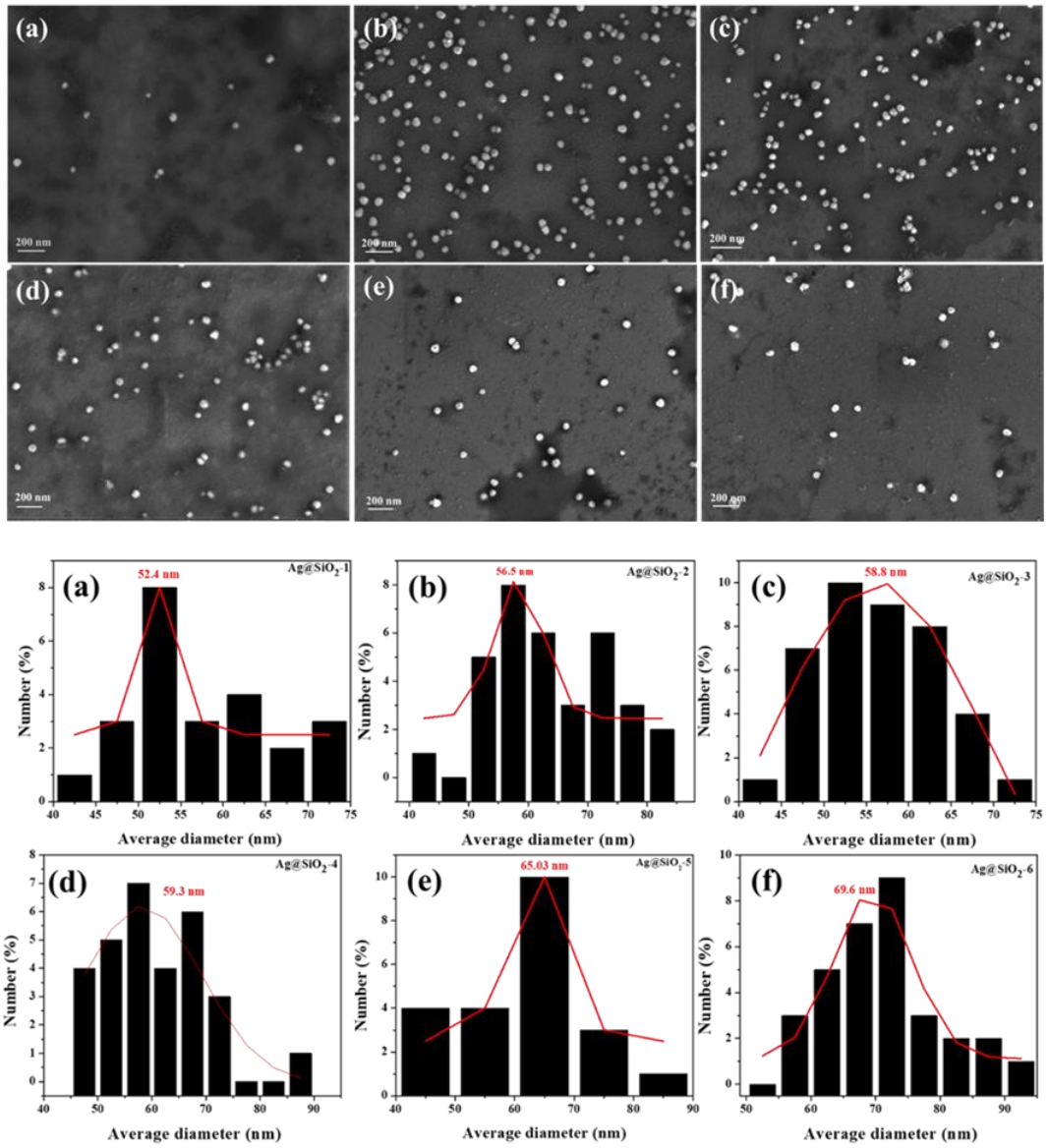

Figure 4A.4. FE-SEM images and the corresponding average size plots of $Ag@SiO_2$ NPs with increase in their shell thickness from (a) to (f).

4A.2.2b. MEF studies of AIEgen loaded $Ag@SiO_2$ NPs

The $Ag@SiO_2$ NPs of different silica thicknesses were used for the MEF study of the uncharged pyridyl AIEgen **NP-4Py**, where the adsorbed AIEgen was separated from the Ag core by the silica shell spacer of a particular thickness. Notably, the contribution of the Ag core in the MEF of the AIEgen molecule was recognized by performing an identical study by adsorbing the same concentration of AIEgen molecules (10^{-5} M) on

silica NPs (blank study), which were devoid of any plasmonic metal. Subsequently, the enhancement factor (EF) of MEF was calculated as the ratio of maximum fluorescence intensity of Ag@SiO_2-AIEgen of various silica thicknesses to the maximum fluorescence intensity of blank sample SiNPs-AIEgen. As shown in **Figure 4A.5b**, the AIEgen fluorescence was significantly quenched when it was adsorbed directly on bare AgNPs without any spacer, due to efficient Nano surface energy transfer (NSET)' between excited AIEgen and AgNPs. However, a significant enhancement in fluorescence was noticed for Ag@SiO_2 (1-6)-AIEgen hybrid NPs and the EF was shown in **Table 4A.1**. The fluorescence intensity increased initially with an increase in shell thickness till Ag@SiO_2-3 case and then decreased continuously thereafter, indicating the distance-dependent nature of MEF. It was clear that two competing processes were operative between AIEgen and AgNPs, namely, fluorescence quenching of AIEgen via NSET and fluorescence enhancement of AIEgen due to one or more possible reasons, such as, near field enhancement and/or modification of the radiative decay rate of the AIEgen. Therefore, MEF initially increased as AIEgen approached closer to Ag surface, but decreased once the distance became less than 11 nm due to probable non-radiative

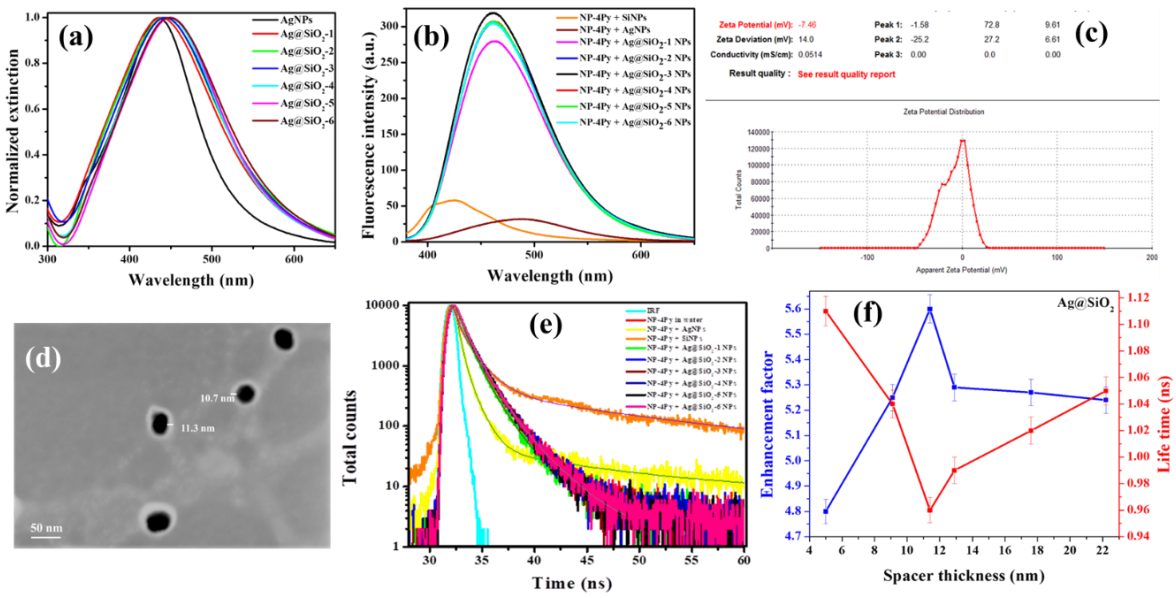

Figure 4A.5. (a) Extinction spectra of core-shell NPs of different thicknesses, (b) MEF study of **NP-4Py** using Ag@SiO_2 NPs, (c) Zeta potential of SiNPs, (d) STEM image of Ag@SiO_2-3 in bright field mode, (e) Lifetime plot of **NP-4Py** in presence of Ag@SiO_2 NPs and (f) Anticorrelated behaviour of enhancement factor of **NP-4Py** (blue squares) and Life time (red squares), when plotted as a function of spacer thickness.

loss. On the other hand, the fluorescence intensity of AIEgen was found to be very modest when it was adsorbed on SiNPs, comparable with the bare AgNPs case. Moreover, a blue shift in the emission maximum of the PS when adsorbed to SiNPs, can be a result of more hydrophobic surface for SiNPs with an average zeta potential value close to zero (**Figure 4A.5c**). Probably, a smaller number of -OH groups are present on the surface of SiNPs, compared to the presence of more -OH groups on silica coated Ag or Au NPs. The highest EF has appeared to be ~5.6 for Ag@SiO_2-3 NPs, where the spacer thickness was estimated to be around ~11 nm, as obtained from the STEM image (**Figure 4A.5d**).

4A.2.2c. Mechanism of MEF

As already stated, there are two probable factors behind fluorescence enhancement. In the case of near field enhancement, along with the increase in the local electric field, the lifetime of the molecule remains unaltered. Whereas, the enhancement via an increase in the radiative decay rate of the molecule is associated with the decrease in a lifetime. Therefore, to understand the mechanism of MEF, we measured the fluorescence lifetime decays of the AIEgen in water and also after adsorption onto AgNPs, SiNPs, and Ag@SiO_2 core-shell NPs (**Figure 4A.5e**). Because, a 'considerable' decrease in a lifetime with associated enhancement in fluorescence, would predict the MEF mechanism via 'increase in radiative decay rate' of AIEgen instead of 'enhancement of the local electric field by the nanoparticle'.[30,33] Further, the different lifetime components of the AIEgen were also evaluated as the decays were fitted using the tri exponential model, as shown in **Table 4A.2**. It was noticed that the fluorescence decay was much faster for **Np-4Py** adsorbed on AgNPs (0.90 ns) than **Np-4Py** in water (1.16 ns) or adsorbed on SiNPs (3.67 ns), similar to previous reports.[34-36] As depicted in **Table 4A.2**, starting from Ag@SiO_2-1, the average lifetime of AIEgens adsorbed on core-shell NPs initially decreased marginally, with an increase in silica shell thickness till Ag@SiO_2-3 case and then subsequently increased to its initial value, with further increase in spacer length. However, no significant changes were observed for the main lifetime component values (τ_1 and τ_2) of the AIEgen during the distance-dependent

behaviour of MEF. Therefore, it can be concluded that while the system demonstrated anti-correlated behaviour between fluorescence intensity and lifetime (**Figure 4A.5f**), however, radiative decay rate should not be considered as the only reason for the enhancement. In fact, the results suggested that the increase of intrinsic radiative decay rate contributed partly to MEF, whereas the near field enhancement effect should be considered as the dominant reason.

Table 4A.1. MEF Enhancement factor of Ag@SiO_2 core shell NPs with different spacer thickness.

	EF MEF
SiNPs	Blank
AgNPs	Quenching
Ag@SiO_2-1 NPs	4.8
Ag@SiO_2-2 NPs	5.3
Ag@SiO_2-3 NPs	5.6
Ag@SiO_2-4 NPs	5.5
Ag@SiO_2-5 NPs	5.4
Ag@SiO_2-6 NPs	5.2

Table 4A.2. AIE molecule's lifetime (ns) values in water and after adsorption onto AgNPs, SiNPs, and Ag@SiO_2 core-shell NPs.

Sample	τ_1(ns)	τ_2(ns)	τ_3(ns)	α_1 (%)	α_2 (%)	α_3 (%)	χ2	**Average life time(ns)**	**Quantum yield**
NP-4Py in water	0.30	1.02	4.36	57.3	26.12	16.58	1.04	1.16	0.053
NP-4Py + AgNPs	0.19	0.84	9.82	62.01	32.72	5.27	1.10	0.90	-
NP-4Py + SiNPs	0.35	1.54	14.79	32.91	42.95	24.14	1.29	3.67	0.012
NP-4Py + Ag@SiO_2 1 NPs	0.26	1.07	7.43	44.17	49.52	6.3	1.10	1.11	0.054
NP-4Py + Ag@SiO_2 2 NPs	0.25	1.07	7.02	47.87	46.04	6.1	1.33	1.04	0.063
NP-4Py + Ag@SiO_2 3 NPs	0.28	1.11	5.83	44.46	50.75	4.79	1.20	0.96	0.067
NP-4Py + Ag@SiO_2 4 NPs	0.27	1.11	6.49	46.3	48.66	5.04	1.36	0.99	0.066
NP-4Py + Ag@SiO_2 5 NPs	0.29	1.12	6.80	49.84	44.58	5.59	1.28	1.02	0.064
NP-4Py + Ag@SiO_2 6 NPs	0.30	1.14	7.03	43.88	51.38	4.74	1.34	1.05	0.062

4A.2.2d. ME-SOG studies of AIEgen loaded Ag@SiO_2 NPs

Subsequently, envisioning the AIEgen loaded nanoparticles as smart PS with enhanced fluorescence, we studied their SOG ability by measuring the degradation of DPBF under white light irradiation (**Figure 4A.6**), in the presence of AIEgen loaded Ag@SiO_2 NPs.[37] The self-degradation of DPBF in the presence of light (**Figure 4A.6a**), was subtracted from the observed data. The ME-SOG capability of AIEgen adsorbed on different

Ag@SiO_2 NPs was presented in **Figure 4A.6b-i**. As depicted in **Figure 4A.6j** and **Figure 4A.6b**, unlike the result obtained in fluorescence of the particles, it was found that the maximum SOG was recorded when AIEgen was directly adsorbed on bare AgNPs. It is known that when a fluorophore is adsorbed or placed very close to a metallic nanoparticle, the particle extracts all electrons in the excited state from the fluorophore, including the ones required for radiative emission.[38] Moreover, silver and gold nanoparticles are more stable than organic dyes and they are capable of generating singlet oxygen, if O_2 molecules are adsorbed on their surface. Furthermore, the energy transfer from the bare nanoparticles to the adsorbed oxygen molecules may be more efficient, resulting in much superior SOG.[39] However, as discussed earlier, the fluorescence of AIEgen was found to be significantly quenched with bare AgNPs, rendering it practically an unimportant combination. Because, the main motive of the study was to look for a PS with brighter fluorescence and a decent SOG capability. Nevertheless, barring bare AgNPs, ME-SOG also followed a similar trend as MEF: SOG was least when AIEgen was adsorbed on SiNPs (**Figure 4A.6i**), but when adsorbed on Ag@SiO_2 NPs, the rates of SOG were greatly enhanced. The silver core played the role of enhancing the production of $^1O_2$ through enhanced absorption of light. The SOG enhancement factor for Ag@SiO_2 NPs was calculated and represented in **Table 4A.3**, which clearly showed that maximum SOG (EF of 9.5) was also obtained in the case of Ag@SiO_2-3 NPs (**Figure 4A.6j**). The observed results were found to be similar with previously reported work on ME-SOG,[25] as they also observed maximum SOG in their system at an optimum distance of ~11 nm between the NPs and PS. They also concluded from their studies that ME-SOG followed a similar distance dependence as MEF.

Table 4A.3. EF_{SOG} using Ag@SiO2 core shell NPs.

	K	EF_{SOG}
SiNPs	0.01184	-
AgNPs	0.1426	12.04
Ag@SiO_2-1	0.08734	7.37
Ag@SiO_2-2	0.10808	9.12
Ag@SiO_2-3	0.11245	9.49
Ag@SiO_2-4	0.08254	6.97
Ag@SiO_2-5	0.08769	7.40
Ag@SiO_2-6	0.08336	7.04

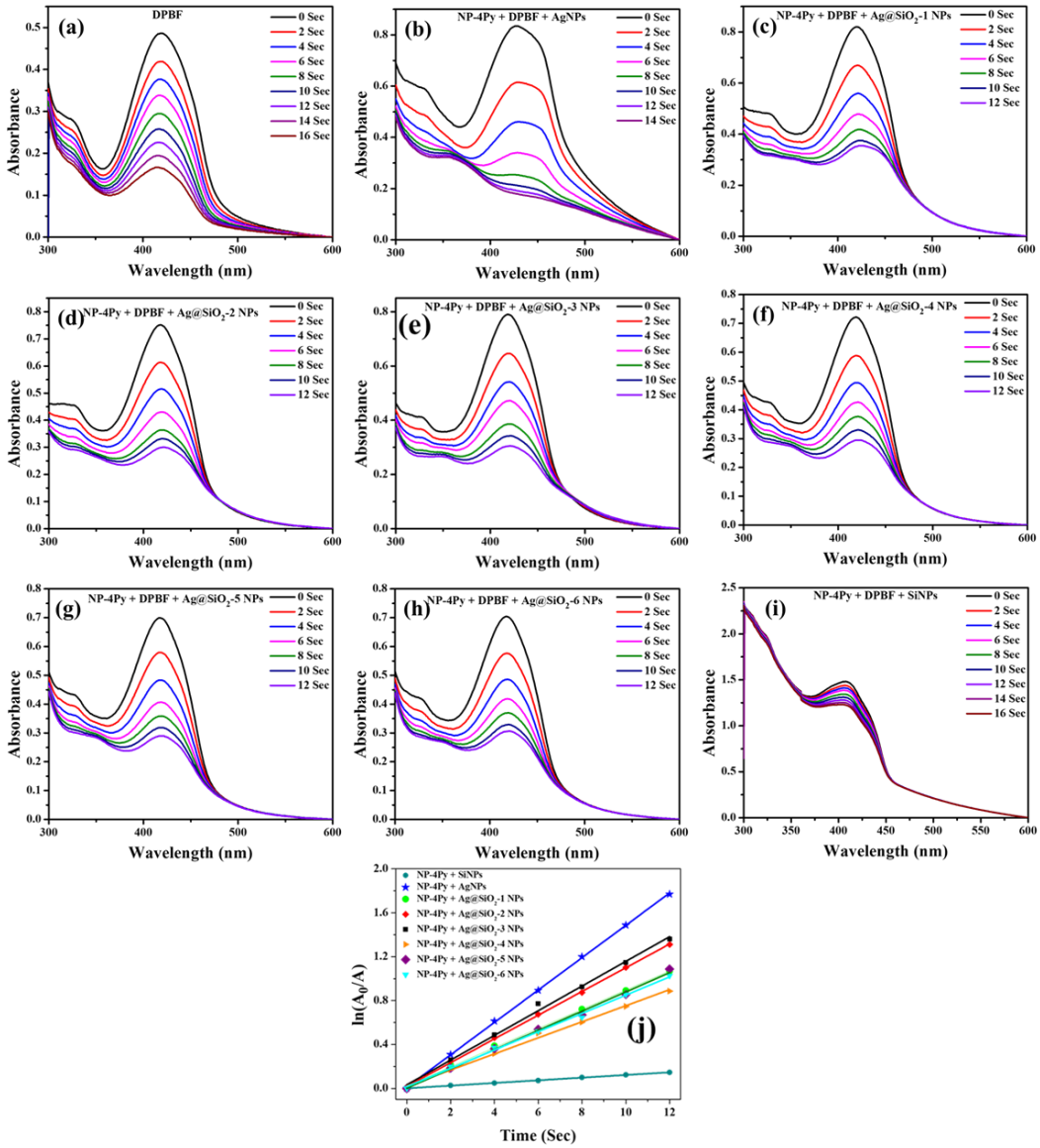

Figure 4A.6. Blank study showing (a) photo bleaching of DPBF, (b-h) SOG generation in presence of $Ag@SiO_2$ NPs of different silica spacer thickness, (i) degradation of DPBF on SiNPs and (j) rate of degradation of 50 μM DPBF in presence of AgNPs, SiNPs and $Ag@SiO_2$ NPs in the presence of 10 μM **NP-4Py** loaded on $Ag@SiO_2$ NPs under 35 mW cm^{-2} white light.

4A.2.3. MEF and ME-SOG studies using Ag-LBL NPs

4A.2.3a. Characterization of Ag-LBL NPs

Next, to understand the critical role of the dielectric spacer, the MEF and ME-SOG studies were performed using a layer-by-layer (LBL) deposition of oppositely charged polyelectrolytes on Ag NPs. The multilayer spacer formation was constructed by the adsorption of oppositely charged molecules via self-sem. The synthesized Ag-LBL NPs were characterized by measuring their extinction spectra, DLS, and zeta potential. As

expected, DLS measurements showed an increase in the size of AgNPs from 49 nm to 68, 74, and 88 nm on adsorption of each polymer layer consecutively (**Figure 4A.7a-c**). From the FE-SEM images of Ag-LBL NPs, it was observed that the average particle size increased from 49 nm to 54 nm, 62 and 74 nm for Ag-1LBL, Ag-2LBl, and Ag-3LBL NPs, respectively (**Figure 4A.7d-f**). The zeta potential variation was also witnessed from -40mV for AgNPs to +31, -33, and +32mV following the first, second, and the third polymer layer adsorption, respectively (**Figure 4A.7a-c)**. As shown in **Figure 4A.8a**, the extinction spectra of AgNPs did not show any considerable shift on the successive adsorption of polyelectrolytes, emphasizing on the good stability of the prepared Ag-LBL NPs.

4A.2.3b. MEF and ME-SOG studies using Ag-LBL NPs

After the successful preparation and characterization of the Ag-LBL nanoparticles, MEF and ME-SOG studies were performed by adsorbing the AIEgen on the NPs. From the MEF studies (**Figure 4A.8b & Table 4A.4**), it was noted that the fluorescence of AIEgen loaded NPs followed the order: Ag-2LBL NPs > Ag-1LBL NPs> Ag-3LBL NPs>> SiNPs, indicating the distance-dependent nature of MEF once again. The highest EF was found to be ~6.4 times for Ag-2LBL NPs, with an average 12 nm thickness of the polymer layer (**Figure 4A.8c**). In this case also, the lifetime studies (**Figure 4A.8d & Table 4A.5**) indicated that MEF was resulted from the collective outcome of increase of intrinsic radiative decay rate and near field enhancement. The highest EF of 9 obtained for ME-SOG (**Figure 4A.9a-d & Table 4A.6**) was acquired at the same spacer length (Ag-2LBL NPs) for highest MEF, registering the simultaneous enhancement of molecular fluorescence and SOG.

Table 4A.4. MEF Enhancement factor of Ag-LBL NPs with different spacer thickness.

	EF MEF
SiNPs	Blank
AgNPs	Quenching
Ag-1LBL NPs	5.1
Ag-2LBL NPs	6.4
Ag-3LBL NPs	4.9

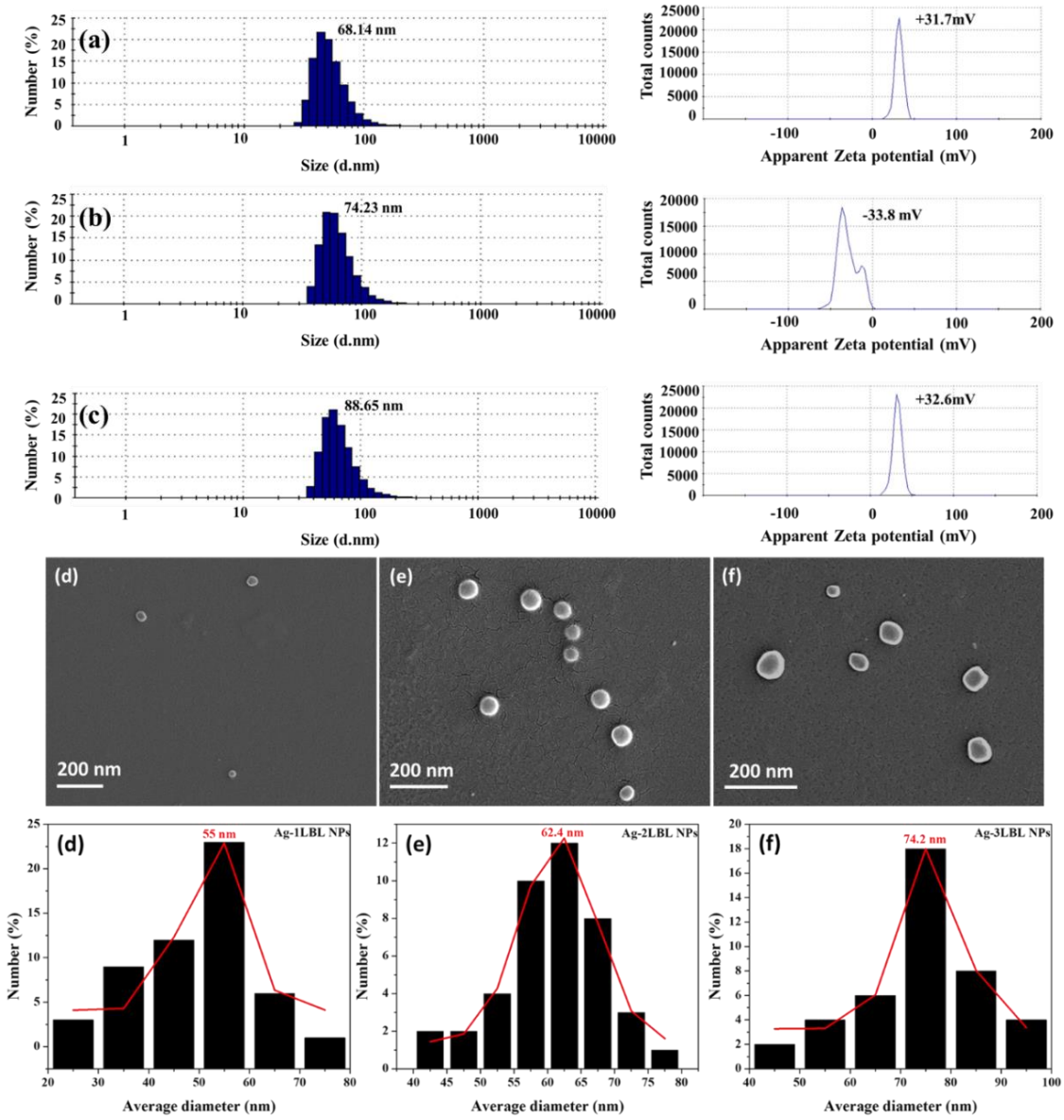

Figure 4A.7. DLS and Zeta potential values of (a) Ag-1LBL, (b) Ag-2LBL, (c) Ag-3LBL NPs; (d), (e) and (f) are the FE-SEM images and the corresponding average size plots of Ag-1LBL, Ag-2LBL and Ag-3LBL NPs respectively.

Table 4A.5. AIE molecule's lifetime (ns) values in water and after adsorption onto AgNPs, SiNPs, and Ag-LBL NPs.

Sample	τ_1(ns)	τ_2(ns)	τ_3(ns)	α_1 (%)	α_2 (%)	α_3 (%)	χ2	Average life time(ns)	Quantum yield
NP-4Py in water	0.30	1.02	4.36	57.3	26.12	16.58	1.04	1.16	0.053
NP-4Py + AgNPs	0.19	0.84	9.82	62.01	32.72	5.27	1.10	0.90	-
NP-4Py + SiNPs	0.35	1.54	14.79	32.91	42.95	24.14	1.29	3.67	0.012
NP-4Py + Ag-1LBL NPs	0.46	1.50	3.34	63	35	1	1.07	1.22	0.061
NP-4Py + Ag-2LBL NPs	0.44	1.33	4.43	67	32	1	1.21	1.17	0.076
NP-4Py + Ag-3LBL NPs	0.45	1.13	2.49	58	35	7	1.07	1.20	0.059

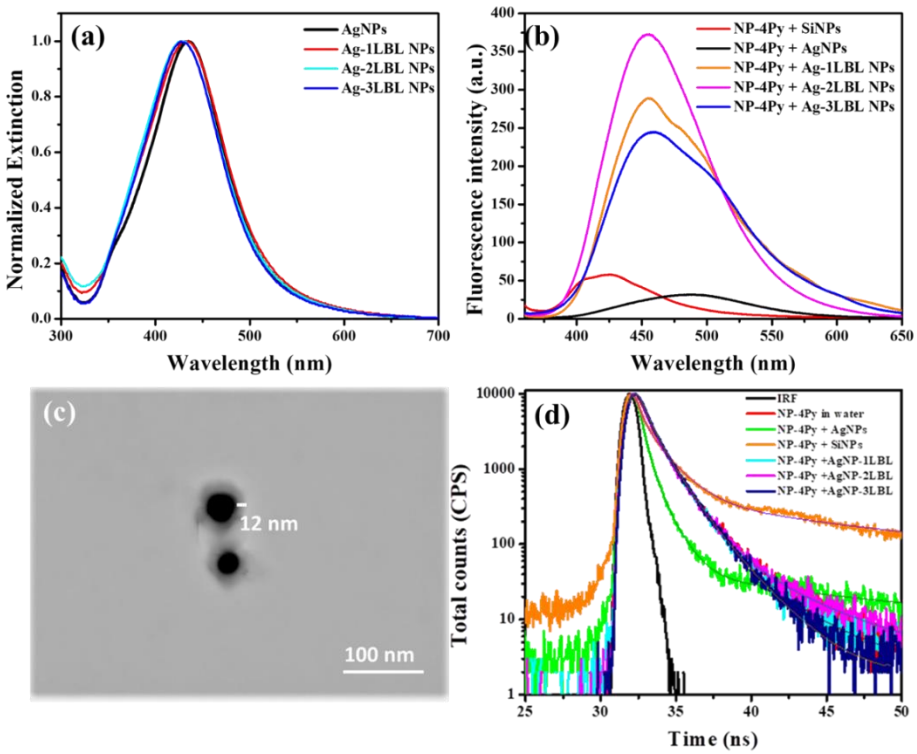

Figure 4A.8. (a) is the extinction spectra of AgNPs and Ag-LBL NPs; (b) is the MEF study of **NP-4Py** using Ag-LBL NPs; (c) is the STEM image of Ag-2LBL NPs in bright field mode, and (d) is the life time plots of **NP-4Py** in presence and absence of Ag-LBL NPs.

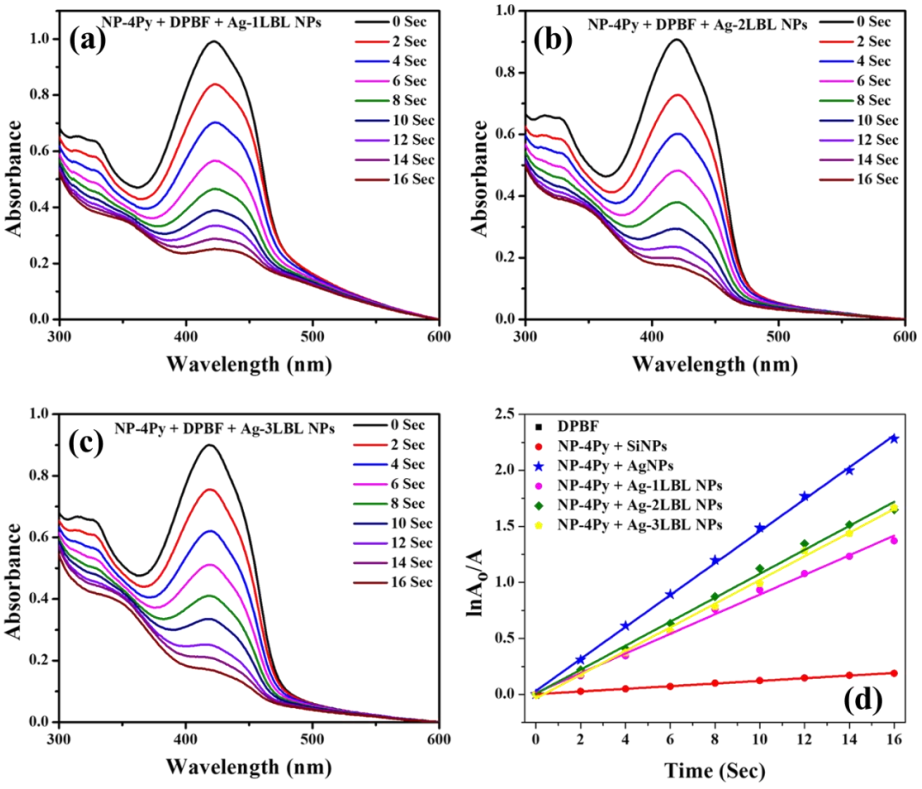

Figure 4A.9. Degradation of 50 μM DPBF in the presence of 10 μM **NP-4Py** loaded on (a) Ag- 1LBL, (b) Ag- 2LBL, (c) Ag- 3LBL NPs under 35 mW cm^{-2} white light.

Table 4A.6. EF_{SOG} using Ag-LBL NPs.

	K	EF_{SOG}
SiNPs	0.01184	-
AgNPs	0.1426	12.04
Ag-1LBL NPs	0.08769	7.40
Ag-2LBL NPs	0.10702	9.03
Ag-3LBL NPs	0.10566	8.92

4A.2.4. MEF and ME-SOG studies using Au@SiO_2 NPs

4A.2.4a. Characterization of Au@SiO_2 NPs with increasing silica thickness

Further, to recognize the essential contribution of the plasmonic metal on the MEF and ME-SOG of the AIEgen, the same studies were performed by replacing Ag with Au. Initially, Au@SiO_2 NPs were analyzed by recording their FE-SEM, DLS, Zeta and extinction spectra. The DLS measurements also showed an increase in the size from 38 nm for bare AuNPs to 78 nm for Au@SiO_2-5, with increasing silica shell thickness (**Figure 4A.10a-e**). The zeta potential value also sequentially decreased to -25mV for Au@SiO_2-5 NPs from -40mV for bare AuNPs (**Figure 4A.10a-e**). The FE-SEM images and the average particle sizes obtained from them also confirmed the successful formation of core-shell NPs (**Figure 4A.11a-e**).

4A.2.4b. MEF and ME-SOG studies using Au@SiO_2 NPs

As depicted in **Figure 4A.12a**, the surface plasmon resonance maxima of AuNPs demonstrated a gradual redshift commensurate to the increase in silica shell thickness. Subsequently, the MEF and ME-SOG studies of the AIEgen were performed using as prepared Au@SiO_2 NPs. As can be seen in **Figure 4A.12b**, the fluorescence of AIEgen was significantly quenched, when adsorbed directly to either SiNPs or bare AuNPs. But, after adsorption of AIEgen on Au@SiO_2 NPs, it was noticed that the fluorescence started increasing with silica spacer thickness up to a certain distance and started decreasing with further increase in thickness (**Figure 4A.12b & Table 4A.7**). The maximum EF of ~ 4.4 was observed in the case of Au@SiO_2-2 NPs, where the optimum

distance was measured to be ~12 nm, as obtained from the FE-SEM image (**Figure 4A.12c**). As shown in **Table 4A.8** and **Figure 4A.12d,** starting from Au@SiO_2-1 till Au@SiO_2-5 case, initial decrease and subsequent increase in the average lifetime of

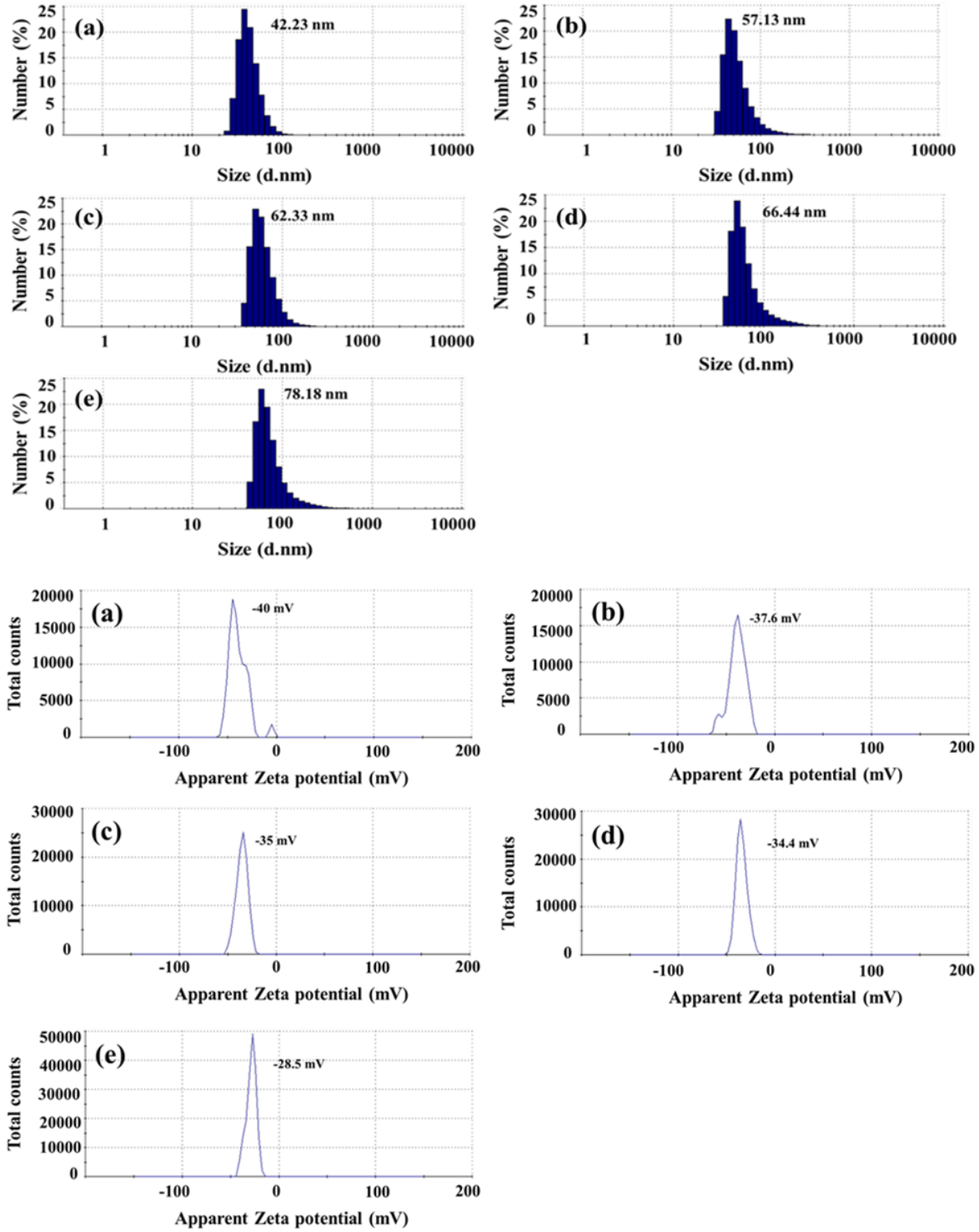

Figure 4A.10. DLS and corresponding Zeta potential plots of (a) Au@SiO_2-1, (b) Au@SiO_2-2, (c) Au@SiO_2-3, (d) Au@SiO_2-4 and (5) Au@SiO_2-5 NPs.

AIEgen was found to be very modest. Moreover, the main lifetime component values (τ_1 & τ_2) of the AIEgen, also furnished an identical trend from Au@SiO_2-1 to Au@SiO_2-5. Therefore, as expected, it can be safely concluded that the mechanism for the MEF was associated partly with the increase of intrinsic radiative decay rate, but mainly from near field enhancement. The ME-SOG studies of the particles (**Figure 4A.13**) indicated, a similar trend in ME-SOG and MEF because, the maximum EF of 10.6 for ME-SOG (**Table 4A.9**), was observed with Au@SiO_2-2 NPs.

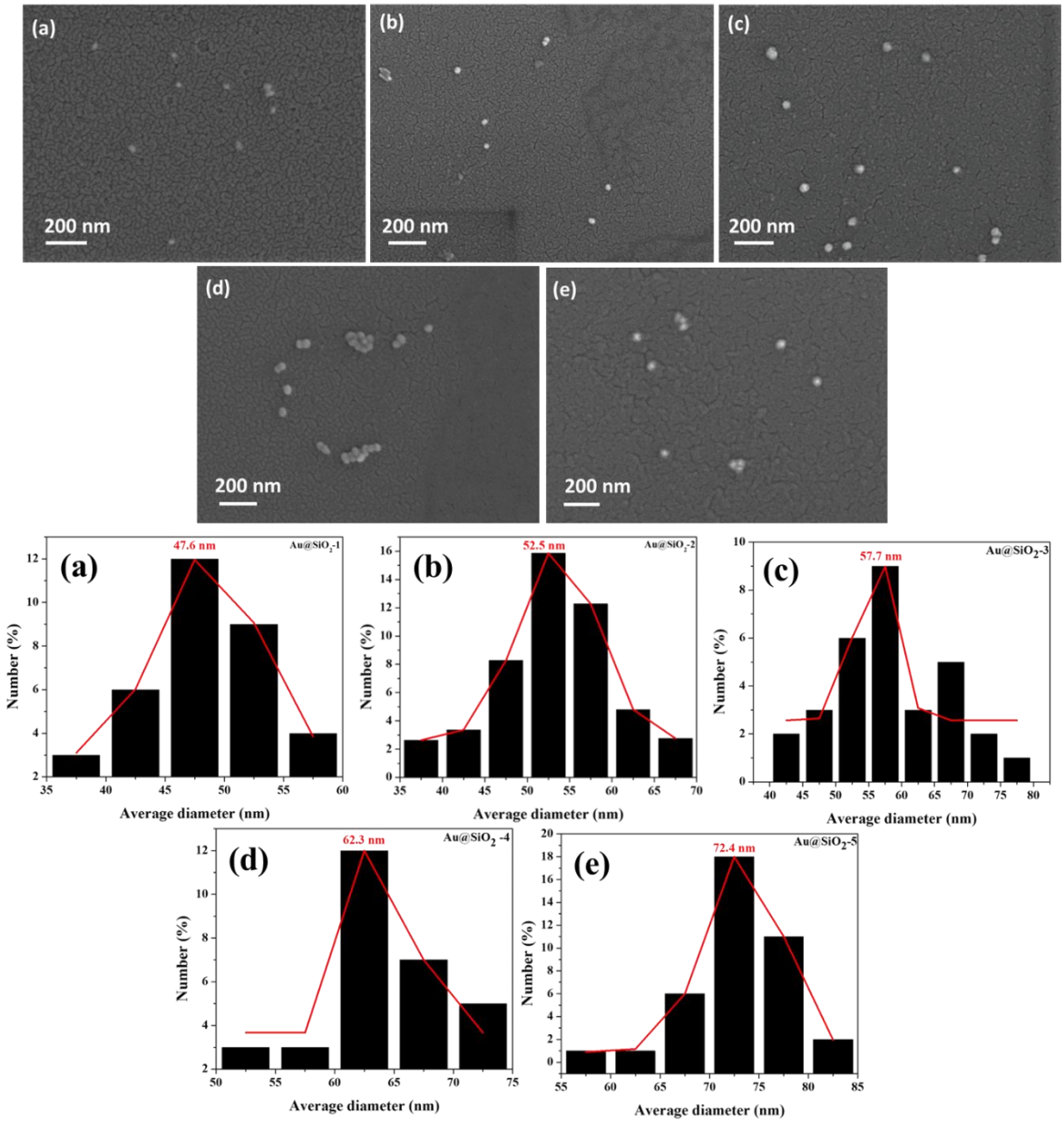

Figure 4A.11. FE-SEM images and histograms with their corresponding average size plots of (a) Au@SiO_2-1, (b) Au@SiO_2-2, (c) Au@SiO_2-3, (d) Au@SiO_2-4 and (5) Au@SiO_2-5 NPs.

Table 4A.7. MEF Enhancement factor of $Au@SiO_2$ core shell NPs with different spacer thickness.

	EF MEF
SiNPs	Blank
AuNPs	Quenching
$Au@SiO_2$-1 NPs	3.18
$Au@SiO_2$-2 NPs	4.4
$Au@SiO_2$-3 NPs	2.9
$Au@SiO_2$-4 NPs	2.6
$Au@SiO_2$-5 NPs	2.4

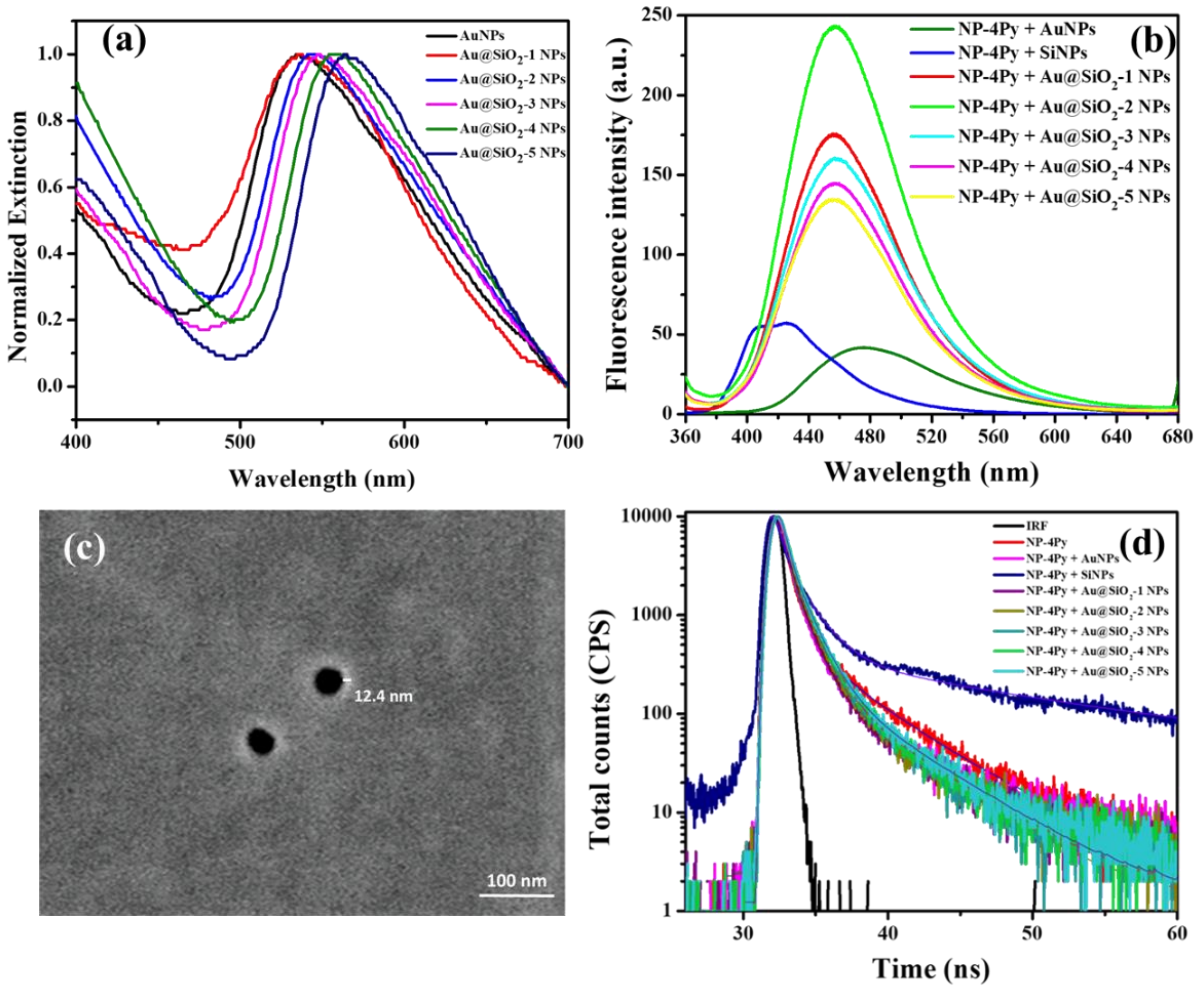

Figure 4A.12. (a) is the extinction spectra of core-shell NPs of different thicknesses, (b) is the MEF study of **NP-4Py** using $Au@SiO_2$ NPs, (c) is the STEM image of $Au@SiO_2$-2 in dark field mode, and (d) is the life time of **NP-4Py** in presence of $Au@SiO_2$ NPs.

Table 4A.8. AIE molecule's lifetime (ns) values in water and after adsorption onto AgNPs, SiNPs, and Ag@SiO_2 core-shell NPs.

Sample	τ_1(ns)	τ_2(ns)	τ_3(ns)	α_1 (%)	α_2 (%)	α_3 (%)	χ2	Average life time(ns)	Quantum yield
NP-4Py in water	0.30	1.02	4.36	57.3	26.12	16.58	1.04	1.16	0.053
NP-4Py + AuNPs	0.24	1.05	6.07	52.89	40.13	6.98	1.23	0.97	-
NP-4Py + SiNPs	0.35	1.54	14.79	32.91	42.95	24.14	1.29	3.67	0.012
NP-4Py + Au@SiO_2 1 NPs	0.31	1.16	5.90	47.92	46.36	5.71	1.21	1.02	0.048
NP-4Py + Au@SiO_2 2NPs	0.28	1.08	5.25	50.5	43.32	6.18	1.14	0.99	0.062
NP-4Py + Au@SiO_2 3NPs	0.26	1.07	4.32	36.28	55.75	7.98	1.12	1.03	0.046
NP-4Py + Au@SiO_2 4NPs	0.27	1.10	4.62	38.01	54.28	7.71	1.15	1.05	0.043
NP-4Py + Au@SiO_2 5NPs	0.29	1.13	4.58	41.76	49.4	8.84	1.11	1.09	0.041

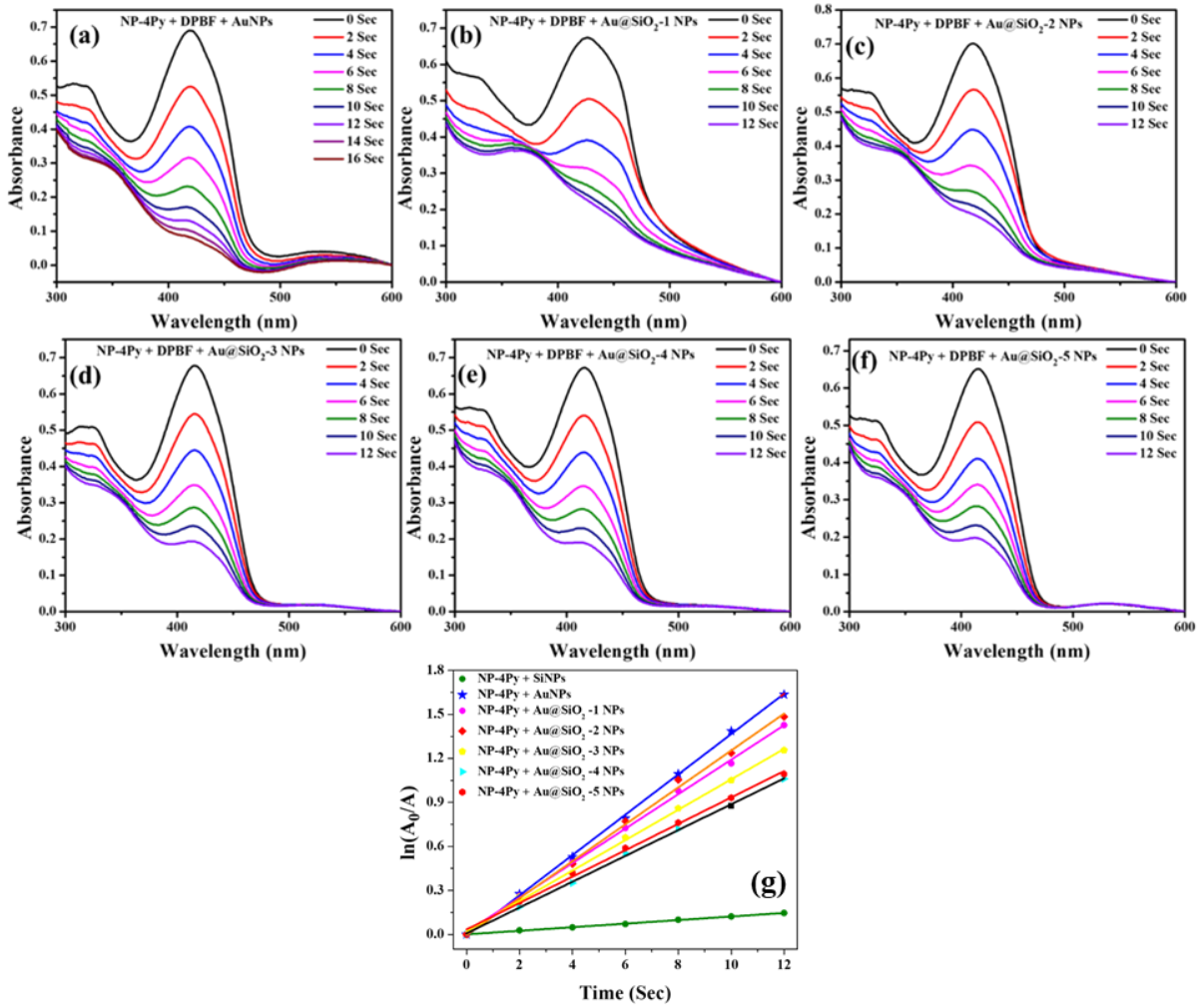

Figure 4A.13. Absorption spectra showing the degradation of 50 μM DPBF in the presence of 10 μM **NP-4Py** loaded on Au@SiO_2 core shell NPs under 35 mW cm^{-2} white light.

Table 4A.9. EF_{SOG} using Ag-LBL NPs.

	K	EF_{SOG}
SiNPs	0.01184	
AuNPs	0.13483	11.38
Au@SiO_2-1	0.11748	9.92
Au@SiO_2-2	0.12582	10.62
Au@SiO_2-3	0.10364	8.75
Au@SiO_2-4	0.088	7.43
Au@SiO_2-5	0.08995	7.59

4A.2.5. MEF and ME-SOG studies using Au-LBL NPs

4A.2.5a. Characterization of Au-LBL NPs

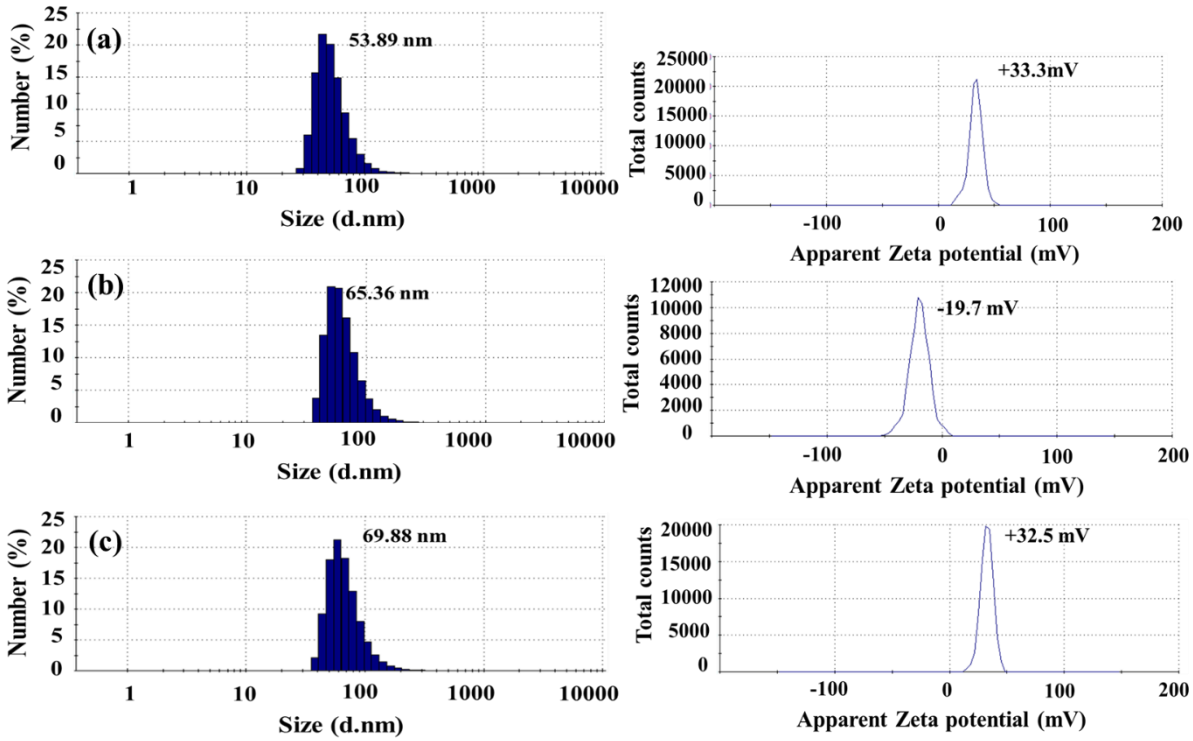

Figure 4A.14. DLS and the corresponding zeta potential plots of (a) Au-1LBL, (b) Au-2LBL and (c) Au-3LBL NPs.

Au-LBL NPs were characterized by DLS, Zeta measurements, FE-SEM and extinction spectra. Similar to Ag-LBL, we noticed a sequential increase in the size of AuNPs from DLS measurements, from 38 nm for bare AuNPs to 65 nm for AuNP-3LBL

(**Figure 4A.14a-c**). The zeta potentials of AuNP, AuNP-1LBL NPs, AuNP-2LBL NPs, and AuNP-3LBL NPs were recorded as -28.7, +33.3, -19.7 and +32.5 mV, respectively, which confirmed the successive adsorption of polyelectrolytes via self-assembly (**Figure 4A.14a-c**). Moreover, the FE-SEM images and their average size plots also demonstrated a considerable increase in the size of NPs after LBL assembly (**Figure 4A.15a-c**). Like Ag-LBL NPs, the prepared Au-LBL NPs also did not exhibit any change in their extinction spectra peak position (**Figure 4A.16a**) with successive addition of the polyelectrolyte layer, indicating their good stability.

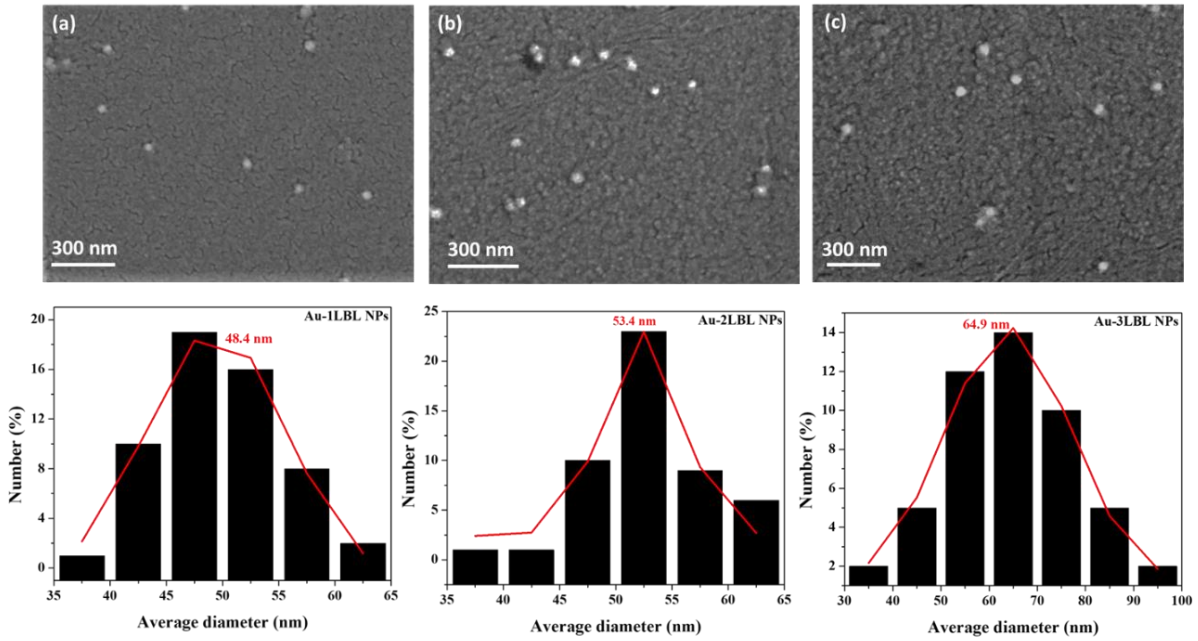

Figure 4A.15. FE-SEM images and the corresponding average size plots of (a) Au-1LBL, (b) Au-2LBL and (c) Au-3LBL NPs.

4A.2.5b. MEF and ME-SOG studies using Au-LBL NPs

While performing the MEF study of the AIEgen using Au-LBL NPs, similar to earlier observation, the fluorescence of AIEgen was found to be least when it was adsorbed on SiNPs and bare AuNPs. With Au-LBL NPs, the maximum EF for MEF was found to be the best among all the sets (~7.9 times) in case of Au-2LBL NPs (**Figure 4A.16b & Table 4A.10**), with a thickness of the polymer layer of ~11 nm (**Figure 4A.16c**). The results obtained from the lifetime measurements (**Figure 4A.16d & Table 4A.11**), suggested that MEF followed a combined mechanism of near field effect and radiative rate enhancement. Further, the ME-SOG experiments using Au-LBL NPs also

significantly offered the second highest EF of ~10.4 times among any sets used in this study, with Au-2LBL NPs (**Figure 4A.17 & Table 4A.12**).

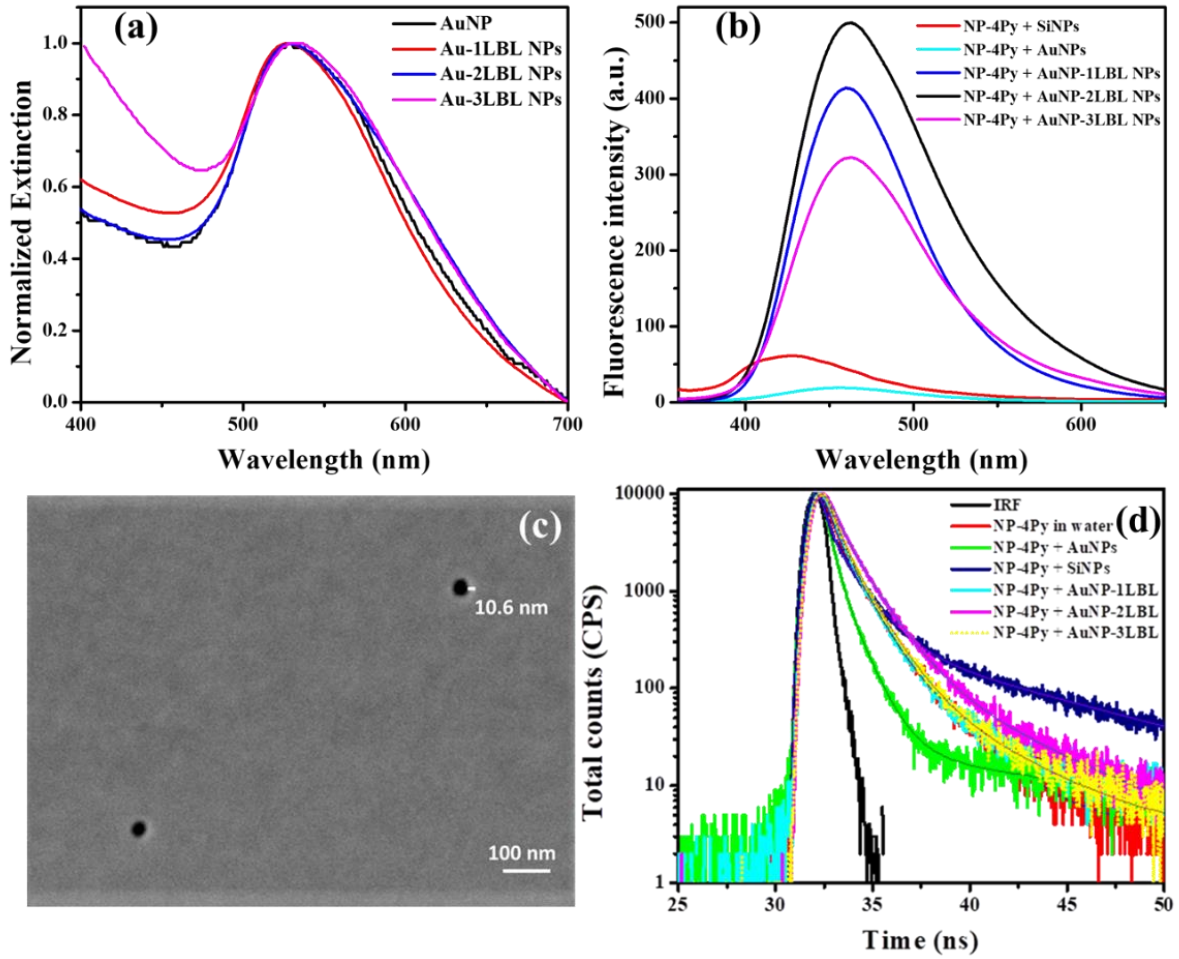

Figure 4A.16. (a) is the extinction spectra of AuNPs and AuNP-LBL NPs, (b) is the MEF study of **NP-4Py** using AuNP-LBL NPs, (c) is the STEM image of AuNP-2LBL NPs in dark field mode, and (d) is the life time plots of **NP-4Py** in presence of Au-LBL NPs.

Table 4A.10. MEF Enhancement factor of Au-LBL NPs with different spacer thickness**.**

	EF MEF
SiNPs	Blank
AuNPs	Quenching
Au-1LBL NPs	6.4
Au-2LBL NPs	7.9
Au-3LBL NPs	5.0

Table 4A.11. AIE molecule's lifetime values in water and after adsorption onto AuNPs, SiNPs, and Au-LBL NPs.

Sample	τ_1(ns)	τ_2(ns)	τ_3(ns)	α_1 (%)	α_2 (%)	α_3 (%)	χ2	Average life time (ns)	Quantum yield
NP-4Py in water	0.30	1.02	4.36	57.3	26.12	16.58	1.04	1.16	0.053
NP-4Py + AuNPs	0.24	1.05	6.07	52.89	40.13	6.98	1.23	0.97	-
NP-4Py + SiNPs	0.35	1.54	14.79	32.91	42.95	24.14	1.29	3.67	0.012
NP-4Py + Au-1LBL NPs	0.28	1.09	6.08	47.76	46.97	5.27	1.19	0.99	0.077
NP-4Py + Au-2LBL NPs	0.31	1.14	4.88	43.67	51.24	5.09	1.17	0.96	0.095
NP-4Py + Au-3LBL NPs	0.32	1.37	6.55	54.37	36.81	8.82	1.23	1.02	0.061

Table 4A.12. EF_{SOG} using Au-LBL NPs.

	K	EF_{SOG}
SiNPs	0.01184	-
AuNPs	0.13483	11.38
Au-1LBL NPs	0.11158	9.42
Au-2LBL NPs	0.12357	10.43
Au-3LBL NPs	0.10052	8.48

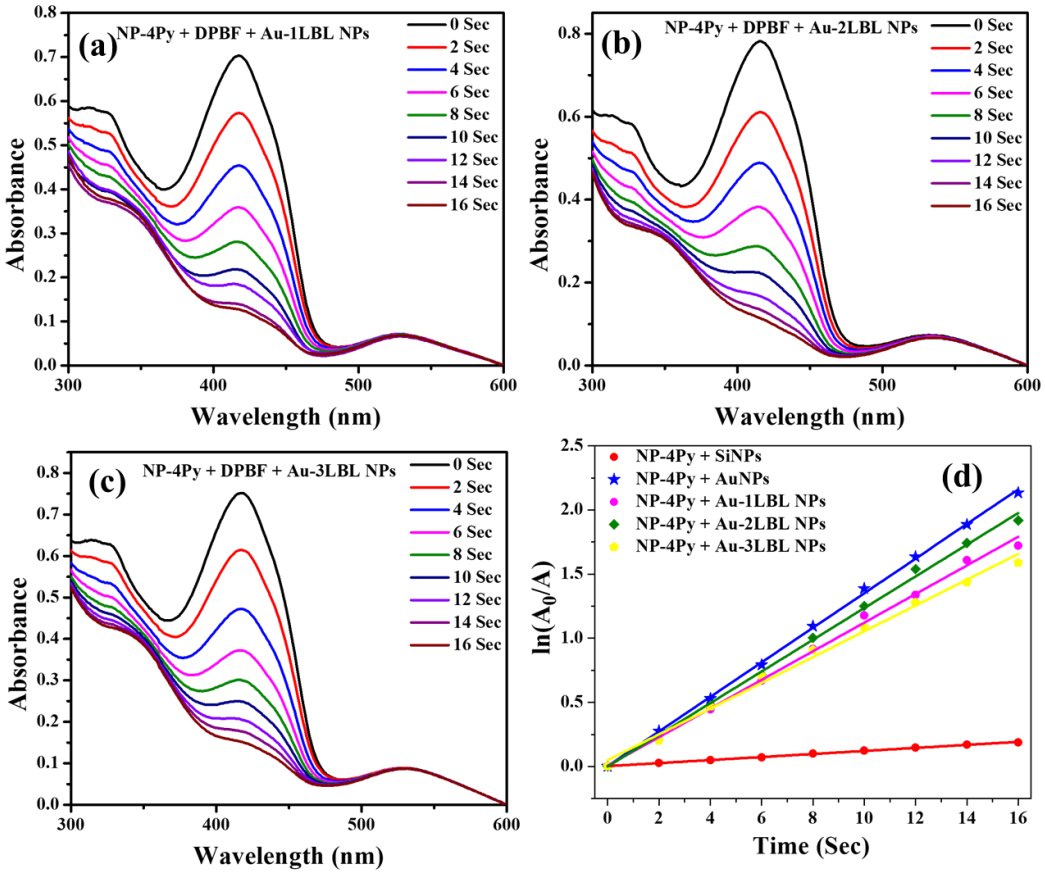

Figure 4A.17. Absorption spectra showing the degradation of 50 μM DPBF in the presence of 10 μM **NP-4Py** loaded on Au-LBL NPs under 35 mW cm^{-2} white light.

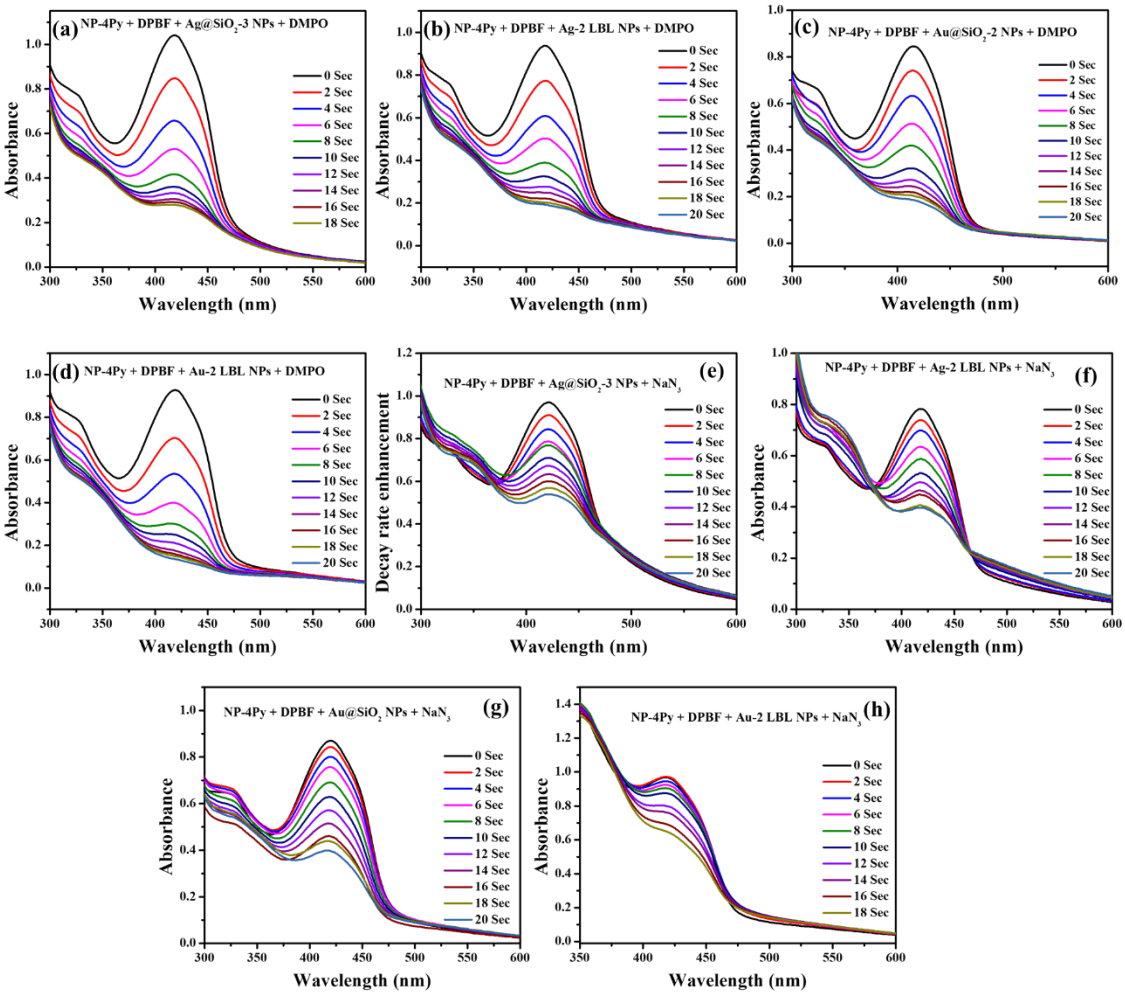

Figure 4A.18. Degradation of 50 μM DPBF in the presence of DMPO, 10 μM **NP-4Py** loaded on (a) $Ag@SiO_2$-3 NPs, (b) Ag-2LBL NPs (c) $Au@SiO_2$-2 NPs, (d) Au-2LBL NPs under 35 mW cm^{-2} white light and Degradation of 50 μM DPBF in the presence of NaN_3, 10 μM **NP-4Py** loaded on (a) $Ag@SiO_2$-3 NPs, (b) Ag-2LBL NPs (c) $Au@SiO_2$-2 NPs, (b) Au-2LBL NPs under 35 mW cm^{-2} white light.

In order to rule out the presence of other possible ROS such as, superoxide and hydroxyl radicals in our reaction mixture, we first measured the degradation of DPBF with 5,5 Dimethyl-1-pyrroline-N-oxide (DMPO), which was a spin trapping probe that could bind with hydroxyl and super oxide radicals but not with $^1O_2$. As, the degradation of DPBF in presence of AIEgen loaded nanoparticles was found to be very similar with and without DMPO (**Figure 4A.18a-d**), the presence of superoxide and hydroxyl radicals was ruled out, suggesting the presence of singlet oxygen as the ROS in the solution. Moreover, to confirm that the decomposition of DPBF was due to $^1O_2$ only, an inhibition test (**Figure 4A.18e-h**) was carried out in the presence of sodium azide (NaN_3), which selectively quenches only $^1O_2$. It was found that the rate of decrease in

the absorption of DPBF was much smaller in presence of NaN_3, suggesting only $^1O_2$ was formed as ROS in the reaction mixture during irradiation.

4A.2.6. Discussion

To summarize the obtained results for selecting the best possible 'smart' PS with enhanced fluorescence, EF values for the MEF and ME-SOG of a given set, were plotted together against the thickness of the spacer (**Figure 4A.19**). From the data, two important observations can be stated as follows. (i) Remarkably, the highest EF for MEF and ME-SOG were obtained at the same spacer length for each set, and the spacer length was registered at a constant value of ~10-12 nm. However, bare nanoparticles were not considered as the best substrate for ME-SOG although they produced the highest EF for SOG, because they also resulted in lowest fluorescence intensity. (ii) Although Ag was a better plasmonic metal, the maximum EF for simultaneous MEF and ME-SOG were obtained with Au nanoparticles with polyelectrolytes as the spacer (**Table 4A.13**).

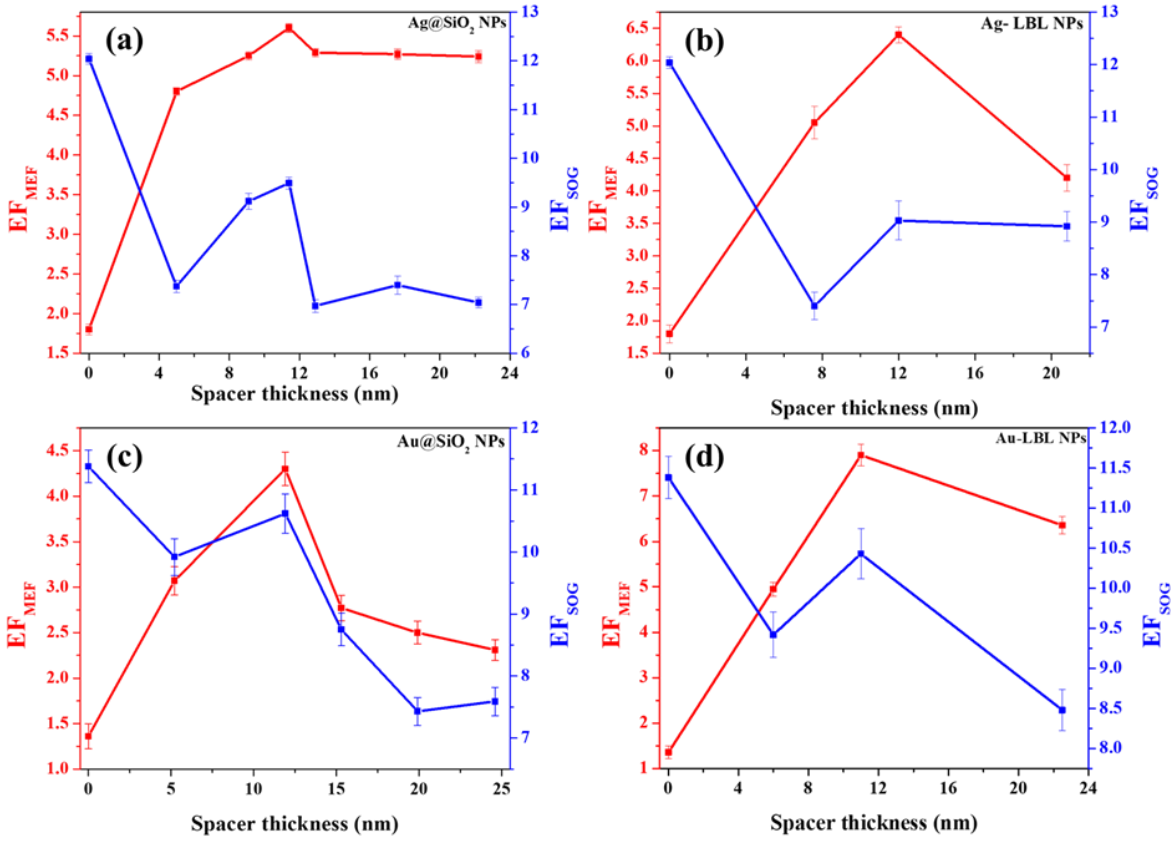

Figure 4A.19. MEF and ME-SOG EF values of the hybrid PS against spacer thickness: (a) $Ag@SiO_2$, (b) Ag-LBL, (c) $Au@SiO_2$ and (d) Au-LBL NPs.

Table 4A.13. The best EF values for MEF and SOG from each of the four PS sets used in the experiment.

Hybrid PS	Spacer thickness (nm)	EF_{MEF}	EF_{SOG}	$\|\Delta\|$ (nm)[#]
Ag@SiO_2-3 NPs	11	5.6	9.5	16
Ag-2LBL NPs	12	6.4	9.0	33
Au@SiO_2-2 NPs	12.4	4.4	10.6	68
Au-2LBL NPs	10.6	7.9	10.4	82

[#] *$|\Delta|$ is the separation between extinction spectrum of NPs with spacer and fluorescence spectrum of AIEgen.*

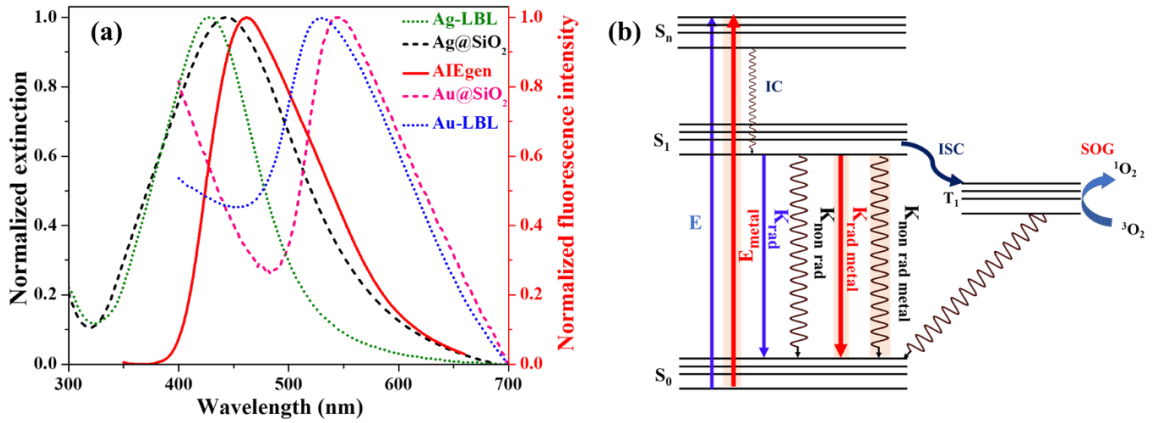

Figure 4A.20 (a) overlap of extinction spectra of nanoparticles and emission spectra of AIEgen; (b) Jablonski diagram demonstrating different radiative and non-radiative processes of the PS molecule.

To analyse the above results, one must consider all the possible radiative and non-radiative processes in the event of a metal-enhanced photochemical process, using a Jablonski Diagram. When the AIEgen emits fluorescence in the close vicinity of the metal nanoparticles, the oscillating dipole of the molecule in the excited state can strongly interact with the surface plasmons of the metal, if there is considerable overlap among fluorescence emission maximum of AIEgen and the SPR maximum of metal nanoparticles. As can be seen from **Figure 4A.20a**, significant overlap was observed between the fluorescence spectrum of AIEgen and the extinction spectra of silica-coated or polyelectrolyte coated nanoparticles. As a result, the concentrated nearfield, produced by the metal nanoparticles, can cause increased excitation rates for the AIEgen to maintain the conservation of energy, resulting in an enhanced emission. However, metal nano particles (MNPs) can also increase the rates of radiative decay of the fluorophore. If the metal results in an increased excitation rate

(E_{metal} in **Figure 4A.20b**), the quantum yield or lifetime of the AIEgen remains unchanged with the increase in fluorescence intensity. While, an increase in the radiative decay rate ($k_{rad\text{-}metal}$) unusually decreases the fluorescence lifetime, with an increase in fluorescence intensity. From the obtained results on MEF in this study, it is obvious that the mechanism of MEF is primarily led by the near field enhancement effect, as only modest to asymptomatic changes are obtained with the fluorescence lifetime values of the AIEgen at different spacer thicknesses.

Moreover, it is to be realized that the radiative fluorescence and non-radiative intersystem crossing (ISC) are two competitive channels for a molecule in the excited state (**Figure 4A.20b**). For the AIEgen, after excitation with the light, the electronic population is depleted from excited S_1 via the emission of fluorescence photons and also via non-radiative transfer to T_1 and subsequently producing $^1O_2$. Therefore, at photo stationary equilibrium, it can be safely anticipated that, both the excited state events occur at a constant rate. At this condition the presence of strong near field produced in presence of metal, enables transferring more population to S_1 from S_0 via stronger absorption process, which will result in fluorescence enhancement, as well as higher SOG via ISC. Therefore, it is easy to understand why the maximum EF of MEF will follow the maximum EF of SOG, at the same distance away from the metal surface. However, the uniformity in the spacer thickness of 10 to 12 nm, associated with the highest EFs for all sets, is a result of the NSET process. Because, strong non-radiative losses are the dominant factor, if the distance is <10 nm between the AIEgen and metal surface. Also, a close look at **Figure 4A.20a** clearly conveys that the probability of non-radiative loss via NSET is much higher for Ag NPs due to a much higher overlap region with AIEgens fluorescence spectrum due to much lower $|\Delta|$ value (**Table 4A.13**), compared to Au NPs. Thus, the study renders AIEgen loaded Au-LBL NPs as the most suitable PS for further exploration.

Subsequently, the photo stability of the nanoparticles was monitored (**Figure 4A.21**), before applying them for bioimaging. Briefly, the emission intensity of the AIEgen loaded nanoparticles at 460 nm was collected at every 10 sec intervals on continuous exposure to light (excitation: 350 nm) for 30 minutes. They were found

photostable, as we did not observe any significant deviation in the fluorescence intensity, within 30 minutes. Considering the good photostability of the theranostic nanoparticles they were further considered as suitable candidates for possible bio-imaging application with biocompatible hybrid Span60-L64 niosomes. Niosomes are well-known drug carrier and a non-ionic vesicle which mimic cell membranes.[40,41] **Figure 4A.22** shows the bright field and fluorescent images of hybrid Span60-L64 niosomes, incubated with Au-2LBL-AIEgen theranostic NPs. The formulations produced a significant fluorescence emission when excited with 405 nm laser (Emission window was 430 - 470 nm). This observation confirmed that the theranostic nanoparticles were found to be suitable as a bio-labelling agent for possible in vitro and in-vivo imaging.

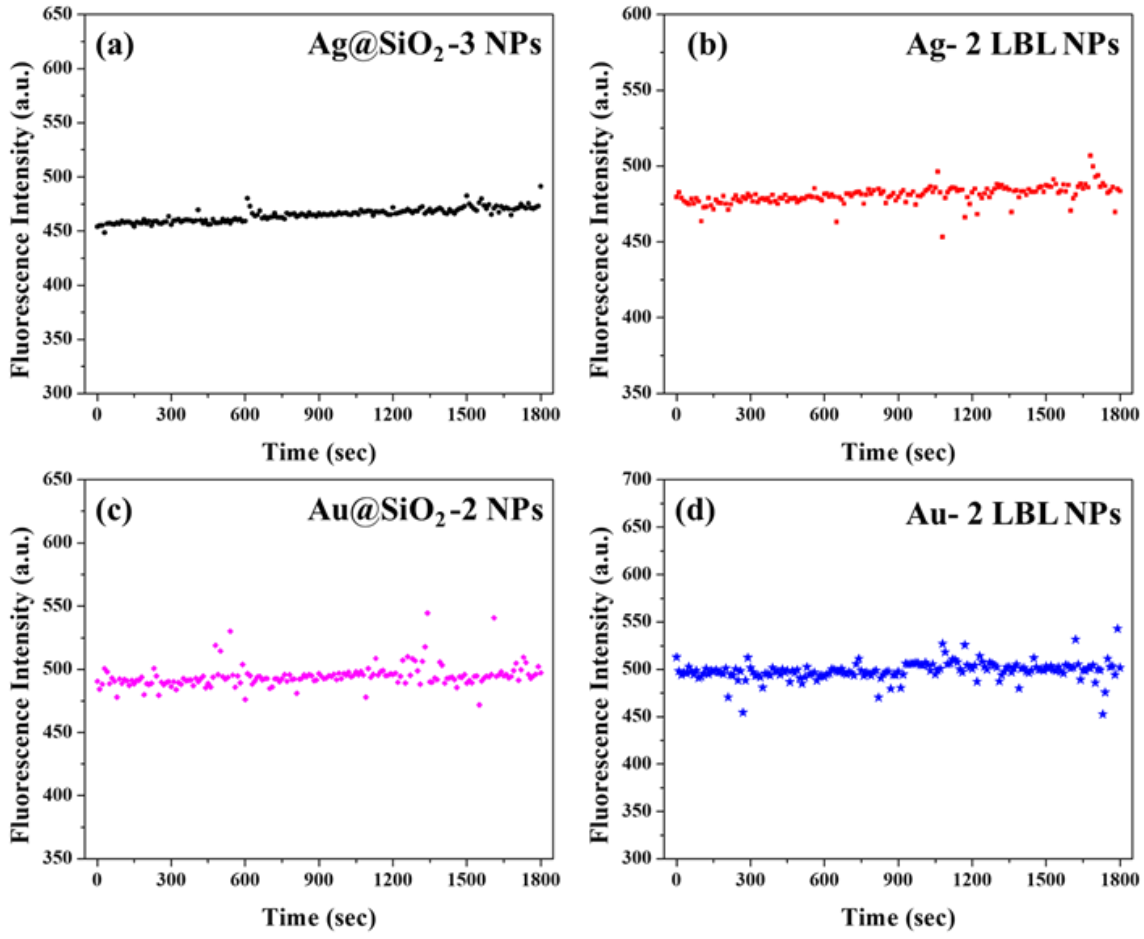

Figure 4A.21. Photostability studies on (a) $Ag@SiO_2$ -3 NPs, (b) Ag- 2LBL NPs, (c) $Au@SiO_2$ -2 NPs, (d) Au- 2LBL NPs. the emission is collected at 460 nm and the excitation wavelength is 350 nm.

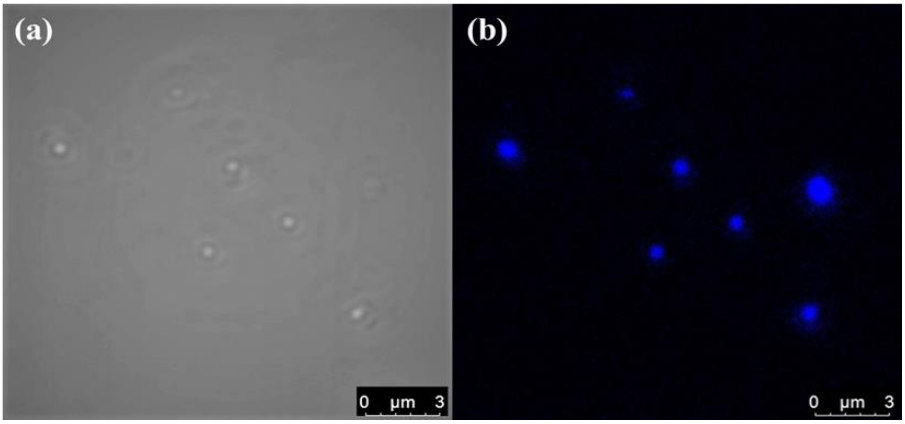

Figure 4A.22. (a) Bright field and (b) Confocal images of niosomes loaded with Au-2 LBL-AIEgen theranostic NPs. The excitation was 405nm and the emission was collected in the range of 430-470 nm.

4A.3. Conclusions and Summary

Ag and Au nanoparticles were synthesized by simple wet chemistry with an average diameter of 49 nm and 42 nm, respectively. Subsequently, they were converted to core-shell nanoparticles of increasing shell thicknesses, using silica coating via Stober's method and polyelectrolyte coating via a layer-by-layer approach. With and without spacers, the nanoparticles were characterized in detail using absorption, DLS, zeta potential, and FE-SEM measurements. Following the adsorption of the neutral pyridyl AIEgen on the Ag and Au core-shell nanoparticles, these theranostic PSs were ascribed for MEF and ME-SOG studies. Enhancement in fluorescence and SOG was evident for the AIEgen across all the PS sets. Appropriate EFs were also evaluated by comparing the fluorescence or SOG of the same amount of AIEgen, adsorbed on a Si nanoparticle. The enhancement was noticed to depend crucially on the spacer's thickness, on which AIEgen was adsorbed. Most importantly, at an optimum distance of ~10-12 nm from the metal surface, simultaneous enhancement in fluorescence and SOG were recorded for all the theranostic PS. The probable mechanism for the enhancement was attributed mainly due to the short-range near field effect, near the plasmonic nanoparticles. The best theranostic property, with EF of 7.9 in fluorescence and EF of 10.4 in SOG, was demonstrated by AIEgen loaded Au-2LBL NPs, with a spacer thickness of ~11 nm. The superiority of Au over Ag probably lied in the fact that Ag nanoparticles were responsible for more non-radiative loss due to NSET as the extent of overlap between the extinction spectra of Ag nanoparticles was more with the AIEgen's florescence

spectrum, compared to the overlap made by the AuNPs. Till date, this is the first report, where we demonstrated the maximum $^1O_2$ production and highest fluorescence from any PS molecule at the same optimum distance from the metal core using the near field enhancement technique. Furthermore, the impact of the nature of the metal core on the fluorescence and SOG of the PS, was also explored for the first time. Knowledge of these two critical aspects will allow us to rationally engineer plasmonic nanomaterials for improved theranostic applications by executing the visual detection of cancer cells and its treatment, rather than beta-testing proof-of-concept systems.

Chapter 4B

Polymer Coated Gold Nanorod Cores Adsorbed with Eosin Y: Engineered Plasmon-Enhanced Nano-Photosensitizers

In the previous chapter, the role of spherical MNPs were studied in detail for co-enhancement of fluorescence and singlet oxygen generation. In this chapter we have explored how the near- and far-field optical properties of anisotropic gold nanorod controls the MEF and ME-SOG property of a nano-photosensitizer.

4B.1. Introduction

In the previous chapter, we studied plasmon enhanced fluorescence and SOG using spherical MNPs and also identified the role of MNP- PS distance in achieving simultaneous MEF and MESOG. Herein, we have explored the possible applications of GNRs in PDT.[1,2] PDT is a non-invasive and selective method that has shown promising performances against different cancer types, with the help of nanoscience and nanotechnology. PDT needs three main components, a photosensitizer (PS), suitable light source, and cellular oxygen, for achieving successful cytotoxic effects to kill the cancer cells.[3,4] Moreover, there is an urgent need to develop theranostics materials that provide a diagnosis and therapy together. Therefore, photosensitizer (PS) with enhanced fluorescence can be a game-changer due to its superior efficacy compared to traditional PS, as it results into Singlet Oxygen Generation (SOG), as well as it produces high fluorescence signal.[5,6] Thus, image-guided PDT is possible with PS with bright fluorescence as it provides a therapeutic outcome with simultaneous ability to trace the disease remission/progression. But traditional PSs exhibits few drawbacks such as very weak fluorescence. Moreover, when the loading of such PS is high to compensate for the low fluorescence yield, production of SOG and fluorescence becomes minimal due to aggregation-caused quenching effects. In addition, as most of the PS molecule absorbs in the visible region, except two-photon PDT, the technique may encounter nontrivial visible light scattering by tissues.[7] It leads to poor imaging contrast and spatial resolution during the confocal imaging, as well as photodamage to biological samples. Thus, it is essential to simultaneously enhance the fluorescence and SOG of the PS molecules, for successfully utilising them in theranostics applications but with minimal incident light intensity.

On the other hand, upon irradiation by an incident electromagnetic field, plasmonic metallic nanoparticles produce LSPR from the collective oscillation of the conduction band electrons. The plasmon decays in ultrafast time scale, however it produces strong near- and far-field effects around the nanoparticle. By virtue of the plasmonic nanoantenna effect, the incident light can be localized in the near field, producing a strong local enhanced electric field that extends from the nanoparticle's

surface to few nm distance from the surface.[8] On the other hand, the far-field properties are explained by the extinction of the light interacting with the localized surface plasmon of the nanoparticles, which results from contributions of two processes, namely, absorption and scattering. The radiative decay of the plasmon leads to scattering, i.e., re-radiation of light into the far-field (hundreds of nanometers) that can increase the level of light trapping in the whole sample and act as a secondary light source.[9,10] Plasmonic metallic nanoparticles (MNPs) can interact very strongly with the fluorophores next to them causing enhancement in their fluorescence and the phenomenon is known as Metal Enhanced Fluorescence (MEF).[11,12] Similarly, metal-enhanced singlet oxygen ($^1O_2$) generation (ME-SOG) is also another emerging application of plasmonics. It has been shown from different plasmon based optical experiments individually that the production of SOG by a photosensitizer or fluorescence of an emitter can be dramatically enhanced, by varying several parameters, including the nanostructure morphology,[13] size,[14] composition,[15] and most importantly photosensitizer/emitter-metal distance.[16] The conjugation of organic molecules via a spacer with various plasmonic nanostructures such as sphere, rod, star, bipyramid, sheet, cluster etc. made up of mainly Ag and Au, was achieved using various strategies, namely, core-shell technique, polyelectrolyte coating, polymer coating etc.[17]

Among the various types of plasmonic nanostructures explored in theranostics, gold nanorods (GNRs) were widely studied due to their several advantages including good biocompatibility, tunable LSPR peaks and excellent photothermal property.[18,19] The dipolar coupling of the electric field and surface plasmons along the short and long axis of the nanorods results into two LSPR bands, namely short-wavelength transverse and long wavelength longitudinal surface plasmon resonance (LSPR).[20,21] Due to the asymmetric shape of the GNRs, the near field and far-field plasmonic effect are much superior compared to symmetric nanoparticles, that had been successfully used in various plasmon enhanced optical processes such as plasmonic catalysis (9,10),[22,23] plasmonic energy conversion,[24] photothermal therapy,[25-27] two photon absorption and emission,[28,29] and photodynamic therapy.[30-34]

However, there are only a handful of reports available on simultaneous enhancement of fluorescence and SOG by hybrid plasmonic nanostructure, providing no correlation between MEF and ME-SOG parameters. But, designing brightly fluorescent photosensitizers with high SOG yield is extremely important for cancer treatment and needs immediate attention. For example, Huang et al. noticed 3-fold and 1.4-fold increase in fluorescence and SOG of chlorin e6 adsorbed on bare GNRs.[35] Xuebin et al. observed co-enhancement in fluorescence and SOG by silica coated GNRs and also identified that the rates of MEF and SOG varied with increase in silica thickness from 2.1 nm to 28.6 nm. They recorded a maximum of 7-fold and 2.1-fold in MEF and SOG of AlC4Pc when the silica thickness is ~10.6 nm.[36] Novikova et al. synthesized various aspect ratio GNRs and coated them with silica shell and reported almost 6.7 and 13 times increase in luminescence and SOG of Mo6 clusters.[37] Also, one of the most important factors for achieving the desired effects is the choice of the PS. An ideal PS should be water soluble, less cytotoxic and its fluorescence shouldn't completely be overlapped by the extinction spectra of the nano cores.[38,39] If there is a complete spectral overlap there is a chance that non radiative energy transfer might dominate and the desirable effect might not be achieved. Hence there is a quest for a rational design of a hybrid theranostics GNR in which GNRs are conjugated with a PS at an appropriate distance, with an aim to significantly enhance the fluorescence and SOG of the PS molecule.

Herein, to achieve this goal, hybrid theranostics nano-photosensitizers were designed, consisting a photosensitizer Eosin Y (Ey) conjugated to layer by layer (LBL) assembled GNRs of different aspect ratios. We report a comprehensive experimental and theoretical investigation of the extent of the near- and far-field plasmonic effect on MEF and ME-SOG of the photosensitizer molecule Ey. The LBL strategy was inspired by our previously reported metal-enhanced nanoplatforms, the negative end of the polarizable molecule Ey binds electrostatically to the positively charged polyelectrolyte coating on GNRs, to extract the best plasmonic effect. Moreover, using LBL method the lowest and highest spacer thicknesses were tightly controlled such that the PS remains within the domain of near field decay length of the GNRs at all times, considering the

short lifetime of plasmon in GNR, around 100 fs. We witness a clear correlation between the near field and far field plasmonic effect of the metal with the MEF and ME-SOG yield from the best hybrid nano-photosensitizer. Among all, the best theranostics property, i.e., highest fluorescence and $^1O2$ yield, was demonstrated by the PS-GNR assembly which showed the highest theoretical near-field effect at the 519 nm wavelength, as well as highest far-field effect in form of maximum scattering of light, measured experimentally.

4B.2. Results

4B.2.1. Characterization of Engineered hybrid Nano-Photosensitizers:

GNRs of different aspect ratios with larger lengths and widths, were synthesized by a seed mediated growth process using CTAB as the stabilizer expecting higher plasmon enhancement efficiency compared to traditional GNRs of 40-50 nm length.[40] By changing the concentration of CTAB during the growth process, GNRs of six different aspect ratios were synthesized and were labelled as GNR1 to GNR6. As shown in the FE-SEM images (**Figure 4B.1a-f**) the average length increased gradually from 115 ± 3.2 to 157 ± 4.6 nm and width decreased from 57.5 ± 2.1 to 40.5 ± 1.8 nm, resulting into the aspect ratios (AR) of the GNRs also increased from 2 ± 0.3 to 3.8 ± 0.9 **(Table 4B.1.)**. The extinction spectra of GNRs exhibited one LSPR and one TSPR band due to their asymmetrical shape, while the LSPR peaks shifted from 699 to 828 nm with an increase in AR (**Figure 4B.1g & Table 4B.1.**). The synthesized GNRs formed stable colloidal suspensions as revealed by their large positive zeta (ζ) potential values (**Figure 4B.1h-m**). Subsequently, using layer-by-layer (LBL) assembly method, the GNRs were coated with polymer layers (**Figure 4B.1n**). The conventional LBL assembly relies on the adsorption of oppositely charged polymers and can be used to fine tune the distance between metal core and photosensitizer. Herein, we have used negatively charged Poly styrene sulfonate (PSS) and a positively charged polymer polyallylamine hydrocholoride (PAH) to prepare the LBL assembly around the metal core. The positive charge due to the presence of CTAB stabiliser on bare GNR, enable the formation of first LBL layer by the electrostatic attraction between CTAB and PSS. It is to be noted here that the polymer was always taken in NaCl solution as it minimized electrostatic

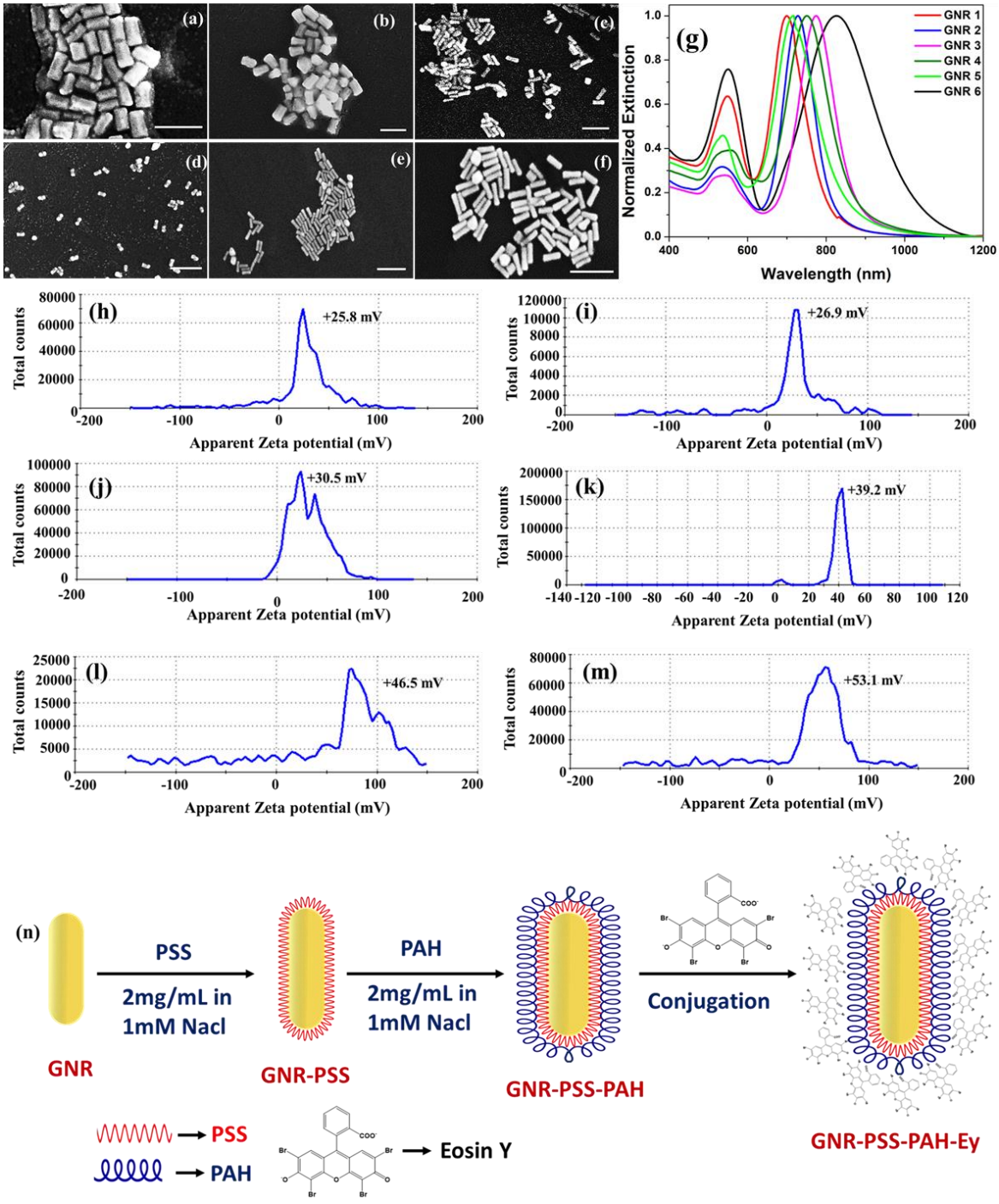

Figure 4B.1. (a)-(f) FE-SEM images of GNR 1-6; (g) extinction spectra of GNRs; Zeta potentials of (h) GNR 1, (i) GNR 2, (j) GNR 3, (k) GNR 4, (l) GNR 5, (m) GNR 6 and (n) schematic illustration of adsorption of polyelectrolytes and Ey on GNR.

repulsions, leading to the layer formation with higher thickness. In the next step, the second LBL layer was easily formed by adsorbing positively charged PAH to negatively charged PSS layer. This process was continued until we obtained LBL assembled GNRs of six different thicknesses, which will be labelled as GNR1a to GNR1f, for GNR1 and in

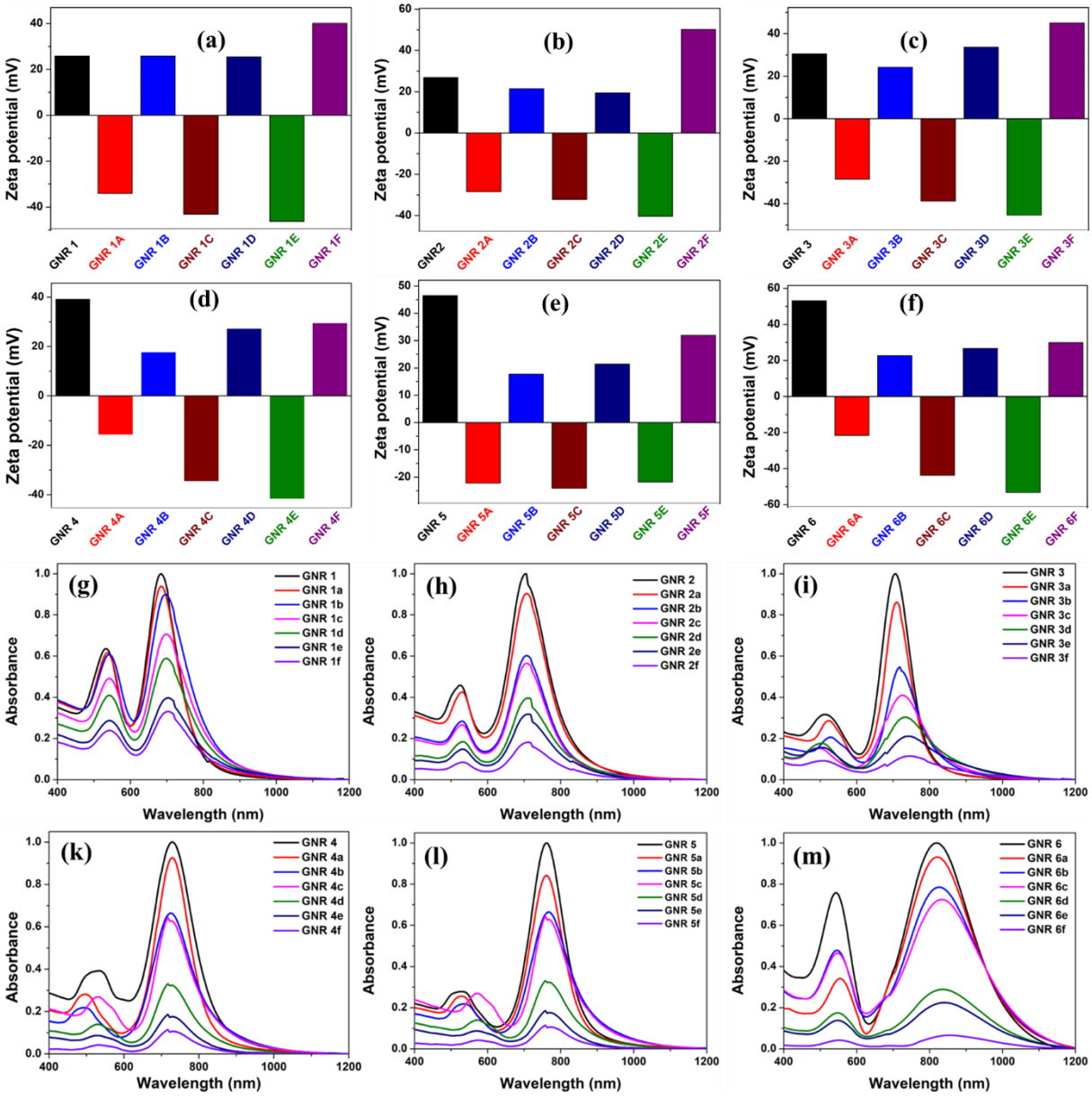

Figure 4B.2. Zeta potential of (a) GNR 1a-1f, (b) GNR 2a-2f, (c) GNR 3a-3f, (d) GNR 4a-4f, (e) GNR 5a-5f, (f) GNR 6a-6f; and extinction spectra of (g) GNR 1a-1f, (h) GNR 2a-2f, (i) GNR 3a-3f, (j) GNR 4a-4f, (k) GNR 5a-5f, (l) GNR 6a-6f.

the same way for other GNRs. The ζ-potential values were monitored after every coating, which indicated a charge reversal at every subsequent layer, confirming the successful formation of LBL coated GNRs (**Figure 4B.2a-f**). The extinction spectra of the LBL assembled GNRs are shown in **Figure 4B.2g-m**. We noticed a small red shift and peak broadening in the extinction spectra of GNR after the LBL assembly, which might be due to decrease in inter nanorod distance or a single polymer chain adsorbing on two or more GNRs.[41] From the FE-SEM images of LBL coated GNRs, as expected the

average size of GNRs increased after each LBL coating. The average polymer layer (spacer) thickness was found to be approximately 2.8 ± 0.8 nm, 6.1 ± 1.3 nm, 9.4 ± 1.2 nm, 12.6 ± 1.8 nm, 15.8 ± 1.3 nm, and 19.7 ± 2.1 nm for LBL a. LBL b, LBL c. LBL d, LBL e, and LBL f respectively (**Figure 4B.3.)**.

Table 4B.1. LSPR band maxima, length, width and Aspect ratio of synthesized GNRs.

S.No.	Length (nm)	Width (nm)	AR	LSPR
1	115 ± 3.2	57.5 ± 2.1	2 ± 0.3	699
2	120 ± 2.3	53.3 ± 0.9	2.25 ± 0.7	716
3	125 ± 2.1	50 ± 1.9	2.5 ± 0.3	728
4	133 ± 4.7	45 ± 1.2	2.95 ± 0.8	751
5	145 ± 3.1	43 ± 1.7	3.37 ± 0.5	774
6	157 ± 4.6	40.5 ± 1.8	3.8 ± 0.9	828

The final step in this multilayer architecture is the adsorption of PS molecules to LBL coated GNRs. For this, the GNR-LBL in water were diluted to optical density (OD) value of 0.1 and the appropriate quantity of Ey in ethanol was added to it and the conjugation was carried out by stirring the reaction for three hours at room temperature in dark. After three hours the reaction was stopped and the conjugated GNRs were purified by centrifugation. From the pellet, we recorded the absorbance spectra of hybrid nanorods (**Figure 4B.4.a-f)**, whereas the supernatant produced the absorption spectra of unconjugated Ey (**Figure 4B.4.g-l**). The study showed that the maximum conjugation of Ey occurred with LBL b, d, and f, where the outer layer was positively charged due to presence of PAH. Moreover, a comparison of the OD values of Ey from the absorption spectra of pellet and supernatant (**Figure 4B.4.**), indicated about very little or no conjugation of Ey to the LBL layers with PSS coating. The ζ value of GNR 4d supernatant was modified substantially after Ey conjugation to become almost neutral (+5 mV) from positive value of +27.2 mV, indicating the unavailability of free amine groups of PAH layer as they were conjugated to Ey molecules (**Figure 4B.5 a-d**).

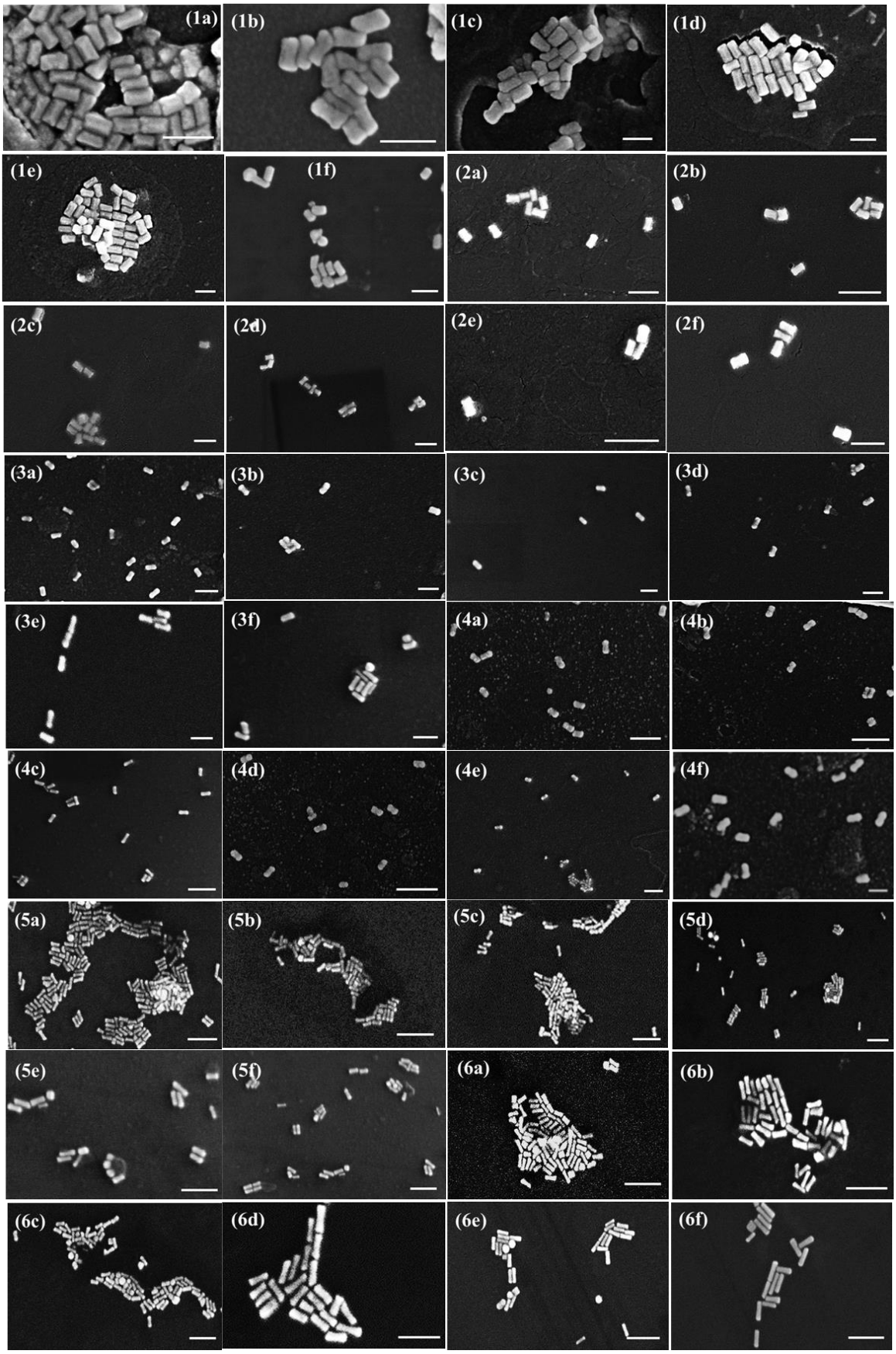

Figure 4B.3. FE-SEM images of GNR 1a-1f to GNR 6a-6f. The scale bar is 200 nm from GNR1a to GNR 3f and 400 nm for GNR 4a to GNR 6f.

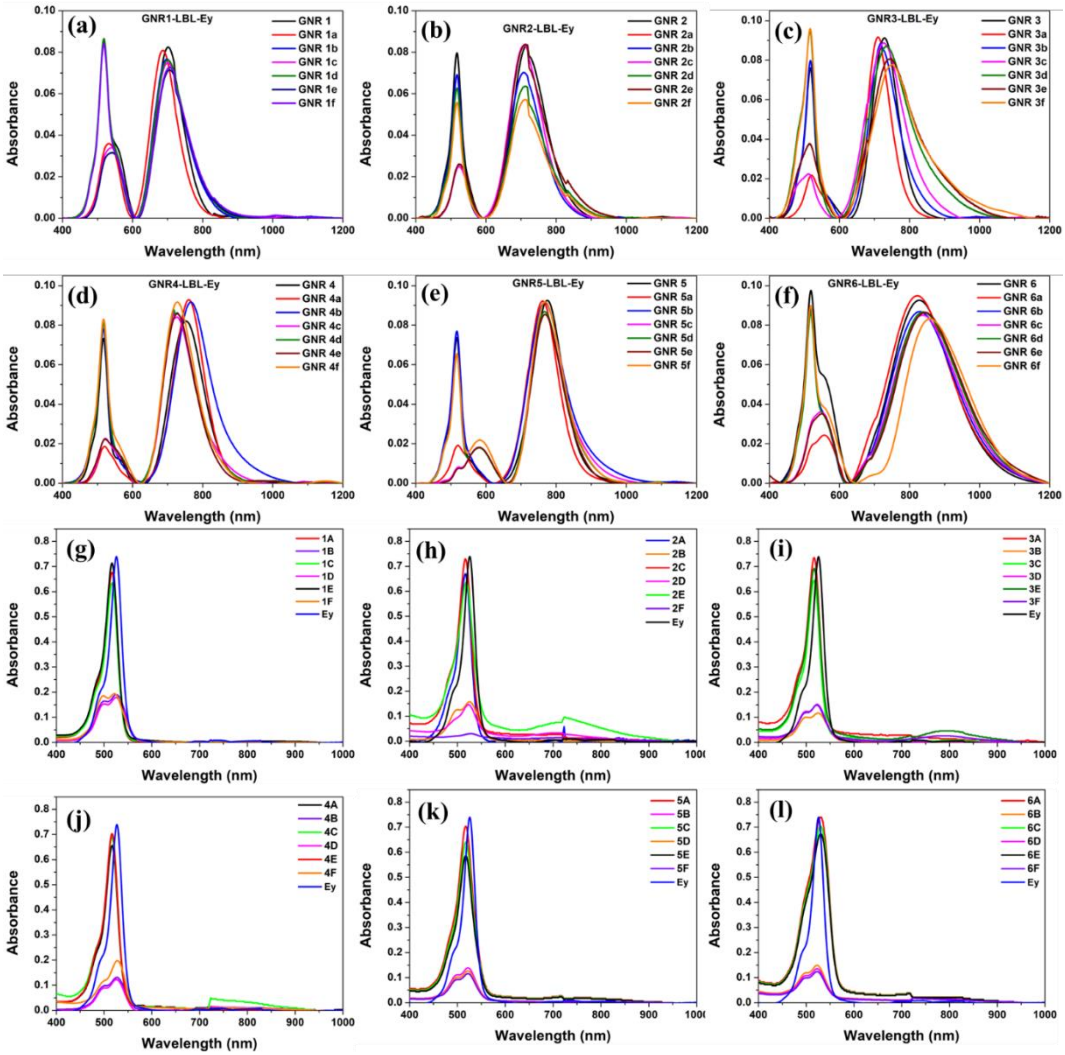

Figure 4B.4. (a)-(f) is the extinction spectra of pellet containing GNR-LBL-Ey and (g) to (l) is the absorbance spectra of supernatant after Ey conjugation.

Whereas, in case of GNR 4c, the value changed from -35 mV to -20 mV after Ey conjugation, indicating the presence of still substantial free sulfonate groups of PSS on the surface. Also, bright green emission of Ey was obtained under UV lamp from the supernatant of GNR 4c (**Figure 4B.5a-d**), whereas, under same condition, the supernatant of GNR 4d produced no emission, indicating the strong conjugation of Ey in case of GNR 4d. Measurement of the zeta potential values of supernatants GNR 4c and GNR 4d (**Figure 4B.5e**) substantiated the fact. Subsequently, the amount of conjugated Ey was also quantified by using a calibration plot with the absorbance of the known concentrations of Ey (**Figure 4B.5f**), and by comparing the supernatant absorbance with in each case. For LBL b, d, and f, the concentration of conjugated Ey to GNRs was found to be in the range ~1-1.25 μM (**Figure 4B.5g)**. However, for the

subsequent MEF and ME-SOG experiments, the Ey conjugated GNR solutions were appropriately diluted to match the final concentration of Ey as 1 μM.

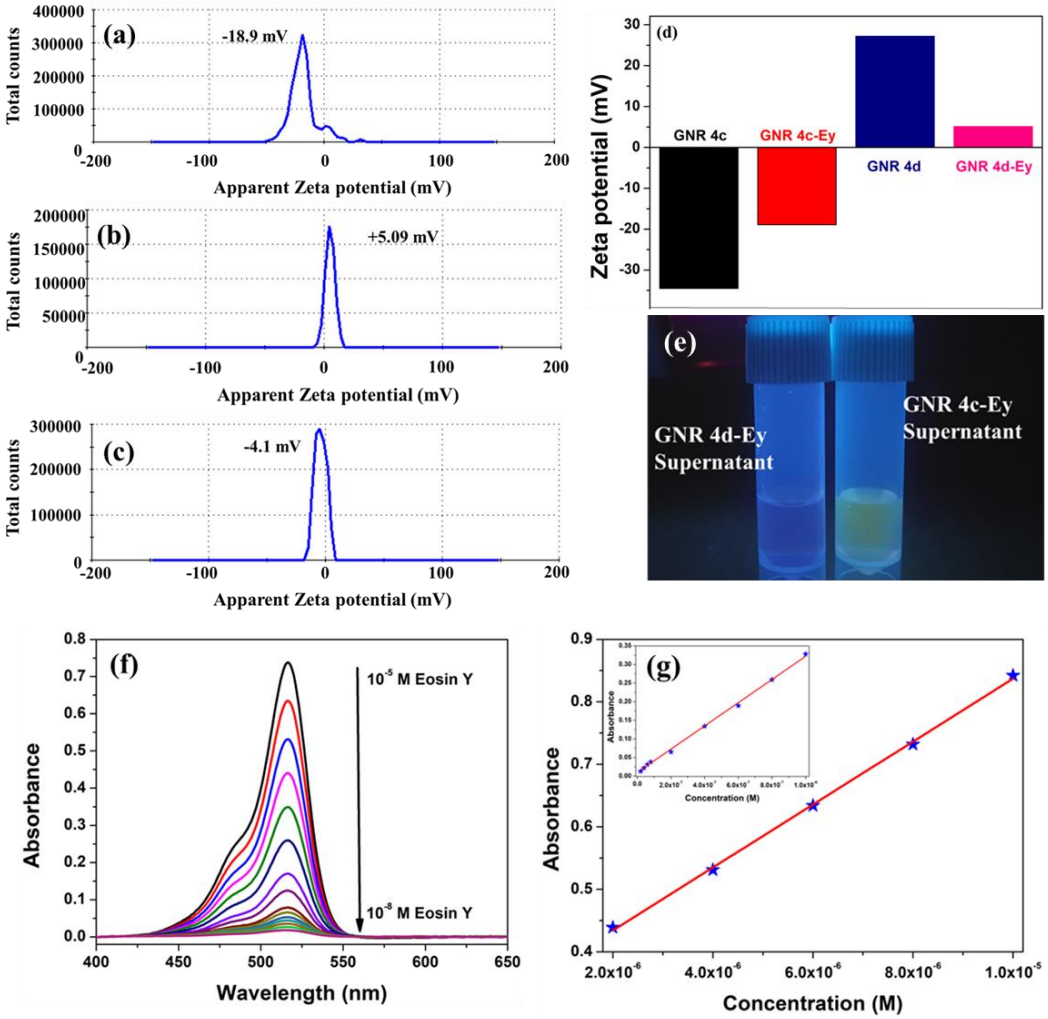

Figure 4B.5. Zeta potential values of supernatants of (a) GNR 4c-Ey, (b) GNR 4d-Ey; (c) Eosin Y, and (d) a representative histogram showing zeta change on GNR 4c and GNR 4d before and after Ey conjugation, (e) A representative photograph of supernatants under UV irradiation; (f) is the absorbance spectra of Ey from 10 μM to 10 nM and (g) is calibration curve of Ey at higher and the inset shows the calibration curve in lower concentration range.

4B.2.2. MEF studies of Ey adsorbed on LBL assembled GNRs

Subsequently, the MEF studies were performed using hybrid GNR of different aspect ratios (GNR 1-GNR 6), where the thickness in each GNR was varied (LBL layer a to f). The fluorescence of Ey was completely quenched when it was directly adsorbed on bare GNRs and also very less fluorescence of Ey was recorded (not shown) when it was adsorbed on PSS layer (LBL a, c and e). Whereas, with the outer layer as PAH (LBL b, d and f), the fluorescence of Ey was found to be significantly higher compared to PSS.

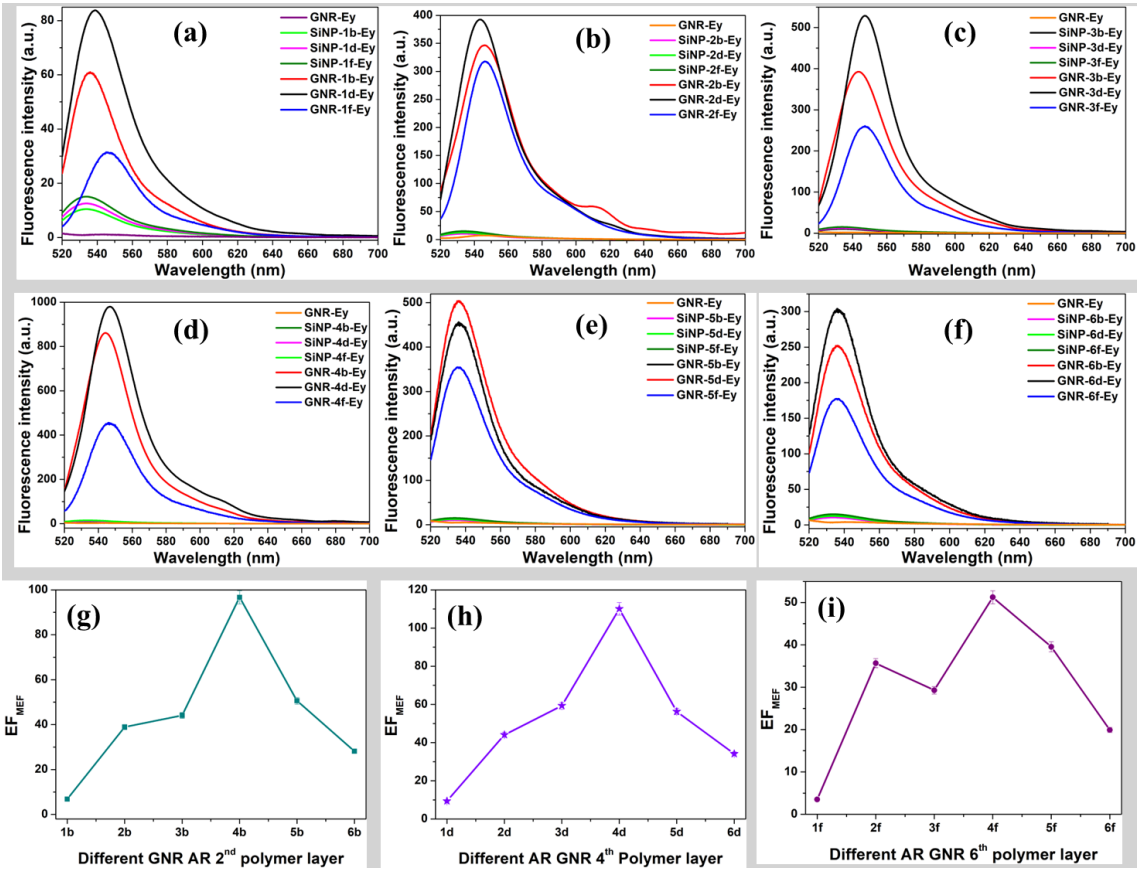

Figure 4B.6. MEF studies of Ey adsorbed on (a) GNR 1a-1f, (b) GNR 2a-2f, (c) GNR 3a-3f, (d) GNR 4a-4f, (e) GNR 5a-5f, (f) GNR 6a-6f; EF MEF plots of different AR GNR with (g) second polymer layer, (h) fourth polymer layer and (i) sixth polymer layer.

With PAH layers, the maximum fluorescence of GNR-Ey was observed for 'LBL d' starting from 'LBL b' and it decreased subsequently for 'LBL f', emphasizing the distance dependent nature of MEF. (**Figure 4B.6a-f**). The MEF enhancement factor (EF) is a critical parameter to choose the best plasmonic material (**Figure 4B.6g-i**). To calculate the EF, an identical MEF study was carried out by adsorbing the same concentration of Ey molecules (10^{-6} M) on LBL assembled SiNPs (control), which were devoid of any plasmonic metal. LBL assembled SiNPs were synthesized by modified Stober's method and the size of these nanoparticles was found to be 120 nm (**Figure 4B.7a and b)**. The conjugation of Ey to SiNPs was similarly carried out and thoroughly characterized (**Figure 4B.7c and d)**. The fluorescence of Ey was found to be negligibly small for SiNP-LBL-Ey hybrids, and also we know that the scattering of SiNPs is less than AuNRs we calculated the number density of both these particles to make sure we aren't over estimating the EF caused by GNRs.

Number density of SiNPs:

Average size of SiNPs = 120 nm diameter = 60 nm radius = 60×10^{-7} cm

Density of TEOS = 0.933 g/mL or 0.94 g/cm^3

Mass of Si precursor = Molecular weight × Molarity × volume/1000

= 208.33 × 4.47 M × 50 mL/1000 = 4.65 g

Total Volume = mass/density = 4.65g /0.94 g cm^{-3} = 4.94 cm^3

Total Volume occupied = $4/3\ \pi r^3 = 4/3 \times 3.14 \times (60 \times 10^{-7})^3 = 9.04 \times 10^{-16}$ cm^3

Number of particles = Total volume/volume of each particle

= 4.94 / $9.04 \times 10^{-16} = 5 \times 10^{15}$ particles/mL

Number density of GNRs:

Average length of GNRs = 133 nm; width = 45 nm radius = 22.5×10^{-7} cm

Density of gold salt = 3.9 g/cm^3

Mass of Au precursor = Molecular weight × Molarity × volume/1000

= 293.83 × 0.5 × 10-3 M × 50 mL/1000 = 7.34×10^{-3} g

Total Volume = mass/density = 7.34×10^{-3} /3.9 g $cm^{-3} = 1.88 \times 10^{-3}$ cm^3

Total Volume occupied = $\pi r^2 h = 3.14 \times (22.5 \times 10^{-7})^2 \times 133 \times 10^{-7} = 2.11 \times 10^{-16}$ cm^3

Number of particles = Total volume/volume of each particle

= 1.88×10^{-3} cm^3/ 2.11×10^{-16} $cm^3 = 9 \times 10^{12}$ particles/mL

After calculation the number density of SiNPs (5×10^{15} particles/mL) was found to be much higher (Calculation above) than the number density of GNRs (9×10^{12} particles/mL, GNR 4). Subsequently, EF of MEF was calculated as the ratio of fluorescence intensity of Hybrid GNR-Ey of various LBL thicknesses to the fluorescence intensity of appropriate control sample SiNP-LBL-Ey. Among all GNR-LBL-Ey hybrids, the highest fluorescence as well as staggering EF of ~110 for MEF was observed with GNR 4d **(Figures 4B.6d and g-i),** where Ey was positioned at a distance of ~12.6 nm from the GNR surface (**Figure 4B.7e**). The fluorescence lifetime values of free Ey, Ey adsorbed on SiNPs and GNR-LBL-Ey were recorded to understand the mechanism of MEF. The average lifetime of Ey in water was reported earlier as 1.44 ns[45,46] which decreased to ~0.84 ns on direct adsorption on bare GNR (**Figure 4B.7f and table 4B.2**), while it increased to 2.64 ns on direct adsorption on polymer coated SiNPs,

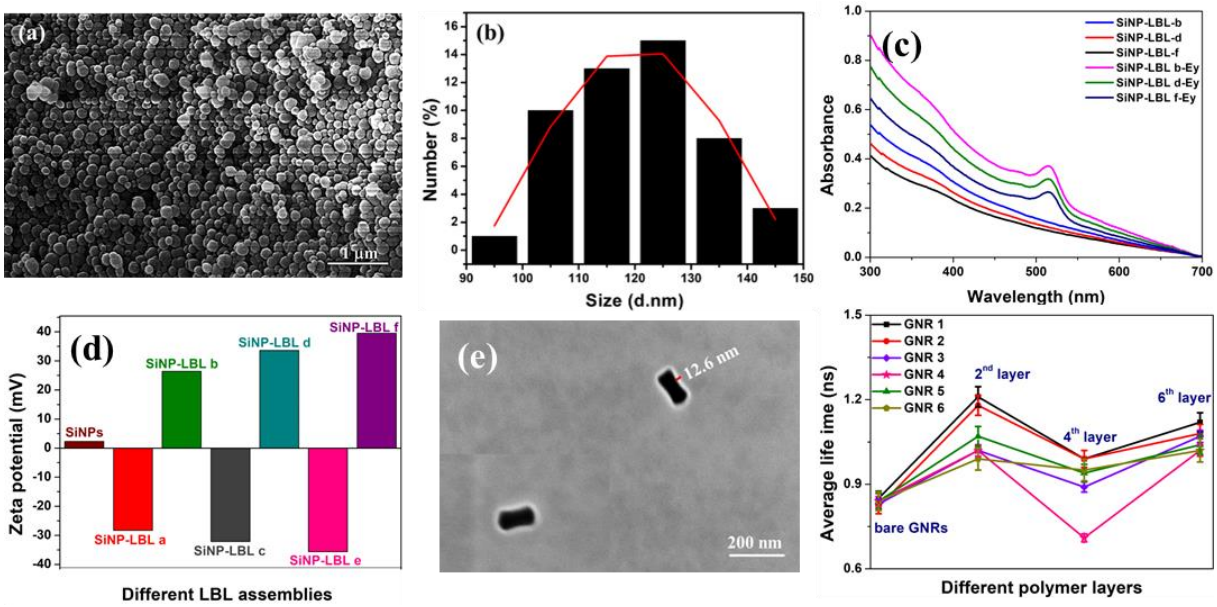

Figure 4B.7. (a) FE-SEM image of SiNPs, (b) Average size plot of SiNPs, (c) Absorption spectra of SiNPs and LBL coated SiNPs, (d) is the Zeta potential of SiNP-LBL NPs, (e) STEM image of GNR 4d taken in dark field mode and the inset shows the same along with layer thickness, and (f) Average life time plots of Ey adsorbed on bare GNRs and GNRs with different polymer layers

similar to previous reports.[17,47] As depicted in **Figure 4B.7f and table 4B.2**, the average life time values for each GNR-Ey hybrid slightly decreased with increase in polymer thickness up to LBL-d and then increased with further increase in polymer coating. Hence, as there is a moderate decrease in the average lifetime of the fluorophore associated with an increase in fluorescence, therefore 'enhancement in the radiative decay rate' is one of the mechanisms contributing to MEF, but it may not be the sole effect. Because, the transition rate of the excitation process of Ey is also dependent on the near field generated close to the nanostructure, as the transition rate is proportional to the square of the local electric field at the transition frequency. Therefore, higher excitation rate is another factor, which may lead to generation of higher fluorescence intensity. Finally, GNR-Ey interactions may also open up new nonradiative decay pathways of the excited electrons in the emitter, by which fluorescence intensity can be quenched as energy can be transferred to the GNR. Therefore, MEF of a hybrid nanostructure is a combined effect of the aforementioned three mechanisms (vide infra).

Table 4B.2. Average lifetime values of free Ey, Ey adsorbed on GNRs, GNR-LBL-Ey and SiNP-NH_2-Ey.

Sample	τ_1 (ns)	τ_2 (ns)	τ_3 (ns)	α_1 (%)	α_2 (%)	α_3 (%)	$\chi 2$	Average life time(ns)
Ey in water	0.80	1.01	1.71	27.63	28.77	43.6	1.19	1.44 ± 0.02
SiNP-NH_2-Ey	0.96	1.78	3.81	27.61	19.08	53.31	1.19	2.64 ± 0.06
GNR1-Ey	0.17	0.82	1.02	10.01	39.92	50.06	1.17	0.85 ± 0.02
GNR 1b-Ey	0.98	1.07	1.51	30.28	32.14	37.58	1.06	1.21 ± 0.03
GNR 1d-Ey	0.82	1.02	1.11	28.44	49.55	22.01	1.18	0.99 ± 0.02
GNR 1f-Ey	0.98	1.09	1.38	35.23	41.08	23.69	1.18	1.12 ± 0.03
GNR 2-Ey	0.65	0.93	1.01	39.98	49.75	10.02	1.10	0.82 ± 0.02
GNR 2b-Ey	0.98	1.27	1.45	51.83	16.69	31.48	1.2	1.18 ± 0.03
GNR 2d-Ey	0.81	0.96	1.25	37.63	30.46	31.66	1.04	0.99 ± 0.02
GNR 2f-Ey	0.86	0.95	1.25	25.08	24.98	49.9	1.01	1.08 ± 0.03
GNR 3-Ey	0.59	0.92	1.08	36.01	49.97	14.02	1.16	0.83 ± 0.01
GNR 3b-Ey	0.89	1.09	1.41	48.17	47.97	3.86	1.16	1.02 ± 0.02
GNR 3d-Ey	0.66	0.81	1.10	15.05	51.35	33.61	1.11	0.89 ± 0.02
GNR 3f-Ey	0.86	1.01	1.36	29.44	39.8	30.75	1.16	1.07 ± 0.01
GNR 4-Ey	0.79	0.83	1.09	37.81	47.79	13.57	1.18	0.84 ± 0.01
GNR 4b-Ey	0.86	1.01	1.22	26.81	50.19	23.01	1.16	1.02 ± 0.02
GNR 4d-Ey	0.62	0.70	1.17	64.32	23.8	11.89	1.13	0.71 ± 0.01
GNR 4f-Ey	0.88	1.01	1.36	49.41	31.09	19.5	1.14	1.02 ± 0.02
GNR 5-Ey	0.46	0.96	1.08	30.66	40.03	29.32	1.14	0.84 ± 0.02
GNR 5b-Ey	0.94	1.04	1.54	48.76	34.41	16.82	1.05	1.07 ± 0.03
GNR 5d-Ey	0.82	0.92	1.06	19.94	30.03	50.03	1.13	0.94 ± 0.03
GNR 5f-Ey	0.89	1.02	1.34	33.51	44.78	21.72	0.99	1.04 ± 0.03
GNR 6-Ey	0.45	0.85	1.09	28.17	30.02	41.81	1.06	0.84 ± 0.03
GNR 6b-Ey	0.89	1.29	1.57	31.33	19.01	28.99	1.04	0.99 ± 0.03
GNR 6d-Ey	0.87	1.02	1.22	50.01	46.85	3.15	1.04	0.95 ± 0.03
GNR 6f-Ey	0.89	0.94	1.24	19.87	49.8	30.33	1.14	1.02 ± 0.04

4B.2.3. MESOG studies using GNR-LBL-Ey

The different GNR-LBL-Ey samples were then used to study their ME-SOG ability, by an indirect method via analysing the photobleaching kinetics of a SOG selective molecular probe Diphenyl benzofuran (DPBF). Prior to the experiment we performed several blank studies by studying the degradation of DPBF with and without light, in

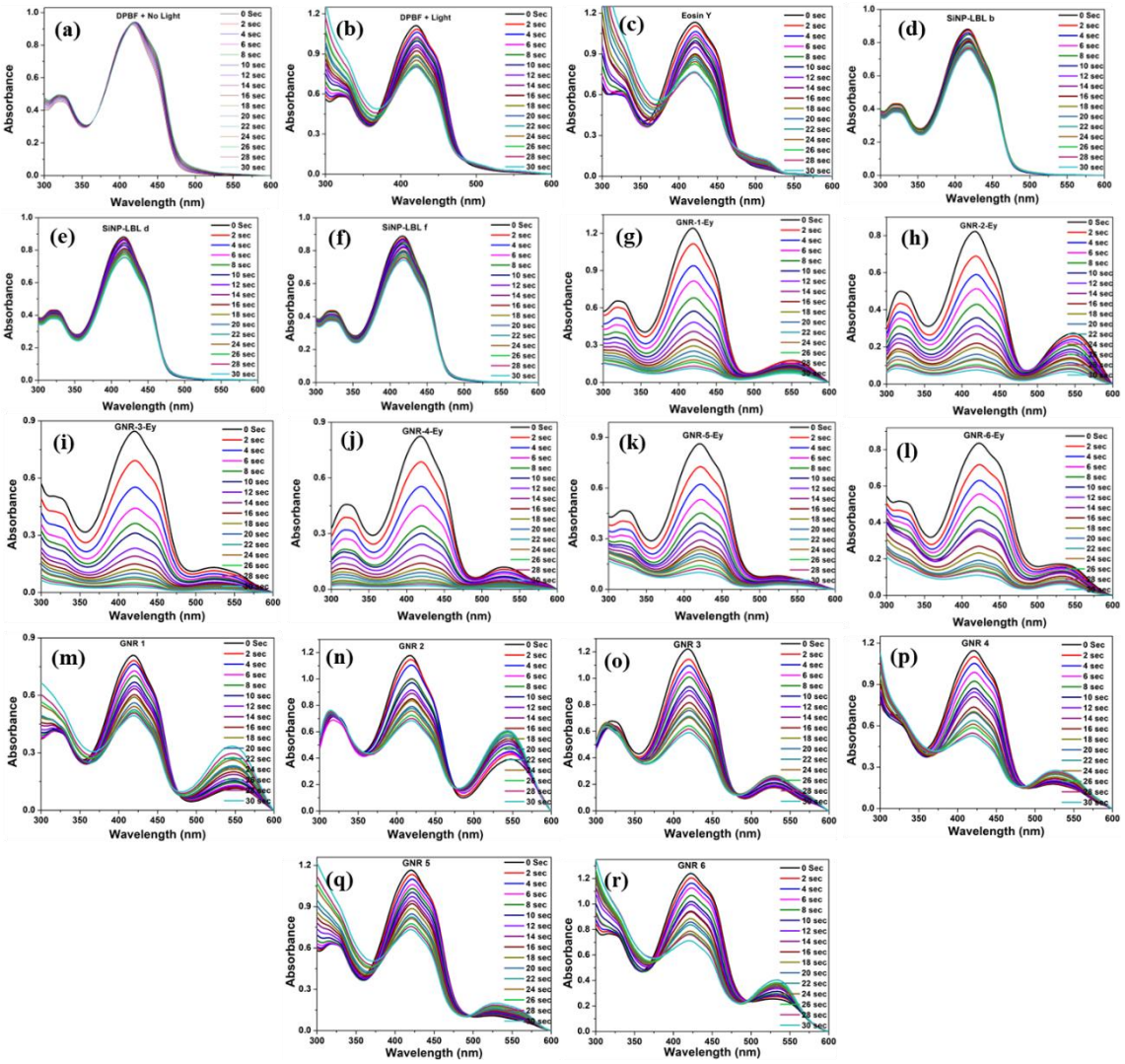

Figure 4B.8. Blank study showing DPBF degradation (a) in the absence of light, (b) presence of light, (c) in presence of 1 μM Ey, (d) on SiNPs-LBL-b, (e) SiNP-LBL-d, (f) SiNP-LBL-f and degradation of DPBF on direct adsorption on to (e) GNR 1-Ey, (f) GNR 2-Ey, (g) GNR 3-Ey, (h) GNR 4-Ey, (i) GNR 5-Ey, (j) GNR 6-Ey, (k) GNR 1, (l) GNR 2, (m) GNR 3, (n) GNR 4, (o) GNR 5, and (p) GNR 6 under 35 mW cm^{-2} white light irradiation.

presence of only Ey-SiNPs and only Ey separately (**Figure 4B.8a-f**). Unlike the results obtained in MEF where there would be quenching of fluorescence of Ey when directly adsorbed on to GNRs (**Figure 4B.8g-r and 4B.9**), we noticed maximum SOG in case of GNR-Ey because of efficient energy transfer from bare NRs to adsorbed oxygen molecules via Ps.[17,43] Despite of its high SOG, it cannot be used for image guided therapies due to its poor or almost zero fluorescence making it practically unimportant. Keeping this in mind we further performed SOG studies in identification of a sample with high fluorescence and decent SOG capacity. Then we found that the samples with LBL layers b, d, and f gave good SOG capacity compared to other samples (a, c and e)

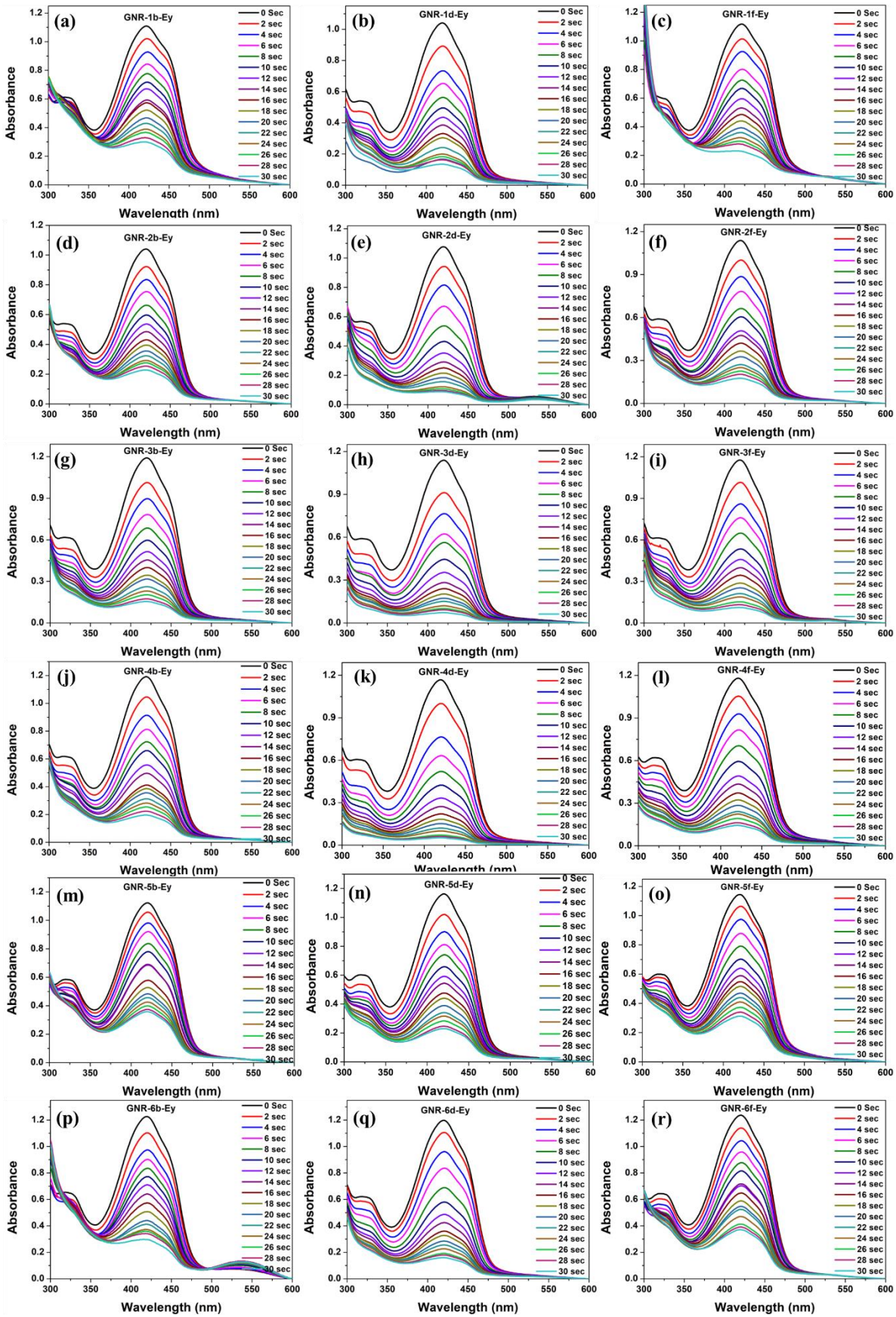

Figure 4B.9. Degradation of DPBF in the presence of Ey adsorbed GNR 1-6 with polymer layers b, d, and f only, under 35 mW cm^{-2} white light irradiation.

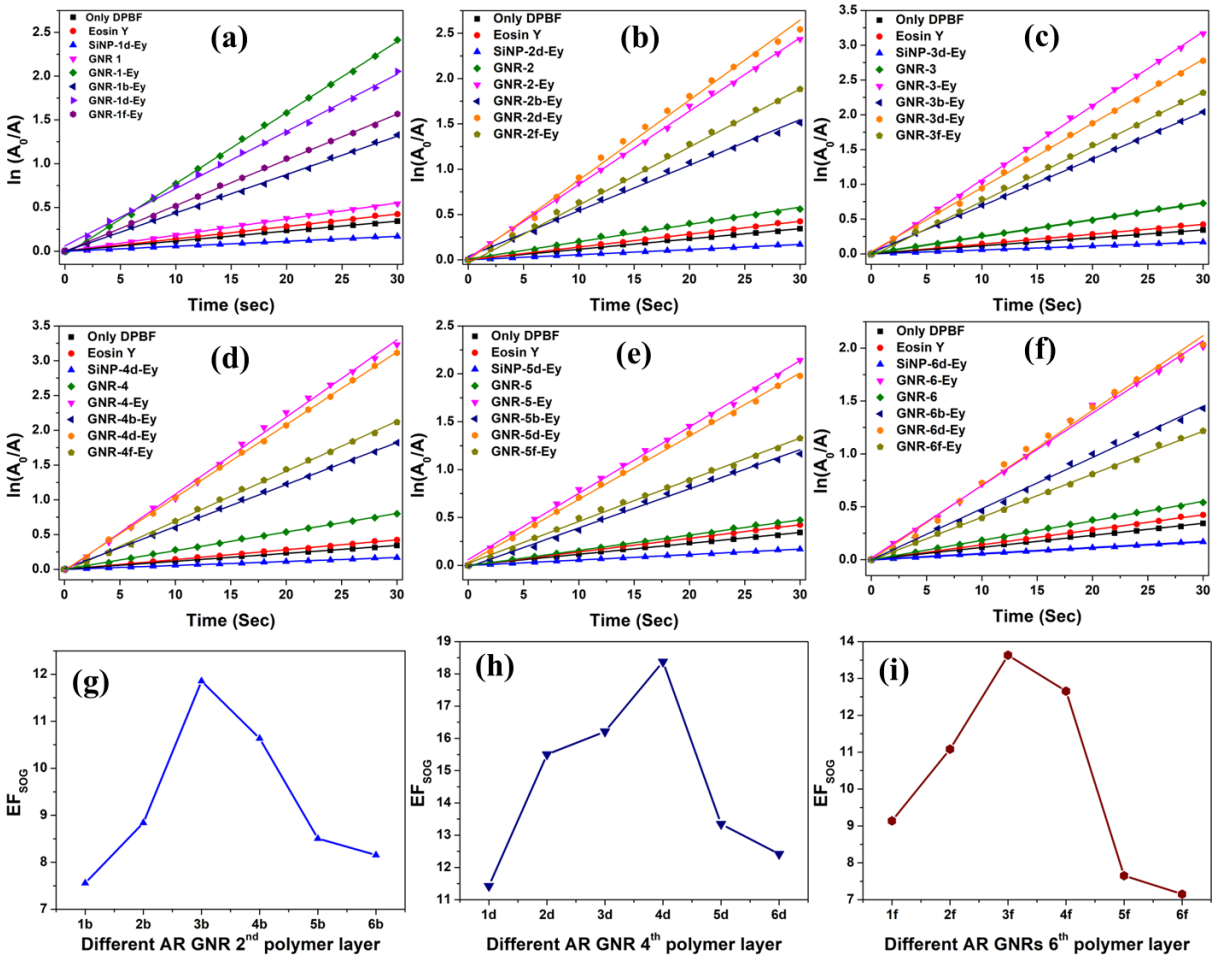

Figure 4B.10. ln (A_0/A) plots depicting the degradation of 50 μM DPBF on (a) GNR 1a-Ey to 1f-Ey, (b) GNR 2a-Ey to 2f-Ey, (c) GNR 3a-Ey to 3f-Ey, (d) GNR 4a-Ey to 4f-Ey, (e) GNR 5a-Ey to 5f-Ey, and (f) GNR 6a-Ey to 6f-Ey under 35 mW cm^{-2} white light irradiation, and SOG EF of Ey adsorbed on different AR GNR with (g) second polymer layer, (h) fourth polymer layer and (i) sixth polymer layer.

where there is poor Ey adsorption. The self-degradation of DPBF was subtracted from all the samples before calculating its SOG rates **(Figure 4B.9.).** To clearly understand the SOG efficiency we have plotted ln (A_0/A) vs time and the slopes obtained from the linearly fitted curves were used to calculate the ME-SOG EF (**Figure 4B.10**). Similar to MEF among different AR of GNRs, GNR-4d demonstrated the maximum SOG when compared to other GNRs as depicted in the **Figure 4B.10.** Later, in order to confirm that the decrease in DPBF degradation is due to $^1O_2$ only, rather than any other reactive oxygen species, we performed two different experiments using DMPO and NaN_3. DMPO specifically binds to hydroxyl and superoxide radicals and we didn't notice any change in the degradation of DPBF in presence of hybrid GNR 4d-Ey particle with and without the addition of DMPO ruling out the presence of hydroxyl and superoxide radicals

(**Figure 4B.11**).[17,44] To confirm the presence of $^1O_2$, we added NaN_3 to the GNR 4d-Ey solution and the degradation of DPBF was studied. In this case, the degradation of DPBF was found to be insignificant which conformed the trapping of in situ generated $^1O_2$ by NaN_3, proving the presence of $^1O_2$ as the ROS (**Figure 4B.11**).[17,44]

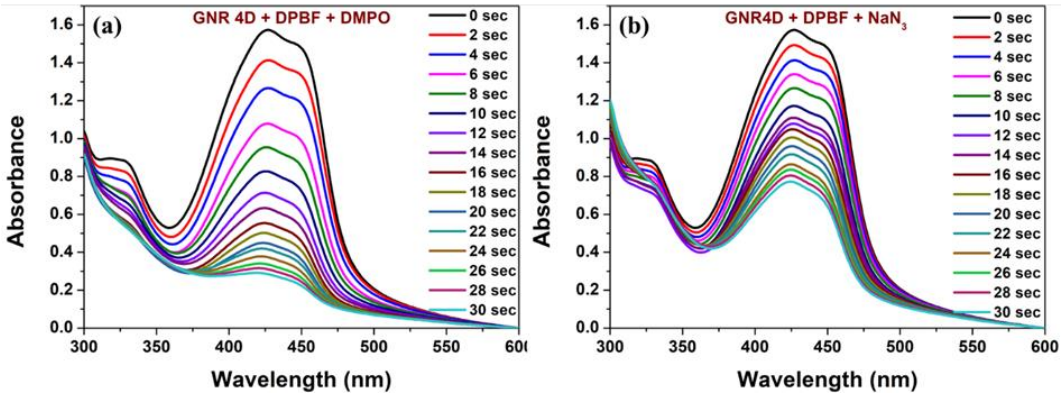

Figure 4B.11. Degradation of 50 μM DPBF on GNR-4d-Ey in the presence of (a) DMPO, and (b) NaN3 under 35 mW cm-2 white light

4B.2.4. COMSOL simulations

In order to understand the role of the near field effect on MEF and ME-SOG of Ey conjugated GNR, COMSOL simulations were carried out to find the electromagnetic field maps for only GNRs, GNRs of different AR but same silica thickness, as well as with silica spacer of different thicknesses (**Figure 4B.12. and 4B.13a**). We used silica instead of polymer spacer for simulation, because irrespective of the material used, we wanted to visualize the field at a particular distance from GNR surface. Moreover, the simulation was easier because the parameters of SiO_2 were readily available. Not only that, SiO_2 is also a dielectric material similar to the polymer used to coat the GNRs. **Figure 4B.13a** shows the electromagnetic field maps of different GNRs with different AR, but with the same thickness of the silica coating (12.6 nm). **Figure 4B.13b** shows the electric field decay as a function of the distance from the silica surface of the GNR, which indicates the rate of the exponential decay of the near field in each case. Among all the hybrid GNRs, the near field damping rate was least for GNR 4d. Therefore, it may be concluded that Ey experiences maximum electric field with GNR 4d compared to other hybrid GNRs justifying the earlier obtained experimental results where GNR 4d produced maximum MEF and MESOG effect. By varying the silica thicknesses for GNR 4, the damping rate was found to decrease with increase in silica spacing (**Figure**

4B.13c), indicating stronger near field for GNR 4 d-f. However, for the free GNRs the highest and lowest near field damping rates were recorded for GNR 6 (AR: 3.8) and GNR 1 (AR: 2), respectively (**Figure 4B.13d**). The result is similar to the already reported data in literature, which estimates higher damping rate with nanorod with higher aspect ratio.[15,20,21]

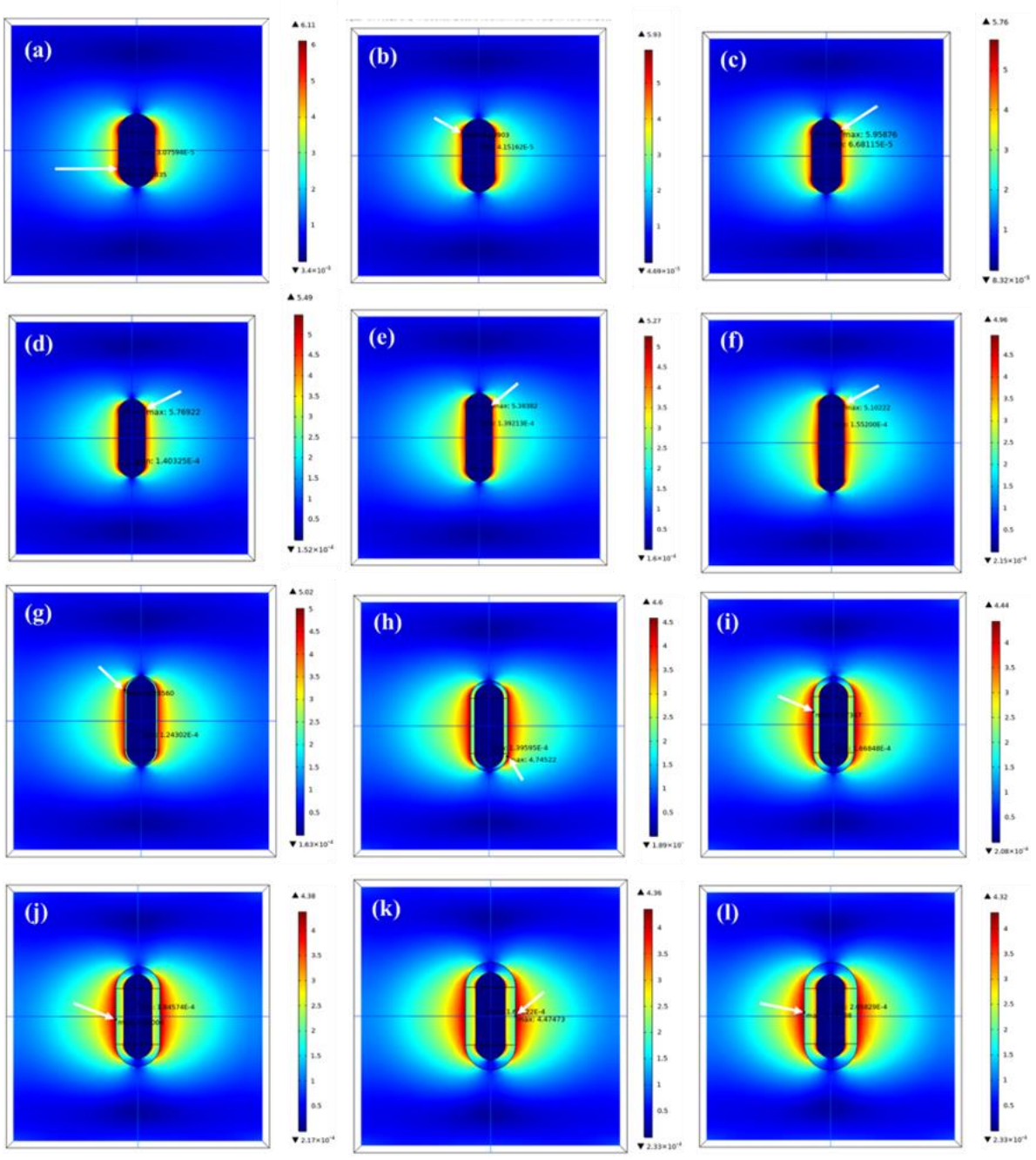

Figure 4B.12. Theoretical Electromagnetic field maps for (a) GNR 1, () GNR 2, (c) GNR 3, (d) GNR 4, (e) GNR 5, (f) GNR 6; (g) GNR 4a, (h) GNR 4b, (i) GNR 4c, (j) GNR 4d, (k) GNR 4e, and (l) GNR 4f. The max value indicated in the figures is the electric field's maximum value and the corresponding enhancement factor is calculated as the fourth power of E_{max})

4B.2.5. Near- and far-field properties of GNRs

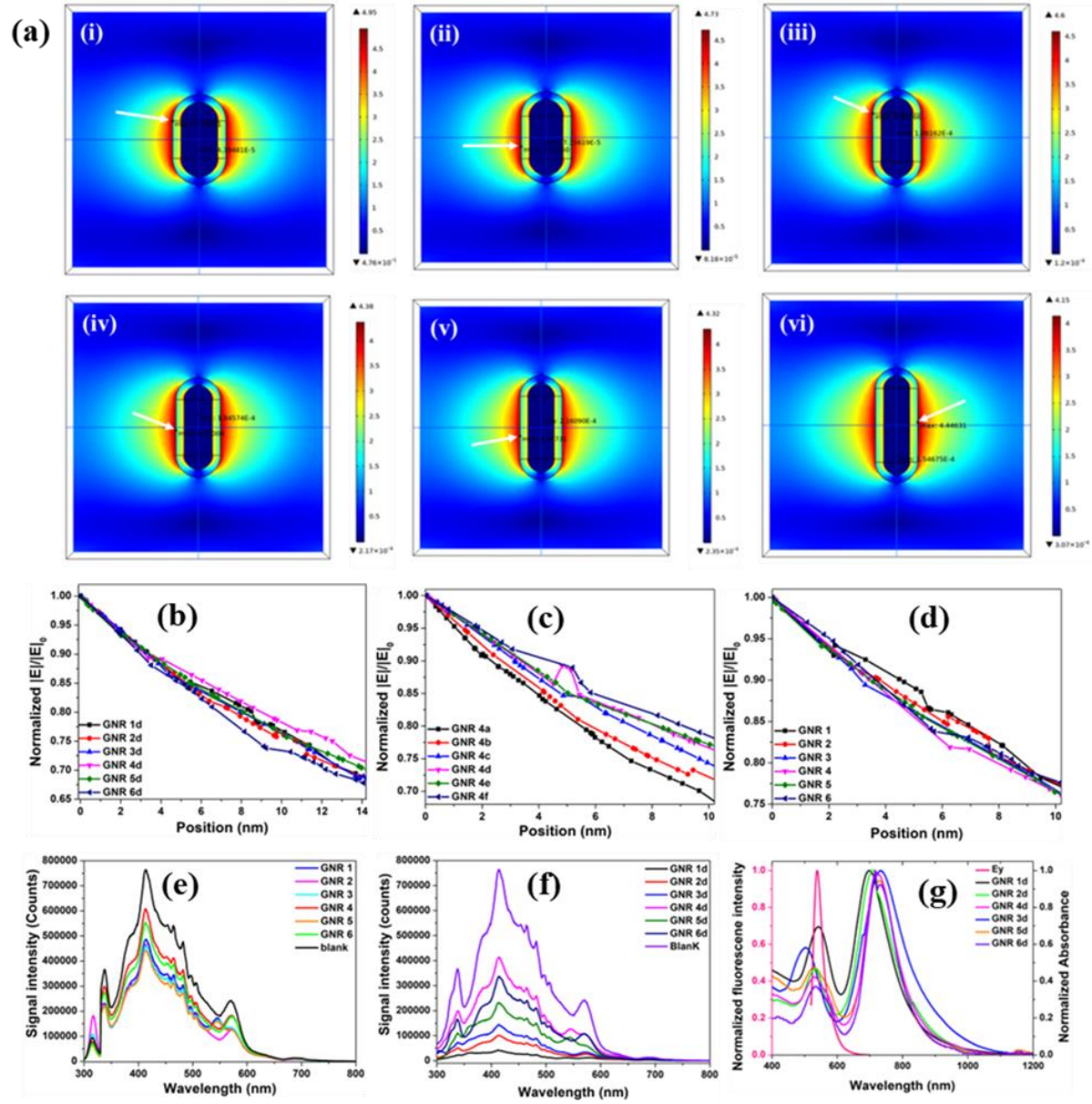

Figure 4B.13. (a)Theoretical Electromagnetic field maps for (i) GNR 1d, (ii) GNR 2d, (iii) GNR 3d, (iv) GNR 4d, (v) GNR 5d, (vi) GNR 6d; excited at 519 nm (The max value indicated in the figures is the electric field's maximum value and the corresponding enhancement factor is calculated as the fourth power of Emax); 1D line plot showing the normalized electric field damping as a function of distance, starting from the silica surface of (b) GNR 1d-6d, (c) GNR 4a-4f, starting from the metal surface: (d) GNR 1-6 (The decays are obtained along the line, as shown in the figure); (e), and (f) are the experimental scattering spectra obtained from GNR 1-6, and GNR 1d-6d, respectively, and (g) shows the overlap between emission spectra of Ey and extinction spectra of GNR 1d-6d-Ey hybrids.

Finally, to understand the role of the far-field effect on MEF and ME-SOG, we performed an experiment using an emission spectrophotometer coupled with integrating sphere to collect only the scattering component of the GNRs with and

without the polymer spacer. It is known that the extinction of light in the far field, is composed by two optical processes, namely, absorption and scattering of the nanostructures. Scattering in the far field creates a secondary light source which can in-turn enhance the light absorption and subsequently the excitation rate of the emitter. As depicted in **Figure 4B.13e**, scattering from GNR 4 was experimentally found to be maximum compared to any other GNRs, indicating the superiority of GNR 4 over other nanostructures in MEF and ME-SOG. When we carried out the same experiment with different GNR with LBL d, it was found again that GNR 4-d produced maximum scattering intensity, agreeing to our earlier observation (**Figure 4B.13f**).

At this point, it is important to consider the competitive nonradiative energy transfer process enforced by the individual GNR on the emitter, by which fluorescence of the emitter is quenched. The extent of nonradiative energy transfer is estimated as the overlap of the emission spectra of Ey and the extinction spectra of polymer coated GNR (**Figure 4B.13g**). Table 1 shows the J integral (overlap) parameter of different GNR with same spacer thickness along with other important parameters. It can be understood from the results that along with the J value, if we also consider the simulated electric filed enhancement factor for each GNR (**Table 4B.3**), GNR 3d and GNR 4d were found to be best performer. However, as discussed earlier, the more scattering component of GNR 4d keeps it ahead of GNR 3d to effectively produce more fluorescence and singlet oxygen (*vide supra*).

Table 4B.3. Summary table showing the Average life time, enhancement factors of MEF and SOG, simulated electric field and J integral values of GNR 1d-6d

S.No.	Sample	EF MEF	Average life time (ns)	EF SOG	Simulated Electric field	J integral (M^{-1} cm^{-1} nm^5)
1	GNR 1d	9.41	0.99 ± 0.02	11.4	27.08	5.68×10^{10}
2	GNR 2d	44.1	0.99 ± 0.02	15.5	26.34	2.83×10^{10}
3	GNR 3d	59.3	0.89 ± 0.01	16.2	24.28	2.42×10^{10}
4	GNR 4d	110.1	0.71 ± 0.01	18.3	21.43	3.02×10^{10}
5	GNR 5d	56.3	0.94 ± 0.03	13.3	20.13	3.08×10^{10}
6	GNR 6d	34.1	0.95 ± 0.03	12.4	19.76	3.98×10^{10}

4A.3. Conclusions and Summary

In conclusion, we synthesized a library of GNRs of six different aspect ratios and six different polymer thicknesses using alternative negatively and positively charged polymers PSS and PAH, respectively. We thoroughly characterized the GNRs using FESEM, UV-Vis study, Zeta potential measurement etc. A potential photosensitizer molecule Ey was conjugated to the GNRs and it was observed that the conjugation of Ey was successful only when the outer layer of GNR was PAH. Subsequently, MEF and MESOG studies of these hybrid theranostic nanoparticles were investigated. It was observed that the fluorescence and rate of SOG increased up to LBL d from LBL b and then decreased subsequently proving the distance dependent nature of these optical processes. To the best of our knowledge this is the first time, a library of GNRs with small variations in their size and AR was explored to find simultaneous enhancement of MEF and MESOG to utilize them for image-guided PDT applications. Among all the GNRs in our synthesized library, GNR 4d offered ~110- and 18-fold increase in fluorescence and SOG production simultaneously. Later, to understand the near - and far-field effect on MEF and MESOG we carried out theoretical investigations by performing COMSOL simulations and experimentally recorded the scattering component of GNRs. The observed plasmon-enhanced spectroscopic signatures of our PS loaded GNRs were corroborated well by the synergistic effects of many radiative and non-radiative processes such as plasmon damping rate, increase in radiative decay rate of emitter, far field effect in the form of scattering, and the energy transfer between the nanorod and the emitter.

Chapter 5A

Bimetallic Ag-Cu alloy Microflowers as SERS substrates with single molecule detection limit

In the previous chapters, the roles of size, shape, composition of MNPs for MEF and MESOG studies were explored. Herein we try to understand the role of bimetallic MNPs in SERS which is also a plasmonic effect similar to MEF but differs in the aspect of analyte adsorption. While, in MEF and MESOG, an optimum distance between MNP and Fluorophore is required, but SERS is observed by the direct adsorption of target molecule on MNP. This chapter is based on the following paper, S. Kaja, and A. Nag; Bimetallic Ag–Cu Alloy Microflowers as SERS Substrates with Single-Molecule Detection Limit, Langmuir, 2021, 37, 44, 13027-13037,

5A.1. Introduction

Surface-enhanced Raman spectroscopy (SERS) is a powerful, non-destructive, and ultrasensitive analytical technique which enables easy and quick detection of analytes even at single molecule level.[1-3] In SERS, Raman signals of laser-irradiated polarizable molecules are enhanced by large plasmonically enhanced local fields at junctions or surfaces of metallic nanostructures.[4-5] It significantly extends the application of traditional Raman spectroscopy by providing molecule-specific chemical fingerprints with increased sensitivity by surpassing the inherent weak signal intensity of Raman scattering.[6] SERS finds significant application in diverse areas, for e.g. forensic science,[7-8] food and environment safety,[9-12] biomolecular analysis,[13] cancer diagnosis,[14] sensing of pesticides, pollutants, heavy metal etc.[15-19] In addition, exploration of single molecules [i.e., single-molecule SERS (SMSERS)] is also extremely important for deeper understanding of the governing principles in SERS. Earlier reports claimed that SERS enhancement factor (EF) of the order $\sim 10^{14}$ –10^{15} were necessary for SM detection.[20-21] It was postulated that such high EF in SERS was resulted from multiplicative contribution of two factors: local electromagnetic (EM) field effect and chemical enhancement (CE).[22] However, it has been realized now that the SERS EFs of $\sim 10^{7}$-10^{9} are sufficient for SM detection for non-resonant scatterers.[23] For resonant scatterers, modest enhancement factors even less than 10^{7}, can reach SM sensitivity.

One of the major challenges of SERS is to optimize the substrates with enhanced efficiency and reproducibility. So, there is always a quest for new substrates which are comparatively inexpensive, reproducible, with appropriate EF for SM detection. The parameters that are extensively explored during optimization are size, shape, inter-particle distance and the dielectric environment of the nanomaterial.[24] Moreover, it is known that SERS is always associated with the presence of hot spots in the substrates, which are highly confined regions in the metallic nanostructures, where the EF for Raman signals can be as high as $\sim 10^{7}$-10^{9}.[25] Earlier, metal nanoparticles made of Ag or Au, were widely used as SERS substrates.[26-27] Later, it was identified that the strength of the hot spots could be varied significantly by altering the shape from simple nanoparticle to anisotropic or pointed structures. Subsequently, a variety of substrates

like rods,[28] dendrites,[29-30] cups,[31] nanocubes,[32] nanostars[33-34] and flowers[35-37] steered the bulk of the SERS studies. Because, these substrates could produce high EF due to their multi-branched structures with abundant hot spots localized at the corners and around the branches. However, most of these studies were performed using monometallic substrates, lacking the information on composition dependent SERS EF. Recently, easily fabricated bimetallic NPs and substrates have gained importance in the scientific community due to promising advantages over the component metal like high stability, excellent optical properties, and improved EF in SERS. Bimetallic systems for e.g., Al-Cu, Au-Ag, Au-Pd, Au-Pt, Ag-Cu, Au-Cu, Pd-Pt[38-44] have been extensively used in SERS.

Since gold, palladium, and platinum are expensive metals, bimetallic SERS substrates made of Ag and Cu with high EF are in high demand. Among all the coinage metals, Ag shows highest plasmonic activity.[45-48] but it is prone to oxidation due to poor structural and chemical stability. Hence, its excellent plasmonic properties are not utilized to full extent. To address this limitation of Ag nanostructures, it is often modified effectively by alloying with cost-effective Cu to provide better stability with superior plasmonic activity than pure Ag. One more advantage of copper is that it oxidizes more than silver, but when Ag-Cu bimetallic NPs are formed, they allow far better oxidation resistance when compared to monometallic NPs.[49] In the past, Chen *et al.* synthesized heterogeneous Ag-Cu nano dendrites and showed that they produced more SERS intensity than pure Ag counterparts.[50] Lee *et al.* synthesized Raspberry-shaped Ag-Cu bimetallic NPs and showed high SERS.[51] Zhang *et al.* synthesized polymer-stabilized monometallic Cu and Ag-Cu NPs and showed that the latter produced better SERS properties.[52] Pal *et al.* synthesized bimetallic Ag-Cu films,[53] and Rao *et al.* synthesized Cu-Ag nanoparticle embedded polymer thin film[54] and showed its efficiency as a broad band spectrum SERS substrate. Nandhagopal *et al.* fabricated Pure Ag and Ag-Cu bimetallic thin films and showed that the latter demonstrated 3-fold increase in SERS efficiency.[55] Bharati *et al.* used Ag-Cu alloy NPs for explosive sensing via SERS.[56] Tran *et al.* fabricated and presented CuO/Ag core-shell nanowires as an excellent substrate for SERS.[57] Rivera-Rangel *et al.* prepared Ag-Cu bimetallic

nano dendrites by electrodeposition method and used it for femtomolar detection of Rhodamine6G via SERS.[58] Dubkov *et al.* demonstrated SERS in the red region using Ag-Cu composite NPs and also reported Ag-Cu bimetallic NPs for detection of ultra-small amounts of substance.[59-60]

In a recent study from our group,[25] we reported SERS EF of ~10^7 for Ag-Au microflower (MF) substrates with attomolar level detection of R6G. We demonstrated Ag rich surface having Au underneath, yielded 30 times enhancement than the pure Ag MF for R6G. Therefore, an intriguing study is intended where new alloy combinations with other plasmonically active metals such as Cu would be used to replace Au in search of better SERS performance, but in an economical way. Hence, in this work, we synthesized cost-effective, reproducible Ag-Cu bimetallic alloy MF SERS substrates on a glass coverslip by simple thermolysis of metal alkyl ammonium halide precursor. Subsequently, we varied the reaction temperature and composition of the alloy to discern the optimum condition for highest SERS efficiency from the substrates. With SERS EF of 10^8, 10% Ag-Cu alloy MF produced optimum 50-fold enhancements in SERS spectra as against pure Ag MF, for resonant Raman-active probe molecule R6G. The same substrate showed trace level detection of R6G at very low concentrations such as 10 zM, leading to observation and analysis of SMSERS spectra of R6G.

5A.2. Results and Discussion

5A.2.1. Optimization of reaction temperature

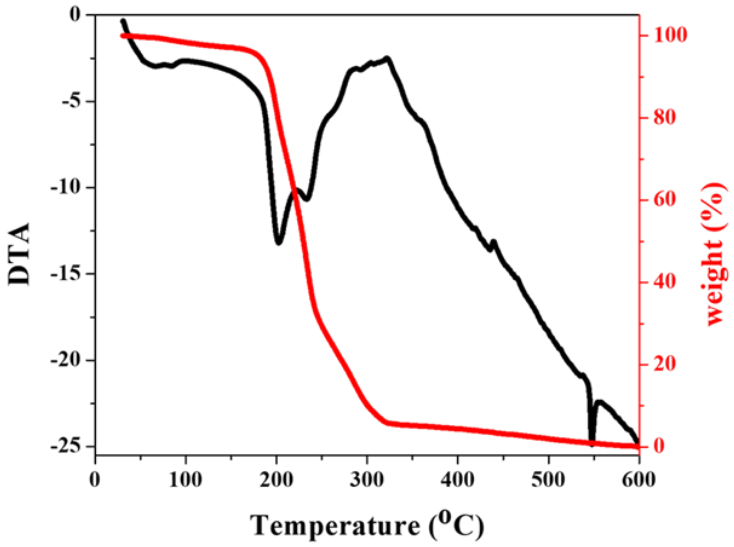

Figure 5A.1. Thermogravimetric Analysis of copper tetra octyl ammonium bromide (CuToABr).

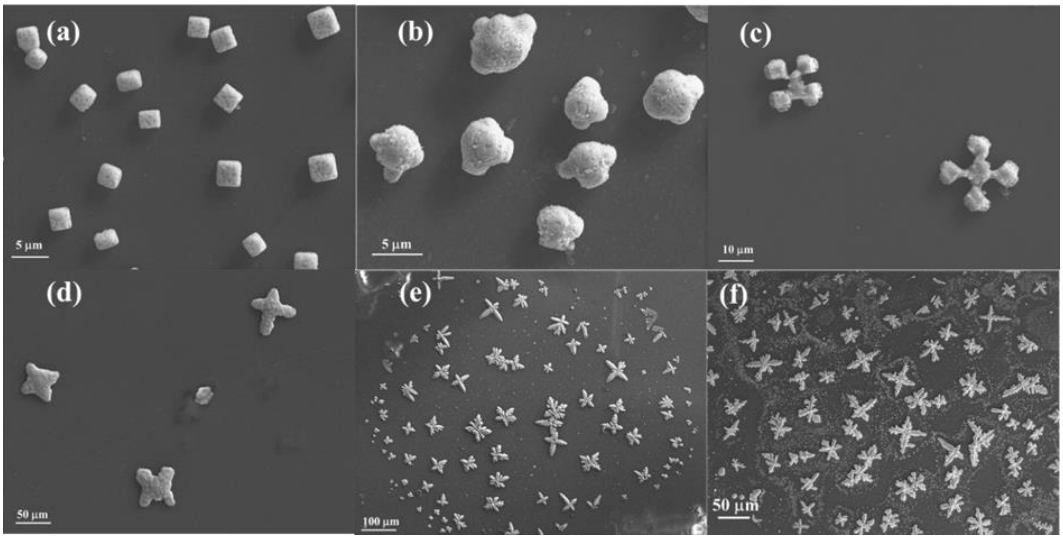

Figure 5A.2. FE-SEM images of 10% Ag-Cu MF at different thermolysis temperatures: (a) 270° C, (b) 290° C, (c) 310° C, (d) 330° C, (e) 350° C and (f) 370° C.

The effect of thermolysis temperature on pure Ag MF formation was previously studied by Mettela *et al*.[61] They have observed the decomposition temperature of Silver tetra octyl Ammonium bromide (AgToABr) around 170 °C from the Thermogravimetric (TGA) analysis. Accordingly, best Ag MFs formation was witnessed at higher temperature of ~ 250 °C, on studying the growth of the structure with sequential increase of temperature. Similarly, in quest of an optimum Ag-Cu bimetallic MF substrate for SERS, a detailed investigation of the role of thermolysis temperature was carried out. At first, when we performed the TGA study of copper tetra octyl Ammonium bromide (CuToABr), unlike AgToABr, it was observed that the decay started around 200 °C and continued till 370 °C (**Figure 5A.1**). This observation steered us to vary the reaction temperature for formation of 10% Ag-Cu alloy MFs from 250 °C to 350 °C, with an interval of 20 °C. Similar to the pure Ag MF case,[61] we noticed the formation of only nano cubes at lower temperature of 270 °C (**Figure 5A.2a)**. With increase in temperature the size of the cubes was found to increase and they started to aggregate into MFs at ~310 °C, as shown in **Figure 5A.2b & 5A.2c**, respectively. Small, distinct MFs were first seen at 330 °C **(Figure 5A.2d)** and their size increased on further heating at 350 °C as depicted in **Figure 5A.2e**, indicating the critical role of the thermolysis temperature in obtaining the correct morphology of the Ag-Cu alloy MF. As expected, temperatures higher than 350 °C didn't illustrate any change in size or shape of alloy MF, as can be seen from **Figure 5A.2e.**

5A.2.2. FE-SEM studies of MFs of different composition

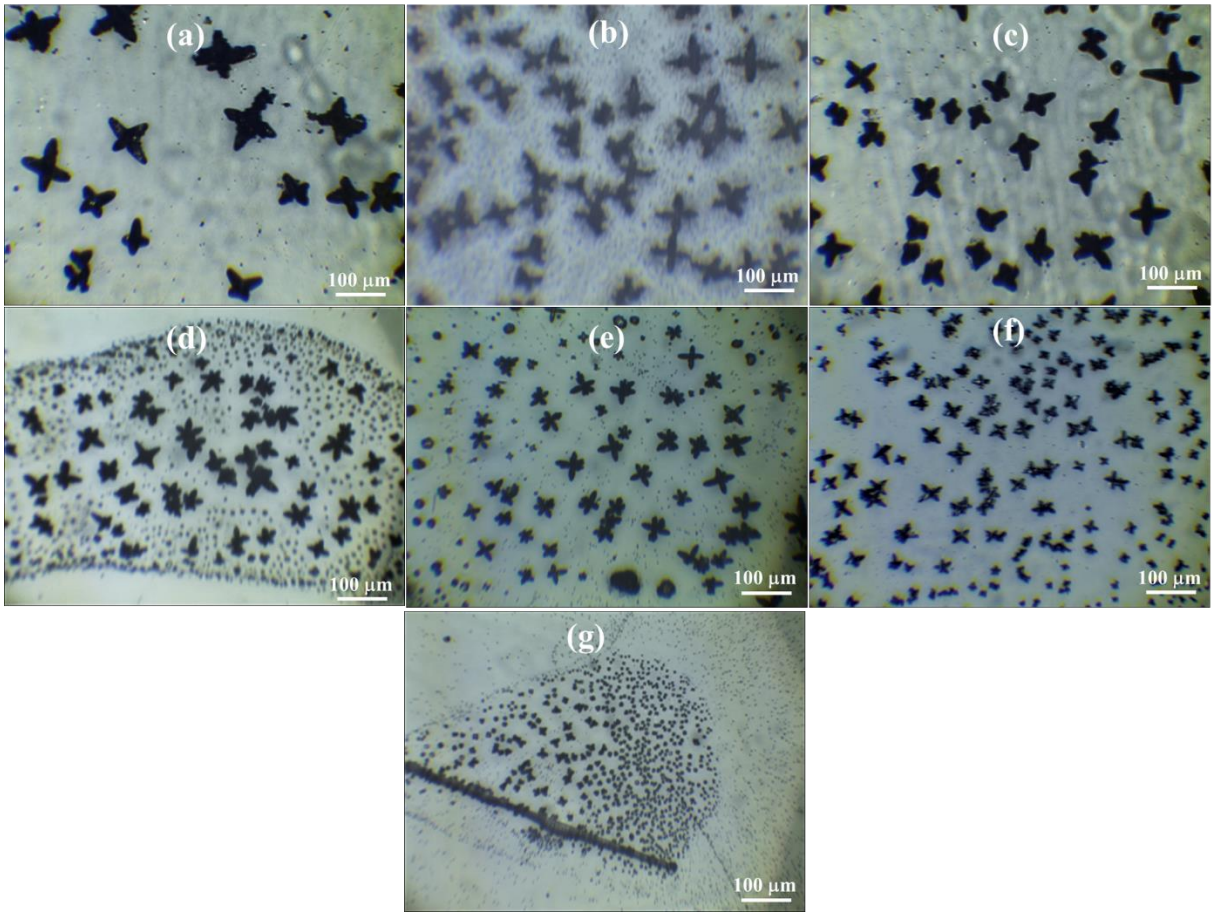

Figure 5A.3. Optical images collected under Raman microscope, using 10X Objective: (a) pure Ag MF, and alloy MFs: (b) 1% Cu, (c) 5% Cu, (d) 7.5% Cu, (e) 10% Cu, (f) 12.5% Cu and (g) 15% Cu.

Subsequently, bimetallic Ag-Cu MFs with various Cu percentages were synthesized varying from 1% Cu to 15% Cu and their surface morphology and shape were studied under Raman microscope (**Figure 5A.3**) and using FE-SEM (**Figure 5A.4 & 5A.5**). While flower-like structures containing 4 - 6 arms, were produced in each case, but the average size of the MF was found to be significantly different as we varied the composition. The maximum size was determined as ~66 µm for Pure Ag MF (**Figure 5A.4a & 5A.5a).** However, it can be clearly seen that the size of the alloy MFs decreased (from 66 µm to 19 µm) with an increase in copper composition in the alloy (**Figure 5A.4b-h & 5A.5b-h).**[53] The average sizes of 1%, 5%, 7.5%, 10%, 12.5% and 15% alloy micro flowers were determined to be ~ 62, 58, 55, 45, 32 and 19 µm, respectively (**Figure 5A.6a-g).** But, at 15% Cu, we observed the formation of nanospheres in addition to MFs (**Figure 5A.4g**). Moreover, it would be evident later that the alloy MFs

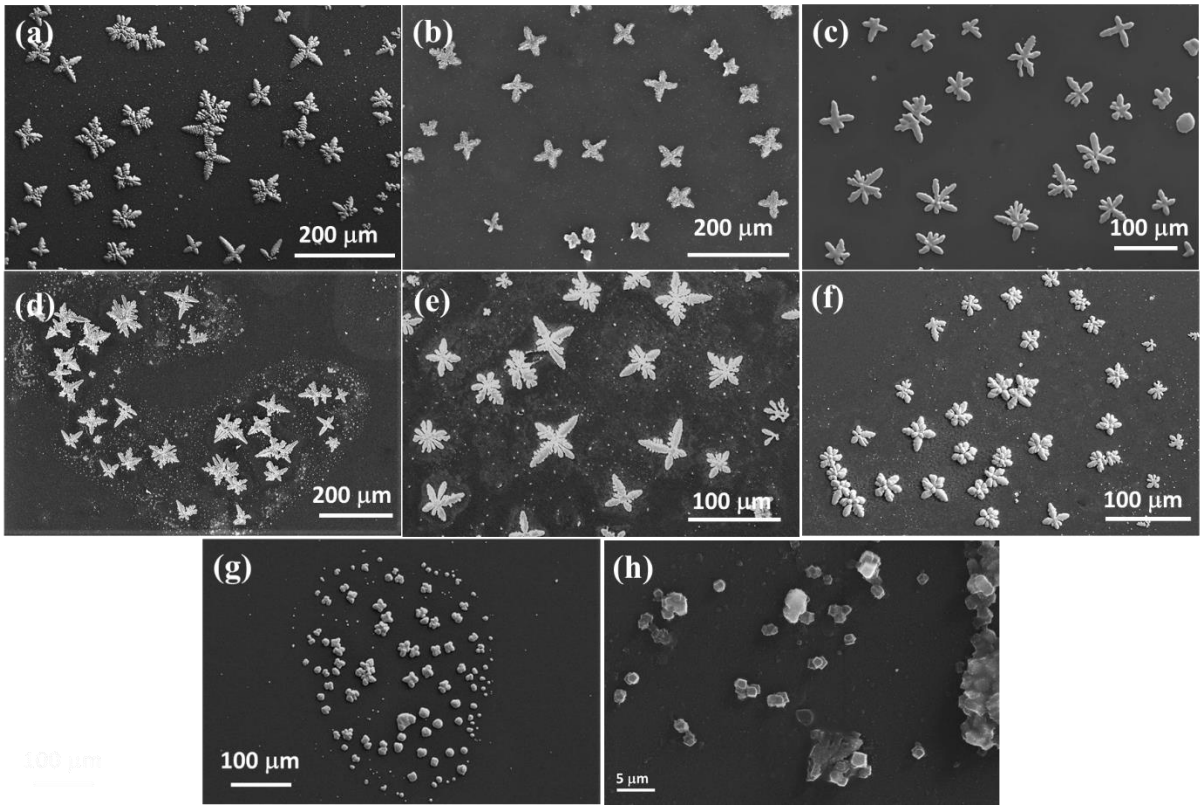

Figure 5A.4. SEM images of (a) pure Ag MF, and alloy MFs: (b) 1% Cu, (c) 5% Cu, (d) 7.5% Cu, (e) 10% Cu, (f) 12.5% Cu, (g) 15% Cu and (h) 20% Cu.

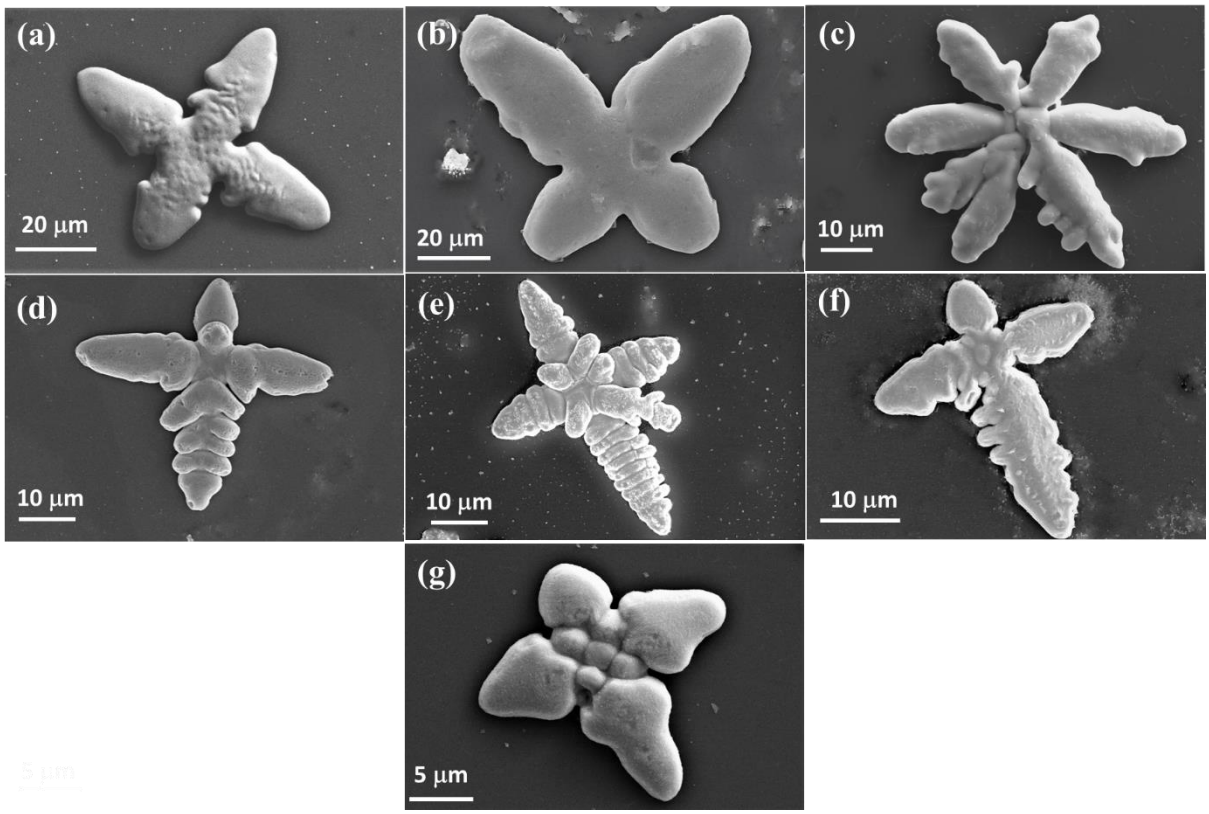

Figure 5A.5. FE-SEM images of (a) Pure Ag MF and alloy MFs at different copper compositions: (b) 1%, (c) 5%, (d) 7.5%, (e) 10%, (f) 12.5% and (g) 15%.

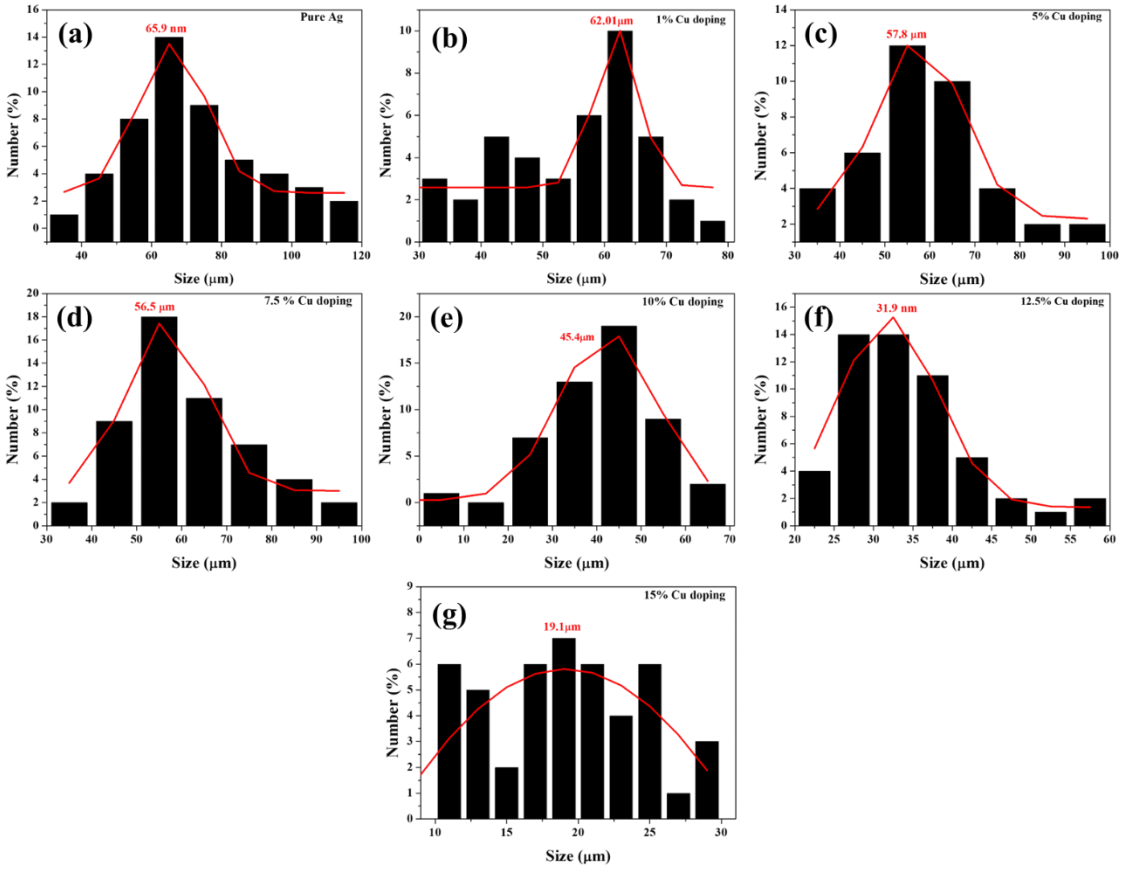

Figure 5A.6. Average size of (a) pure Ag MF, and alloy MFs: (b) 1% Cu, (c) 5% Cu, (d) 7.5% Cu, (e) 10% Cu, (f) 12.5% Cu and (g) 15% Cu.

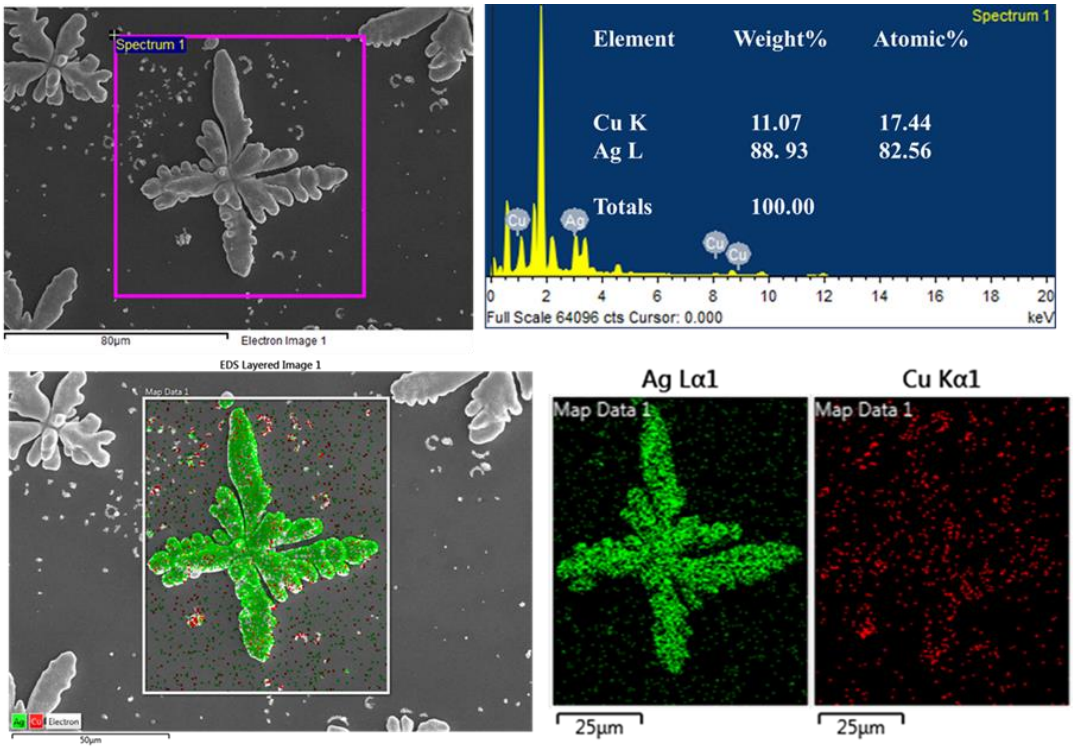

Figure 5A.7. EDX and elemental mapping of 10% Ag-Cu MF.

prepared at 350 °C produced maximum SERS signal (*vide infra*). Hence, we carried out our synthesis at 350 °C for all bimetallic Ag-Cu MFs, where copper percentage was varied from 1% to 20%. However, any attempts of making alloys with more than 15% of Cu led only to the formation of nanospheres instead of MFs, as can be seen from **Figure 5A.4h**. Moreover, the weight percentage of Ag and Cu obtained from the elemental mapping data of EDX experiment on 10% Ag-Cu MF, confirmed the successful alloy formation (**Figure 5A.7)**.

5A.2.3. XRD, XRF and optical characterization of the MFs

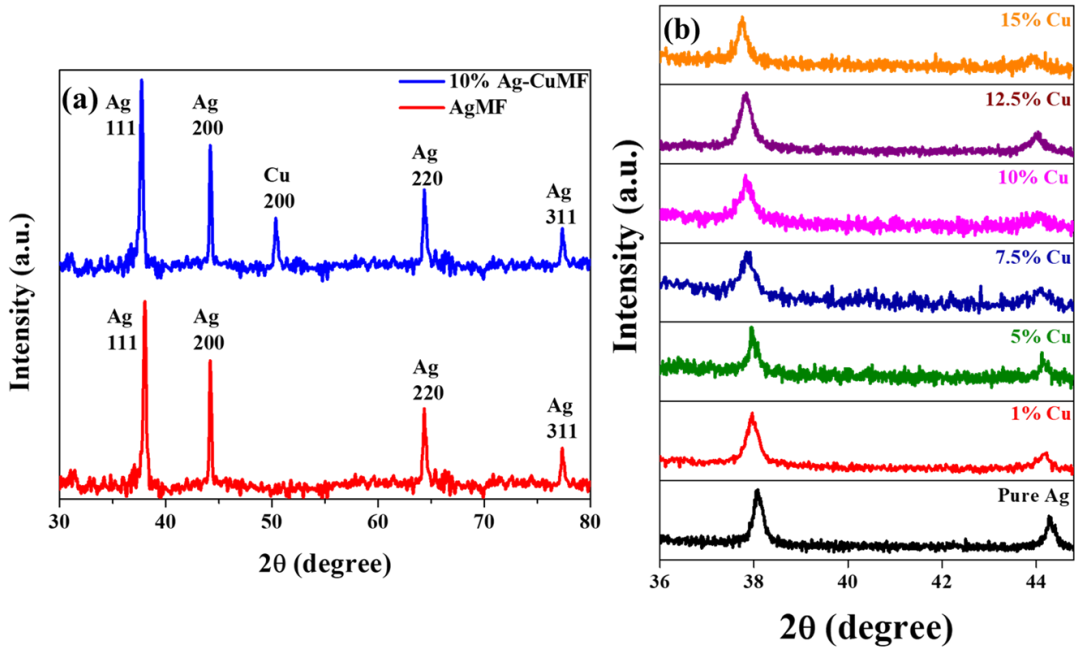

Figure 5A.8. (a) XRD patterns of pure Ag MF and 10% Ag-Cu MF and (b) XRD patterns of Pure Ag and different % composition of Ag-Cu MFs from 36° 2θ to 45° 2θ portraying peak shift and broadening.

We performed X-Ray diffraction studies on the pure Ag and Ag-Cu alloy substrates for structural characterization. The XRD pattern of pure Ag MF **(Figure 5A.8a)** showed peaks at 2θ values of 38.1°, 44.2°, 64.3°, and 77.8° corresponding to the (111), (200), (220), and (311) planes of crystalline Ag, respectively.[62] In the XRD pattern of 10% Ag-Cu MF, we observed an additional peak at 2θ value of 50.5° corresponding to the Cu (200) plane, indicating the Ag-Cu alloy formation. Moreover, we also performed a slow scan from 35° - 45° 2θ range to detect any alteration in the Ag peak, upon increasing Cu percentage in the alloy. Interestingly, we noticed a small

shift in peak at 38.1° 2θ and small broadening in the peak at 44.2° 2θ with increasing Cu percentage, indicating the successful formation of Ag-Cu alloy **(Figure 5A.8b).**

Further, XRF studies were performed on pure Ag and bimetallic alloy MFs to understand the bulk elemental composition of the substrates (**Figure 5A.9a-c**). The characteristic Ag $L_{\alpha 1}$ and Ag $L_{\beta 1}$ were observed peaks at 2.98 and 3.15 keV as shown in the **Figure 5A.9a**[25]**,** Ag $K_{\alpha 1}$, Ag $K_{\beta 1}$, and Ag $K_{\beta 2}$ peaks were observed at 22, 24.9, and 25.4 keV respectively for pure Ag and Ag-Cu bimetallic flowers as shown in **Figure 5A.9b**.[63] The pure Ag MFs didn't show any Cu $K_{\alpha 1}$ or Cu $K_{\beta 1}$ peak, as expected. Upon increasing the composition of Cu, we noticed a systematic decrease in intensity of Ag $K_{\alpha 1}$, Ag $K_{\beta 1}$, and Ag $K_{\beta 2}$ peaks and an increase in the intensity of Cu $K_{\alpha 1}$ and Cu $K_{\beta 1}$ peak as demonstrated in **Figure 5A.9a** and **Figure 5A.9c** respectively, confirming successful alloying. The Ag and Cu elemental compositions obtained from ED-XRF are presented in **Table 5A.1**, which shows a good agreement between the feed and the resulting ratios.

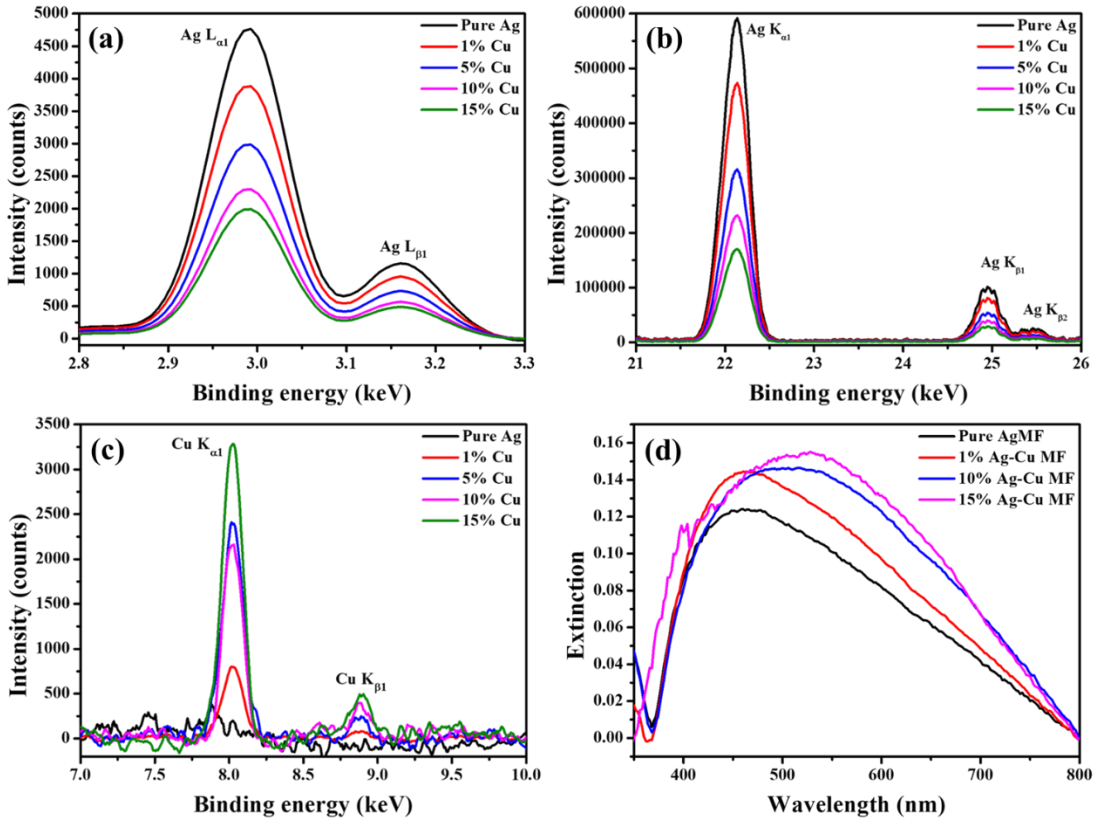

Figure 5A.9. ED-XRF spectra of different MFs with increasing percentage of copper: (a) Ag L_{α}, (b) Ag K_{α}, (c) Cu K_{α} and (d) The extinction spectra of the microflowers with increasing % of Cu.

Table 5A.1. The elemental composition of Ag and Cu in pure Ag and Ag-Cu MFs obtained through ED-XRF.

Sample	Composition	
	Ag	Cu
Pure Ag	100%	0%
1% Cu	98.51%	1.49%
5% Cu	95.96%	4.04%
7.5% Cu	92.88%	7.12%
10% Cu	88.38%	11.62%
12.5% Cu	85.99	13.51%
15% Cu	83.73	16.27%

UV-Visible spectrophotometry was also used to measure the extinction spectra (**Figure 5A.9d**) of the microflowers. It is already known that spherical Ag and Cu nanoparticles display surface plasmon resonance (SPR) bands at ≈400 and ≈600 nm, respectively.[64] Although in our case, for pure Ag MF, a redshifted broad SPR band with a peak at 460 nm was observed. This red shift and broadening of the SPR band in comparison with pure Ag nanoparticle might had been resulted from the aggregation of smaller particles into larger particles during the MF formation and their wide size distribution. In comparison to pure Ag MF, we observed a further broadening and red shift in the SPR band of the alloy MF with increase in Cu content, confirming the Ag-Cu alloy MF formation successfully. However, the obtained peak position at ≈510 nm for 10% alloy MF stated that the contribution of Ag component was much larger in the Ag rich Ag-Cu alloy MF substrates.

5A.2.4. Surface analysis of MFs using XPS technique

XPS studies were performed on Ag and Ag-Cu MF substrates to investigate the surface composition and valence states of Ag and Cu. **Figure 5A.10a** shows the XPS survey spectra of pure Ag and Ag-Cu MF with increasing % composition of Cu, in which the characteristic peaks of C, O, Ag and Cu were seen. The peaks were calibrated using the C 1s peak at 284.4eV. The high-resolution narrow scan spectra of Ag (**Figure 5A.10b**) in both pure Ag and alloy substrates showed the characteristic peaks at 367.6 and 373.6 eV corresponding to Ag $3d_{5/2}$ and $3d_{3/2}$, confirming the oxidation state of Ag as metallic

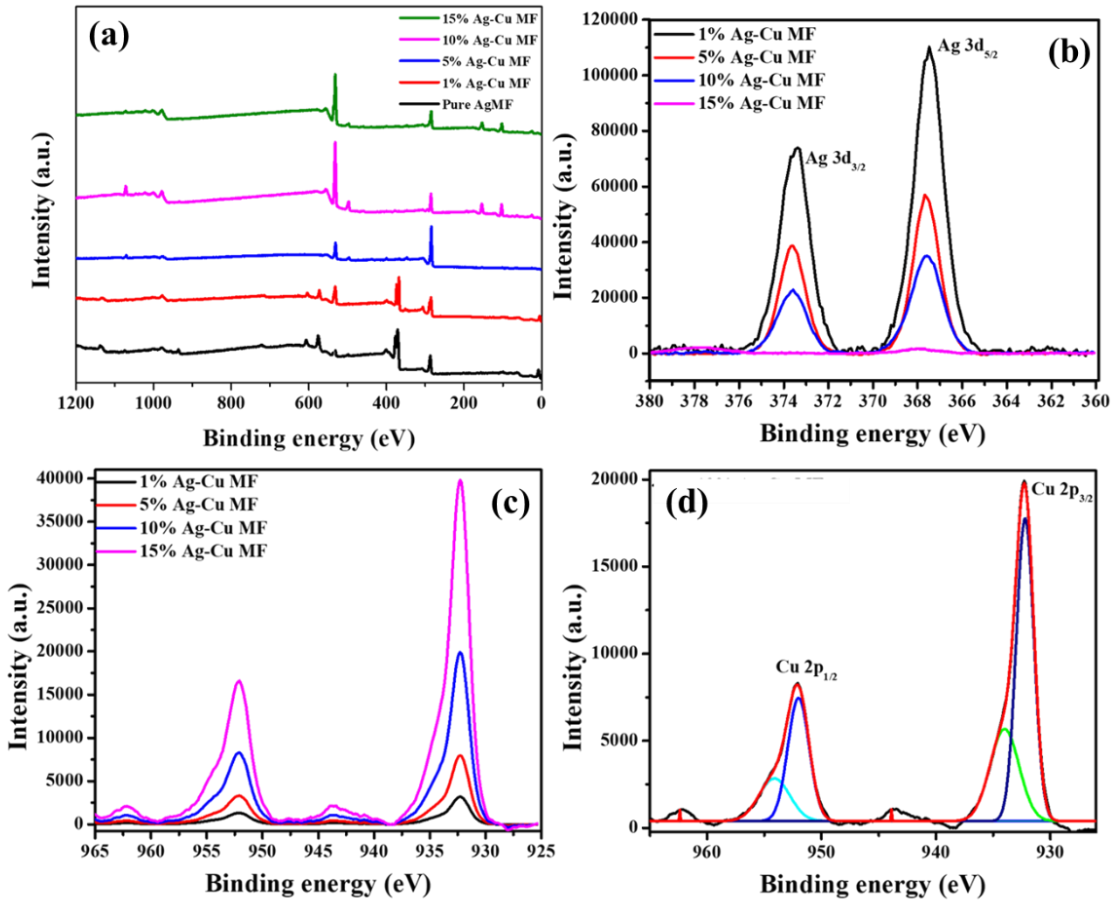

Figure 5A.10. (a) XPS survey spectra of pure Ag and Ag-Cu MF; high-resolution XPS spectra of (b) Ag 3d and (c) Cu 2p with increasing copper % composition: (d) deconvolution of high-resolution Asymmetric XPS spectra of Cu 2p peak of Ag-Cu MFs.

Ag^0.[53,62] Later, we collected the XPS spectra of alloy substrates with increasing the percentage composition of Cu, we noticed a decrease in peak intensity of Ag 3d orbital (**Figure 5A.10a**) with an increase in the peak intensity for Cu 2p orbital (**Figure 5A.10c**), exactly in an opposite way. Moreover, when we collected the high-resolution spectrum of copper for Ag-Cu alloy substrate, it showed two asymmetric peaks at 952.3 and 932.2 eV (**Figure 5A.10d**). The deconvolution of these peaks indicated Cu in both elemental and oxidized states as Cu^0 and Cu^{+2}. Because, we observed the presence of spin-orbit doublets of Cu $2p_{1/2}$ and Cu $2p_{3/2}$ at two different binding energies 932.2 and 951.9 eV for Cu^0; whereas 934.7 and 954.8 eV for Cu^{+2}.[53] However, in both the peaks the peak intensity of Cu^{+2} was found to be lower than Cu^0, indicating the formation of Cu^{+2} in smaller quantities compared to Cu^0.[62]. **Table 5A.2.** summarizes the surface

elemental compositions of the various microflower substrates, as XPS was a powerful technique to probe the surface composition within a depth of 2 nm. The results obtained from **Figure 5A.10** and **Table 5A.2.** clearly showed that Cu composition at the surface was not increased linearly as per feed ratio, rather a much higher percentage of Cu in each composition, indicated a Cu rich surface in the alloy.

Table 5A.2. Surface atomic composition of Ag and Cu in MF substrates, as obtained from XPS.

Sample	Atomic % of Ag	Atomic % of Cu	Ag:Cu Ratio
Pure AgMF	100	0	1:0
1% Ag-CuMF	90.84	9.16	1:0.10
5% Ag-CuMF	26.96	73.04	1:2.7
10% Ag-CuMF	18	82	1:4.55
15% Ag-CuMF	12.48	87.52	1:7.01

5A.2.5. SERS Studies

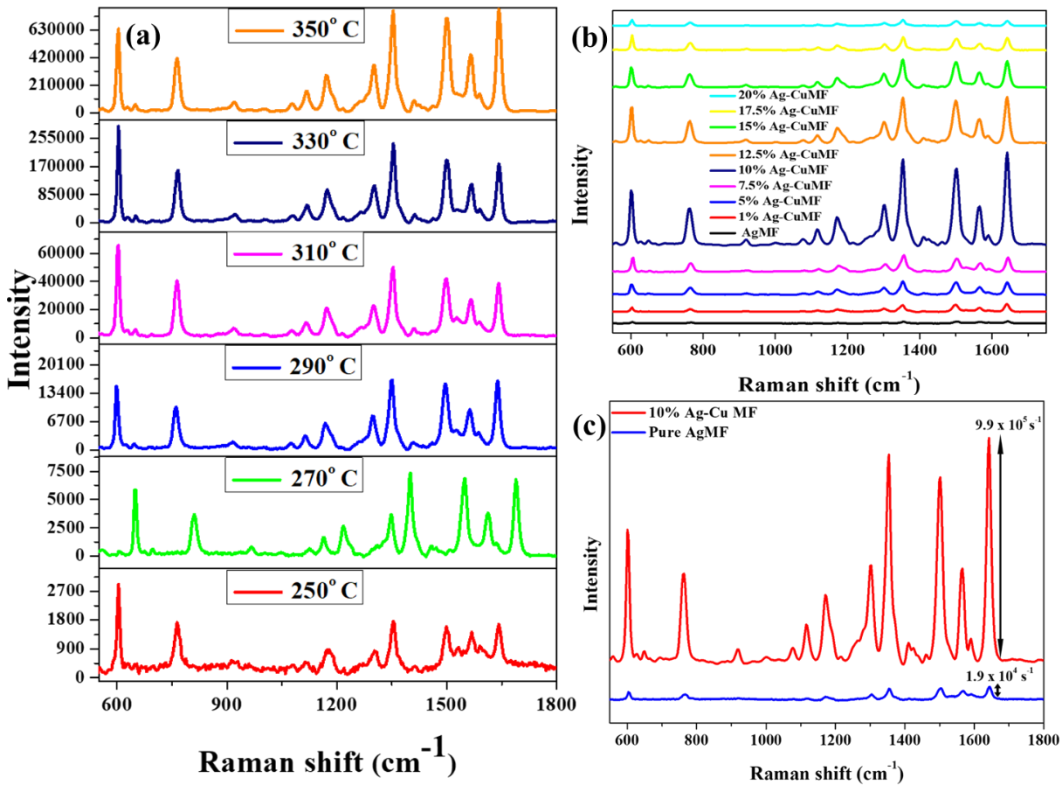

Figure 5A.11. (a) SERS spectra of on 10% Ag-Cu MFs synthesized at different temperatures, (b) comparative SERS spectra of R 6G on different compositions of MFs synthesized (c) Comparison of SERS spectra of R6G obtained from pure AgMF and 10% Ag-Cu MF. All spectra are obtained with 1 s exposure time along with 30 accumulations, after excitation with 532 nm laser with average power 13 μW.

To study the efficacy of bimetallic MFs as SERS substrates, we used R6G as the analyte molecule, being resonant scatterers at our excitation wavelength of 532 nm. 1 μM R6G solution (in methanol) was drop casted on freshly prepared Ag and alloy MF substrates, followed by an excitation with laser light. As mentioned earlier, during optimization of reaction temperature for the MF preparation, we performed SERS studies on MFs synthesized at all temperatures and observed that the maximum SERS signal for R6G was obtained from the substrates synthesized at 350 °C, as shown in **Figure 5A.11a** (*vide supra*). Subsequently, we compared the SERS efficacy of alloy MFs of different compositions against pure Ag MF prepared at 350 °C. It was evident that Ag-Cu alloy MFs contributed to significantly higher SERS signal for R6G compared to the pure Ag MFs (**Figure 5A.11b**). Notably, with respect to the 1650 cm^{-1} peak of R6G, we recorded a significant ~50-fold enhancement in the peak intensity with 10% Ag-Cu alloy against pure Ag substrate (**Figure 5A.11c**). As can be inferred from this result, the maximum SERS signal was recorded with 10% alloy, rendering it as the best possible Ag-Cu alloy MF substrate in this study. Beyond 10% Cu, the substrates were formed with less rigidity affecting the SERS efficacy with concomitant decrease in the signal.

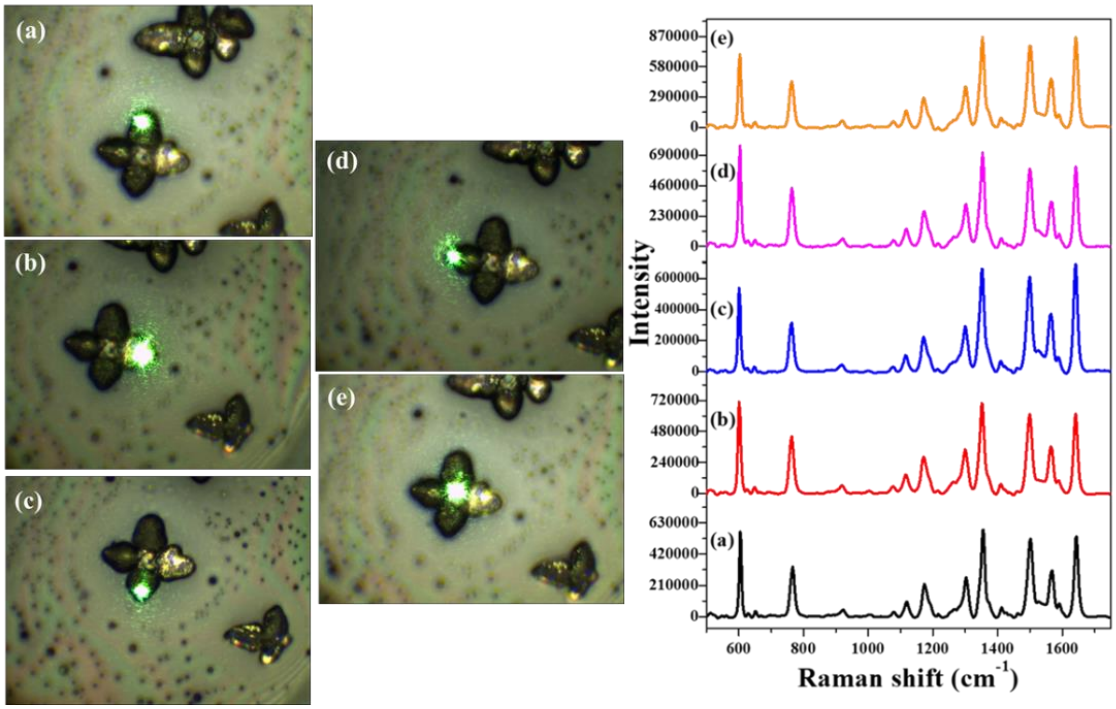

Figure 5A.12. SERS spectra of R6G, collected from different parts of the flower. The alphabets (a-e) marked on the optical image corresponds to the marking on SERS spectra which depicts the intensity variation across different parts of 10% Ag-Cu MF.

We also checked if there was any variation in the signal intensity obtained from different parts of a MF substrate. For this, we collected SERS spectra at different parts of a given MF and observed that the intensities were comparable (**Figure 5A.12.**), with slightly higher value from the centre of the MF. Therefore, we have collected Raman spectra from the centre of the MF to maintain uniformity.

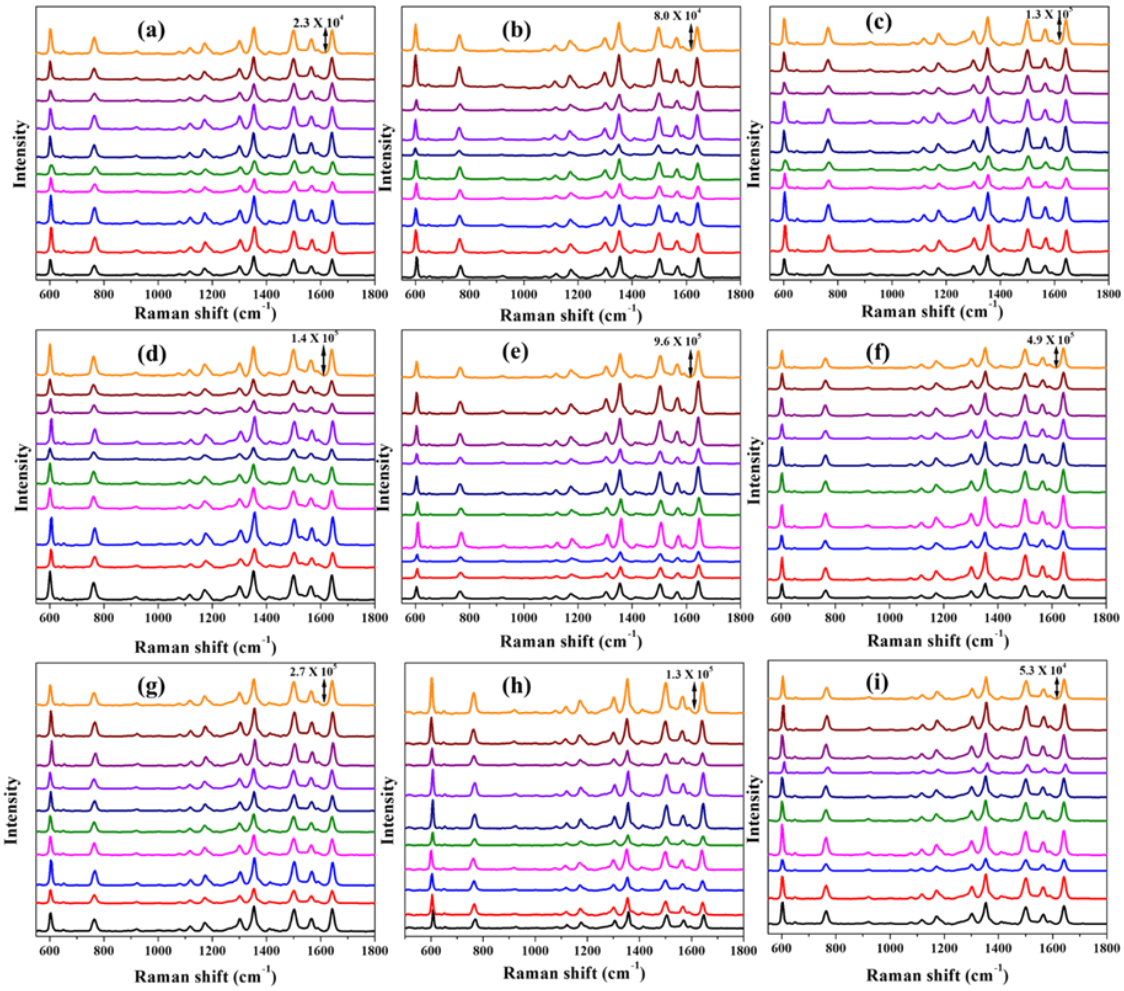

Figure 5A.13. Comparison of SERS intensity between different MFs in a given set using R6G as the reporter molecule. (a) Pure Ag, (b) 1%, (c) 5%, (d) 7.5%, (e) 10%, (f) 12.5%, (g) 15%, (h) 17.5% and (i) 20% Cu. In each of the above sets 10 different SERS spectrum was shown, as collected from different MFs present in a same set. The range of the SERS Intensities (for the representative 1650 cm^{-1} peak) across different spectrum, are as follows: Ag MF: 1.8-2.4 x 10^4, 1%: 5.1-8.9 x 10^4, 5%: 0.7-1.3 x 10^5, 7.5%: 1.06-1.58 x 10^5, 10%: 8.9-9.7 x 10^5, 12.5%: 3.8-5.1 x 10^5, 15%: 2.4-3.1 x 10^5, 17.5%: 0.8-1.5 x 10^5 and 20%: 4.6-6.2 x 10^4. It can be clearly seen that the order of magnitude is same for different spectrum in each set, although there are variations in the absolute intensity, as expected.

We have also compared the efficacy of different MFs in a given set, by measuring SERS intensity of R6G from different MF substrates. As expected, we observed a small variation in SERS intensities with no change in order of magnitude, as shown in **Figure**

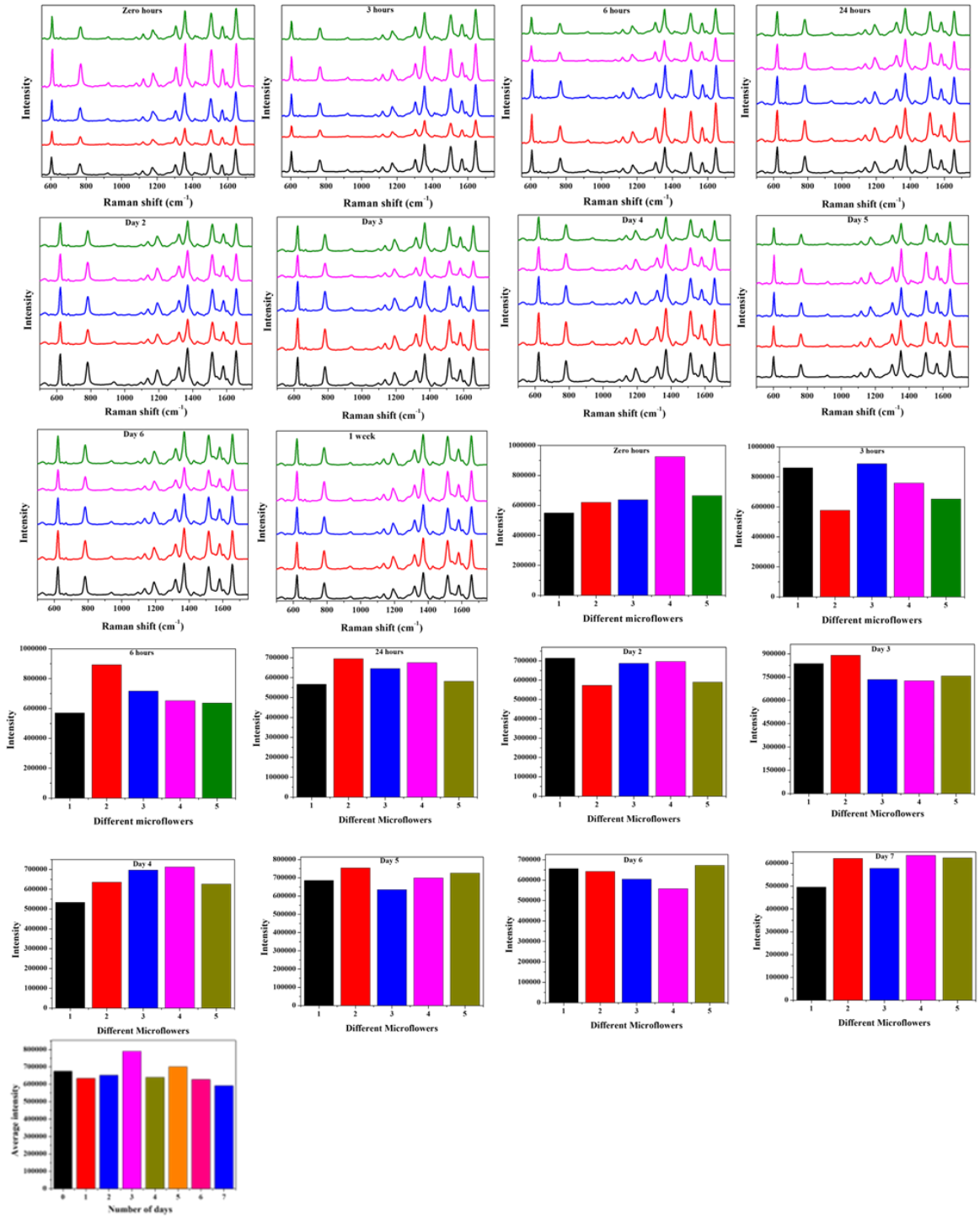

Figure 5A.14. SERS spectra of R6G adsorbed on 10% Ag-Cu MFs at different time intervals (0 hours, 3 hours, 6 hours, 24 hours, 2 days, 3 days, 4 days, 5 days, 6 days and a week) to see if there is any degradation of the substrates and the histograms corresponds the same. The final bar plot showing the average values of the SERS intensities from different 10% Ag-Cu MFs for a given day and comparing them against different days.

5A.13. Further, we carried out SERS experiments as a function of time, to find out if there is any degradation of the substrates (**Figure 5A.14**). For this, different sets of

pure Ag and 10% alloy MFs were prepared and used at different time intervals. The pristine microflowers were reduced by $NaBH_4$ and kept untouched. R6G was only loaded on the substrate, just before the collection of spectra. In each set, randomly 5 different microflowers were selected to collect R6G SERS spectra. In each case, the bar plot (**Figure 5A.14**) showed the Raman intensity of representative 1650 cm^{-1} peak of the corresponding spectra. We have also calculated the average values of the SERS intensities from different MFs for a given day and compared them against different days. It could be clearly seen from the **Figure 5A.14**, that up to 1 week, there was no degradation of the 10% Ag-Cu alloy substrate as the intensities were comparable. We observed that SERS intensities of R6G remained comparable up to 1 week for 10% Ag-Cu alloy MF with slight variation across different microflowers suggesting no visible degradation of the SERS substrates. Moreover, as presented in **Figure 5A.15.** 10% alloy MF was successfully employed to obtain clear and resolved characteristic peaks of R6G at an ultralow 10^{-20} M (10 zM) concentration, indicating the unprecedented efficiency of Ag-Cu alloy MFs, superseding the efficiency of similar Ag-Au MFs presented in our earlier report.[25]

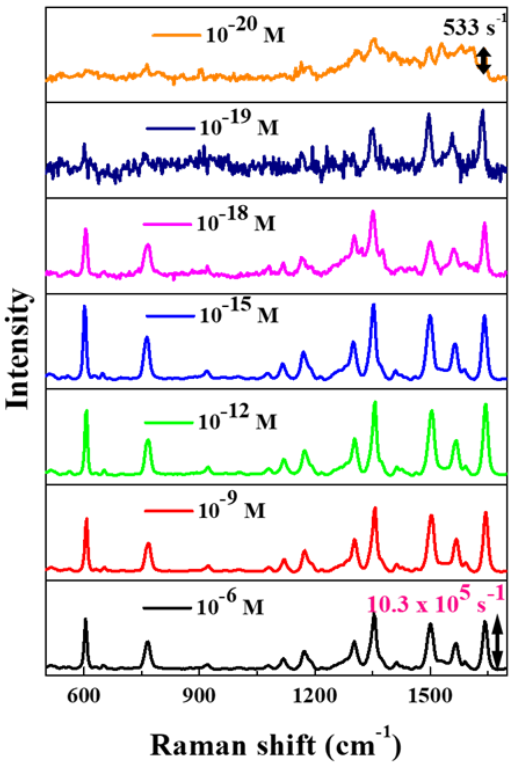

Figure 5A.15. Zeptomolar level SERS based detection of R6G using 10% Ag-Cu MF.

5A.2.6. Calculation of Enhancement factor (EF)

SERS enhancement factor (EF) of the MF substrates was obtained by using non-resonant and non-fluorescent reporter molecule 1,2,3-benzotriazole (BTA) instead of R6G, as its strong fluorescence denied the collection of Raman signals in bulk at our experimental conditions. The method to calculate the SERS EF relies on the relative measure of the number of analyte molecules on SERS substrate that yields the similar Raman intensity under bulk measurement.

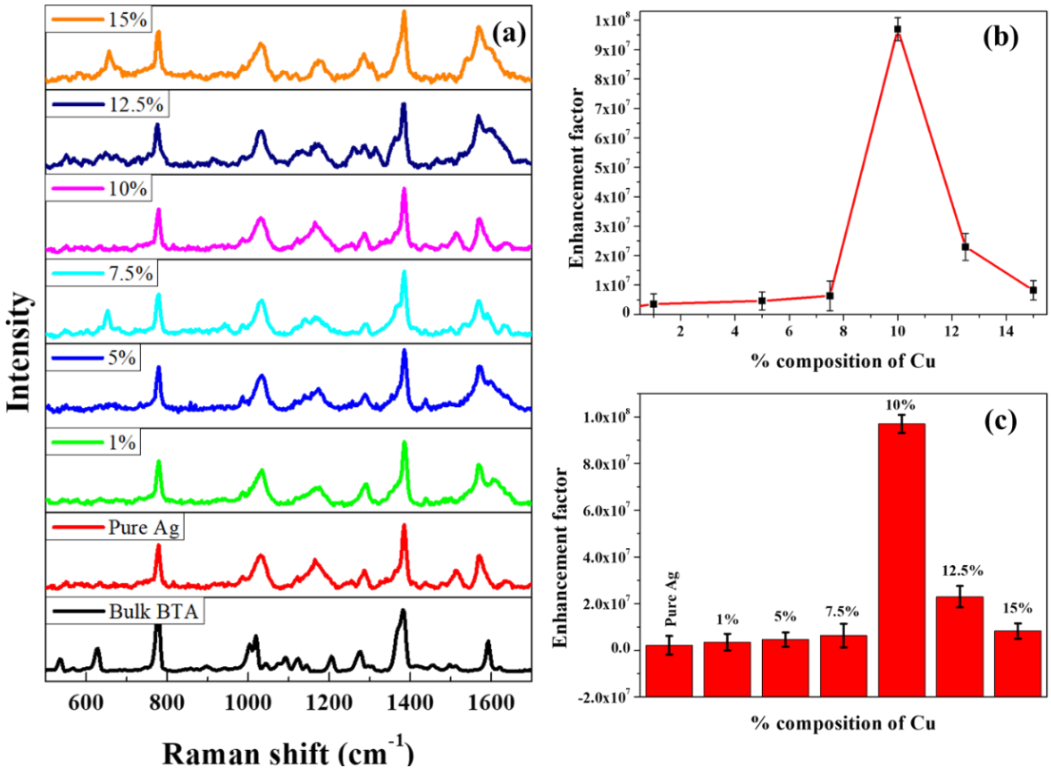

Figure 5A.16. Bulk and SERS Raman spectra of BTA on different compositions of Ag-Cu MFs, (b) plot of enhancement factor v/s Cu composition and (c) represents the histogram for the same.

The detailed method to obtain EF, can be found below. Briefly, when a small amount of solid BTA powder sample was positioned in a coverslip and excited with laser radiation, it yielded a signal comparable to that observed from a single microflower loaded with 10 µM of BTA solution in methanol (**Figure 5A.16.**). Subsequently, the SERS EF was calculated by using the equation: $\mathbf{EF = (I_{SERS}/I_{Raman}) \times (N_{Bulk}/N_{Surface})}$, Where I_{SERS} and I_{Raman} were the intensities of a band in SERS and normal Raman spectra of the BTA molecule, respectively. The number of analyte molecules illuminated under the laser beam in normal Raman (bulk) and SERS experiments were referred as N_{bulk}

and $N_{surface}$ respectively. For a particular composition of the MF, the EF was calculated from 15 randomly selected MFs on the same substrate. And, the calculated average EF for different MFs is listed in **Table 5A.3**. As anticipated, a significant two order of magnitude higher EF was obtained for 10% Ag-Cu alloy MF against pure Ag MF (**Figure 5A.16. & Table 5A.3**). Enhancement factor is calculated as follows:

$$\mathbf{EF = (I_{SERS} / I_{Raman}) \times (N_{bulk} / N_{surface})}$$

Where, I_{SERS} and I_{Raman} are the intensities of a band in SERS and normal Raman of the BTA molecule, respectively. The number of analyte molecules which are illuminated under the laser beam in normal Raman (bulk) and SERS experiments are termed as N_{bulk} and $N_{surface}$, respectively.

We have used the following experimental conditions to acquire the Raman spectra.

Laser beam spot size (diameter): 2 µm, radius (r) = 1 µm

Rayleigh range (h) = $\frac{\pi\omega_0{}^2}{\lambda} = \frac{3.14 \times 4 \times 10^{-12} m^2}{532 \times 10^{-9} m} = 23.6\ \mu m$

= 23.6 x 10^{-4} cm

Laser spot area = A = πr^2 = 3.14 x 10^{-8} cm^2

Focal volume = A x h = 74.1 x 10^{-12} cc

$N_{surface}$ is the product of C, the surface density of BTA and A, the laser spot area respectively.

Surface density of BTA for $N_{surface}$ calculation:

40 µL of 1 µM BTA solution was spreaded over a coverslip containing the microflowers, having area of ~4 cm^2. This yielded the surface density of BTA on the SERS substrate is 6 x 10^{12} molecules/cm^2, assuming homogeneous spreading.

So, $N_{surface}$ = 6 x 10^{12} x 3.14 x 10^{-8} = 18.8 x 10^4.

Raman spectrum of solid BTA powder is used for N_{bulk} calculation. Considering, density of BTA as 1.36 g/mL and molecular weight 119.127 gm/ mol, number of BTA molecules present in the focal volume (N_{bulk}) is:

$$\mathbf{N_{Bulk} = \frac{Ah\rho}{m} = \frac{74.1 \times 10^{-12} \times 1.36 \times 6.02 \times 10^{23}}{119.127} = 5.1 \times 10^{11}.}$$

so, $\frac{N_{Bulk}}{N_{Surface}} = \mathbf{2.7 \times 10^6}$

I_{SERS}/ I_{Raman} is evaluated to be considering the integrated intensity of BTA, for 2 different bands (740 cm^{-1} and 1348 cm^{-1}) from surface enhanced and normal Raman spectrum as following. The enhancement factors for pure Ag and Ag-Cu microflowers are ~ 10^6 and 10^8, respectively.

Table 5A.3. Average enhancement factor of MFs of different compositions.

Composition	Enhancement factor
Pure AgMF	2.2×10^6
1% Ag-Cu MF	3.5×10^6
5% Ag-Cu MF	4.6×10^6
7.5% Ag-Cu MF	6.3×10^6
10% Ag-Cu MF	9.7×10^7
12.5% Ag-Cu MF	2.3×10^7
15% Ag-Cu MF	8.2×10^6

Table 5A.4. The table shows the SPR Peak Wavelength (λmax), Magnitude of the frequency difference between the Exciting Laser and the SPR Peak (|Δν|), and SERS EF of different microflower substrates.

Sample	λ_{max} (nm)	$\lvert\Delta\nu\rvert$ (cm^{-1})	SERS EF (10^6)
Pure Ag	455	3181.03	2.2×10^6
1% Ag-Cu MF	461	2894.98	3.5×10^6
10 % Ag-Cu MF	509	849.38	9.7×10^7
15% Ag-Cu MF	526	214.41	8.2×10^6

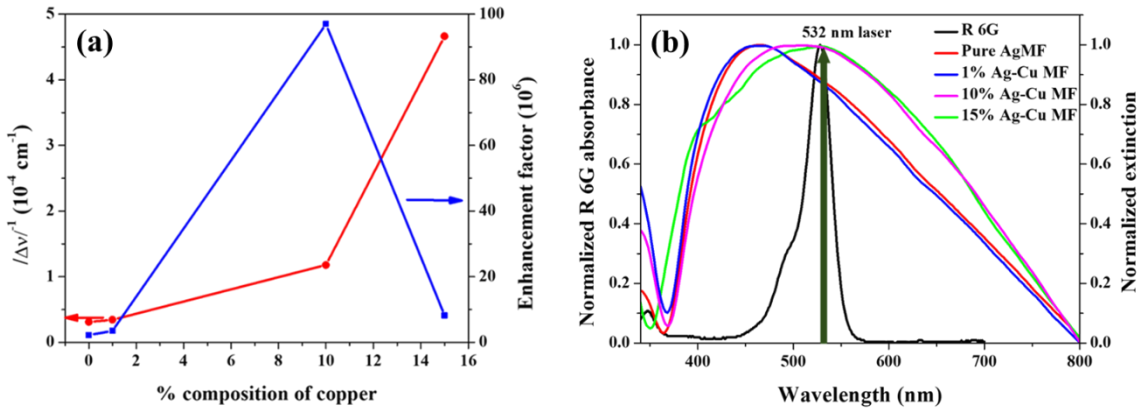

Figure 5A.17. (a) Plot of the SERS EF and $|\Delta\nu|^{-1}$ against the % composition of MF (0 represents pure AgMF) and $\Delta\nu = \nu_l - \nu_{SPR}$, where ν_l = frequency of the excitation laser, ν_{SPR} = frequency of the SPR peak for the Pure Ag and Ag-Cu alloy MFs and (b) The picture shows the SPR of MFs and absorption of R6G.

The excellent efficacy of 10% Ag-Cu alloy MF in SERS detection, can be explained as following. It is known that the EF of metal nanoparticle based SERS substrates is likely to be influenced by the resonance correlation between the SPR peak and the excitation laser wavelength.[65] Following an earlier reported procedure by Kesava Rao *et al.*,[65] for each of the substrates shown in Fig. 3d, we calculated $|\Delta\nu|$ (**Table 5A.4**), where $\Delta\nu = \nu_{Ex} - \nu_{SPR}$; ν_{Ex} corresponds to the frequency of the excitation laser (λ = 532 nm) and ν_{SPR} is the frequency of the SPR peak for each substrate. Subsequently, from the plot of $|\Delta\nu|^{-1}$ along with EF, against % composition of copper (**Figure 5A.17a**), it was found that the maximum EF was obtained with the 10% Ag-Cu alloy substrate having an SPR peak that was slightly blue-shifted with respect to the excitation laser, rather than with the substrate that has a nearly resonant SPR (i.e., with the lowest $\Delta\nu$), eg. with 15% Ag-Cu alloy. However, one must also consider the fact that with sequential increment of Cu in the alloy, the extinction band was found to be broadened (**Figure 5A.17b**). The linewidth of an extinction band of a nanostructure is directly associated to its ability to confine and enhance the incident electromagnetic field.[66] Therefore, a trade-off definitely exists between the two factors: 'resonance' and 'broadening' of the SPR peaks of the substrates, which controls the maximization of the EF. In our case, incorporation of 15% Cu into Ag shifted the SPR peak closer to the excitation wavelength, but concomitantly broadened the extinction peak resulting into much lower EF value. However, at a lower value of Cu, for 10% Ag-Cu alloy substrate, the opposing impacts of the two factors resulted favourably to the maximization of the EF. Secondly, although Cu was a significantly less plasmonic metal compared to Ag, we conjectured this increase in EF with addition of Cu was due to synergistic effect of Cu, securing Ag to remain in its active plasmonic state Ag^0 with no oxidation. Because, we have observed earlier from the XPS data, that the top surface in the Ag-Cu alloy was found to be rich in Cu having Ag underneath.

5A.2.7. Detection of SMSERS event of R6G

Fascinated by the enhanced SERS efficiency of 10% alloy MF with EF of 10^8 and Zeptomolar level detection of R6G, we attempted to detect and explore SMSERS behaviour of R6G. It is a well-established and accepted fact that the fluctuation in SERS

spectra is a characteristic signature of SMSERS, under a strong local electric field.[67] In **Figure 5A.18**, we showed a sequence of 10 spectra, consecutively recorded from the same spot on a 10% alloy MF, with 10 s acquisition time per spectrum for two concentrations of R6G, at 10^{-15} M and 10^{-18} M.

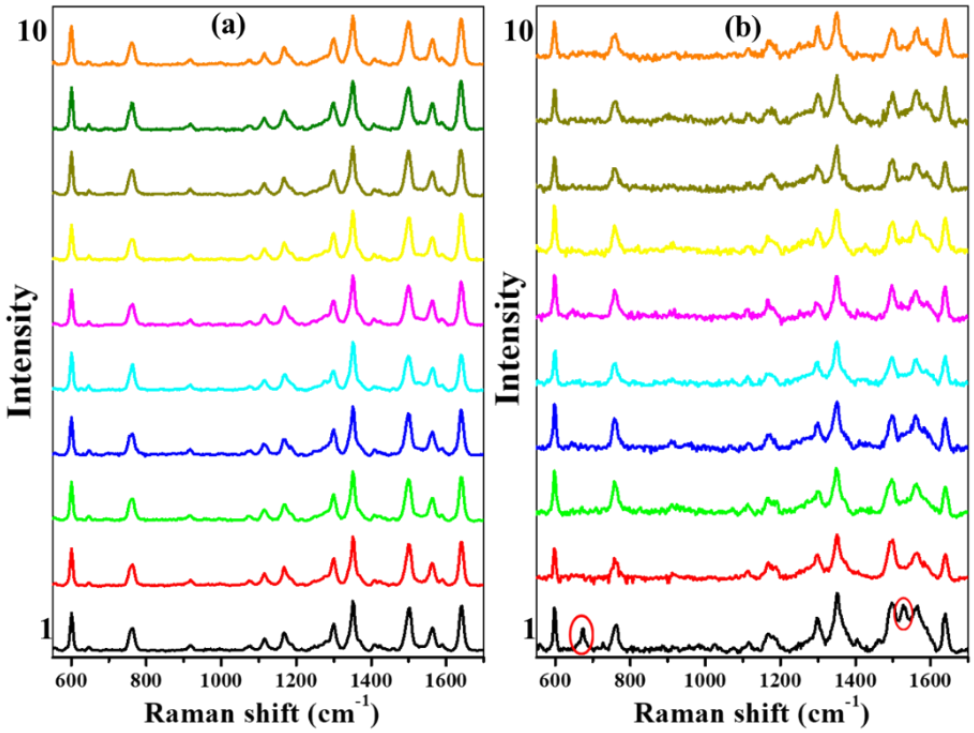

Figure 5A.18. R6G SERS Spectra of (a) 10^{-15} M and (b) 10^{-18} M samples, in a sequence of 10 consecutive acquisitions, with 10 s collection time per acquisition.

When 40 µL of R6G was spread across 4 cm² (area of a coverslip), it could be easily shown that the number of molecules per cm² would be ≈ 6 x 10^3 and ≈ 6 for 10^{-15} M and 10^{-18} M, respectively. Therefore, at our experimental conditions, the single molecule limit was definitely accessible at attomolar level only. As can be seen form **Figure 5A.18a**, we did not observe any fluctuation in the SERS spectra from many-molecule experiment recorded at 10^{-15} M. But, for aM sample, in addition to the normal spectrum of R6G, we observed two other lines at 670 cm^{-1} and 1534 cm^{-1}, which appeared and disappeared at the very beginning of the acquisition (sequence 1, **Figure 5A.18b** and **Figure 5A.19a-b**). R6G contains a very strong External Group Mode (EGM) at 1528 cm^{-1} in IR, which remains very weak or absent in SERS, as the intense bands in Raman for R6G should be sensitive to the core π-electron system (xanthene ring) of

R6G.[68] So, the appearance and disappearance of the 1534 cm^{-1} peak, without changing the intensities of other lines, can be accomplished with small reorientation of the molecule (an attempt by the molecule to walk due to thermal diffusion) subject to the complex field generated at the hot spot.[69] However, minute changes in the inter-particle distance could also lead to similar changes in SERS intensities even in many-molecule conditions. But in our case the average power of the laser was feeble 13 μW and also, we did not observe any fluctuation for many-molecule experiment. So, the possibility of any artifact can be excluded, establishing SMSERS behaviour. Moreover, the other peak at 670 cm^{-1} is a combination peak of two IR modes at 660 and 677 cm^{-1},[68] which again remain very weak or absent in SERS. Agreeably, the deconvolution of the peak actually showed two frequencies at 673 and 684 cm^{-1} (**Figure 5A.18c**), emphasizing a single molecule diffusion.

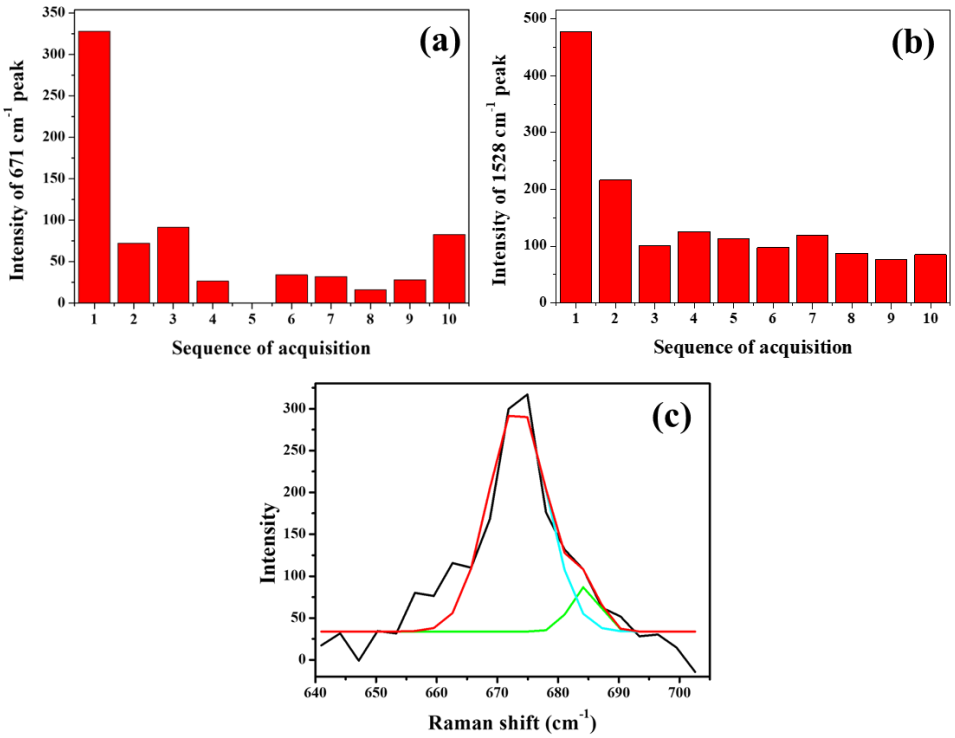

Figure 5A.19. The histogram represents intensity of (a) 671 cm^{-1}, (b) 1528 cm^{-1} peaks obtained for 10^{-18} M sample while recording the SMSERS event. (Note that the number represents the sequence of acquisition) and (c) Deconvolution of SERS peak of R6G at 670 cm^{-1}.

5A.3. Conclusions and Summary

Ag-Cu bimetallic alloy MFs of various compositions were synthesized by simple thermolysis, characterized in detail and successfully used as SERS substrates. With

increase in Cu content in the alloy, the Raman intensity of the reporter molecule R6G gradually increased in comparison to pure Ag MFs, and reached to highest SERS intensity at 10% Cu. The XPS analysis revealed that top surface of the alloys was Cu rich with underneath Ag. It was confirmed that Cu remained in the form of Cu^{0} and partly in the form of Cu^{+2} on the top surface, protecting Ag to remain in its active plasmonic state Ag^{0} with no oxidation. Remarkably, we recorded a significant ~50-fold SERS enhancement for R6G with optimal 10% Ag-Cu alloy against pure Ag substrate, which superseded even the best SERS performance of our earlier reported Ag-Au alloy MF substrates. However, further increase in Cu percentage resulted in less intense Raman signals because any attempt with equal to or more than 15% Cu led only to the formation of nanospheres instead of MFs. 10% Ag-Cu alloy MF registered SERS EF of 10^{8}, a significant two orders of magnitude higher as against EF of 10^{6} from pure Ag MF. The same 10% Ag-Cu MF substrate showed unprecedented SERS efficacy by detecting R6G at ultralow concentrations of 10 zM, opening up the possibility of detecting SMSERS. Intriguingly, the fluctuation in the SERS spectra of R6G at attomolar level, involving two IR peaks of R6G at 670 cm^{-1} and 1528 cm^{-1}, suggested that we observed single molecule diffusion on alloy substrate. Because, an attempt of a single molecule to walk due to thermal diffusion at the hot spot may enable it to experience a complex local field momentarily, which would be absent in SERS for many-molecule experiment. Finally, more cost-effective alloy combinations like Ag-Cu MFs presented in this work, would be worthwhile to explore for tuning the SERS response for sensing important analyte molecules and energy harvesting applications.

Chapter 5B

Bimetallic Ag-Cu alloy SERS substrates as label-free biomedical sensor: femtomolar detection of anticancer drug Mitoxantrone with multiplexing

In the previous chapter, we demonstrated how the SERS efficiency can be significantly enhanced by tuning the surface composition of the substrate resulting in the collection of a Raman spectra from a single molecule. Here, we have studied the role of excitation wavelength on SERS, resulting in phenomena like SERRS and its successful demonstration in ultra-sensitive and multiplexed detection of anti-cancer drugs Mitoxantrone and Doxorubicin. This chapter is based on the following paper, S. Kaja, A. V. Mathews, V. V. K. Venuganti, and A. Nag; Bimetallic Ag–Cu Alloy SERS Substrates as Label-Free Biomedical Sensors: Femtomolar Detection of Anticancer Drug Mitoxantrone with Multiplexing, Langmuir., 2023, 39, 15, 5591-5601.

5B.1. Introduction

Mitoxantrone (MTO) is a synthetic anthracycline derivative (1,4-dihydroxy-5,8-bis[2-(2-hydroxyethyl)-amino] ethylamino-9,10-anthracenedione dihydrochloride), which is prolifically used in the treatment of non-Hodgkin's lymphoma,[1] acute myeloid leukemia,[2] metastatic breast cancer [3] and ovarian cancer.[4] In addition, it is also used to treat multiple sclerosis.[5] MTO is usually administered intravenously to the patients during chemotherapy, and the dosage varies from person to person. The dosage, however, shouldn't exceed 2mg/mL, otherwise severe side effects such as anaemia, alopecia, tachycardia, severe myelosuppression, congestive heart failure etc. can be observed.[6] The effectiveness of chemotherapy depends on the availability of MTO at the target site. Normally, pharmacokinetic analysis of a chemotherapeutic is performed by withdrawing blood samples at regular time intervals in preclinical and clinical models. Therefore, the analytical method chosen to quantify the chemotherapeutic within the blood sample has to provide lowest limit of quantification and detection. In recent past, several optical and non-optical analytical methods have been used for the quantitative determination of MTO such as electrochemistry,[7] voltammetry,[8] HPLC,[9] radio-immunoassays,[10] electrophoresis,[11] resonance Rayleigh scattering,[12] chemiluminescence,[13] fluorescence [14,15] and surface-enhanced Raman scattering (SERS).[16] Apart from fluorescence and SERS, all the other methods are time-consuming and also require sophisticated analytical instruments with specific sample pre-treatment steps, limiting their use. Though fluorescence is a simple, sensitive it also has its own limitation. Most often, the emission spectra of the organic fluorophores are very broad (100 nm). Therefore, it is challenging to clearly detect multiple analytes in a mixture due to spectral overlap from various fluorophores present in the biological matrix, restraining it's use for multiplexing strategies. Also, fluorescent labelling autofluorescence from biological matrix and photobleaching of the fluorescent dyes are other disadvantages, which lead to extended monitoring times using this technique. Therefore, label-free vibrational technique like SERS is gaining considerable importance for biological analysis in recent days due to sharp fingerprint spectra, making it feasible to detect multiple analytes simultaneously (Multiplexing).[17]

SERS involves the adsorption of analyte molecules onto a plasmonic metallic substrate resulting in Raman signal enhancements of the molecules in the order of ≥ 10^6. [18] Among a wide range of metallic substrates, coinage metals such as Ag, Au, and Cu are mainly used since their surface plasmon resonance (SPR) peaks lie in the electromagnetic spectrum's visible region, which matches closely with the commonly used Raman excitation wavelengths.[19-21] But then, keeping in mind the advantages of bimetallic substrates over monometallic counterparts, such as higher stability, oxidation resistance of alloys, tunable optical properties, and facile fabrication, many substrates like Ag-Au, Au-Cu, Ag-Cu have been synthesized and used as excellent SERS substrates.[22-24] Most importantly, bimetallic substrates produced higher SERS enhancement factors with more hotspot formation. Various bottom-up approaches are utilized to produce such substrates by using solid platforms like glass or silica, comprising colloidal nanoparticles or assembly of metal nanoparticles. The most important factor for the substrates produced by this strategy is lower production cost and the substrates can be easily scaled up. Moreover, it is noticed that the SERS substrates formed by the assembly or fusion of the metal nanoparticles with abundant hot spots, give rise to plasmon coupling/hybridization effects, leading to very high SERS enhancement factors.[25,26] Therefore, plasmonic substrates with branched structures are the most popular in various SERS applications.

In this work, we employ easily synthesized Ag-Au and Ag-Cu bimetallic alloy micro flower substrates [22,24] on a glass coverslip, for the sensitive SERS-based detection of MTO at ultra-low concentrations. Further, it is known that the intensity of the SERS signals can be enhanced in surface-enhanced resonance Raman spectroscopy (SERRS), which produce an additional enhancement factor of 10^2-10^3.[27,28] For SERRS to occur, the SPR maxima of the substrate and the absorption maxima of the adsorbed analyte molecule on the SERS substrate should be at resonance with the excitation laser wavelength. However, if the excitation wavelength is off-resonance (higher or lower λ) for the analyte molecule but at resonance with the SPR peak of the substrate, it is known as pre-resonance and can be labelled as SE(R)RS. We successfully employed both Ag-Au and Ag-Cu substrates for the detection of MTO using two different

excitation laser sources (532nm and 632.8 nm), to find out that lowest detection limit for MTO was in fact obtained with Ag-Cu substrate at 632.8 nm excitation, in a SERRS study. To the best of our knowledge, there is only a handful of reports available in the literature on the detection of MTO, using either SERS or SERRS technique. For instance, McLaughlin et al. have shown MTO detection up to 10 pM using a method based on SERRS in a flow cell using silver colloid as their substrate.[29] Later, Ackermann et al. have quantitively monitored the fluctuations of anti-cancer drug MTO based on SERRS assay on a microfluidic device.[30] Wu et al. demonstrated an approach for kinetic monitoring of drugs flowing within the intravenous drug delivery tubing using a plasmonic nano dome array surface using SERS. They have also reported the multiplexing of anti-histamine drug promethazine and anti-cancer drug MTO using their SERS substrate.[31] Later, Wallace et al. demonstrated a pM detection of MTO using silver colloid Array pillars as their SERS substrates.[32] More recently, Ponlamuangdee et al. reported a micromolar detection of MTO using graphene oxide/gold nanorod decorated, plasmonically active paper via SERS.[16] While the above-mentioned sensors were developed using sophisticated fabrication procedures, but still the lowest detection limit was found to be in pM range for MTO. So, there is an immediate need for SERS substrates that can be synthesized easily without complex steps, and able to detect even lower concentrations of MTO beyond pM.

In this work, we report the efficient use of the Ag-Cu substrate for the ultra-sensitive detection of MTO in water, with a 'limit of detection (LOD)' value of 1 fM. Moreover, we demonstrate the multiplexing ability of the sensor between MTO and Doxorubicin (DOX) in water and spiked mouse blood plasma using two different laser lines 532nm and 632.8 nm, which can study both SERS and SERRS phenomena. The Ag-Cu substrates meet most of the important requirements for a useful biomedical sensor: simple preparation steps, can be scaled up easily, less-expensive and very good SERS efficiency in presence of biological media. Thus, the sensor can be used for clinical monitoring purpose due to its high sensitivity and multiplexing ability, which should accelerate the screening of important drugs directly in the blood and plasma of cancer patients.

5B.2. Results and Discussion

5B.2.1. Characterization of alloy MFs and absorption spectra of the anticancer drugs

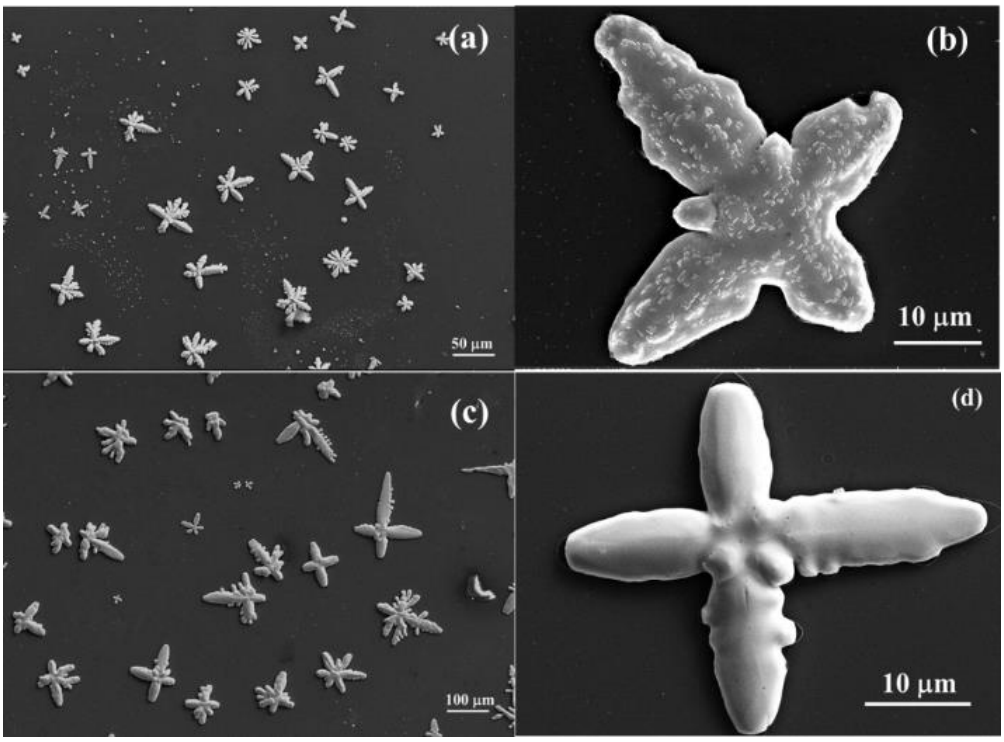

Figure 5B.1. FE-SEM images of (a) Ag-Cu and (c) Ag-Au MFs; (b) and (d) represents the higher magnification SEM images of Ag-Cu and Ag-Au MFs respectively.

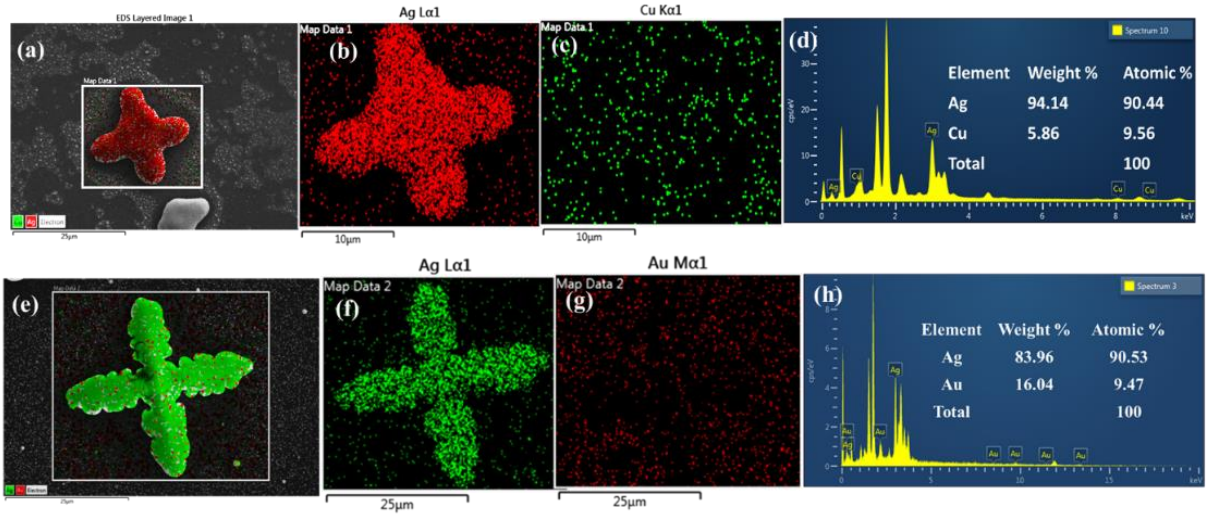

Figure 5B.2. corresponds to EDX and elemental mapping of (a) Ag-Cu MF, (b) Ag, and (c) Cu, and (d) is the atomic and weight percentage of Ag and Cu obtained from a single Ag-Cu MF; EDX and elemental mapping of (e) Ag-Au MF, (f) Ag, (g) Au, and (h) is the atomic and weight percentage of Ag and Au obtained from a single Ag-Au MF.

The synthesis and detailed structural, morphological characterization of the bimetallic Ag-Au and Ag-Cu micro flowers, were provided in our previous reports.[22,24] Briefly, as obtained from the SEM images (**Figure 5B.1**), the MFs were found to consist 4 to 6 branches offering abundant hot spots, which were formed due to the fusion of smaller nanoparticles during the thermolysis step. The average size of Ag-Cu and Ag-Au MFs for different compositions, varied in the range of 20 μm to 60 μm. We employed Ag-Au and Ag-Cu substrates of various compositions for SERS efficiency study towards the detection of MTO. Moreover, from the EDX mapping, the distribution of gold and copper within Ag MF, confirmed the alloy formation (**Figure 5B.2**).

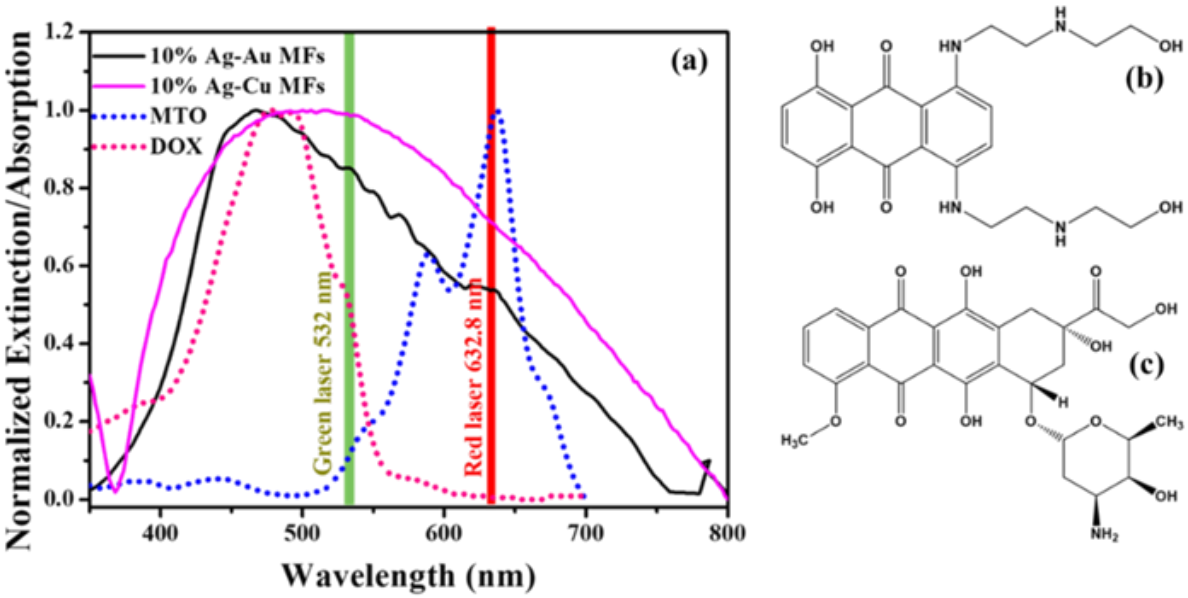

Figure 5B.3. (a) Extinction spectra of bimetallic Ag-Cu and Ag-Au MFs and absorption spectra of DOX and MTO in methanol (the concentration of drugs is 1 μM); (b) and (c) are the molecular structures of MTO and DOX.

It is well known that the surface plasmon resonance (SPR) maxima for pure Ag, Au, and Cu nanoparticles are found around ~400, ~520, and ~600 nm, respectively. The extinction spectra of 10% Ag-Au and 10% Ag-Cu MFs, were exhibited in (**Figure 5B.3**). Evidently, the SPR spectrum was found to be very broad for Ag-Cu substrate compared to Ag-Au MFs, indicating to different electromagnetic field enhancement factors between the two substrates. The extinction maximum of 10% Ag-Au and 10%

Ag-Cu substrates were found to be ~466 and ~516 nm, respectively. Even though the major component of these bimetallic MFs was Ag, the shift in SPR maxima from 400 nm towards higher wavelengths and spectral broadening, could be suggested due to the presence of Au and Cu in the alloy substrate, as well as aggregation and interconnection of the nanoparticles resulting into MF formation during the thermolysis. From **Figure 5B.3**, it was inferred that both the SERS substrates were resonant with 532 nm excitation, however, the excitation was found to be off-resonance with respect to the absorption maximum of MTO, implying SE(R)RS condition. The 632.8 nm excitation was very weakly resonant with Ag-Au substrate but it was at resonant with the absorption maxima of MTO leading to resonance Raman scattering (RRS). However, SERRS condition for MTO was only achieved with Ag-Cu substrate with 632.8 nm excitation (**Figure 5B.3**& **Table 5B.1**). Furthermore, to perform the multiplexing study of MTO with DOX (*vide infra*), the UV-Vis absorption spectrum of the DOX was also compared with the excitation wavelengths in the same way and the analysis was summarized in **Table 5B.1**.

Table 5B.1. Pre-resonance and resonance conditions for the anticancer drug molecules.

Drug molecule	Ag-Au		Ag-Cu	
	532 nm	632.8 nm	532 nm	632.8 nm
MTO	SE(R)RS	Weak SERS + RRS	SE(R)RS	**SERRS**
DOX	SE(R)RS	Weak SERS	SE(R)RS	SE(R)RS

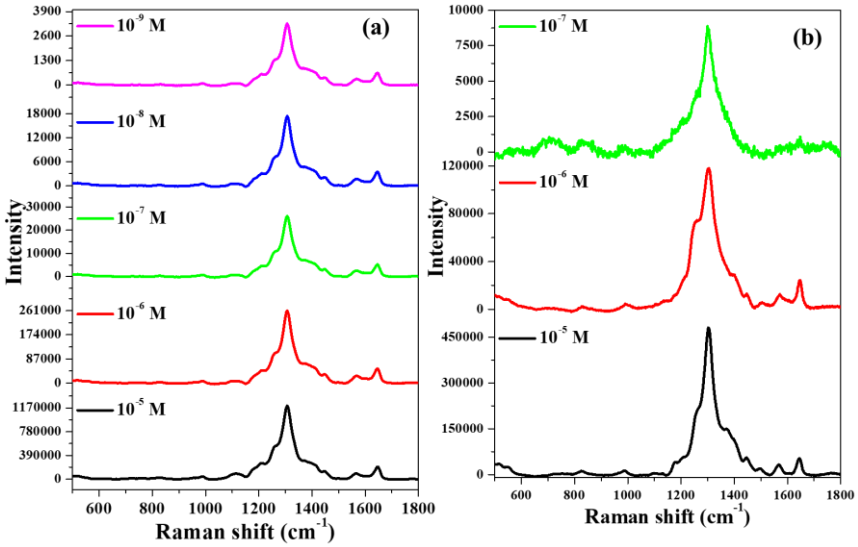

Figure 5B.4. SERS spectra of MTO on 10% Ag-Au MFs using (a) green laser and (b) red laser, collected using 50X Objective with ~13 μW laser power, 1 sec exposure time, and 30 accumulations.

5B.2.2. SERS based detection of MTO using bimetallic Ag-Au and Ag-Cu MFs

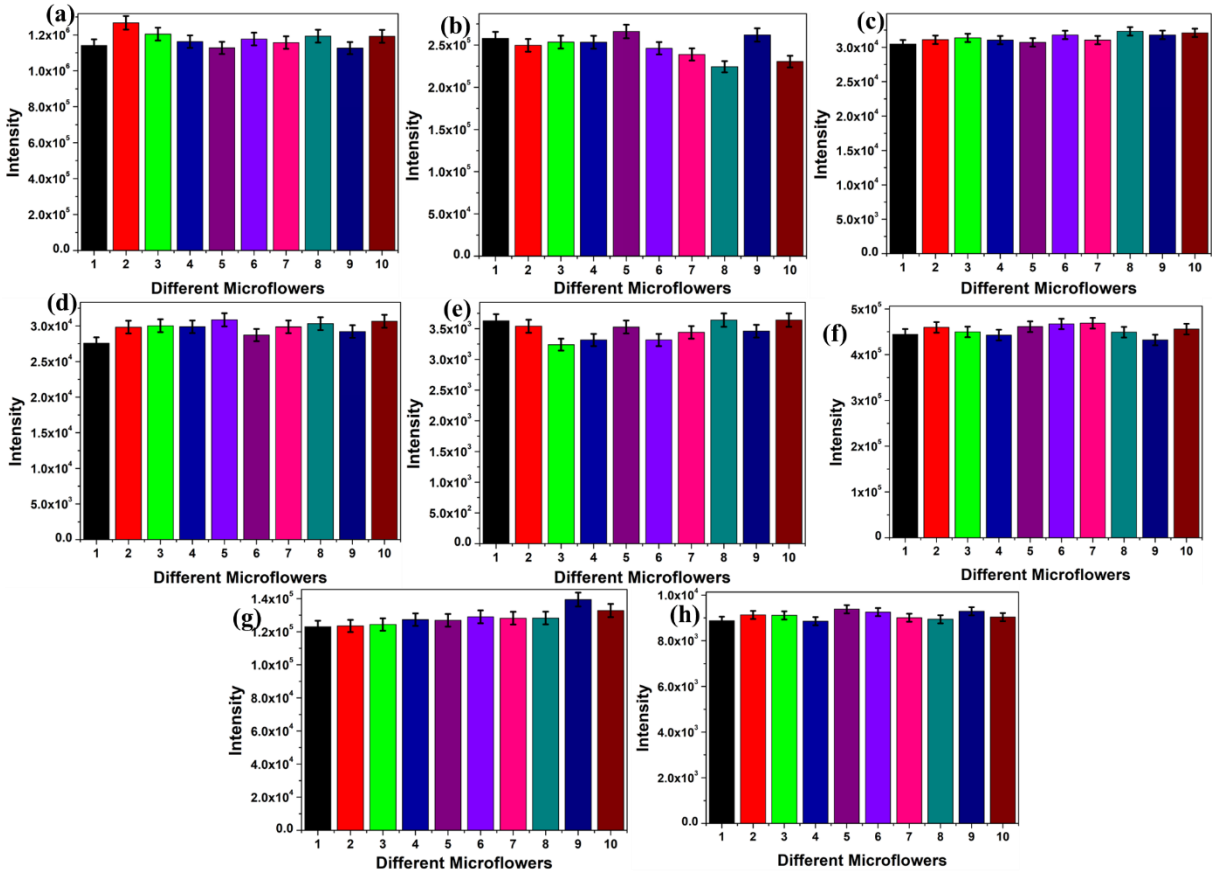

Figure 5B.5. SERS spectra and their corresponding histograms showing Raman intensities of MTO on 10% Ag-Au MFs (a) 10^{-5}M, (b) 10^{-6}M, (c) 10^{-7}M, (d) 10^{-8}M and (e) 10^{-9}M taken on 10 different MFs using green laser; (d) 10^{-5}M, (e) 10^{-6}M, and (f) 10^{-7}M on different flowers using red laser.

Many previous reports suggested that maximum EFs and lower detection limits for an analyte molecule are obtained when the excitation wavelength of the laser was close to the SPR maximum of metal nanoparticles (MNPs).[16,33] **Figure 5B.4.**, shows the SE(R)RS and SERS spectra of MTO adsorbed on 10% Ag-Au MFs, when excited with 532 nm, and 632.8 nm excitation lasers, respectively. As can be seen from the figure, a strong peak at 1304 cm^{-1} corresponding to C-C stretching and few smaller peaks in the 1500 - 1700 cm^{-1} region (see **Table 5B.2.**), was observed for MTO.[34] As expected, we observed that the intensity of the representative 1304 cm^{-1} peak of MTO, was stronger with 532 nm excitation compared to 632.8 nm, for a given concentration. The limit of quantification (LOQ) values for MTO were found to be 1 nM and 100 nM using green and red laser, respectively. We have also collected the spectra at 10 different

places on a single MF to compare the uniformity of SERS substrate and a histogram was plotted to understand the standard error as shown in the **Figure 5B.5.** When we performed the same study using 5% Ag-Au substrates (**Figure 5B.6 & Figure 5B.7**), the LOQ values were found to be 10 nM, from both the lasers. As compositions with more than 10% Au didn't produce any MFs, therefore we limited our studies with these two compositions only.

Table 5B.2. SERS frequencies (cm^{-1}) of Mitoxantrone (MTO) using two different laser excitations. A, B and C refers to the three six-membered rings of MTO from left to right (Fig. 1d), whereas vs, s, m, w, vw refer to very strong, strong, medium, weak and very weak, respectively.

SERS Frequencies of MTO (cm^{-1})		Peak Assignment mode, symmetry, [fragment of the chromophore: A – C]
532 nm	632.8 nm	
1646 (s)	1645 (s)	ν(C=O), A_1
1565 (m)	1567 (m)	ring stretch, A_1
1499 (m)	1497 (m)	ring stretch coupled with ν(C-O), B_2
1450 (v)	1448 (v)	ring stretch coupled with ν(C-O), A_1
1304 (vs)	1305 (vs)	ring stretch coupled with ν(CO), A_1
1256 (m)	1256 (m)	ν(C-N), A_1, [C]
1173, 1110 (w, vw)	1175, 1110 (w, vw)	δ(CC-H) coupled with ν(C-0) and ν(C-N), A_1
986 (w)	988 (w)	ν(C-C), A_1, [B]
830, 550 (w, vw)	828, 550 (w, vw)	def ring, A_1, [A and C]
524 (w)	522 (w)	δ(C=O), A_1, [B]
468 (m)	466 (m)	δ(CC-O), A_1, [A]
437 (w)	435 (w)	δ(CC-N), A_1, [C]

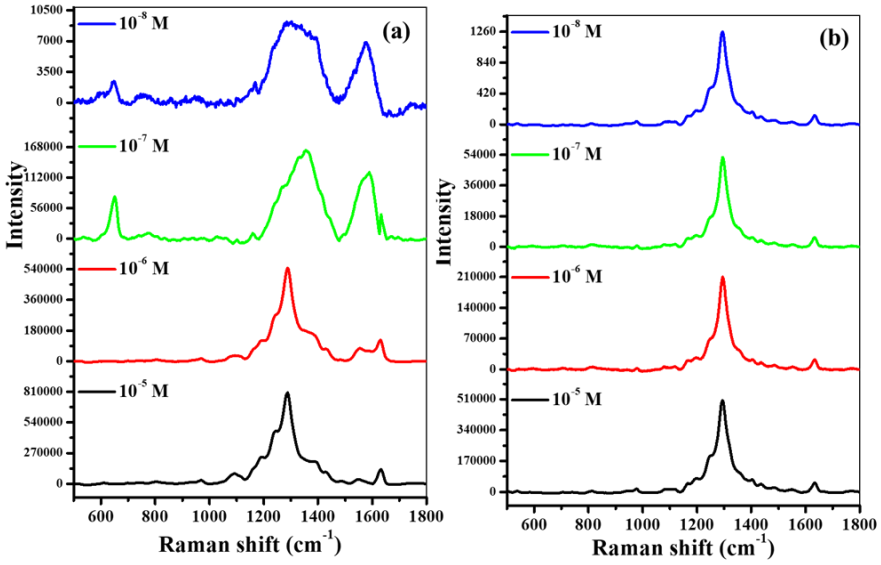

Figure 5B.6. SERS spectra of MTO on 5% Ag-Au MFs using (a) green laser and (b) red laser, collected using 50X Objective with ~13 μW laser power, 1 sec exposure time, and 30 accumulations.

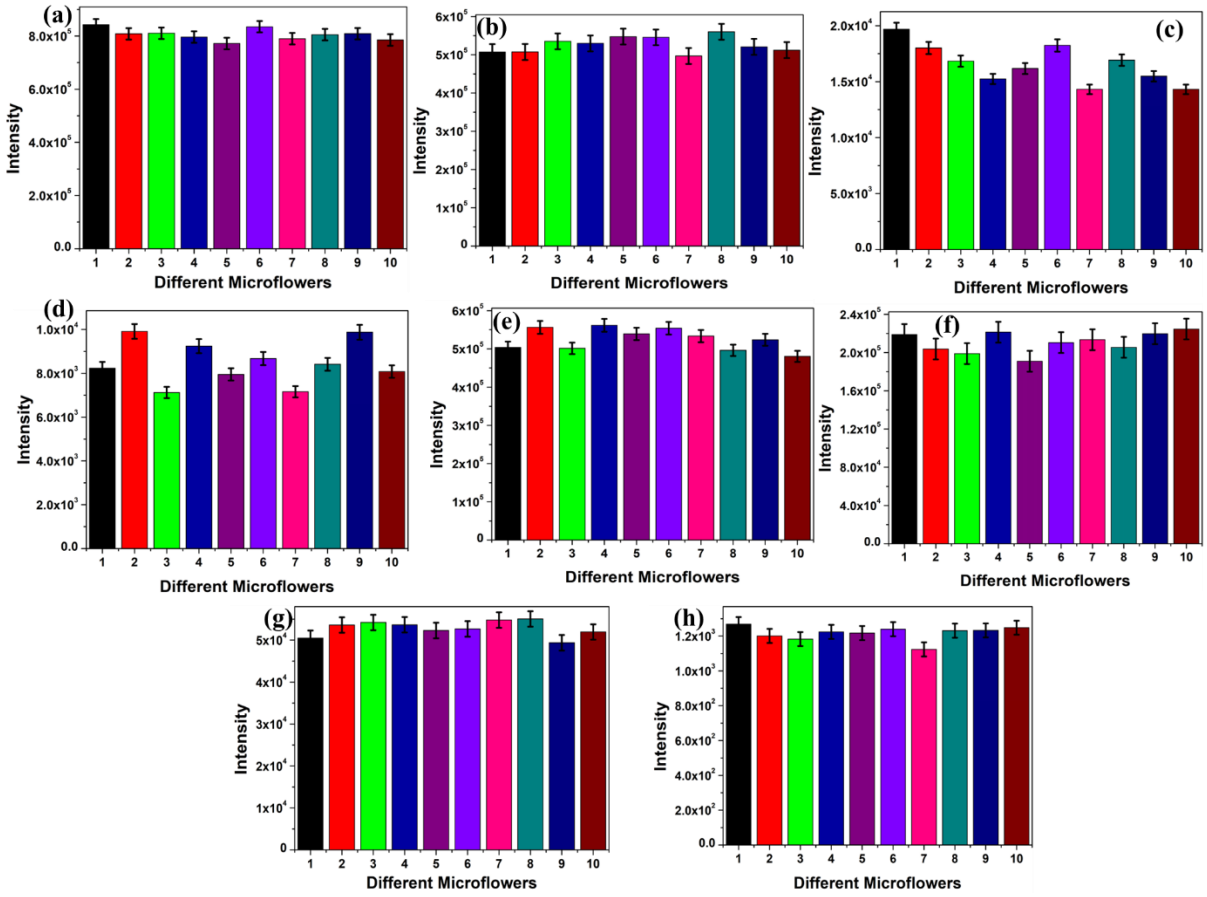

Figure 5B.7. SERS spectra and their corresponding histograms showing Raman intensities of MTO on 5% Ag-Au MFs (a) 10^{-5}M, (b) 10^{-6}M, (c) 10^{-7}M, (d) 10^{-8}M and (e) 10^{-9}M taken on 10 different MFs using green laser; (f) 10^{-5}M, (g) 10^{-6}M, and (h) 10^{-7}M on different flowers using red laser.

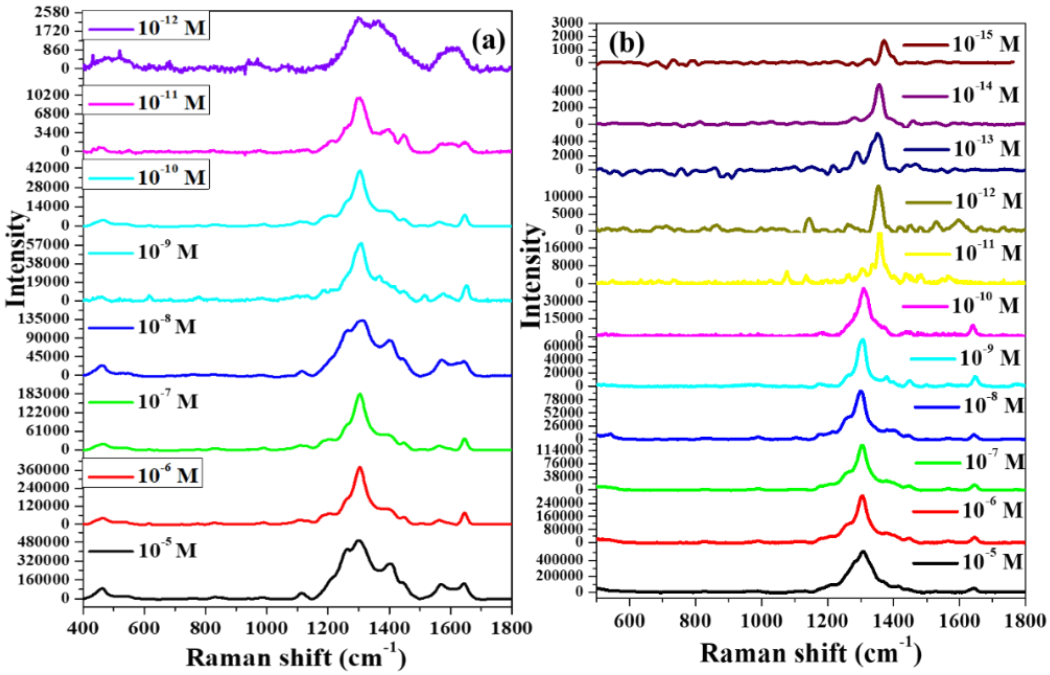

Figure 5B.8. SERS spectra of MTO on 10% Ag-Cu MFs using (a) green laser and (b) red laser, collected using 50X Objective with ~13 μW laser power, 1 sec exposure time, and 30 accumulations.

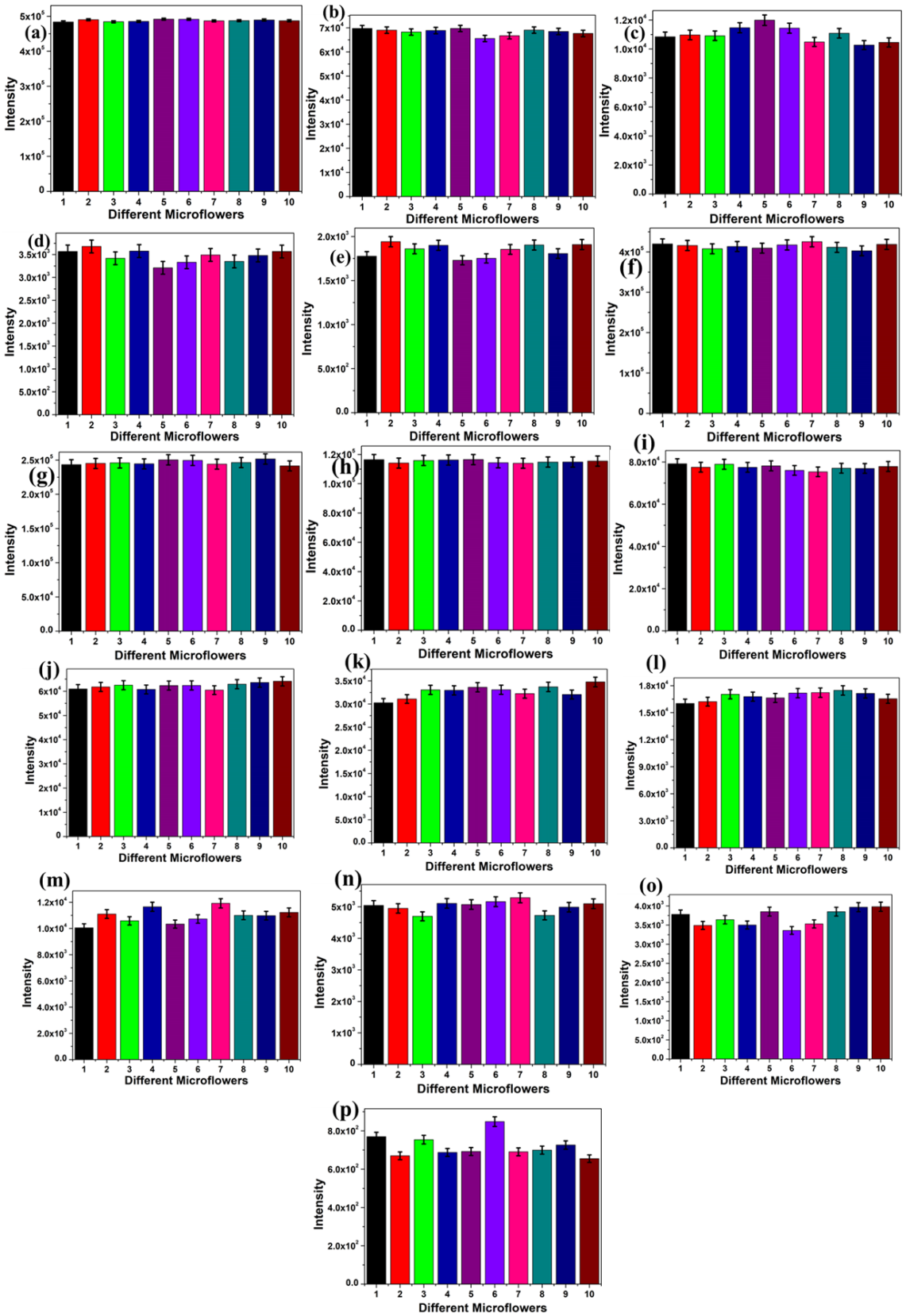

Figure 5B.9. SERS spectra and their corresponding histograms showing Raman intensities of MTO on 10% Ag-Cu MFs (a) 10^{-5}M, (b) 10^{-6}M, (c) 10^{-7}M, (d) 10^{-8}M, and (e) 10^{-9}M, taken on 10 different MFs using green laser; (f) 10^{-5}M, (g) 10^{-6}M, (h) 10^{-7}M, (i) 10^{-8}M, (j) 10^{-9}M, (k) 10^{-10}M, (l) 10^{-11}M, (m) 10^{-12}M, (n) 10^{-13}M, (o) 10^{-14}M, and (p) 10^{-15}M MTO on different flowers using red laser.

Table 5B.3. shows the relative standard errors obtained from each data set.

Sample	Concentration	Green laser	Red laser
5% Ag-Au	10^{-5} M	2.677265	5.408464
	10^{-6} M	3.951441	5.16974
	10^{-7} M	10.6751	3.486863
	10^{-8} M	11.60923	3.329733
10% Ag-Au	10^{-5} M	3.624507	2.569614
	10^{-6} M	5.430137	3.80594
	10^{-7} M	1.946866	1.961942
	10^{-8} M	3.29186	-
	10^{-9} M	4.20104	-
5% Ag-Cu	10^{-5} M	3.039262	3.085739
	10^{-6} M	0.900525	0.766169
	10^{-7} M	3.545342	1.423318
	10^{-8} M	5.631177	1.680372
	10^{-9} M	-	1.537207
10%Ag-Cu	10^{-5} M	0.585643	1.597854
	10^{-6} M	1.943525	1.332876
	10^{-7} M	4.820426	0.855548
	10^{-8} M	4.046527	1.531589
	10^{-9} M	3.969496	1.94947
	10^{-10} M	-	4.020599
	10^{-11} M	-	2.786818
	10^{-12} M	-	5.183319
	10^{-13} M	-	3.656339
	10^{-14} M	-	5.942283
	10^{-15} M	-	8.026357
12.5% Ag-Cu	10^{-5} M	1.232874	2.040965
	10^{-6} M	2.385639	2.560059
	10^{-7} M	2.174897	0.886457
	10^{-8} M	1.841609	1.044028
	10^{-9} M	-	1.207712
	10^{-10} M	-	2.843731
	10^{-11} M	-	1.63835
	10^{-12} M	-	5.832108
15% Ag-Cu	10^{-5} M	2.258583	2.2353
	10^{-6} M	2.477299	4.656525
	10^{-7} M	3.713567	2.606901
	10^{-8} M	3.754505	2.975569
	10^{-9} M	-	3.194039
	10^{-10} M	-	4.271939
	10^{-11} M	-	6.636943
	10^{-12} M	-	6.24839

Similarly, for 10% Ag-Cu substrates as depicted in **Figure 5B.8**, we observed well-resolved peaks for MTO till 1 pM, using 532 nm excitation. However, with red laser, we obtained clear and well-resolved characteristic peaks of MTO at an ultralow 10^{-15}M (1 fM) concentration, indicating the unparalleled efficiency of Ag-Cu alloy MFs, superseding the efficiency of similar SERS substrates presented till date for MTO detection. As we are dealing with ultralow detection of analytes, therefore SERS signal

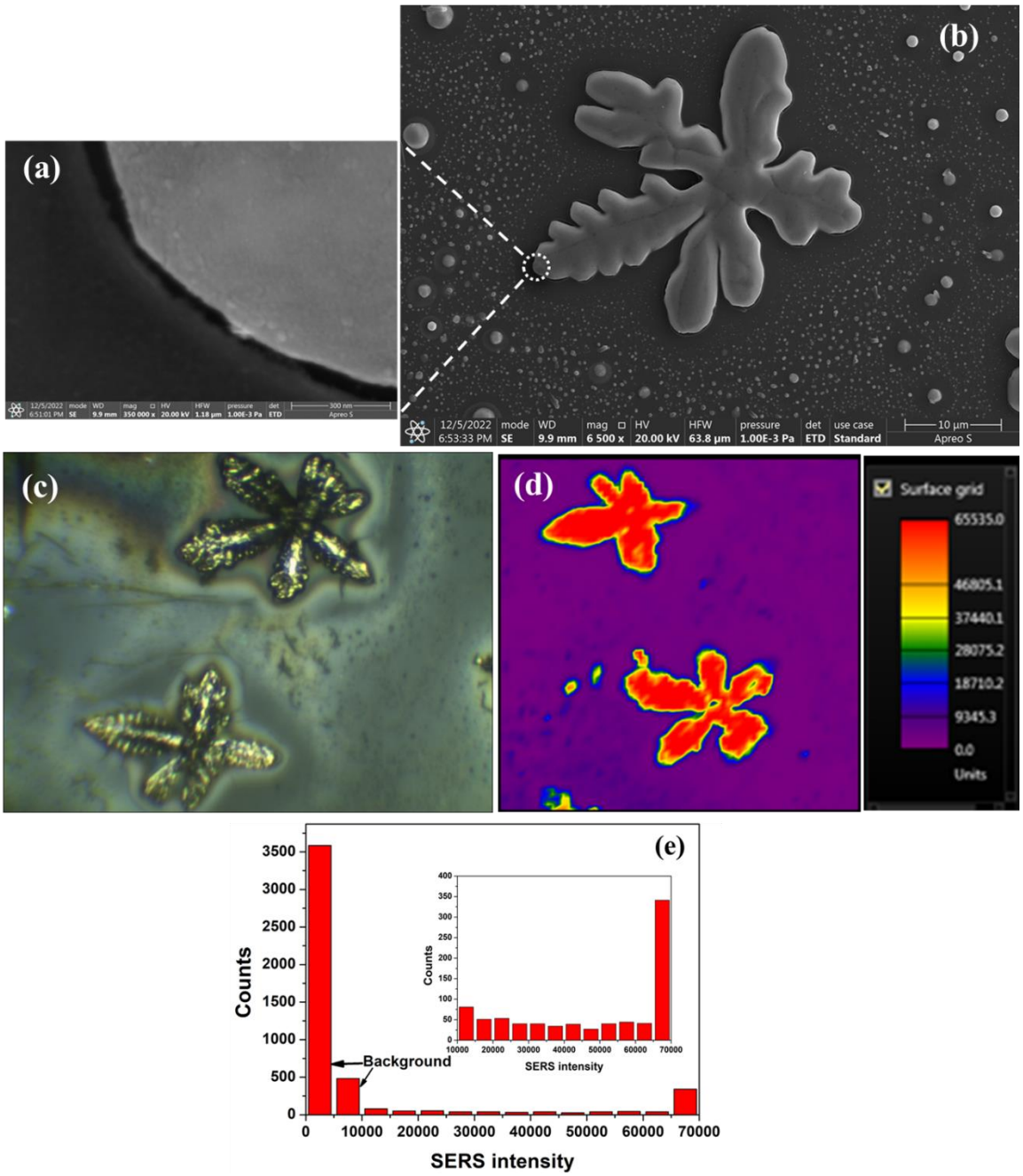

Figure 5B.10. (a) Zoomed in FE-SEM image of a MF tip, (b) is the FE-SEM image of a 10% Ag-Cu MF; (c) Optical image of 10% Ag-Cu MFs and (d) their corresponding Raman mapping based on intensity. (e) Histogram of SERS counts from (d) to demonstrate the density of hotspots, where the inset shows the counts obtained from the total area in (d).

Table 5B.4. A comparison of LOD values of MTO using different analytical methods including SERS.

S.No.	Detection method	Substrate	LOD	References
1	Absorbance	Gold Nanoparticles	7.8 nM	[14]
2	Chemiluminescence	Diperiodatoargentate (DPA)	22 µM	[13]
3	Electrochemical	molecularly imprinted polymer (MIP) film	30 nM	[7]
4		AgNPs and polythiophene (PT) supported on the multiwall carbon nanotubes	13 nM	[38]
5		carbon paste electrode (CPE) with electropolymerization of glycine	1 µM	[39]
6		CPE amplified with ZIF-8 and 1-butyl-3-methylimidazolium methanesulfonate (BMIMS)	3 nM	[40]
7		Nanosilica grafted by sulfonic acid	36.8 µM	[41]
8	Electrophoresis	Background electrolyte along with organic modifier	11.2 µM	[11]
9	Fluorescence	MIP@rQDs@SiO_2 probe	67 µM	[15]
10		calf thymus DNA modified on glutathione stabilized gold nano clusters	20 nM	[42]
11		MOF- hydrogel hybrid	2.25 nM	[43]
12		CdTe quantum dots	0.22 µM	[44]
13	HPLC	-	4.5 nM	[9]
14	Radio immuno assay	antisera from rabbits immunized with mitoxantrone-BSA antigen	0.1 nM	[10]
15	Voltammetry	CS-Dispersed Graphene Modified Glassy Carbon Electrodes	10 nM	[8]
16	SERS	Plasmonic Nanodrome Array	2.25 nM	[31]
17		Graphene oxide/gold nanorod	5 µM	[16]
18		Silver colloid	40 pM	[29]
19		Silver colloid	0.2 mM	[30]
20		Silver pillar arrays	2.9 pM	[32]
21		Ag-Cu Microflowers	**1 fM**	This work

uniformity and reproducibility across different MFs are key factors. Keeping that in mind, SERS intensity of MTO as a function of its concentration and excitation wavelength, was recorded across different MF substrates, to examine the sample-to-sample reproducibility and we also calculated the relative standard error for each set of MFs. Across different MF substrates, we observed a negligibly small variation in SERS intensities of representative peak at 1304 cm^{-1}, with no change in the order of magnitude, as shown in Figure **5B.9**. This is because, regardless of its size and number

of branches, every MF for a particular composition is a random fusion of nanoparticles (Fig. **Figure 5B.10 a & b**). Therefore, the nature of the plasmonic hotspots and subsequent electromagnetic enhancement factors are reasonably similar for different MF substrate, resulting in comparable SERS efficiencies. We observed that for most of the cases, the relative standard errors were less than 5%. The detailed analysis of relative standard errors with lowest and highest values, can be found at **Table 5B.3**. Also, in order to know about the density and heterogeneity of hotspots in a MF substrate, we have performed SERS mapping studies (**Figure 5B.10 c-e**) on a representative 10% Ag-Cu MF. From mapping data, we identified that plasmonic hotspots are homogeneously distributed across the MF.

Table 5B.5. LOD values of MTO using Ag-Au and Ag-Cu bimetallic MFs with different compositions and different lasers.

Substrate	Composition	Limit of detection	
		Green Laser	Red laser
Ag-Au	5%	10^{-8} M	10^{-8} M
	10%	10^{-9} M	10^{-7} M
Ag-Cu	5%	10^{-8} M	10^{-9} M
	10%	10^{-12} M	**10^{-15} M**
	12.5%	10^{-8} M	10^{-12} M
	15%	10^{-8} M	10^{-12} M

We further calculated the limit of detection (LOD) value of the sensor using the equation LOD = 3.3 σ/k, Where, σ is the standard deviation, and k is the slope as shown in the **Figure 5B.11**. **Figure 5B.11a.** showed a series of SERS spectra of MTO with a linear increase in the concentration, while **Figure 5B.11b.** demonstrated the plot of intensities of 1304 cm^{-1} peak from the spectra, with increase in concentrations of MTO. When the obtained data were fitted with a linear equation, the LOD was found to be 0.96 fM, matching exactly with the LOQ value of the sensor. This implies that the lowest quantity of MTO in a test sample can be determined quantitatively. **Table 5B.4**.

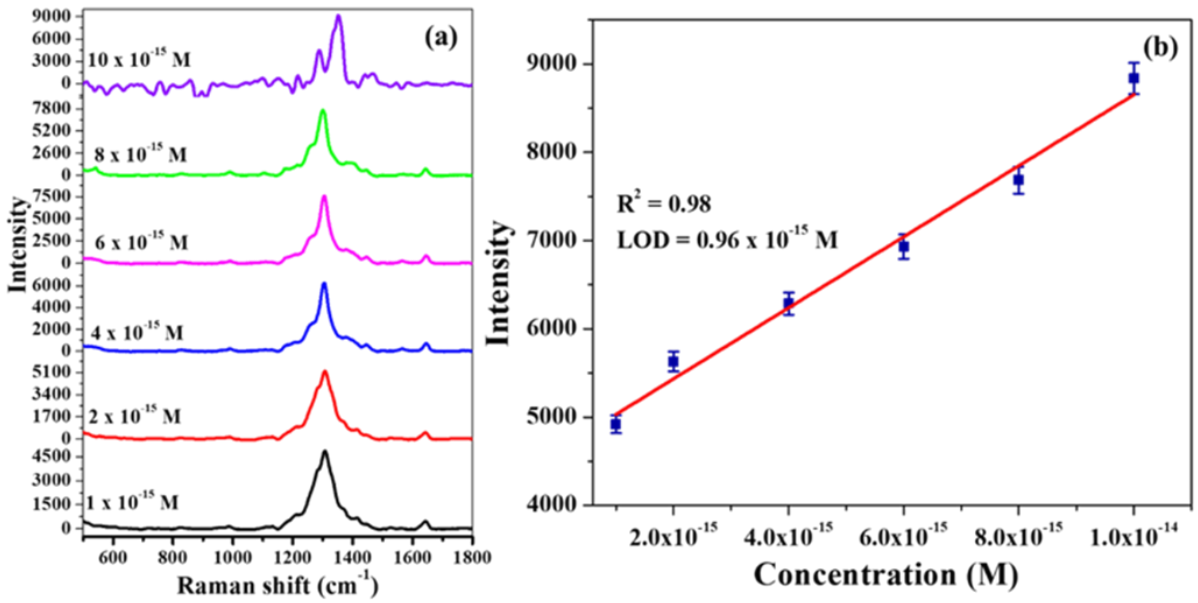

Figure 5B.11. (a) SERS spectra of MTO with various concentrations obtained on 10% Ag-Cu MFs using red laser, and (b) is the plot between SERS intensity of 1304 cm^{-1} peak and concentration of MTO in the linear range.

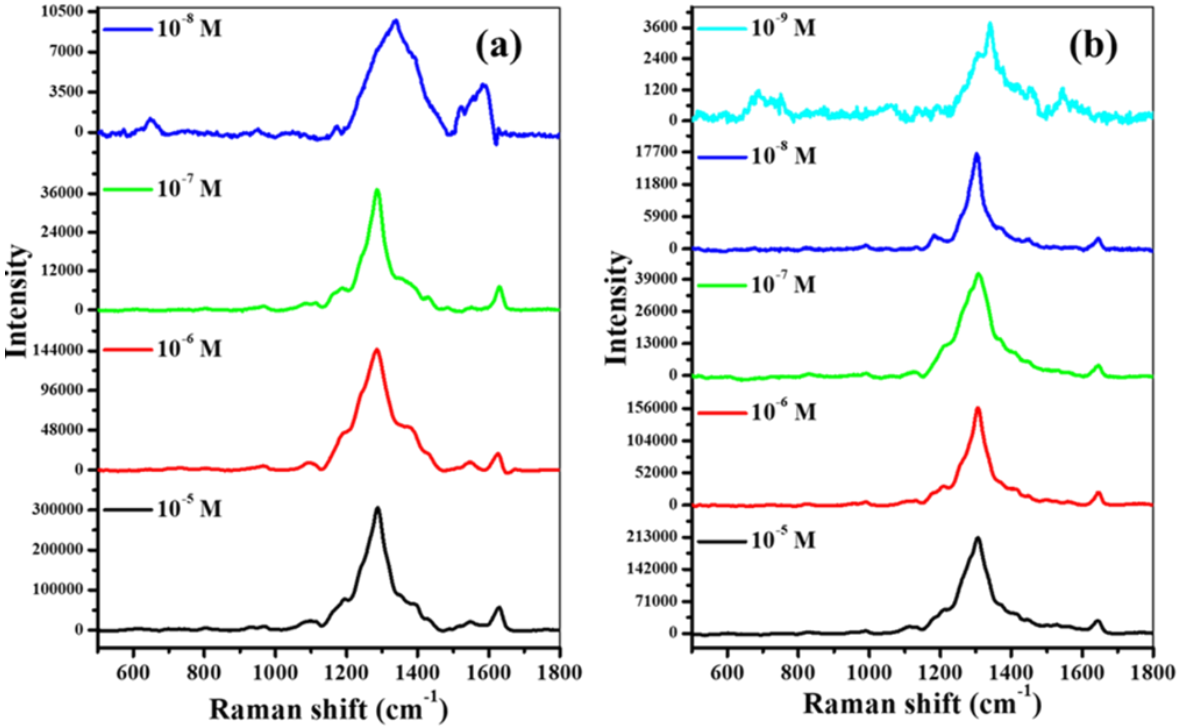

Figure 5B.12. SERS spectra of MTO on 5% Ag-Cu MFs using (a) green laser and (b) red laser, collected using 50X Objective with ~13 μW laser power, 1 sec exposure time, and 30 accumulations.

listed a comparison of numerous LOD values of MTO by various analytical sensors, which were reported till date for MTO detection. As can be seen form the data presented, the Ag-Cu sensor demonstrated the best detection efficiency for MTO, till

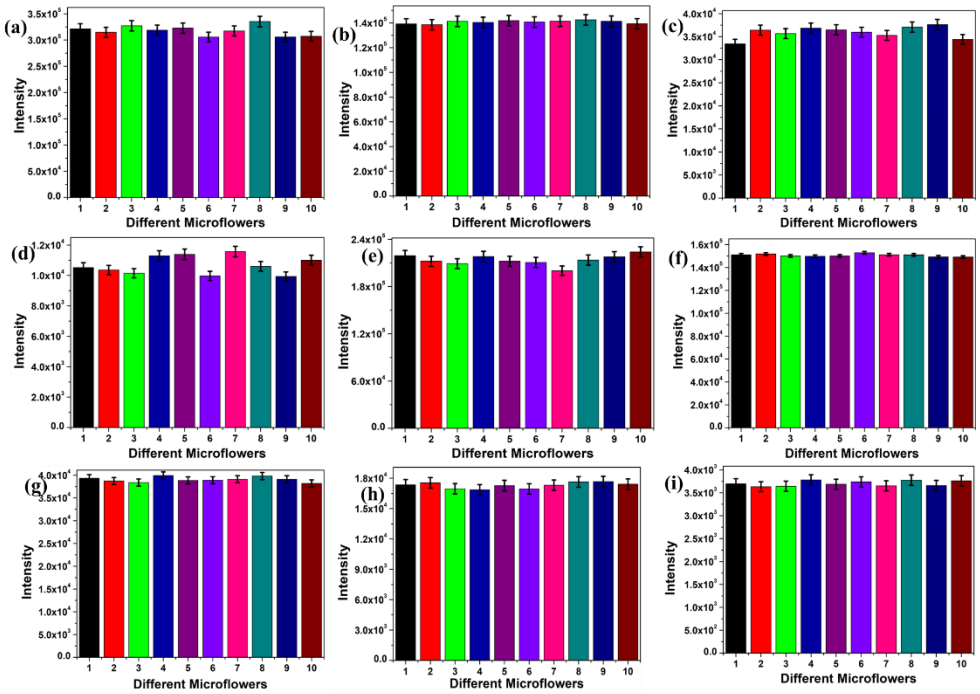

Figure 5B.13. SERS spectra and their corresponding histograms showing Raman intensities of MTO on 5% Ag-Cu MFs (a) 10^{-5}M, (b) 10^{-6}M, (c) 10^{-7}M, and (d) 10^{-8}M taken on 10 different MFs using green laser; (e) 10^{-5}M, (f) 10^{-6}M, (g) 10^{-7}M, (h) 10^{-8}M, and (i) 10^{-9}M MTO on different flowers using red laser.

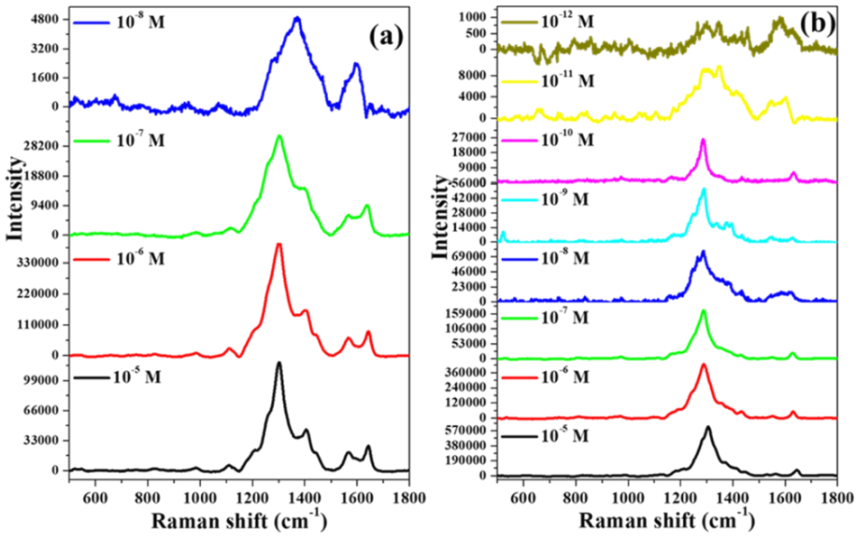

Figure 5B.14. SERS spectra of MTO on 12.5% Ag-Cu MFs using (a) green laser and (b) red laser, collected using 50X Objective with ~13 μW laser power, 1 sec exposure time, and 30 accumulations.

date. Such unprecedented LOD value of MTO using 632.8 nm laser, could be accounted due to SERRS since the laser wavelength coincided exactly with the absorption maximum of the molecule and also closely overlapped with the maximum of the LSPR spectrum of the substrate. Furthermore, by varying the composition (from 5% to 15% Cu), we found that the 10% Ag-Cu substrate produced the best SERS detection capability for MTO, as shown in **Table 5B.5**. and **Figures 5B.12 to Figure 5B.17.**

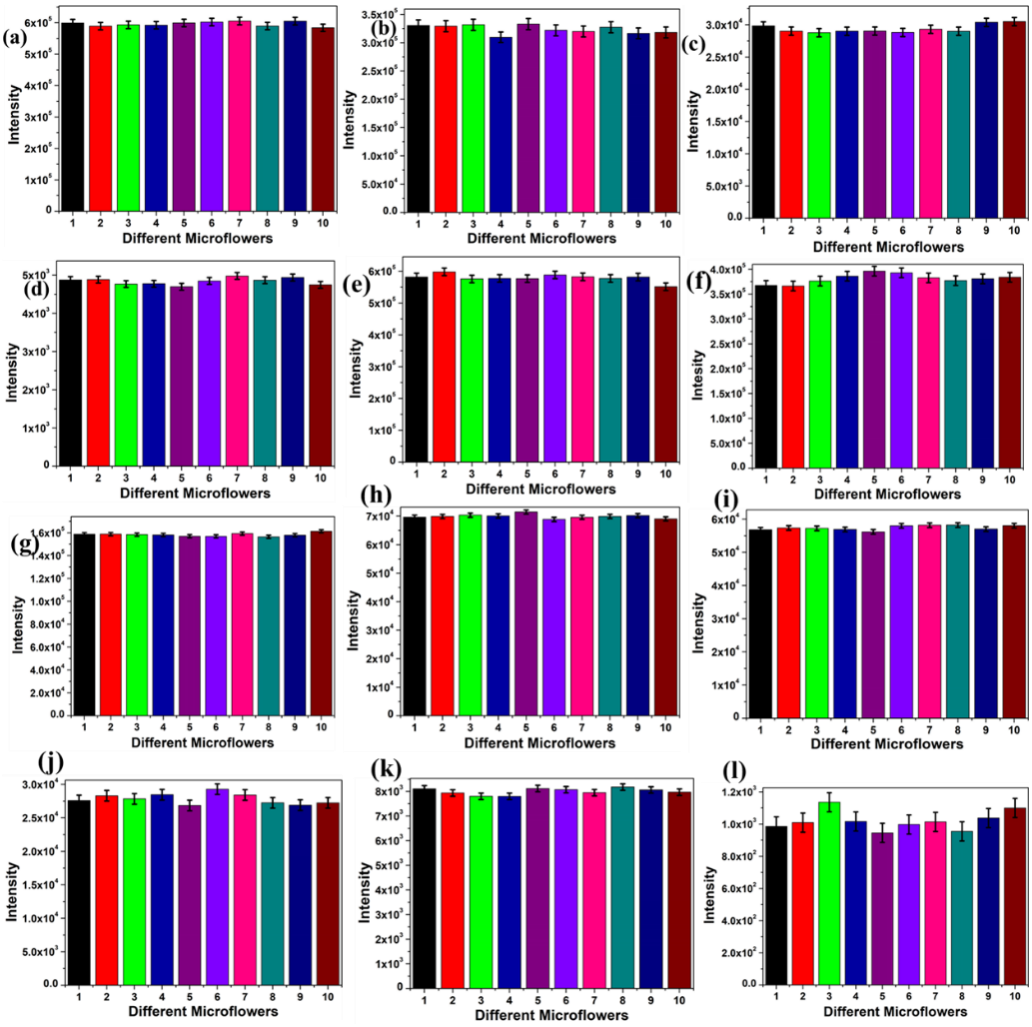

Figure 5B.15. SERS spectra and their corresponding histograms showing Raman intensities of MTO on 12.5% Ag-Cu MFs (a) 10^{-5}M, (b) 10^{-6}M, (c) 10^{-7}M, and (d) 10^{-8}M taken on 10 different MFs using green laser; (e) 10^{-5}M, (f) 10^{-6}M, (g) 10^{-7}M, (h) 10^{-8}M, and (i) 10^{-9}M (j) 10^{-10}M, (k) 10^{-11}M, and (l) 10^{-12}M, MTO on different flowers using red laser.

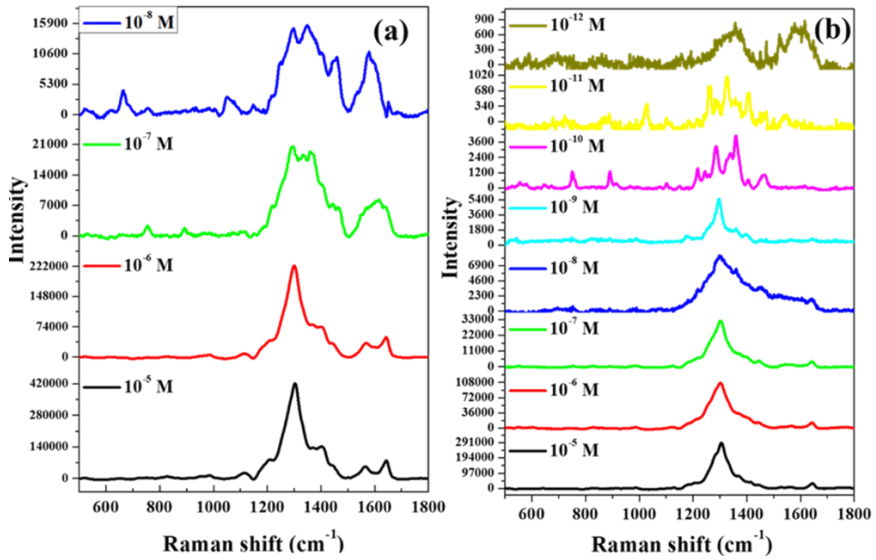

Figure 5B.16. SERS spectra of MTO on 15% Ag-Cu MFs using (a) green laser and (b) red laser, collected using 50X Objective with ~13 μW laser power, 1 sec exposure time, and 30 accumulations.

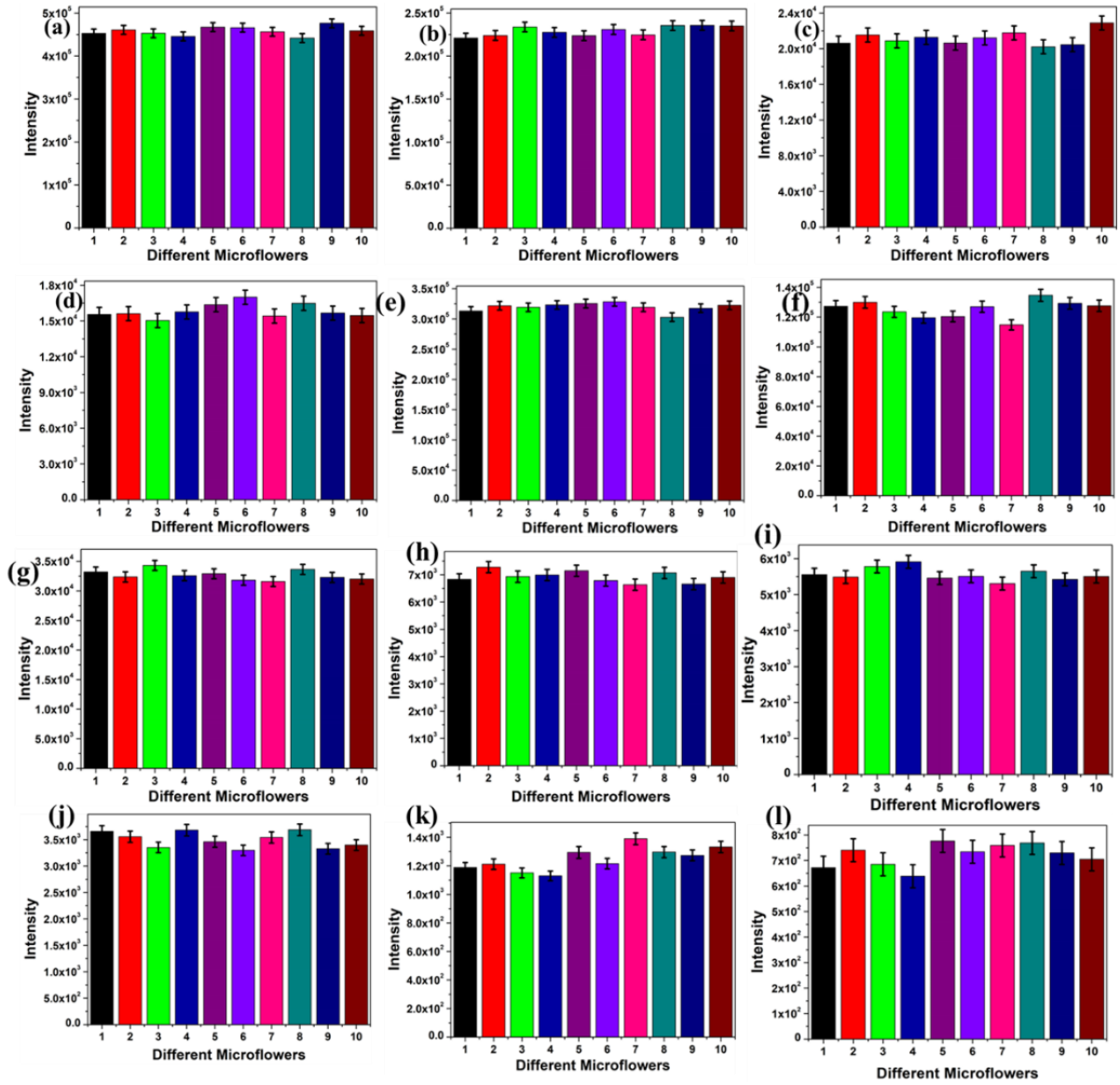

Figure 5B.17. SERS spectra and their corresponding histograms showing Raman intensities of MTO on 12.5% Ag-Cu MFs (a) 10^{-5}M, (b) 10^{-6}M, (c) 10^{-7}M, and (d) 10^{-8}M taken on 10 different MFs using green laser; (e) 10^{-5}M, (f) 10^{-6}M, (g) 10^{-7}M, (h) 10^{-8}M, and (i) 10^{-9}M (j) 10^{-10}M, (k) 10^{-11}M, and (l) 10^{-12}M, MTO on different flowers using red laser.

5B.2.3. COMSOL Simulation results

In our earlier SERS studies, we have demonstrated the superior SERS performance of the Ag-Au and Ag-Cu alloy substrates over pure Ag substrates, emphasizing the better stability of the bimetallic substrates from the aerial oxidation. Moreover, in our earlier report[24] and this study also, between the two bimetallic substrates, we recorded higher SERS enhancement with Ag-Cu, compared to Ag-Au. Therefore, in order to probe the difference between the local field enhancement effect on 10% Ag-Au and 10% Ag-Cu substrates, COMSOL simulation study was carried out on appropriately chosen models

using both 532 and 632.8 nm excitations. As, MFs were formed from the aggregation of smaller nanoparticles (**Figure 5B.10.**), three different models were used for the study with progressive complexity: NP dimer, 2D Array of NPs and random arrangement of NPs (**Figure 5B.18 to Figure 5B.21)**.

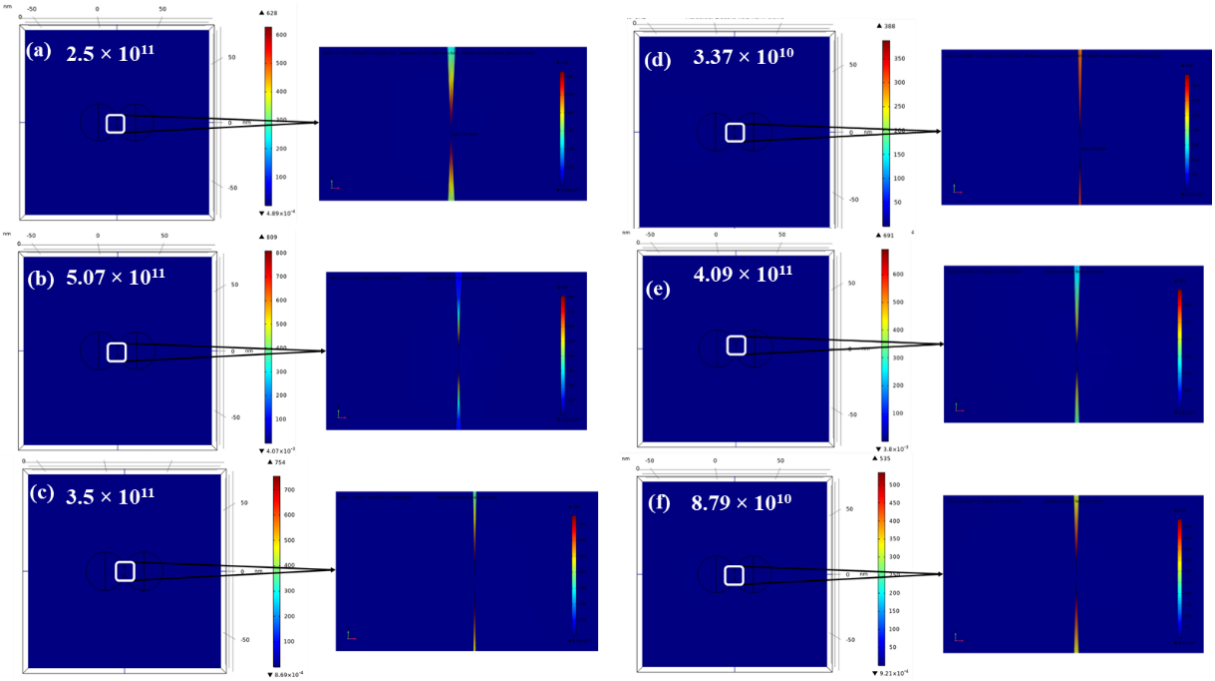

Figure 5B.18. Theoretical Electromagnetic field maps and calculated enhancement factors of interconnected dimer nanoparticles made up (a, d) Pure Ag, (b, e) 10% Ag-Au and (c, f) 10% Ag-Cu at 532 nm and 632.8 nm wavelength respectively.

For interconnected dimers, the amount of field enhancement or enhancement factor (which is the ratio of the highest electric field to the applied electric field in the specified region) was found to be much higher when compared to the dimers with 1nm gap, for all compositions (**Figure 5B.18 to Figure 5B.21 and Table 5B.6**). Further, we noticed that for 532 nm incident wavelength for the interconnected structures, the values of EF for pure Ag were slightly lower than that of Ag-Au and Ag-Cu NP dimers. For 632.8 nm, the enhancement for Ag was found to be one order less than that of the Ag-Au alloy nanoparticles. For the dimers with 1 nm gap in the junction, the EF factors were found similar at both the wavelengths for all compositions (**Figure 5B.19**). However, the dimer structure was far from our actual experimental structure.

Figure 5B.20 demonstrated the electric field maps at the 'xy plane' of the interconnected nanoparticles arranged in 2D array, for the 532 and 632.8 nm excitation. For both the excitation wavelengths, the results showed that the EFs of Ag

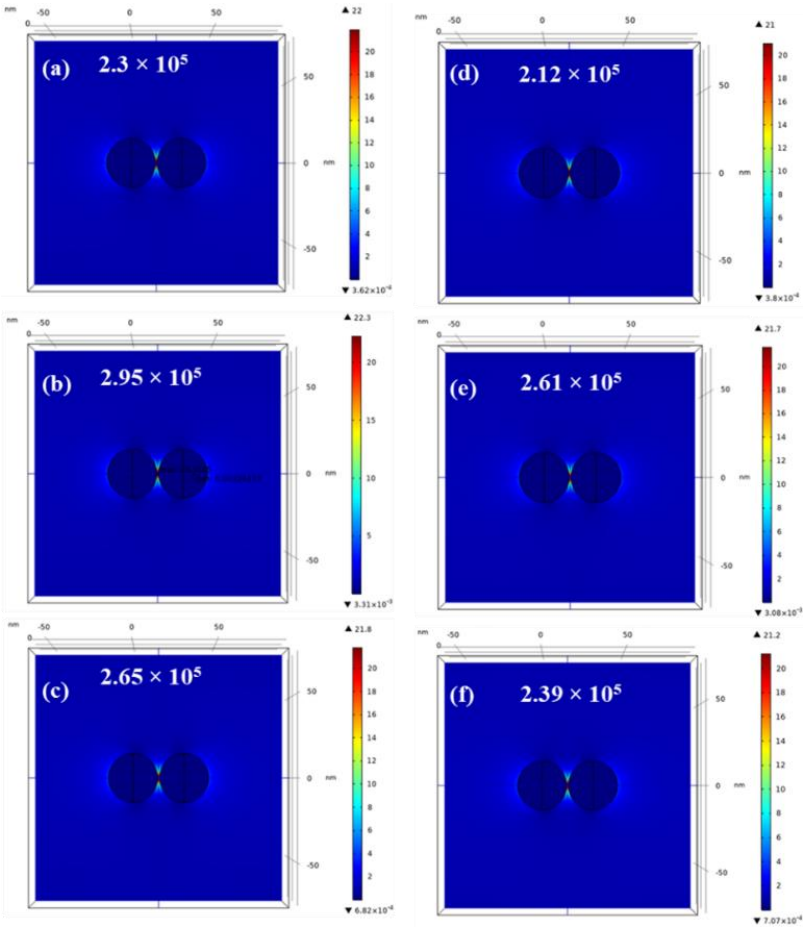

Figure 5B.19. Theoretical Electromagnetic field maps and calculated enhancement factors of dimer nanoparticles with 1nm gap made up (a, d) Pure Ag, (b, e) 10% Ag-Au and (c, f) 10% Ag-Cu at 532 nm and 632.8 nm wavelength respectively.

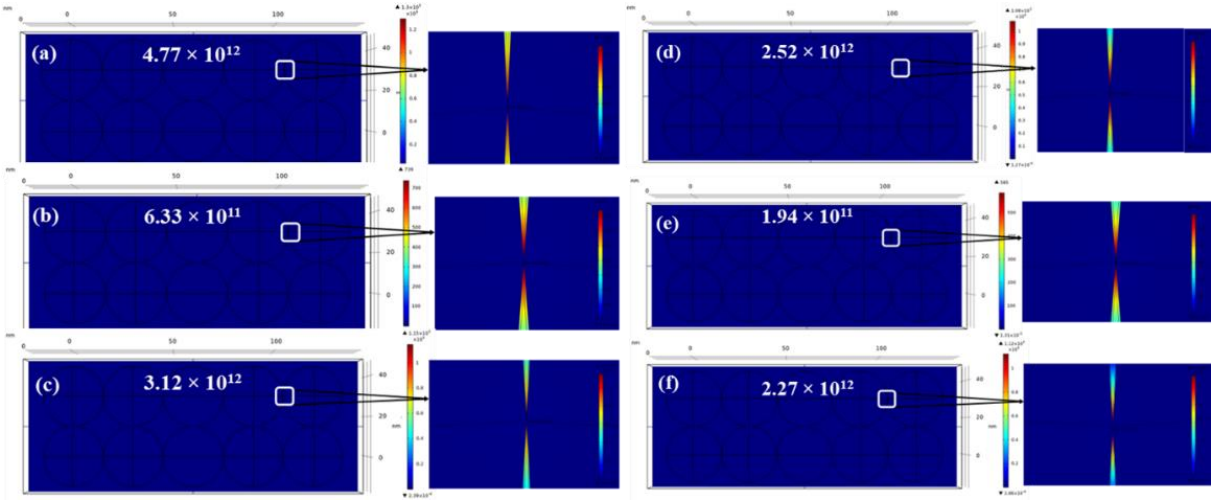

Figure 5B.20. Theoretical Electromagnetic field maps and calculated enhancement factors of interconnected Array of nanoparticles made up (a, d) Pure Ag, (b, e) 10% Ag-Au and (c, f) 10% Ag-Cu at 532 nm and 632.8 nm wavelength respectively.

and Ag-Cu MFs were comparable (~10^{12}) and one order of magnitude higher compared to Ag-Au (~10^{11}) (**Table 5B.6**). For the array structures with 1 nm gap in the junction,

the EF factors were found to be similar at both the wavelengths for all compositions, providing no useful information (**Figure 5B.21**). Finally, the simulations were performed using a model where 100 nanoparticles were arranged randomly, ensuring that the adjoining nanoparticles might be fused or encompassing a gap between them. In this case also, the results (**Figure 5B.22 and Table 5B.6**) showed that the EFs of Ag and Ag-Cu MFs were comparable and found to be higher compared to Ag-Au.

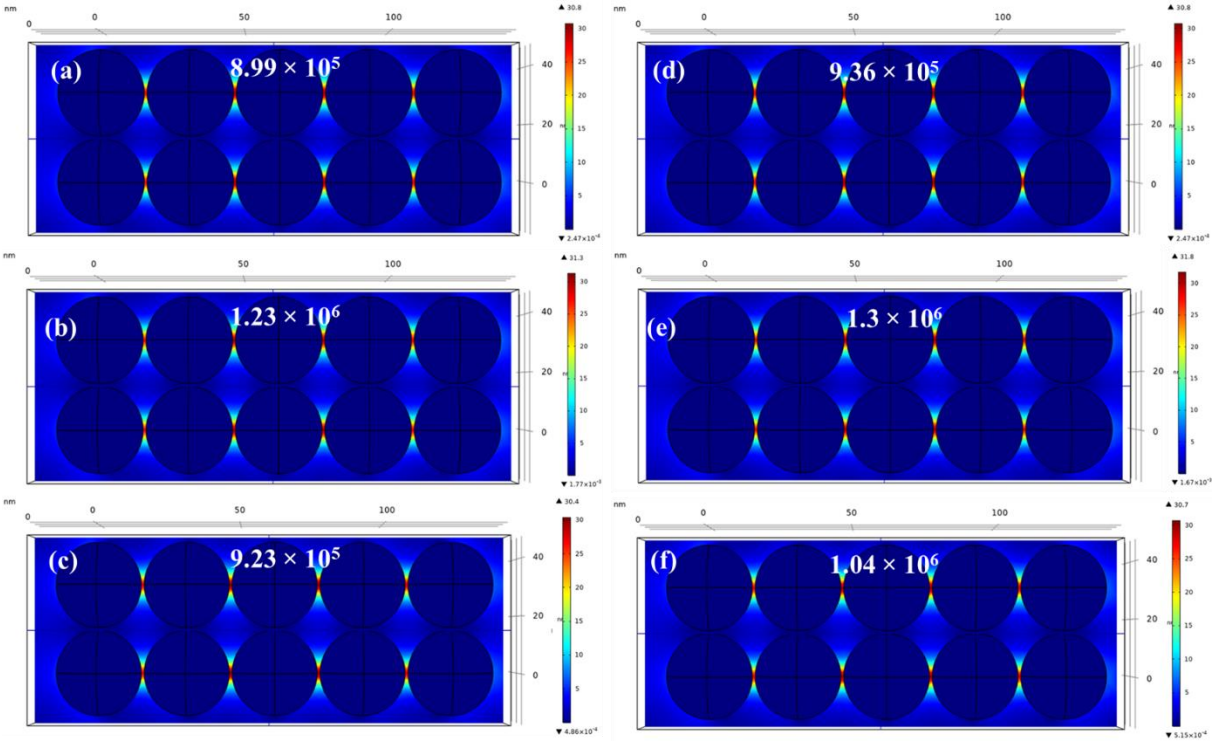

Figure 5B.21. Theoretical Electromagnetic field maps and calculated enhancement factors of Array of nanoparticles with 1nm gap made up (a, d) Pure Ag, (b, e) 10% Ag-Au and (c, f) 10% Ag-Cu at 532 nm and 632.8 nm wavelength respectively.

Therefore, according to the simulation, the order of the enhancement factor is as following: Ag~Ag-Cu > Ag-Au, whereas experimental SERS enhancement factors follow the order: Ag-Cu> Ag-Au > Ag. This anomaly between theoretical prediction and experiment about the pure Ag case can be rationalized as following. Ag is highly oxidizable in air hence the theoretical EF factor reduces considerably in experimental conditions. In case of Ag-Au MF, earlier it is observed experimentally that, Ag-Au nanoparticle has shown much better plasmonic activity compared to pure metals as Au is one of the highly efficient plasmonic metal. Chaffin *et. al.* also theoretically showed that Ag/Au alloyed NPs provide stronger SERS enhancements than pure Ag or pure Au

NPs[42]. In our case, we observed that the surface of Ag-Au alloy is Ag rich through XPS data. Combined with the Ag rich surface and stable Au underneath, Ag-Au shows a better experimental EF than that of pure Ag, probably due to synergistic effect.

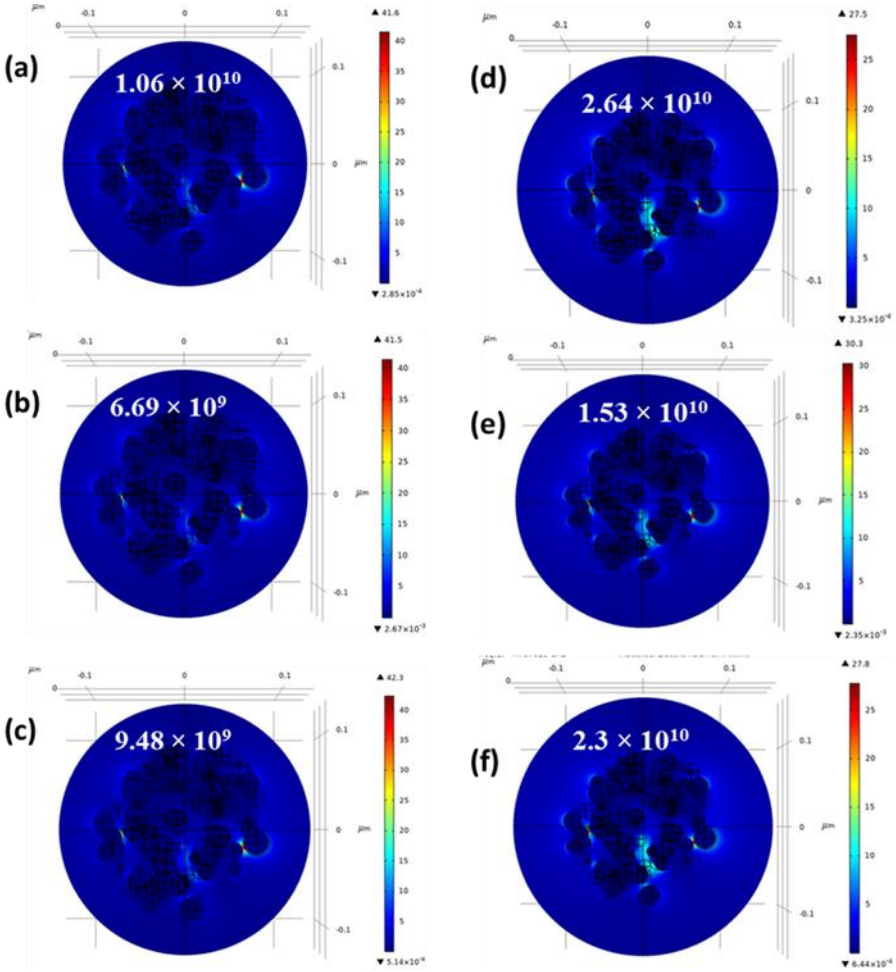

Figure 5B.22. Theoretical Electromagnetic field maps and calculated enhancement factors of a 100 randomly arranged nanoparticles made up (a, d) Pure Ag, (b, e) 10% Ag-Au and (c, f) 10% Ag-Cu at 532 nm and 632.8 nm wavelength respectively.

On the other hand, theoretically predicted EF for Ag-Cu MF were found to be comparable to that of pure Ag and one order higher compared to Ag-Au, using 2D array model and randomly arranged NPs. Experimentally, the SERS efficiency of Ag-Cu was also found to be higher compared to Ag-Au. Moreover, unlike Ag-Au surface, the surface of Ag-Cu bimetallic MF was found to be Cu rich[24]. Also, in Ag-Cu bimetallic MFs, Cu acted as the sacrificial metal, where Cu was oxidized itself in presence of air while enabling Ag to remain in its pure metallic state underneath which is highly plasmonic in nature. But in Ag-Au alloy the top surface was Ag rich, which was prone

to oxidation. Therefore, Ag-Cu was found to be a better SERS substrate experimentally for R6G and MTO molecules compared to Ag-Au. The results were found to be comparable with that of the similar simulation results mentioned in other reports.[43] The higher EF of Ag-Cu MFs could also be accounted due to the higher electrical conductivity of Cu compared to Au. In another recent study using ultrafast pump-probe spectroscopy, Sakir et.al. have shown that rapid electron transfer between plasmonic metals is a contributing factor to the SERS activity. They have shown that it occurs in the ultrafast time scale (<100 fs) between interconnected Ag nanostructures and seed Au nanoparticles[44]. Similar electron transfer can also augment the SERS activity in the alloy substrates demonstrated in this manuscript, albeit more in Ag-Cu substrate.

Table 5B.6. A summary of simulated EFs of Pure Ag and alloy MFs with increase in structural complexity using both green and red lasers (green color = 532 nm & red color = 632.8 nm laser).

Substrate	Arrangement of Nano particles				
	Dimer		2D Array		Random arrangement of 100 NPs
	1 nm gap	interconnected	1 nm gap	interconnected	
Pure Ag	2.3×10^5 2.12×10^5	2.5×10^{11} 3.37×10^{10}	8.99×10^5 9.36×10^5	4.77×10^{12} 2.52×10^{12}	1.06×10^{10} 2.64×10^{10}
10% Ag-Au	2.95×10^5 2.61×10^5	5.07×10^{11} 4.09×10^{11}	1.23×10^6 1.3×10^6	6.33×10^{11} 1.94×10^{11}	6.69×10^9 1.53×10^{10}
10% Ag-Cu	2.65×10^5 2.39×10^5	3.5×10^{11} 8.79×10^{10}	9.23×10^5 1.05×10^6	3.12×10^{12} 2.27×10^{12}	9.48×10^9 2.3×10^{10}

5B.2.4. Multiplexed detection of MTO and DOX in water using 10% Ag-Cu MFs

MTO is primarily used in the treatment of non-Hodgkinson lymphoma and breast cancer. In aggressive stages of cancer, MTO is combined with other drugs such as Doxorubicin, cyclophosphamide, vincristine, prednisolone, etc., to overcome drug resistance and improve the efficiency of chemotherapy. Therefore, it becomes necessary to simultaneously determine the trace level of drug concentrations in the blood and plasma of the cancer patients, for better clinical monitoring. MTO belongs to Anthraquinone class of compounds whereas DOX is an anthracycline antibiotic. Though these drugs belong to different groups there are few structural similarities such as three fused aromatic rings, C=O group and -OH groups, resulting into few

similar peaks such as ring stretching vibrations and C=O stretching, in plane bending etc. We observed peaks at 1642 and 1622 cm^{-1} corresponding to C=O stretching vibrations of ring B of MTO and DOX respectively, with the red laser (**Figure 5B.23 and Table 5B.7**). Even though these drugs have a similar fused structure, the main strong peaks corresponding to aromatic ring stretching are observed at different Raman shift for both the drugs due to difference in the functional groups attached to them. A very strong characteristic aromatic ring stretching peak was observed for MTO at 1304 cm^{-1} and for DOX at 1240 cm^{-1} (**Figure 5B.23 and Table 5B.7**). On the other hand, one of the main differences in MTO and DOX is the presence of NH_2 groups in MTO. Therefore, the important -NH_2 stretching and bending vibrations at 1256 cm^{-1} in MTO, is absent in DOX.

Table 5B.7. peak assignment for SERS frequencies of DOX. A, B and C refers to the three 6 membered rings of MTO from left to right (**Figure 5B.3c**)

SERS Frequencies of DOX (cm^{-1})		**Peak Assignment**
532 nm	**632.8 nm**	
1632	1622	ν(C=O) stretching of ring B
1584	1586	Hydrogen chelated C=O coupled to C=C stretching
1524	1510	ν(C=C) stretching of ring A
1442,1376,1326	1404,1369,1314	Aromatic ring stretching
1312.1244,1159	1297, 1232,1146	In plane C-O, C-O-H and C-H bending mode
996	990	ν(C-C) stretching of ring A
466	447	ν(C=O) in plane bending

To demonstrate the multiplexing capability of the Ag-Cu SERS sensor, we selected and intended to also detect DOX in presence of MTO. We prepared 1 μM solutions of MTO and DOX in water, separately and as a mixture, and drop cast on our MF substrate on the cover slip. It was allowed to dry and the SERS spectra were recorded using both the green and red lasers. As shown in **Figure 5B.24**, when the SERS spectra of the individual drugs were compared with the SERS spectra of the mixture of drugs, we successfully detected the representative Raman peaks corresponding to both DOX and MTO, demonstrating that our substrate could be used for multiplexed detection (*vide supra*).

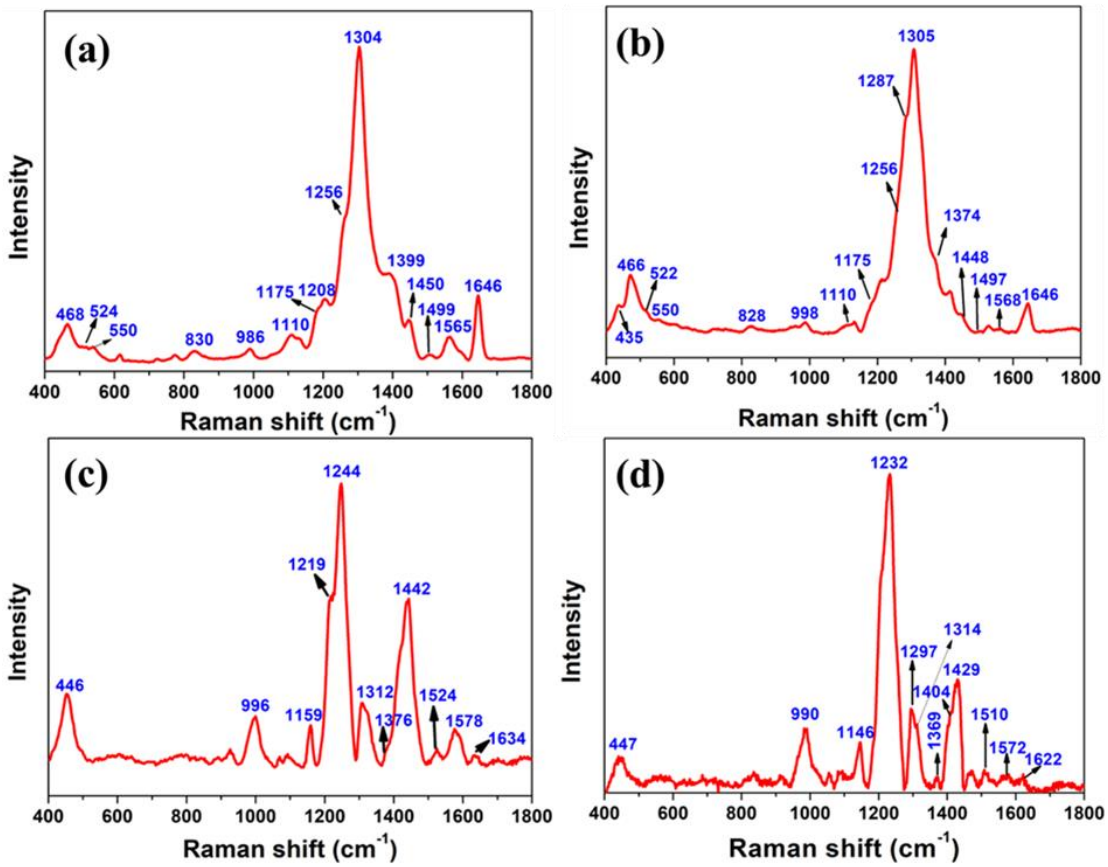

Figure 5B.23: SERS spectra showing the peak assignment of MTO (a) green, (b) red laser; DOX (c) green and (d) red laser.

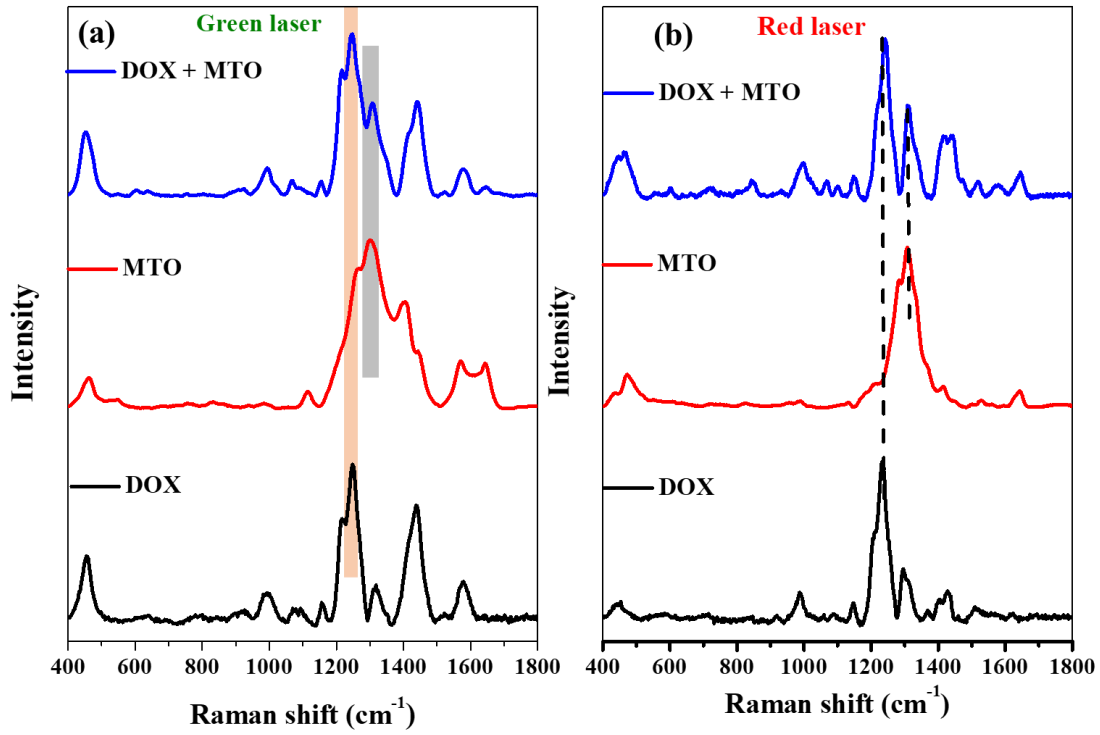

Figure 5B.24. multiplexed SERS spectra of 1 μM solutions of MTO and DOX together in water using (a) green laser and (b) red laser (the shaded part or the dotted lines indicate the peaks arising from individual drugs in the multiplexed sample).

5B.2.5. Multiplexed detection of MTO and DOX in blood plasma using 10% Ag-Cu MFs

Inspired by the multiplexing ability of the Ag-Cu substrate to detect both the drugs simultaneously in water, the same study was targeted in mouse blood plasma. As shown in **Figure 5B.25**, we observed sharp, well resolved SERS peaks for both MTO and DOX even in blood plasma without any dilution. For both the lasers, the LOD values of MTO and DOX were found to be 1 pM and 10 nM, respectively. Therefore, the bimetallic Ag-Cu alloy SERS substrate deems fit as a biomedical sensor for the anticancer drugs, which can function in direct contact with the biological medium, without any additional processing steps for the sample. Compared to water, in plasma the lowering of the detection sensitivity of the sensor for MTO is obvious with the red laser and it can be explained as following. Firstly, the molecular absorption of MTO depends strongly on pH of the medium and we observed that the absorption value of the ~ 630 nm peak of MTO decreased significantly with increase in pH (**Figure 5B.26**).

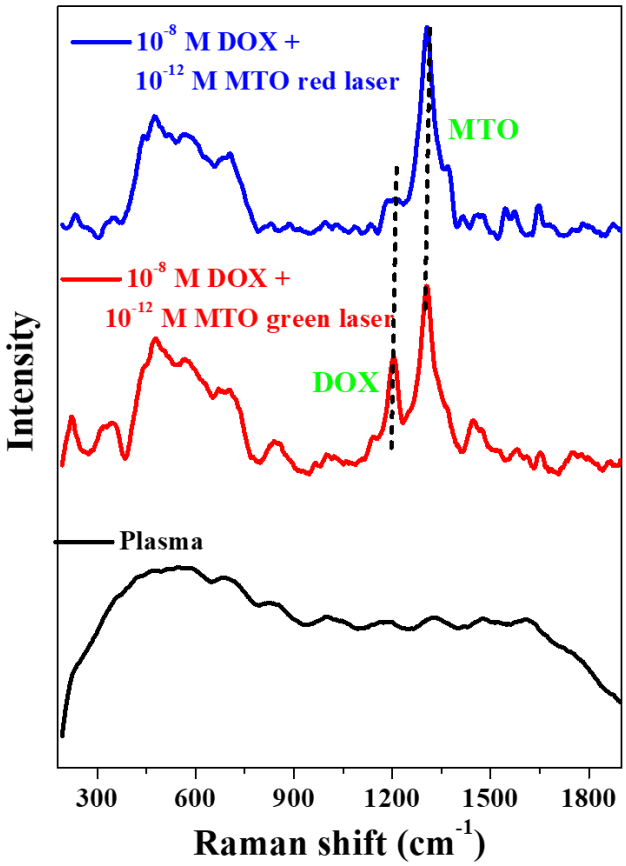

Figure 5B.25. Multiplexed SERS spectra of 1 pM and 10nM solutions of MTO and DOX together in plasma using a green laser and red laser. The strong fluorescing background of plasma is also shown.

It is known that pH of the plasma is close to 7.4. Therefore, due to less intense resonance interaction of the molecular absorption peak with the excitation laser light, the efficiency of the SERRS process was lowered leading to a decrease in the detection capability of the sensor in plasma. However, with 532 nm excitation, the LOD value of the sensor for MTO remain unaltered, as the molecular absorption of MTO at 532 nm was found to be unaffected with the increase in pH (**Figure 5B.26**). Secondly, the plasma produced a very strong fluorescing background (**Figure 5B.25**) during the SERS experiments, due to the presence of fluorescent proteins, hindering the detection process.

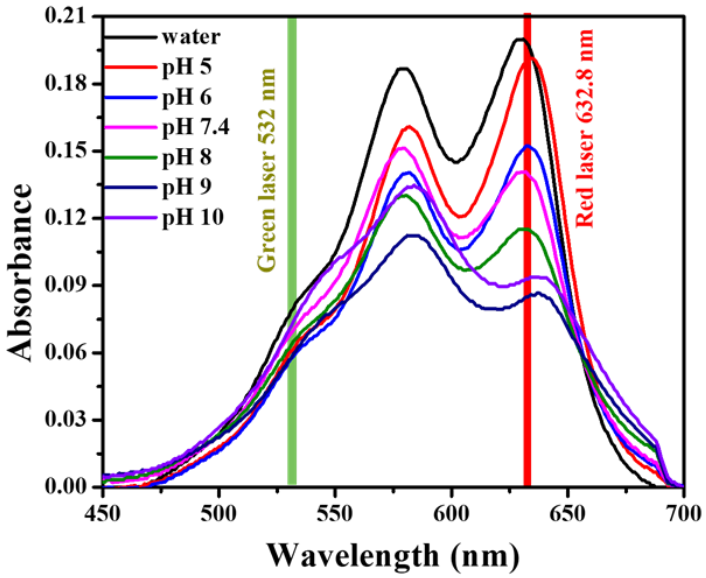

Figure 5B.26. Absorption spectra of MTO at different pH solutions.

5B.3. Conclusions and Summary:

A comparison of SERS performance between Ag-Au and Ag-Cu bimetallic alloy microflower SERS substrates of varying compositions, was demonstrated towards the detection of important anticancer drug MTO. Two different excitation laser sources, 532 nm and 632.8 nm, were used for the SERS experiments and 10% Ag-Cu was found to be the best SERS substrate among others. With 632.8 nm excitation, 10% Ag-Cu substrate satisfied the condition of Surface Enhanced Resonance Raman Scattering (SERRS) for the detection of MTO and superseded the performance of 10% Ag-Au substrate. The best LOD value of 10% Ag-Cu sensor for MTO was found to be 1 fM,

being the lowest till date measured by using any analytical technique. The superiority of Ag-Cu substrate over Ag-Au substrate was investigated using theoretical COMSOL simulation studies on the appropriately equivalent plasmonic structures. The simulated electric field enhancement maps from the studies, indicated higher electromagnetic field enhancement for Ag-Cu substrates than that of Ag-Au substrates, validating the experimental result. The probable reason could be the higher electrical conductivity of Cu compared to Au. Further, the 10% Ag-Cu alloy substrates demonstrated efficient multiplexing detection of MTO with another anticancer drug Doxorubicin (DOX), in water and mouse blood plasma. After spiking the drug mixture to the blood plasma directly without any dilution, the best LOD values of the sensor for MTO and DOX were found to be 1 pM and 10 nM, respectively. With the recent development of portable and miniaturized Raman spectrometers, the day is not far away that such SERS sensors will be used routinely for clinical applications.

Chapter 6

Ag-Au-Cu Trimetallic Alloy Microflower: A Highly Sensitive SERS Substrate for Detection of Low Raman Scattering Cross-Section Thiols

In this chapter, we explored the synthesis of tri metallic microflowers composed of Ag, Au and Cu keeping Ag composition fixed and changing the composition of Au and Cu. We studied the role of surface atom on specific adsorption/binding capacity towards smaller Raman cross section thiol molecules and their SERS. This chapter is published in Langmuir (Just accepted).

6.1. Introduction

Sensitive detection of small molecule thiols such as L-Cysteine (L-Cys), thiophenol (TP) and its derivatives is critical for safeguarding the environment, protecting human health, and maintaining the integrity of industrial processes and products. Among the twenty amino acids, thiol-containing L-Cys is one of the most important non-essential amino acids required for important body functions like protein synthesis, metabolism, detoxification, and biological signaling.[1,2] Deficiency of L-Cys can cause many problems such as delayed growth, hair depigmentation, lethargy, skin lesions, and liver damage.[3,4] Elevated levels of L-Cys also may cause cardio vascular disease, neurotoxic disorder, and blockage of kidney and bladder.[5] On the other hand, thiophenols can easily penetrate the human body by inhalation or skin absorption which aggravates various disorders, such as oxidative stress, cell death due to cytotoxicity, enzyme inhibition, and skin and respiratory irritation.[6] Therefore, measurement of L-Cys, thiophenol and its derivatives levels is important for clinical diagnosis and environmental restoration. Many optical as well as non-optical analytical techniques have been used so far to detect thiols, such as chemiluminescence,[7] voltammetry,[8] fluorescence,[9] photoelectrochemical method,[10] time-resolved photoluminescence spectroscopy,[11] high-performance liquid chromatography,[12] electrochemical methods,[13] and a handful of SERS-based methods.[14-17] However, most of these techniques suffer from individual drawbacks such as interference from other analytes, time consuming operation, complex substrate preparation, and difficult synthesis of fluorescent probes. Using the above-mentioned state-of-the art techniques, the lowest detection limit of thiols was found to be in the range of 1 μM to 10 pM, till date. So, there is an immediate need for further development of highly sensitive methods to detect L-Cys and thiophenols at even lower concentrations beyond 10 pM. However, the method should be simple, economical, and robust in any type of environmental conditions.

Surface enhanced Raman spectroscopy (SERS) is a powerful and sensitive spectroscopic technique that provides unique vibrational fingerprint information for a wide range of analyte molecules based on the inelastic scattering of light.[18,19]. Since its accidental discovery in 1977, a wide variety of plasmonic metals such as Ag,[20] Au,[21]

Cu,[22] Pd,[23] Al,[24] etc., have been used for various SERS applications by fabricating SERS substrates of various shapes, including nanoparticles,[25] rods,[26] stars,[27] flowers,[28] wires,[29] dendrites,[30] etc. Although SERS substrates of mono-metallic composition of Ag and Au have been extensively explored, recently, multi-metallic SERS substrates have been gaining tremendous attention due to the synergistic effects that can greatly enhance the plasmonic and chemical properties compared to monometallic counterparts. In our recent studies, we demonstrated the superior SERS performance of bimetallic Ag-Au and Ag-Cu alloy microflowers (MFs) compared to the SERS performance of pure Ag microflowers.[31,32] Similarly, trimetallic SERS substrates have also gained importance in recent years to complement the individual advantages of each SERS active material. For instance, trimetallic substrates such as Ag-Au-Cu nanodendrides,[33] Au/Pt/Ag[34] and Au/Pd/Pt colloidal nano composites,[35] Au@Pd-Pt core shell NPs[36] and nano cubes,[37,38] Ag-Au-Pt nano cages,[39] Ag networks with Au-Pd NPs,[40] Ag-Au-Pd NPs, trimetallic nano meshes[41] were synthesized and used for various applications such as detection of important analytes, catalysis, and in situ chemical reaction monitoring. For all the above-mentioned reports, trimetallic structures provided superior SERS efficacy over the mono and bimetallic counterparts. However, most of the trimetallic SERS substrates were prepared using expensive Pt and Pd metal, with tedious and time-consuming synthetic route. It is to be also noted that, till now there is no report on ultrasensitive detection of thiols with LOD less than 0.1 nM, using any SERS substrates.[42,43]

Herein, we demonstrate a simple one-step thermolysis to prepare the trimetallic Ag-Au-Cu microflower SERS substrates, their detailed characterization, and their application in the label-free detection of L-Cys and aromatic thiols. We recently demonstrated the superior SERS performance of the bimetallic Ag-Au and Ag-Cu alloy MF substrates (with SERS enhancement factors in the range of 10^7 to 10^8) over monometallic Ag MF substrates. However, for the bimetallic substrates the top surface was found to be Ag-rich in Ag-Au, and Cu-rich in Ag-Cu MFs. Subsequently, we were unsuccessful in using the same bimetallic SERS substrates, as well as pure Ag substrates, for aliphatic thiol L-Cys detection (*vide infra*). This was due to the

susceptibility of the Ag/Cu surface to aerial oxidation, as well as less affinity of Ag and Cu towards the sulphur atom of cysteine. Therefore, a gold-rich surface in a trimetallic SERS substrate was required to facilitate the detection of important thiol-containing molecules with very small Raman scattering cross section, such as L-Cys and thiophenols. Subsequently, SERS efficiency studies were conducted for the trimetallic MFs, which showed that the MFs with an Ag-Au-Cu composition of 90-7-3 and 90-3-7 jointly registered the highest SERS efficiency, comparable to that of the best bimetallic SERS substrate. Between the two substrates, due to the higher percentage of Au on the top surface and the resulting strong Au-S binding interaction, the trimetallic substrate Ag-Au-Cu with a composition of 90-7-3 was used for the sensitive detection of L-Cys and thiophenols, with LOQ value 1 nM and 1 pM, respectively. L-Cys detection was successfully demonstrated at various pH values. Moreover, multiplexed detection of three analytes in a mixture: L-Cys, Glutathione (GSH) and thiophenol was successfully carried out using the trimetallic SERS sensor.

6.2. Results and Discussion

6.2.1. FE-SEM studies of trimetallic MFs of different composition

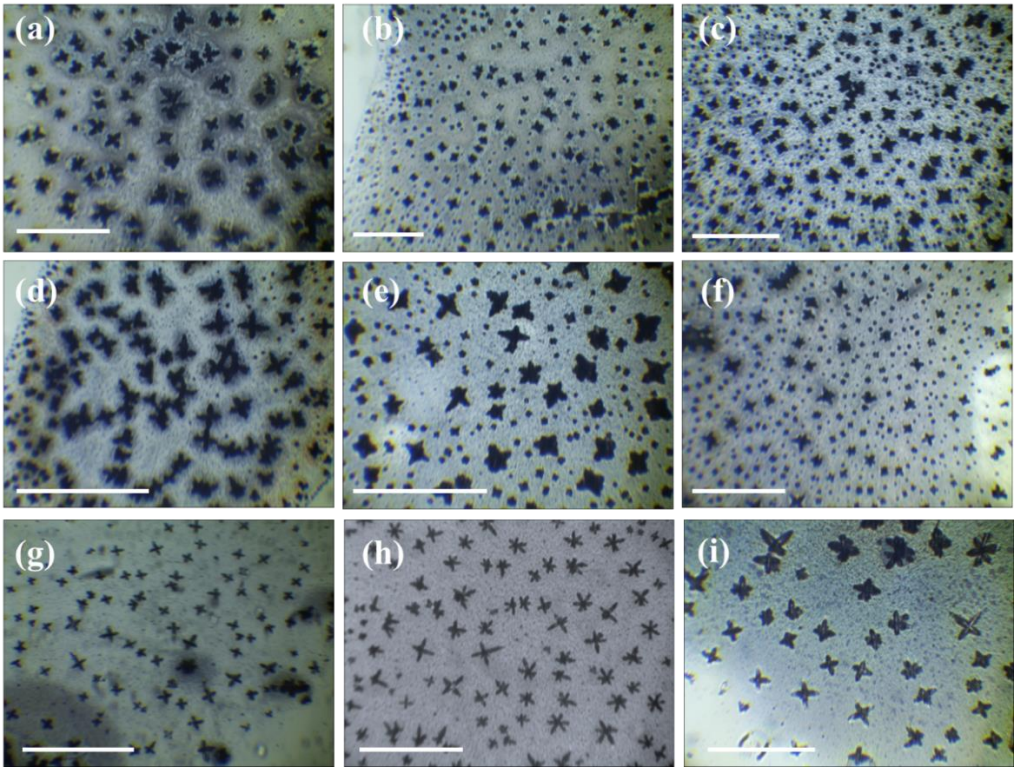

Figure 6.1. Optical images of trimetallic MFs with different compositions such as (a) TM91, (b) TM82, (c) TM73, (d) TM64, (e) TM55, (f) TM46, (g) TM37, (h) TM28, and (i) TM19. (Scale bar is 200 μm).

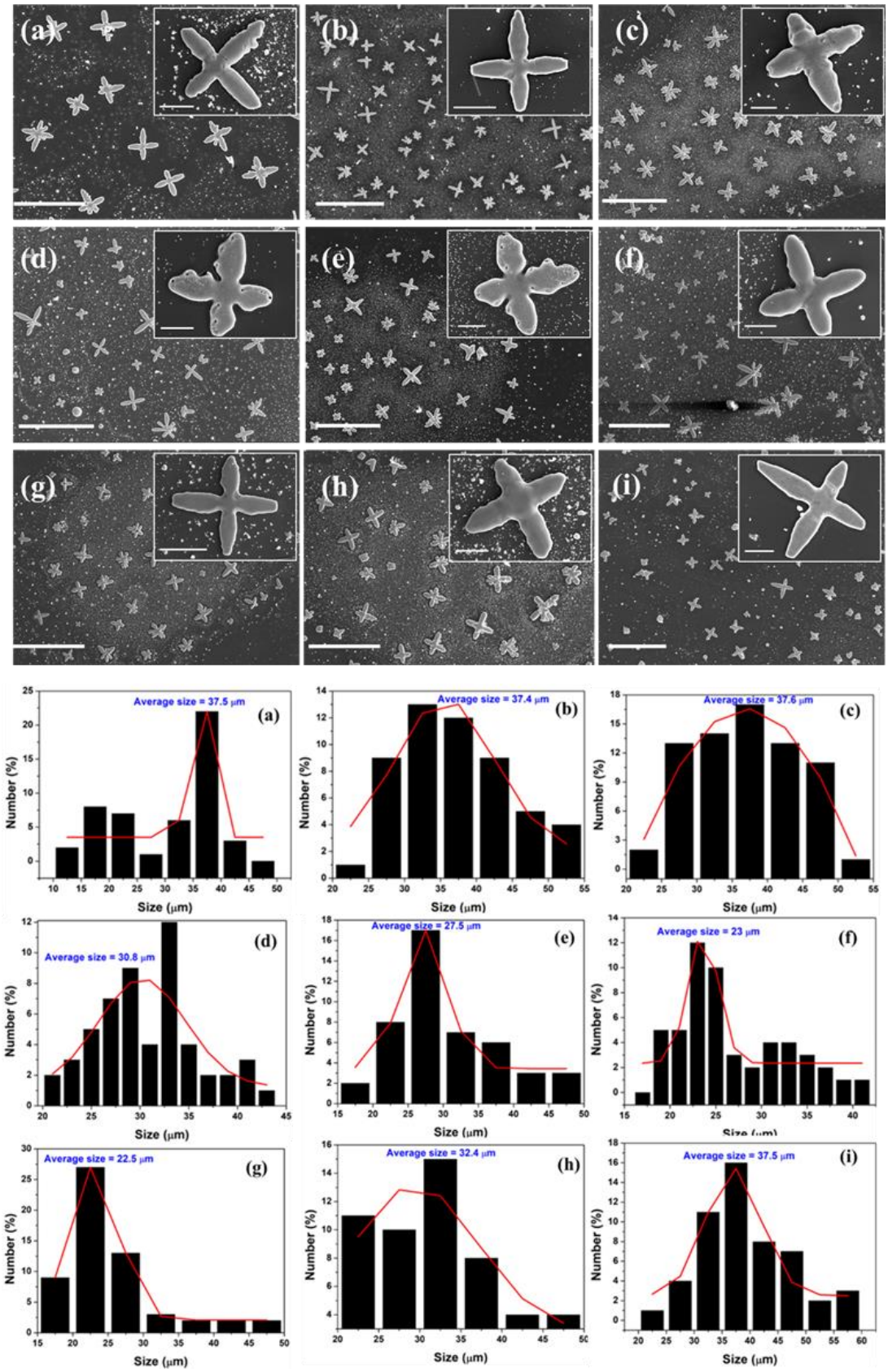

Figure 6.2. FE-SEM images of trimetallic MFs with different compositions: (a) TM91, (b) TM82, (c) TM73, (d) TM64, (e) TM55, (f) TM46, (g) TM37, (h) TM28, and (i) TM19 (scale bar in all the images is 200 μm). the inset of (a) to (i) represents the FE-SEM image of single MF at higher magnification and the scale bar is 10 μm. The histograms (a) to (i) represents the average particle size of the same.

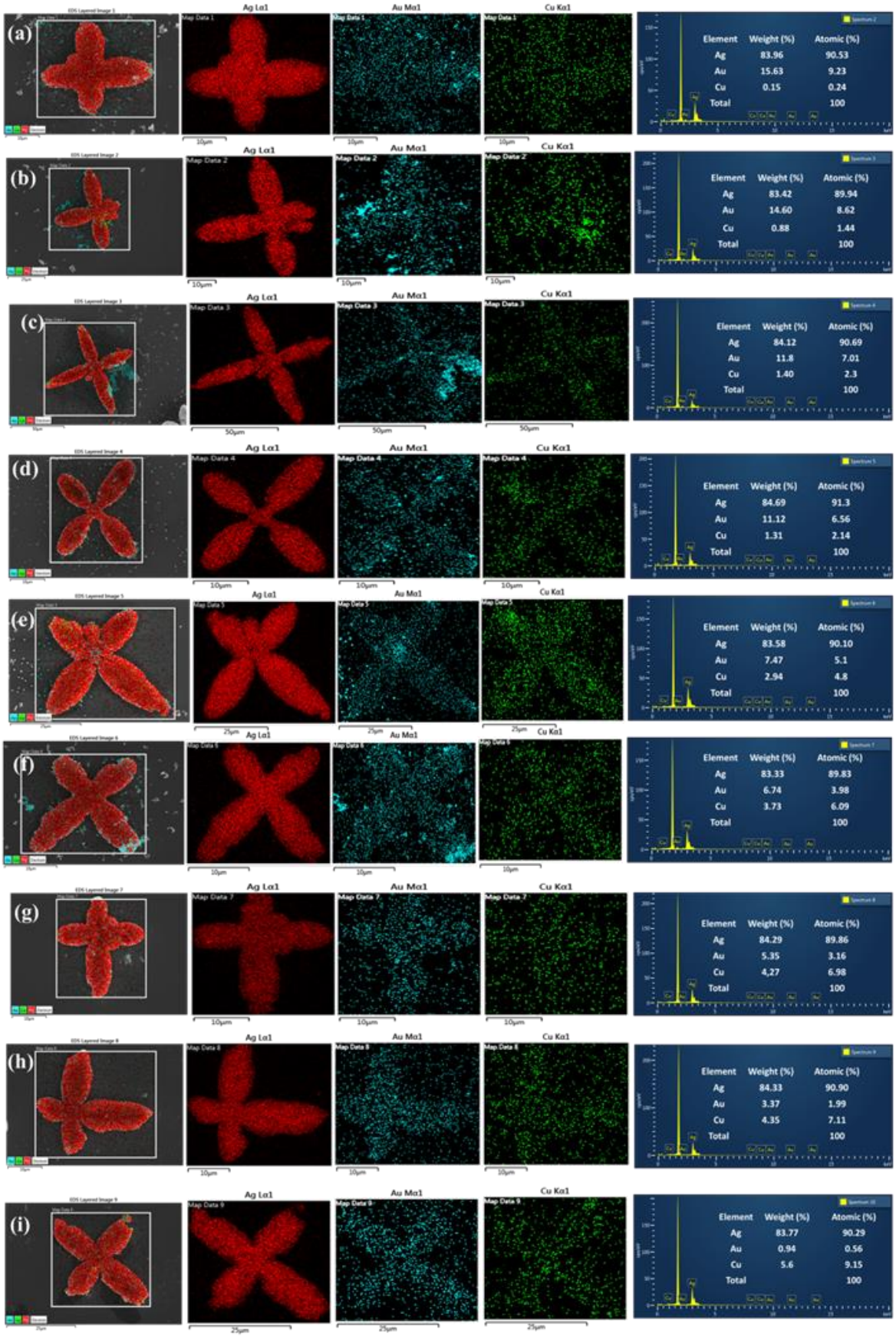

Figure 6.3. Elemental mapping and EDX (a) TM91, (b) TM82, (c) TM73, (d) TM64, (e) TM55, (f) TM46, (g) TM37, (h) TM28, and (i) TM19 MFs.

In our earlier reports, we optimized the thermolysis temperature at 250°C and 350°C for bimetallic Ag-Au (90-10) MFs and Ag-Cu (90-10) MFs, respectively, by utilizing the knowledge of the decomposition temperature of AgToABr and CuToABr. This optimization was done to obtain the best substrates with the correct morphology. Similarly, in the search for an optimum trimetallic MFs with a fixed Ag percentage (90%) and various Au and Cu percentages, the thermolysis temperature was maintained at 350°C. Subsequently, we studied the surface morphology and shape of the trimetallic Ag-Au-Cu MFs using Raman microscopy (**Figure 6.1**) and FE-SEM (**Figure 6.2a-i**). In each case, flower-like structures containing 4-6 arms were produced with minimal size variation, but the average size of the MFs differed for different compositions. The maximum size was determined to be ~38 μm for the composition TM73, whereas the minimum size of ~23 μm was registered for TM37 MFs (**Figure 6.2j-r**). Based on our previous studies, where we observed that bimetallic MFs with 90% Ag and the remaining 10% consisting of another plasmonic metal (Au or Cu) offered the best SERS performance, we limited this report to synthesizing trimetallic MFs with 90% Ag and sequentially varying the percentage of Au from 1% to 9% and Cu from 9% to 1%. Moreover, the atomic percentages of Ag, Au and Cu obtained from the elemental mapping analysis using energy-dispersive X-ray spectroscopy (EDX) for all compositions confirmed the successful alloy formation (**Figure 6.3**).

6.2.2. Structural and optical characterization of MFs using WAXS and UV-Vis studies

The structural composition of trimetallic MFs was further studied and compared with the bimetallic MFs by recording their diffraction patterns using wide angle X-ray scattering (WAXS) technique. As shown in **Figure 6.4a**, we noticed prominent diffraction peaks at 38.1° and 44.2° for Ag-Au bimetallic MFs,, corresponding to Ag (111) and Au (111), Ag (200) and Au (200) planes, respectively.[44] Since Ag and Au have similar lattice constraints, it is difficult to separate peaks arising from Ag and Au diffraction patterns. For Ag-Cu MFs three diffraction peaks were observed at 38.1° and 43.5° due to Ag, along with an additional peak at 50.4° corresponding to the Cu (200)

plane. The major difference between the diffraction patterns of Ag-Au and Ag-Cu MF substrates was the shift of the peak from 44.2° to 43.5° along with broadening, possibly resulting from the overlap of Cu (111) and Ag (200) planes. Similar to the Ag-Cu diffraction pattern, for the TM73 and remaining trimetallic MFs, we also observed three diffraction peaks at 38.1°, 43.5° and 50.4°, indicating the presence of Ag, Au and Cu.[44,45] We also recorded the WAXS spectrum for all the remaining trimetallic substrates and observed a gradual decrease in the intensity of the Ag/Au (111) peak from TM91 to TM19. Additionally, we noticed a slow increase in the peak intensity of Cu (200) when moving from TM91 to TM19, implying a decrease in Au concentration and an increase in Cu concentration in MFs (**Figure 6.4b)**, Moreover, upon deconvoluting the peak at 43.5° for TM73, we observed the presence of two peaks at 43.2° and 43.5°, corresponding to the diffraction patterns of Cu and Ag/Au, respectively (**Figure 6.4c**).

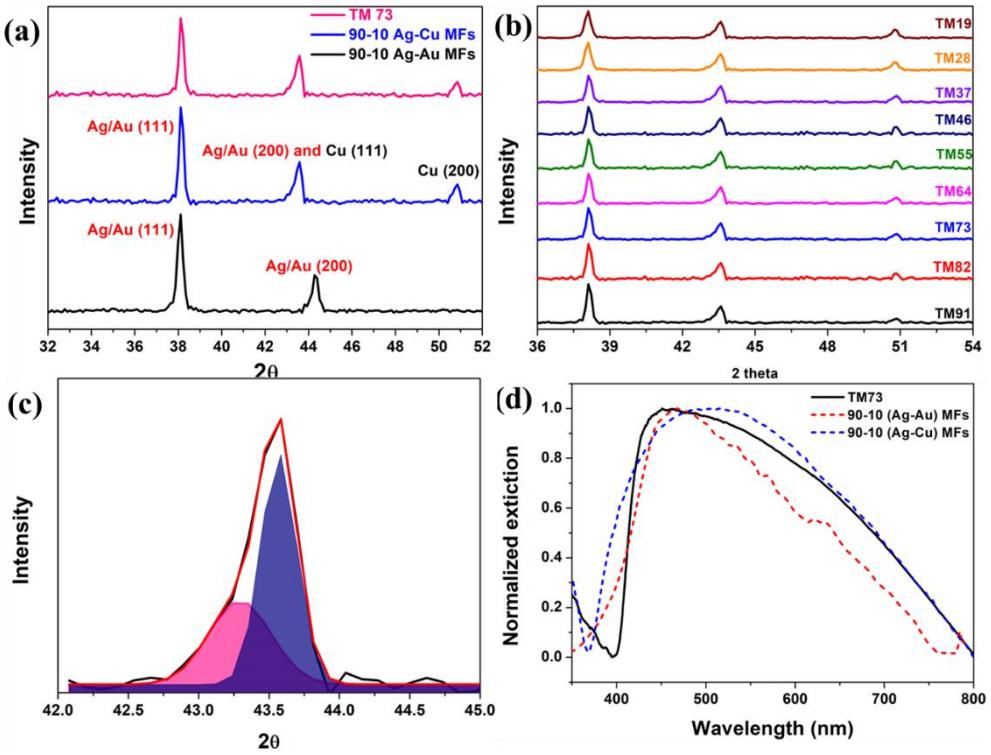

Figure 6.4. (a) WAXS patterns of 10% Ag-Au, 10% Ag-Cu and TM73 MFs, (b) WAXS patterns of trimetallic substrates from TM19 to TM91, (c) Deconvolution of peak at 43.5° of TM73 and (d) extinction spectra of (90-10) Ag-Au, (90-10) Ag-Cu and TM73

Subsequently, we recorded the LSPR extinction spectra of MFs to understand their optical properties. It is known that the extinction maxima for pure Ag, Au and Cu

nanoparticles are observed at ~400 nm, ~540 nm and ~600 nm, respectively. When we recorded the extinction spectra of TM73 MFs, a very broad band in the range of 400 nm to 800 nm was observed with a maximum at ~450 nm, as portrayed in **Figure 6.4d**. We infer that the broadness in the extinction spectra is due to the aggregation of the individual smaller nanoparticles during MF formation, which is characteristic of highly branched structures like this, due to their hybridized plasmon resonances.[30,41] Further, when we compared the extinction spectra of Ag-Au and Ag-Cu bimetallic MFs, we found that Ag-Au was less broad with LSPR maxima at 450 nm, whereas Ag-Cu was very broad with LSPR maxima at 520 nm. Therefore, a close look at the extinction spectrum for TM73 MFs ensured that it was a hybrid of the extinction spectra for (90-10) Ag-Au and (90-10) Ag-Cu bimetallic MFs (**Figure 6.4d**), supporting the formation of trimetallic hybrid nanostructures representing the plasmonic properties of Ag, Au and Cu.

6.2.3. Analysis of bulk and surface composition of the MFs using ED-XRF and XPS studies

The energy-dispersive X- ray fluorescence (ED-XRF) technique was used to study the composition of pure Ag MF and trimetallic MFs, as shown in **Figure 6.5a-c** and **Table 6.1**. We observed the characteristic Ag $K_{\alpha 1}$, Ag $K_{\beta 1}$, and Ag $K_{\beta 2}$ peaks at 22 keV, 24.9 keV, and 25.4 keV, respectively, for both pure Ag MFs and trimetallic MFs.[31,32,46] It was noted that pure Ag MF demonstrated the highest peak intensity, whereas all the other trimetallic MFs displayed lower intensities compared to that of pure Ag MFs, as shown in **Figure 6.5a**. However, the intensity variation for different trimetallic MFs followed a non-monotonic dependence on the composition. We also observed peaks at 2.98 keV and 3.15 keV corresponding to Ag $L_{\alpha 1}$ and Ag $L_{\beta 1}$, respectively, as depicted in **Figure 6.5b**. Furthermore, for trimetallic substrates, we noticed peaks matching to Cu $K_{\alpha 1}$ and Cu $K_{\beta 1}$ at 8.03 and 8.91 keV, respectively, and a peak corresponding to Au L_{α} at 9.7 keV, as depicted in **Figure 6.5c**. [31,32,45,46] A sequential decrease (Au L_{α} at 9.71 keV) and increase (Cu $K_{\alpha 1}$ at 8.03 keV) in the peak intensities with the change in the composition of Au and Cu indicated the formation of trimetallic hybrid alloy structures (**Figure**

6.5c), with a fixed Ag percentage. As expected, we didn't observe any peaks pertaining to Cu $K_{\alpha 1}$, Cu $K_{\beta 1}$ and Au L_{α} in pure Ag MFs. The Ag, Au and Cu elemental compositions of the substrates obtained from ED-XRF are presented in **Table 6.1**, which displays a decent agreement between the feed and the resulting ratios.

Table 6.1. Elemental compositions of Ag, Au and Cu obtained from ED-XRF in pure Ag, bimetallic Ag-Au, Ag-Cu and trimetallic Ag-Au-Cu MFs of different compositions.

Substrate	Bulk composition obtained from XRF		
	Ag	Au	Cu
Pure Ag	100	0	0
TM91	92.0	6.3	1.7
TM82	91.8	6.1	2.1
TM73	91.3	5.4	3.3
TM64	90.4	5.1	4.5
TM55	89.9	4.6	5.5
TM46	90.4	3.4	6.2
TM37	91.4	2.3	6.3
TM28	90.6	1.3	8.1
TM19	90.2	0.7	9.1

Subsequently, in order to understand the valence states of the metals and surface composition of the MFs, XPS studies were performed. The XPS survey spectra were collected for the trimetallic MFs, and we observed the characteristic peaks of C, O, Ag, Au and Cu as shown in the **Figure 6.5d**. Peak calibration was done using the C 1s peak at 284.4 eV. Later, high-resolution narrow scan spectra of individual metals were collected to determine the oxidation state of these metals on the surface of MFs. It is known from prior XPS studies on Ag that, Ag^0 and Ag^{+1} hold very similar binding energies (approx. 368.2 eV and 373.2 eV corresponding to $3d_{5/2}$ and $3d_{3/2}$, respectively) that are difficult to distinguish due to instrument's resolution limit of ~0.45 eV. This remarkably close binding energy between 0 and +1 oxidation states of Ag is believed to be due to the positive charge generation in the zero-valent state itself.[31,47,48] Therefore the obtained $3d_{5/2}$ and $3d_{3/2}$ peaks of Ag at 367.9 eV and 373.9 eV, respectively (**Figure 6.5e**) for pure Ag MF and trimetallic MFs, indicates the presence of Ag as both Ag^0 and Ag^{+1}. Similarly, we collected the high-resolution narrow scan spectrum for Au in the range of 80 eV to 94 eV and observed the peaks matching to Au

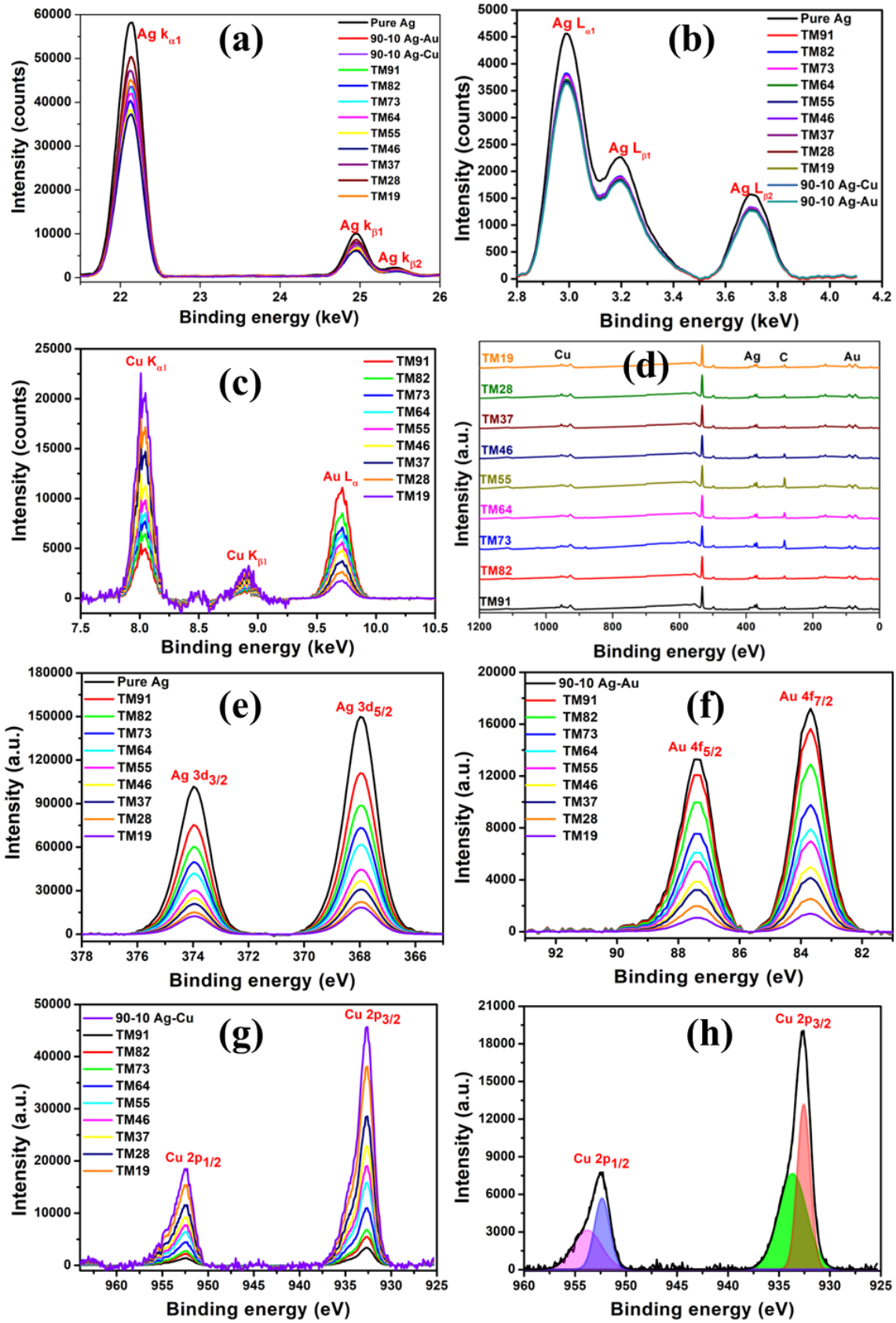

Figure 6.5. ED-XRF spectra of pure Ag MF and trimetallic MFs: (a) Ag $K_{\alpha1}$, Ag $K_{\beta1}$, and Ag $K_{\beta2}$ peaks; (b) XRF spectra of Ag $L_{\alpha1}$ and Ag $L_{\beta1}$ peaks; (c) Cu $K_{\alpha1}$, Cu $K_{\beta1}$ and Au L_{α} peaks; (d) XPS survey spectra of all TM MFs; High resolution XPS spectra of (e) Ag 3d, (f) Au 4f, (g) Cu 2p of trimetallic MFs and (h) deconvolution of Cu 2p spectra of TM73.

$4f_{5/2}$ and $4f_{3/2}$ at 87.3 eV and 83.6 eV respectively, as displayed in **Figure 6.5f**. These peaks indicate the presence of Au in its metallic Au^0 state.[49,50] Later, we also performed a high- resolution XPS scan of Cu and found two asymmetric peaks at 952.5 eV and 932.6 eV, corresponding to Cu $2p_{1/2}$ and Cu $2p_{3/2}$, respectively (**Figure 6.5g**).[51-53] On deconvolution, we noticed the presence of spin orbit doublets at two different binding energies of 932.2 eV and 952.8 eV for Cu^0 and at 934.7 eV and 953.8 eV for Cu^{+2}, individually confirming the presence of Cu in both Cu^0 and Cu^{2+} state as portrayed in **Figure 6.5h**. However, the peak intensities of Cu^0 were higher than those of Cu^{2+}, indicating that most of the copper is in zero-valent state rather than the bivalent state, indicating lesser oxidation. However, the most astounding result was obtained from the calculation of surface composition (**Table 6.2**), which indicated that the surface composition with respect to Ag, Au or Cu percentage was significantly different compared to their respective feed ratios, resulting in the top surface of the MFs being either Au or Cu-rich. This is ideal as a trimetallic substrate with an Au-rich surface. If it produces a comparable SERS EF of 90-10 Ag-Cu bimetallic MF, it can be easily exploited for the detection of L-Cys, as it may enable the covalent linkage between sulfur atom of L-Cys and the metal surface.

Table 6.2. Surface compositions of trimetallic Ag-Au-Cu MFs of different compositions obtained from XPS.

Substrate	Surface composition obtained from XPS		
	Ag	Au	Cu
Pure Ag	100	0	0
TM91	26.3	72.1	1.8
TM82	22.6	68.7	8.7
TM73	21.9	61.5	16.6
TM64	7.1	57.2	35.7
TM55	9.1	45.6	45.4
TM46	4.9	31.5	63.6
TM37	4.8	21.3	73.8
TM28	2.5	18.8	78.6
TM19	2.8	12.4	83.8

6.2.4. SERS Efficiency studies with trimetallic MFs

The SERS efficiency was measured for all the trimetallic substrates of various compositions, using Rhodamine 6G (R6G) as a probe molecule. On freshly prepared trimetallic MF substrates, 1 μM R6G solution in methanol was drop-cast, followed by irradiation with 532 nm laser light. As can be seen from **Figure 6.6a**, the highest SERS intensity of R6G was produced on TM73 among other trimetallic substrates, making it the best possible trimetallic alloy MF substrate in this study. When comparing the SERS intensities obtained from TM73 with the SERS performance of pure Ag, bimetallic Ag-Au, and Ag-Cu MFs, TM73 showed a similar SERS efficiency as (90-10) Ag-Cu MFs. Moreover, it was found to be superior compared to pure Ag and (90-10) Ag-Au MFs.[31,32] SERS intensity of R6G on (90-10) Ag-Cu MFs was used as a benchmark standard, since (90-10) Ag-Cu MFs produced the highest SERS EF (~10^8) among any other MF substrate produced by us. We collected the SERS spectra from the centre of the MFs to maintain uniformity. Furthermore, as shown in detail in our earlier reports, only a small variation in SERS intensities of the probe molecules was observed across different MFs with no change in the order of magnitude, indicating the reliability of the measurement technique.

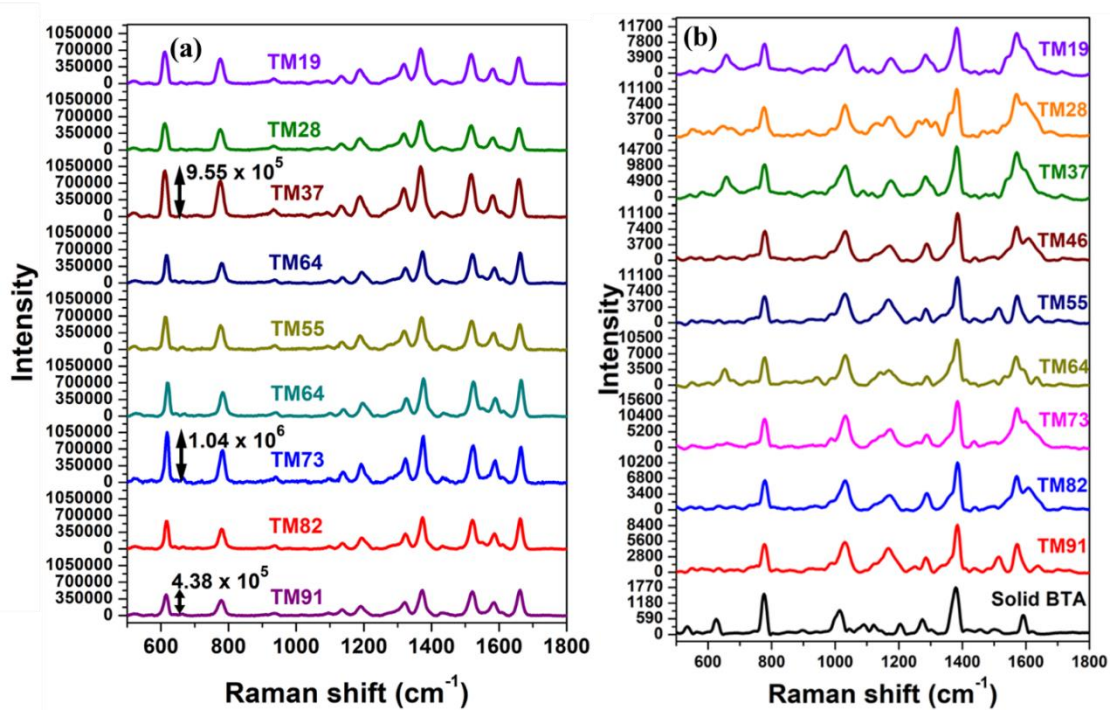

Figure 6.6. (a) SERS spectra of 1 μM R6G in methanol, adsorbed on trimetallic MFs of different compositions; (b) Normal Raman spectra of solid BTA powder and SERS spectra of BTA on all TM MFs.

Subsequently, the SERS enhancement factor (EF) of the trimetallic MF substrates was calculated using the reporter molecule 1,2,3-benzotriazole (BTA). The SERS EF is calculated based on the relative measure of the number of reporter molecules on the MF substrate that produces the similar Raman intensity of representative peaks, under normal (bulk, non-SERS) condition. The SERS spectra of BTA on different MF substrates and bulk condition, are provided in **Figure 6.6b**, and the detailed method to obtain the EF can be found in our previous report. [31,32] For a certain composition of the MF, the EF was calculated from ten randomly selected MFs on the same coverslip, and the calculated average EF for different MFs is displayed in Table 3. As shown in **Table 6.3**, the EF of TM73 (9.2 x 10^7) and TM37 (9.3 x 10^7) substrates was found to be similar and comparable to that of the 90-10 (Ag-Cu) bimetallic MFs (9.7 x 10^7), qualifying them as suitable SERS substrates for further exploration in the detection of L-Cys. However, the main difference between TM73 and TM37 substrates is the composition of the top surface, with TM73 being Au-rich and TM37 being Cu-rich. Therefore, we expect a difference in efficiency between them for SERS-based detection of L-Cys.

Table 6.3. SERS Enhancement factors of different MFs of different compositions.

Substrate	Enhancement factor
90-10 Ag-Cu	9.7×10^7
TM91	5.5×10^7
TM82	6.7×10^7
TM73	9.2×10^7
TM64	6.8×10^7
TM55	7.3×10^7
TM46	6.7×10^7
TM37	9.3×10^7
TM28	8.5×10^7
TM19	8.8×10^7

We collected the SERS spectra from the center of the MFs to maintain uniformity. Furthermore, as shown in detail in **Figure 6.7 & 6.8**, only a small variation in SERS intensities of R6G was observed across different MFs with no change in the order of magnitude and a less than 7% standard deviation value as shown in **Table 6.4.**,

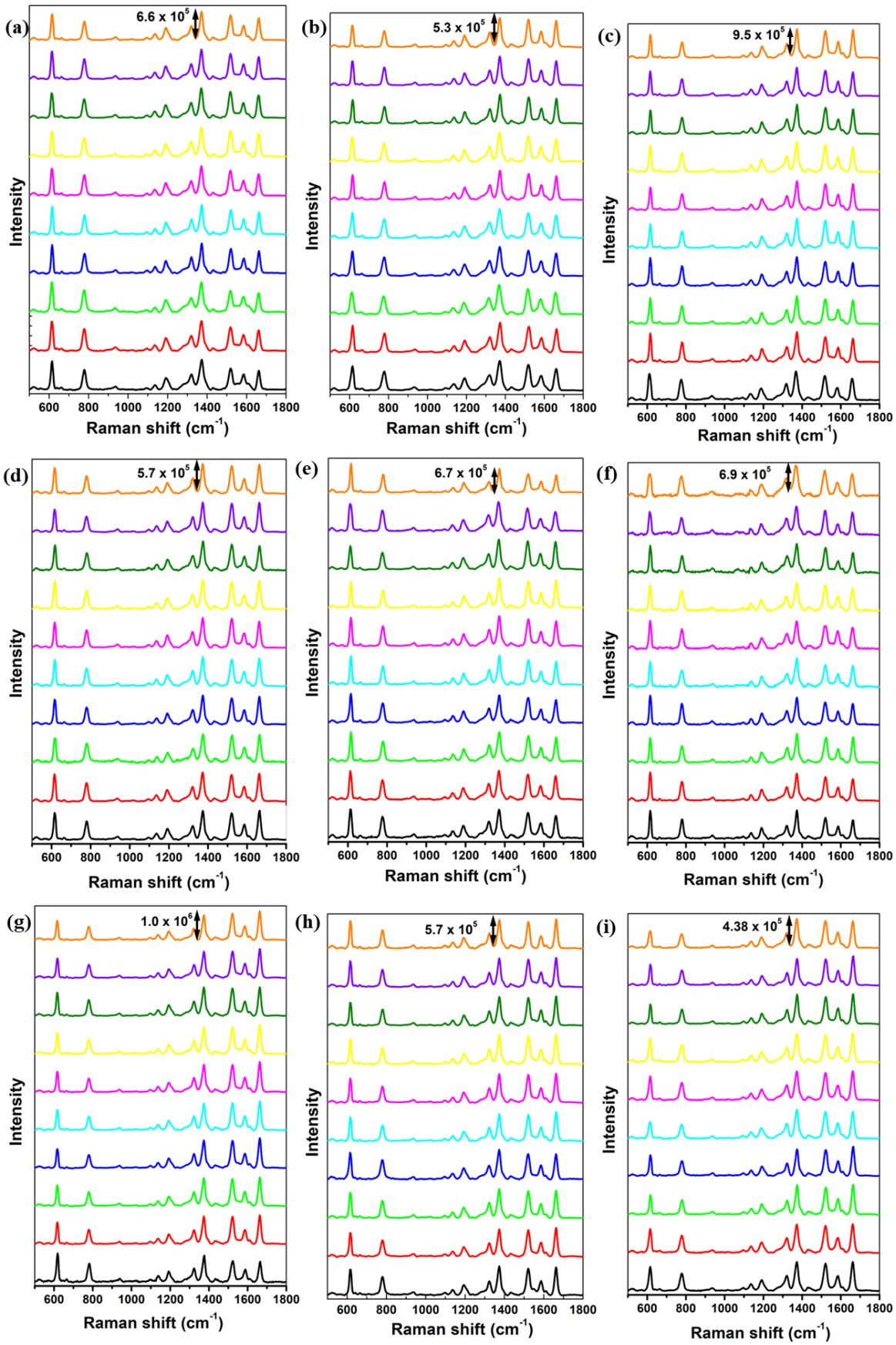

Figure 6.7. SERS spectra of 1 μM R6G on (a) TM19, (b) TM28, (c) TM 37, (d) TM 46, (e) TM 55, (f) TM 64, (g) TM 73, (h) TM 82, and (i) TM 91. The spectra are collected from 10 different microflowers.

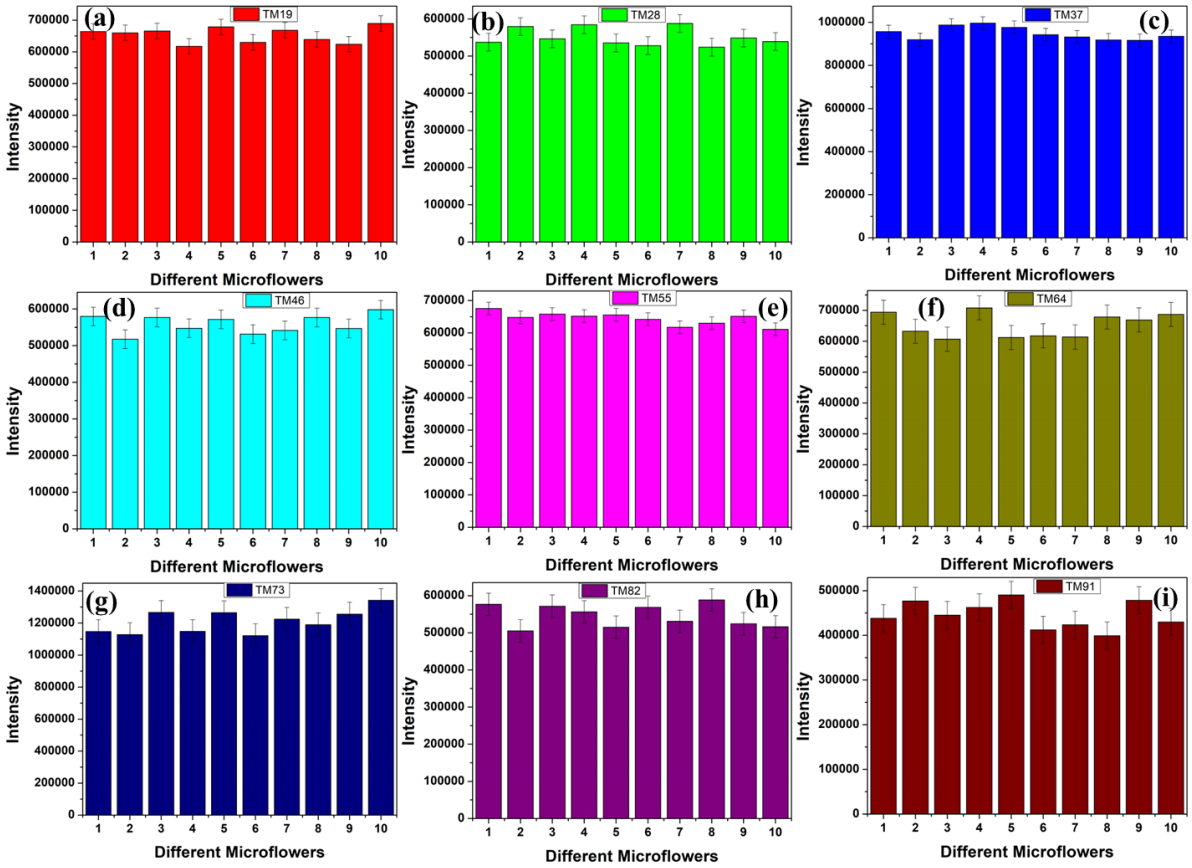

Figure 6.8. Histograms showing SERS intensities of 1 μM R6G on (a) TM19, (b) TM28, (c) TM 37, (d) TM 46, (e) TM 55, (f) TM 64, (g) TM 73, (h) TM 82, and (i) TM 91. In each case, the histogram depicts the Raman intensity of demonstrative 1360 cm^{-1} peak of the corresponding spectra, obtained from different MFs.

Table 6.4. The relative standard errors in % of each data set of Figure 6.8.

S.No.	Substrate	Average Standard deviation (%)
1	TM19	3.74
2	TM28	4.33
3	TM37	3.13
4	TM46	4.55
5	TM55	3.03
6	TM64	6.02
7	TM73	6.11
8	TM82	5.56
9	TM91	6.88

indicating the reliability of the measurement technique. Additionally, we also evaluated the stability of the substrates over a period of time. For this, the freshly

synthesized trimetallic MFs were reduced using $NaBH_4$ and the substrates (in different coverslips) were kept safely aside. At different time points, R6G was adsorbed to a particular coverslip and SERS spectra were collected in the same way as mentioned before, till one-week time (**Figure 6.9.**). In each timepoint, the histogram depicts the Raman intensity of demonstrative 1650 cm-1 peak of the corresponding spectra from

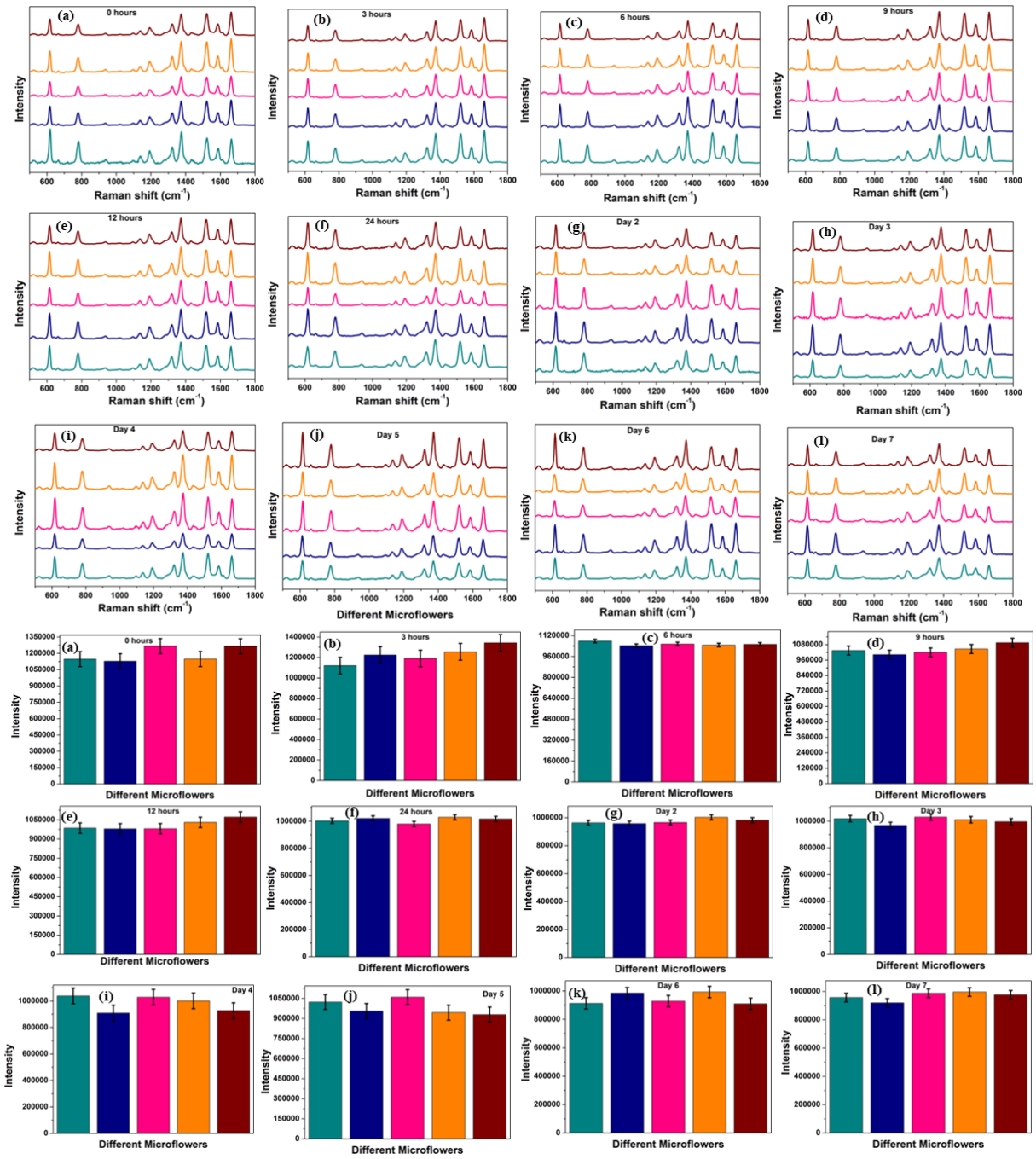

Figure 6.9. SERS spectra of R6G adsorbed on TM 73 MFs at different time intervals from immediate reduction to a week after reduction to see if there is any degradation of the substrates and the histograms represents the intensity of SERS 1650 cm^{-1} peak.

5 randomly chosen MFs present on the same coverslip. It was observed that there was a small decrease in the SERS intensity from zero hour to six hours, however the SERS intensity was found to be same from six hours to one-week time, indicating the good stability of the substrates.

6.2.5. Label-free detection of L-Cys and thiols using TM73 MF substrate.

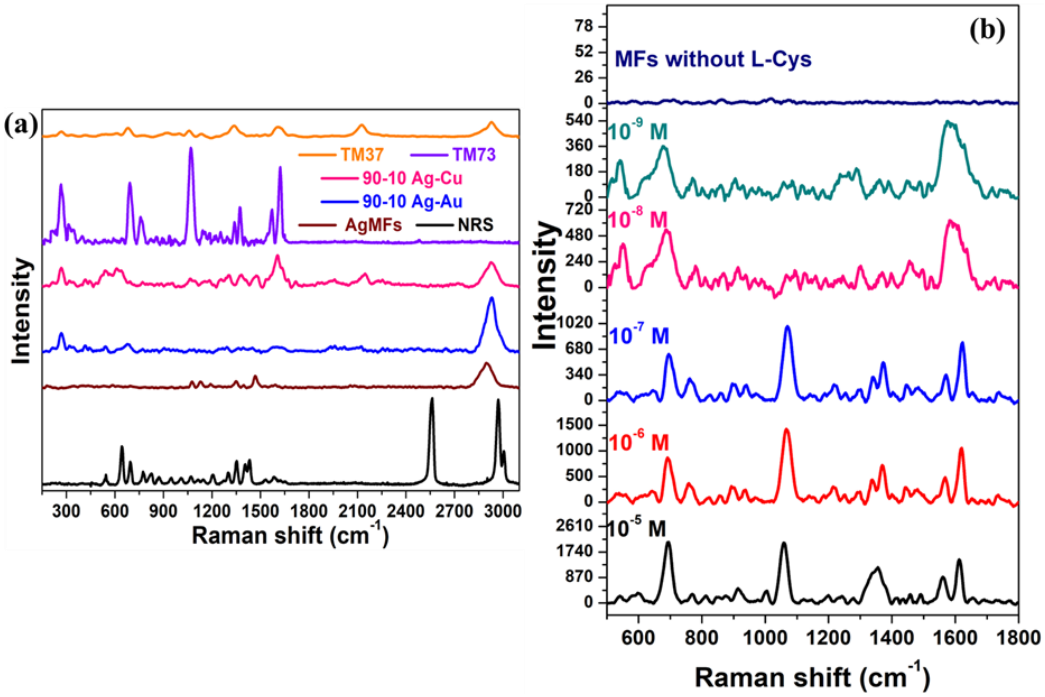

Figure 6.10. (a) Normal Raman spectra (NRS) of solid L-Cysteine powder and SERS spectra of L-Cys on different MF substrates; (b) SERS based detection of L-Cys using TM73.

Figure 6.10a compares the Raman spectra of solid L-Cys powder with the SERS spectra of L-Cys (40 µL, 10 µM solution in water) adsorbed on different MF substrates, including TM73. We recorded clear and distinct SERS peaks of L-Cys from TM73 MFs. The SERS spectra of L-Cys were found to be very different on TM73 compared to the bulk condition, due to the appearance of new peaks in SERS and the disappearance of important peaks from bulk L-Cys. One notable difference is the complete absence of the characteristic SH vibration at 2557 cm^{-1} in the bulk L-Cys spectrum, which is not present in the SERS spectrum. However, a peak at 269 cm^{-1} in the SERS spectrum confirms the Au-S vibration,[54-58] indicating the covalent linkage between sulphur and the metal. Similar observations of the disappearance of the SH peak and appearance of S-metal linkages were made for the other SERS substrates such as pure Ag MF,

bimetallic Ag-Au and Ag-Cu MFs, and even TM37 MFs. However, the signal-to-noise ratio of the peaks in those substrates was found to be very poor (**Figure 6.10a**). The highest SERS intensity of L-Cys was observed with TM73 among all MF substrates, which is consistent with earlier obtained XPS data indicating an Au-rich surface in TM73 MFs. This result highlights the importance of optimizing the surface composition in SERS, especially for molecules like L-Cys where specific adsorbate-adsorbent interactions play a major role. We can safely conclude that L-Cys forms a stronger bond with Au of TM73 substrate compared to Ag or Cu, as it is known from earlier reports that Au has the highest affinity towards sulphur compared to Cu and Ag, with the affinity order being Ag<Cu<Au.[59] Therefore, due to the very weak adsorption of L-Cys on pure Ag, bimetallic Ag-Cu (Cu-rich) and Ag-Au (Ag-rich), as well as TM37 (Cu-rich), we observed insignificant SERS enhancement of L-Cys (*vide supra*). This led us to exclude these substrates, except TM73, for further detection of L-Cys at lower concentrations.

As shown in **Figure 6.10b**, TM73 MF was successfully employed to obtain clear and resolved characteristic peaks of L-Cys at lower concentrations, with a limit of quantification (LOQ) of 1nM. This is significant as L-Cys is one of the smallest aliphatic thiols with a very small 'Raman scattering cross section (σ_{RS})' value. The σ_{RS} of L-Cys was found to be ~10^{-31} cm^2 (**Table 6.5. and calculation 6.2.6.).** Subsequently, we also explored the efficacy of the trimetallic sensor in the ultrasensitive detection of aromatic thiophenol and its derivatives such as ATP, BTP, FTP and NTP (**Figure 6.11**.). Due to the relatively higher σ_{RS} values of the aromatic thiols (σ_{RS} of thiophenol[60] and other aromatic thiols are ~10^{-30} cm^2 and ~10^{-29} cm^2, respectively) compared to L-Cys, the LOQ values were obtained as 1 pM for all except 4-NTP whose LOQ was one order less and found to be 0.1 pM. This exceptionally lower LOQ for NTP might be due to the presence of nitro substituent at the para position, making the molecule more polarizable compared to other aromatic thiophenols, leading to higher Raman scattering intensity. **Table 6.6. and 6.7.,** ESI provides a comprehensive assessment of the sensor by comparing various limits of detection (LOD) values for L-Cys and aromatic thiols reported using different analytical techniques, including SERS. As can

be seen, the LOQ value obtained in our study is much superior to the obtained LOD values from fluorescence and electrochemical sensors, as well as existing SERS-based sensors. To the best of our knowledge, this is the best LOQ demonstrated by any analytical method for the detection of aromatic thiol. This demonstrates the unparalleled efficiency of TM73 MF substrates, considering that the SERS signal of L-Cys and thiophenols is typically weak due to its small Raman scattering cross-section and low molecular symmetry.[61] Moreover, the main advantage of our sensor, compared to other SERS-based sensors, is its simple one-step synthesis, allowing for reproducible preparation of many substrates in a short time.

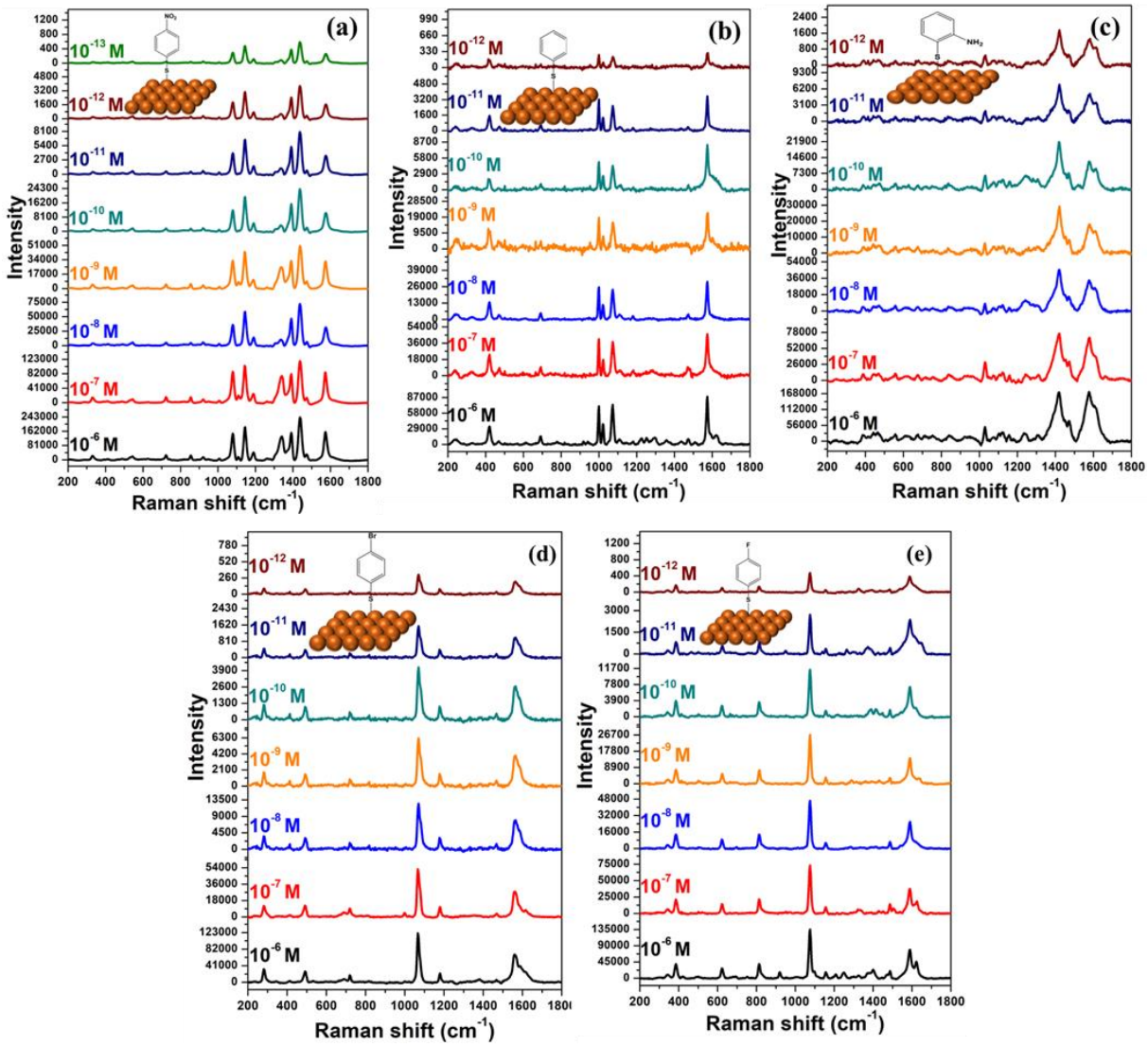

Figure 6.11. SERS spectra of different concentrations of (a) 4-nitro thiophenol (NTP), and (b) thiophenol (TP), (c) 4-Amino thiophenol (ATP), (d) 4-Bromo thiophenol (BTP), and (e) 4-Fluoro thiophenol (FTP).

Table 6.5. Calculated σ_{RS} values of L-Cys and other aromatic thiols. #F value is the integrated peak area under the peak of interest.

S.No	Molecule	Peak (cm^{-1})	F value#	σ_{SERS} (cm^2)	σ_{RS} (cm^2)
1	L-Cys	1069	1833	$4.33 \pm 0.13 \times 10^{-23}$	$4.46 \pm 0.13 \times 10^{-31}$
		1570	752.3	$1.75 \pm 0.14 \times 10^{-23}$	$1.83 \pm 0.14 \times 10^{-31}$
2	TP	1072	14496.3	$3.42 \pm 0.17 \times 10^{-22}$	$3.53 \pm 0.17 \times 10^{-30}$
		1573	23817.9	$5.63 \pm 0.18 \times 10^{-22}$	$5.80 \pm 0.18 \times 10^{-30}$
3	ATP	1473	48767.6	$1.15 \pm 0.10 \times 10^{-21}$	$1.18 \pm 0.10 \times 10^{-29}$
		1576	293805	$5.67 \pm 0.09 \times 10^{-21}$	$5.84 \pm 0.09 \times 10^{-29}$
4	FTP	1075	79506.1	$1.88 \pm 0.19 \times 10^{-21}$	$1.93 \pm 0.19 \times 10^{-29}$
		1589	79917.2	$1.89 \pm 0.14 \times 10^{-21}$	$1.94 \pm 0.14 \times 10^{-29}$
5	BTP	1066	79808.9	$2.28 \pm 0.11 \times 10^{-21}$	$2.94 \pm 0.11 \times 10^{-29}$
		1560	26031.7	$5.34 \pm 0.16 \times 10^{-21}$	$5.51 \pm 0.16 \times 10^{-29}$
6	NTP	1144	112819.6	$2.66 \pm 0.17 \times 10^{-21}$	$2.75 \pm 0.17 \times 10^{-29}$
		1437	199288	$4.71 \pm 0.13 \times 10^{-21}$	$4.85 \pm 0.13 \times 10^{-29}$

6.2.6. Calculation of Raman cross section:

We calculated the Raman cross section (σ_{RS}) of L-Cys as well as aromatic thiols. The procedure for calculating Raman cross section was taken from literature. The first thing to be noted for calculating σ_{RS} is noting down the Raman photon flux (F) which is the integrated area under the peak of interest after subtracting the background. Then the Raman collection (η_c) efficiency was given by the expression

$$\eta_c = D^2/16n^2f^2$$

where D and f are the diameter and the focal length of collection objective lens respectively and n is the refractive index of the analyte used. η_c is calculated and found as ~ 0.01.

Then scattered Raman power (PRS) is given by the equation: $P_{RS} = Fh\nu p/\eta_c$

Where $h\nu_p$ is photon pump energy which is equal to 3.69×10^{-19} J for 532 nm laser. Raman scattering efficiency is given as

$$\eta_{RS} = P_{RS}/P_P$$

Where Pp is the laser power incident on the substrate. SERS cross section (σ_{SERS}) is given as

$$\sigma_{SERS} = \eta_{RS} / N$$

where N is the number of the molecules per cm^2 and Raman scattering is given as the division of σ_{SERS} by enhancement factor of the substrate used,

$$\sigma_{RS} = \sigma_{SERS} / EF$$

Considering the absorption spectra of thiols **(Figure 6.12a.)** used and the laser wavelength used, we can tell the absorption bands are non-resonant with the laser wavelength and the enhanced signals are solely due to SERS rather than surface enhanced resonance Raman spectroscopy (SERRS).

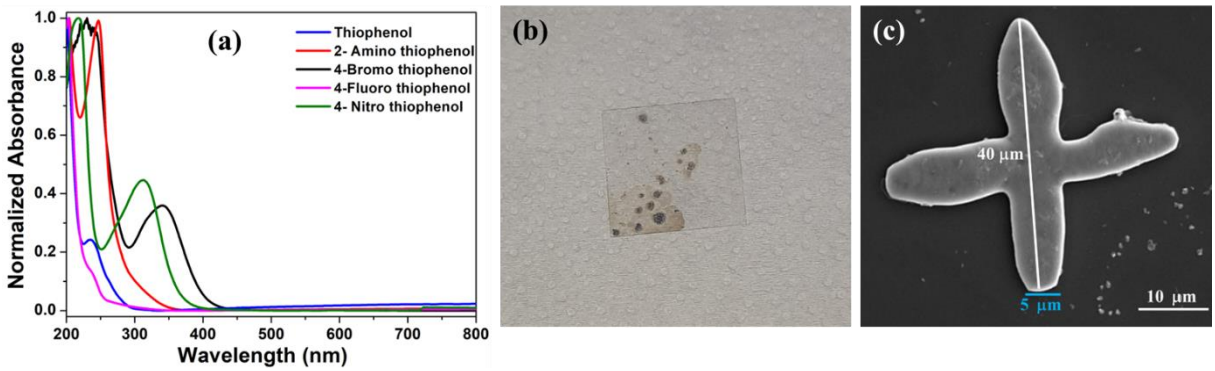

Figure 6.12. (a) Absorbance spectra of Aromatic thiols, (b) picture of a coverslip showing the formation of MFs in patches, and (b) SEM image of the TM73 MF showing length and width of MF arm.

The number of molecules (N) is calculated as follows:

Area of the coverslip used for substrate synthesis = 2 × 2 = 4 cm^2

Area of Microflowers (Average arm size = 40 µm) = 40 µm × 40 µm = 1600 $µm^2$

Therefore, average number of MFs formed on the coverslip (if we assume it is 100% occupied by MFs) is given as = 4 cm^2 / 1600 $µm^2$

$$= 4\ cm^2 / 1600 \times 10^{-8}\ cm^2$$

$$= 25 \times 10^4\ MFs$$

But, MFs are formed in patches as shown in the **(Figure 6.12b)** and assuming only 20% of coverslip is occupied by MFs, then the number of MFs would be ~ 50000 MFs. We then calculated the effective area occupied by these 50000 MFs as the following.

Effective area occupied by a single MF of length = 40 μm and width = 5 μm is 200 μm² (length × width) and there are 2 arms, therefore the total effective area occupied by MFs with 2 arms is 400 μm² (See **Figure 6.12c)**. The effective area occupied by 50000 MFs is given as = 50000 × 400 μm² = 200 × 10^{-3} cm² and the number of molecules present in the effective area: 24 x 10^{12} molecules (40 μL of 10^{-6} M solution was spread). So, Number of molecules/cm² is 0.12 × 1015.

Table 6.6. A comparison of LOD values of L-Cysteine using different analytical methods including SERS.

S.No.	Method of detection	Substrate	LOD	References
1	Absorption	Mesoporous nickel oxide nanoflowers	1.1 μM	62
2	Circular dichroism	Metal coordinated polymers	1.55 μM	63
3	Colorimetry	Covalent organic framework	0.05 ~ 8 μM	64
4		Citrate capped silver nanoparticles	5.1 nM	65
5		Rutile TiO2 NPs	2 μM	66
6		BiVO4 Nanoparticles	0.569 μM	67
7		CuNPs	0.10 μM	68
8		CeO_2/CoO nanocomposites	3.71 μM	69
9		Ru@V_2O_4 nanocomposite	0.139 μM	70
10		Carbon dots	12 nM	71
11	Electrochemical	Multi walled Carbon nanotubes	0.04 ± 0.001 μM	72
12		Ni2P nanocrystallines anchored on black phosphorus nanosheets	2 nM	73
13		β-MnO2 nanowires modified glassy carbon	70 nM	74
14		in-situ poly(Cys) modified SPGE	5.5 μM	75
15	Fluorescence	Carbon quantum dots	0.045 μM	76
16		Photonic crystal Film	3.23 nM	77
17		tetrahydro-acridine salt hybrid coumarin dye	46 nM	78
18		Rhodamine based probe	7.5 nM	79
19		benzothiazole moiety	0.58 μM	80
20		Lyso-CDC	14.4 nM	81
21		BODIPY based probe	11.2 nM	82
22		Ln–K–MOFs	0.149 μM	83
23		Carbon dots	0.036 μM	84

24		Chlorinated coumarin–benzothiazolium	0.5 nM	[85]
25		vinyl-functionalized carbon dots	42.48 nM	[86]
26		phenanthrene[9,10-d] imidazole derivatives	215.64 nM	[87]
27		7-(IDF), a phenylalanine derivative	24.3 μM	[88]
28		pyrene-based probe	0.446 μM	[89]
29		nanoprobe Nano-PH1	89 nM	[90]
30		ZHJ-X probe	3.8 μM	[91]
31		Dopamine functionalized CuO NPs	35 nM	[92]
32		Citrate capped CdS carbon dots	5.4 nM	[93]
33		NPY probe	0.663 μM	[94]
34		hybrid fluorescent dyad (HMN)	4.25 μM	[95]
35		ABT-MVK Probe	19 nM	[96]
36	Two photon Absorption	novel D-π-A-π-D type compounds	0.15 μM	[97]
37	SERS	Au@hg-C3N4 hybrids	10^{-8} M	[16]
38		chiral shuriken-shaped plasmonic structures	10^{-8} M	[14]
39		Wrinkled Aluminum based Quantum sensor	1 nM	[15]
40		Au/SnO/Ag Heterogeneous Films	0.1 nM	[17]
41		Ag-Au-Cu Microflowers	1 nM (LOQ)	This work

Table 6.7. A comparison of LOD values of Aromatic thiols using different analytical methods including SERS.

S.No.	Name of Thiophenol	Method of detection	Substrate	LOD	References
1	Aromatic thiols	Colorimetry	Spiropyran	40 μM	[98]
2	Thiophenol	Fluorimetry	BODIPY	34 nM	[99]
3	Aromatic thiols		Resorufin–dinitrophenyl	70 nM	[100]
4	4-Nitro thiophenol and 4-Amino thiophenol	SERS	Nano structured gold	1 mM	[101]
5	L-Cysteine and Aromatic thiols		AuNPs	10 nM	[102]

6	Thiophenol		Au films decorated by AgNPs	0.1 nM	[103]
7	Thiophenol, Amino thiophenol, Fluro thiophenol, Bromo thiophenol		Ag-Au-Cu Microflowers	1 pM (LOQ)	This work
8	Nitro thiophenol		Ag-Au-Cu Microflowers	0.1 pM (LOQ)	This work

6.2.7. Detection of L-Cysteine at different pH to understand the adsorption morphology

The most important factor that influences the adsorption morphology of L-Cys on the metal surface is the solution pH because L-Cys molecules contain three different functional groups: amine, carboxyl and thiol. Depending on the pH, the formation of anionic, zwitterionic, or cationic species of L-Cys can promote additional adsorption possibilities, leading to an enhancement of the Raman signal. Therefore, identifying the correct vibrational fingerprints of L-Cys as a function of solution pH will enable us to understand the adsorption morphology of L-Cys correctly in our SERS measurement. **Figure 6.13a.** shows the SERS spectra of aqueous solutions of L-Cys at different pH values (ranging from acidic to basic) adsorbed on TM73. In all pH conditions, we can identify the presence of an Au-S bond at 268 cm^{-1}, indicating that the L-Cys molecule binds to the Au surface by forming an Au-S covalent linkage. However, progressively stronger Au-S interaction was observed as the pH increased, resulting in the highest SERS intensity of the peak at pH 13. As a result of the stronger Au-S covalent linkage at higher pH, the C-S bond of L-Cys becomes more rigid, and the Raman intensity of the band at 690 cm^{-1} decreases sequentially with the increase in pH, disappearing completely at pH 13. In flexible bonds, there is greater freedom for electron cloud deformation, allowing for the redistribution of their charge density in response to an external electric field. This leads to higher polarizability and intense Raman signals. However, in more rigid chemical bonds, there is limited freedom for electron cloud deformation, resulting in less easily distorted electron density. Therefore, the polarizability of the C-S bond tends to be lower, leading to very weak or no Raman

signal at higher pH. In contrast to the disappearing C-S vibration peak with an increase in pH, the CSH bending vibration at 758 cm^{-1} increases with the increase in pH, possibly due to higher polarizability of the group resulting from changes in the environment.

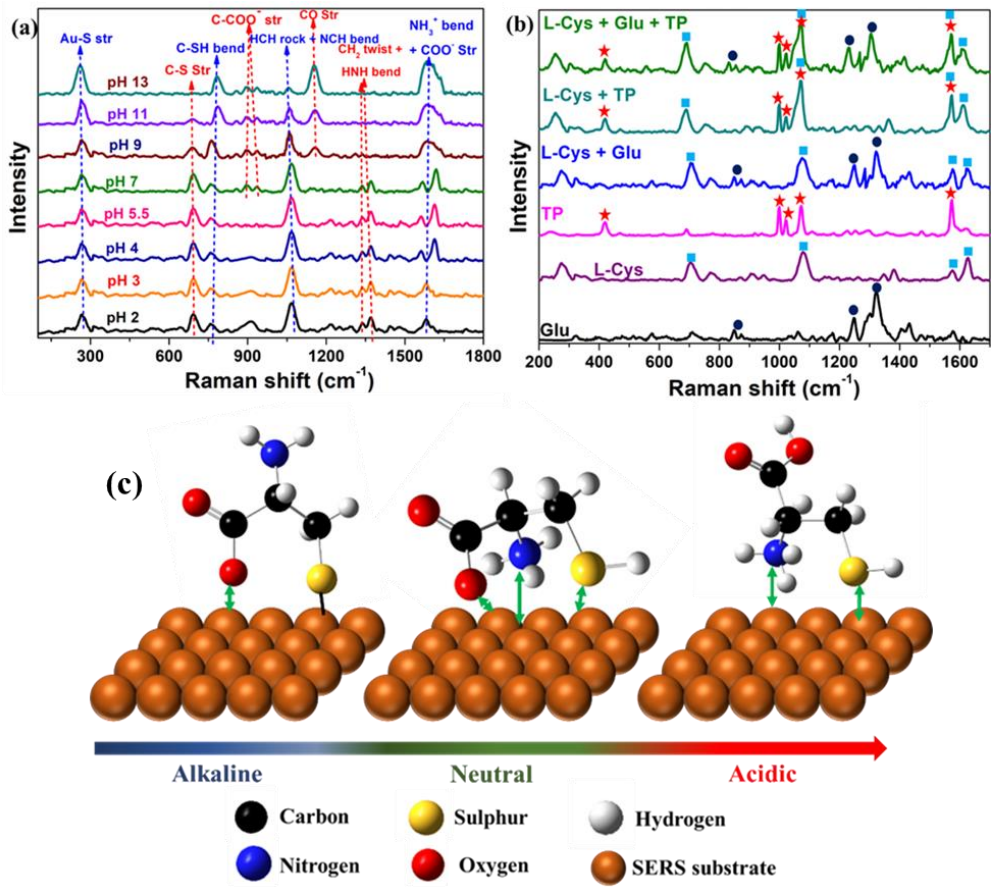

Figure 6.13. (a) SERS spectra of 1 μM L-Cys adsorbed on TM73 at different pH; (b) Multiplexed SERS spectra of 1 μM solutions of L-Cys, GSH and 1 nM TP together in water (red stars represent the peaks arising from TP, navy dots represent GSH peaks and cyan squares represent peaks corresponding to L-Cys. **Scheme 6.1.** A schematic representation of L-Cys adsorption on TM73 Trimetallic MFs with Au rich surface.

Moreover, we have also noticed prominent changes in the corresponding Raman peaks arising from the -COOH and -NH_2 groups, moving from acidic to alkaline pH (**Figure 6.13a and Table 6.8.**). While the peak at 914 cm^{-1}, due to HCN bend from the -NH_2 group, was prominent at pH 2 but disappeared at pH 5.5, the twin peaks of C-COO bend at 899 cm^{-1} and 934 cm^{-1} appeared only at pH 7, but they maintained same intensity throughout the alkaline pH range. This result can be explained based on different conformations and thereby different adsorption morphologies of L-Cys on the Au surface at different pH levels, as shown in **Figure 6.13c**. It was presumed that NH_3^+

and COO^- demonstrate prominent interactions with the Au surface under acidic and alkaline pH conditions, respectively. No SERS signals or very weak signals were observed if the groups were far from the TM73 surface, whereas for the groups which were close the Au surface, the increase in the signal was observable. At neutral pH, L-Cys exists in zwitterionic form and remains in a stable conformation, where both NH_3^+ and COO^- are close to the gold surface. This adsorption behaviour of L-Cys was further supported by the weakening of the 1072 peak (HCH rock + NCH bend) at higher pH, while the appearance of the new peak at 1160 cm^{-1} (CO stretch) at pH 9 continued until pH 13 with increasing intensities. Furthermore, the vibrations ascribed to CH_2 twist and HNH bend were clearly visible at 1341 cm^{-1} and 1369 cm^{-1} until pH 7 and disappeared afterwards. The broad peak at 1577 cm^{-1} was a combined vibrational signature of NH_3^+ bending and COO^- stretching. Between pH 4 to 7, the broad peak was separated into two resolved peaks at 1520 cm^{-1} (COO^- stretch) and 1620 cm^{-1} (NH_3^+ bending).

Table 6.8. Vibrational frequencies (in cm^{-1}) from the normal Raman spectrum (NRS) of L-Cys powder and SERS spectra of L-Cys solution adsorbed on TM73 MFs. Peak intensities are represented by alphabets such as VS, M, W, VW which means very strong, medium, weak, and very weak respectively.

NRS of L-Cys	SERS of L-Cys at different pH on TM73			Peak assignment
	Acidic	Neutral	Alkaline	
	266 (M)	266 (S)	266 (VS)	Au-S str
544	-	-	-	
643	-	-	-	C-N str + CCO bend
694	691 (VS)	691 (M)	688 (VW) Broad	C-S str
776	758 (W)	764 (M)	782 (S)	C-SH bend
818	-	-	-	HCS bend
869	-	893 (M)	899 (M)	C-COO^- str
940	-	937 (M)	937 (M)	
1005	914 (M) Broad	-	-	HCN bend
1063	1066 (VS)	1066 (M)	1060 (VW) Broad	HCH rock + NCH bend
1199	-	1159 (VW)	1156 (S)	CO str
1299	-	-	-	CCH bend
1344	1335	1335		CH_2 twist + HNH bend

	1369	1369	-	
1427	-	-	-	CH_2 bend
1581	1584 (Broad asymmetric)	1562	1587 (Very broad)	$^+NH_3$ bend + Asymmetric COO^- str
		1619		
2557	-	-	-	SH str
2968	-	-	-	CH str
3004	-	-	-	NH_2 str

6.2.8. SERS-based multiplexed detection of L-Cys, thiophenol, and GSH using TM73

To understand the efficacy of our SERS substrate in a complex matrix, we performed multiplexing based detection of L-Cys in presence of other analytes like GSH and TP. GSH is a tripeptide composed of three amino acids: cysteine, glutamic acid, and glycine. It can potentially interfere with the detection of L-Cys, depending on the specific method used for detection. Fluorescence-based sensing is the most commonly used analytical technique for the detection of L-Cys[104-106] as it provides a fast and sensitive response when the -SH group of L-Cys interacts with the organic probe molecule. However, in the biological sample where both GSH and L-Cys are present, the suitability of the detection method relies on distinguishing L-Cys from GSH. The fluorescence-based method cannot separate the fluorescence response of potential interfering molecule GSH from the signal of L-Cys due to the structural similarity between them. Although the generated fluorescence signal by GSH is much less compared to L-Cys, it may still lead to false positives or inaccurate quantification. Many separation techniques, such as high-performance liquid chromatography (HPLC) or capillary electrophoresis (CE), can separate and resolve L-Cys from GSH based on their retention time and electrophoretic mobility, respectively, but they are tedious processes. On the other hand, thiophenols are aromatic organic sulfur containing compounds extensively used in agriculture, chemical, and pharmaceutical industries and would possess major threat to humans and also potential environment pollutant.[43] SERS is the most appropriate method to simultaneously determine the trace levels of L-Cys, GSH and TP in a mixture. To demonstrate the multiplexing capability of the TM73 SERS sensor, we prepared 1 μM solutions of L-Cys and GSH, 1 nM solution of TP

separately in water and as a mixture, and drop-cast them on trimetallic MF substrate on the cover slip. After allowing them to dry, we recorded the SERS spectra of the samples **(Figure 6.13b.)**. As shown in **Figure 6.13b.**, we observed numerous peaks for GSH in the range of 300 cm-1 to 1600 cm-1, arising from different stretching and bending vibrations of the carboxyl, amino and sulfhydryl groups of Glycine, Cysteine, and Glutamic acid skeleton of GSH. The most prominent vibrations were Au-S interaction at 322 cm^{-1}, C-CN stretching at 848 cm^{-1}, C-C Stretching at 872 cm^{-1}, N-C and C-C stretching at 1247 cm^{-1}, COO^- symmetric stretch at 1320 cm^{-1}.[107-109] We also noticed important peaks of TP at 419 cm^{-1}(C-C stretching), 999 cm^{-1}(C-C-C ring bending), 1023 cm^{-1} (C-H ring bending), 1072 cm^{-1} (C-C-C in plane vibration), and 1573 cm^{-1} (symmetric ring stretching as well as C-S stretching vibrations).[42] However, as seen in **Figure 6.13b**, when comparing the individual SERS spectra of L-Cys, TP and GSH with the SERS spectrum of the mixture, we were able to easily detect clearly resolved, intense representative Raman peaks corresponding to all analytes. Thus, this result confirms that the trimetallic label-free SERS sensor can successfully distinguish L-Cys from the interfering molecules TP and GSH in a mixture using the multiplexing method.

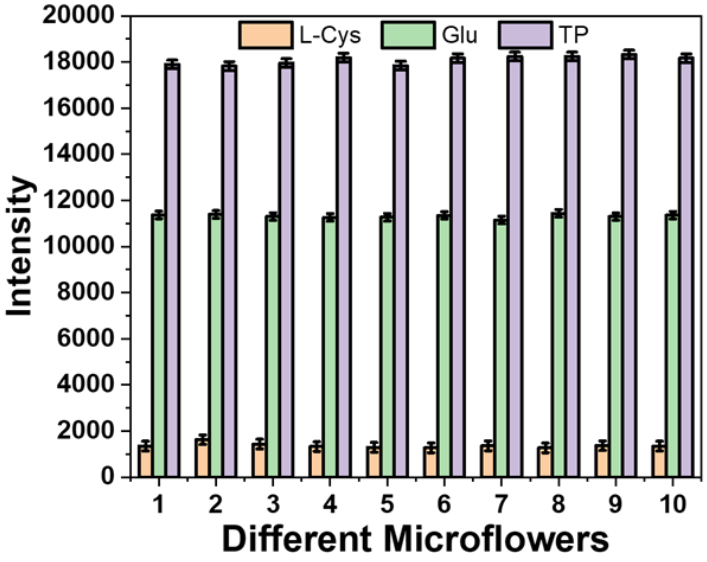

Figure 6.14. Histogram depicting negligibly small variation in SERS intensity values of 689 cm^{-1} peak of L-Cys, 1310 cm^{-1} peak of Glu, and 1576 cm^{-1} peak of TP across 10 different Microflowers on same coverslip. The standard deviation values were found to be as 3.20%, 1.60% and 0.97% for L-Cys, Glu and TP, respectively.

6.3. Conclusions and Summary

Using simple thermolysis, Ag-Au-Cu trimetallic alloy MFs of various compositions were synthesized. The percentage of Ag was kept constant, and the Au and Cu ratio was varied. The MFs were characterized in detail and successfully demonstrated as SERS-based sensors. The trimetallic MFs showed a composition-dependent SERS response for the reporter molecule R6G, with TM73 and TM37 identified as the most efficient SERS substrates. The calculated SERS enhancement factors (EFs) were found to be the same for both substrates (9×10^7), and the EF was comparable to the previously reported highest SERS EF achieved using bimetallic Ag-Cu MFs (10^8). However, XPS studies revealed significant differences in surface composition between TM73 and TM37. While Ag was common underneath both substrates, TM37 had a Cu-rich surface, while the top surface of TM73 was found to be Au-rich. Subsequently, TM73 MF substrates demonstrated SERS-based label-free detection of the small, biologically important molecule L-Cys with unprecedented efficacy, displaying one of the best limits of quantification (LOQ) values of 1nM. However, TM37 MFs produced insignificant SERS enhancement of L-Cys. The probable reason for TM73 showing much superior efficacy towards L-Cys compared to any other MF substrate could be the higher affinity of Au towards sulphur compared to Cu and Ag. This study highlights the importance of optimizing surface composition in SERS studies along with achieving the desired highest EF. L-Cys detection was possible across the complete pH range, as intense and clear SERS spectra of L-Cys were obtained at all pH values, ranging from acidic to basic pH. The variation in the specific fingerprint vibrations of L-Cys as a function of pH clearly indicated different adsorption morphologies of L-Cys on the TM73 substrate in different pH regions. While the Au-S linkage was evident across the complete pH range, L-Cys was additionally found to be adsorbed via the -COOH group at basic pH, via the $-NH_2$ group at acidic pH, and via both the -COOH and $-NH_2$ groups at neutral pH. Furthermore, TM73 demonstrated efficient multiplexing detection of L-Cys with the potential interfering analyte molecule GSH in water. Additional exploration of these trimetallic Ag-Au-Cu substrates is ongoing in our laboratory for sensing and plasmonic catalysis applications.

Chapter 7

Conclusions and Future perspectives

In this chapter, the overall work done in this thesis is presented and the future scope of the work is also discussed.

Conclusions

The main aim of this thesis was to study different plasmon enhanced spectroscopies and its use for ultra-sensitive detection of analytes and theranostics. The major areas of plasmonics covered in this thesis are metal enhanced fluorescence (MEF), Metal enhanced singlet oxygen generation (MESOG), and surface enhanced Raman spectroscopy (SERS). In this thesis, different types of nanomaterials, thin film substrates were engineered and harnessed for various plasmon enhanced studies.

In **chapter 3**, we studied the role of size of AuNPs and distance between AuNP and polymer PAH for attaining maximum MEF. The less-fluorescent reporter molecule PAH, when adsorbed on silica coated 45 nm AuNPs, was benefitted with tremendous 280-fold fluorescence enhancement compared to free PAH in homogeneous environment. The enhancement was found to depend crucially on the distance between the metal and the fluorophore, while ~11 nm being the optimum separation for the highest enhancement. Among different AuNPs, the highest enhancement was accomplished with the average diameter of 45 nm, whereas 22 nm and 60 nm particles showed moderate and lowest enhancement, respectively. Further, the PAH adsorbed fluorescent nanoparticles were demonstrated as a selective 'turn-off' sensor for picric acid in water with a detection limit of 79 nM.

In **chapter 4**, we studied the role of isotropic and anisotropic particles for simultaneous MEF and metal enhanced singlet oxygen generation (MESOG). In **chapter 4A,** a library of hybrid MNPs comprising of AuNPs, AgNPs with various spacers such as silica coating and layer-by-layer assembled polymers were synthesized by simple wet chemistry method. The neutral AIE active fluorogen NP-4-Py was adsorbed on the NPs and these theranostic PSs were ascribed for MEF and ME-SOG studies. The enhancement was noticed to depend crucially on the spacer's thickness, on which AIEgen was adsorbed. Most importantly, at an optimum distance of ~10-12 nm from the metal surface, simultaneous enhancement in fluorescence and SOG were recorded for all the theranostic PS. The probable mechanism for the enhancement was attributed mainly due to the short-range near field effect, near the plasmonic nanoparticles. The best theranostic property, with EF of 7.9 in fluorescence and EF of

10.4 in SOG, was demonstrated by AIEgen loaded Au-2LBL NPs, with a spacer thickness of ~11 nm. The superiority of Au over Ag probably lied in the fact that Ag nanoparticles were responsible for more non-radiative loss due to NSET as the extent of overlap between the extinction spectra of Ag nanoparticles was more with the AIEgens' florescence spectrum, compared to the overlap made by the AuNPs. The best combination was also used for confocal imaging of bilayer vesicles using confocal microscopy. In **chapter 4B**, similar studies were performed using anisotropic GNRs. The role of aspect ratio and distance between GNR and a water-soluble Photosensitizer Eosin Y (Ey), was studied. Appropriate COMSOL simulations were also performed to understand the role of near field and far field effects in MEF. Among the library of 36 different nano theranostic hybrids, we identified GNRs with length 133 nm and width 45 nm and Ey at a distance of ~12.6 nm, that produced ~110 times enhancement in fluorescence and 18 times enhancement in SOG.

In the second half of the thesis, we explored one more important phenomenon of plasmonics, i.e., surface enhanced Raman spectroscopy (SERS). We explored the use of various bimetallic and trimetallic thin film substrates for ultra-sensitive detection of useful analytes. In **chapter 5A**, we carefully synthesized and optimized the reaction temperature and composition of bimetallic Ag-Cu MFs and used them as SERS substrates. We identified that the MFs of composition Ag 90% and Cu 10% synthesized at 350 °C, gave the best enhancement factor of ~10^8. We used these MFs for single molecule sensing of Rhodamine 6G. we also studied the role of surface composition on the SERS efficiency. In **chapter 5B**, we utilized the surface enhanced resonance Raman scattering phenomenon (SERRS) for femtomolar detection of an anti-cancer drug Mitoxantrone (MTO) using red laser. We also used Ag-Cu substrates for multiplexed detection of MTO in presence of another potential anti-cancer drug Doxorubicin. Finally, in **chapter 6**, we synthesized trimetallic Ag-Au-Cu MFs and optimized the surface composition for identifying a composition that can provide decent enhancement factors with an Au rich surface to explore the Au-S dynamic linkage and used it for ultra-sensitive sensing of various aliphatic and aromatic thiols such as L-

Cys and thiophenol derivatives. We also explored multiplexed sensing of 3 analytes together.

Specific contributions of the research work presented in this thesis

Table 7.1. Best plasmonic nanoparticles presented in this thesis for MEF and ME-SOG.

Chapter Number	NP	Spacer thickness	Molecule adsorbed	Work highlight
3	45 nm AuNPs	11.2 nm silica shell	PAH	280-fold enhancement in fluorescence; Selective detection of PA with LOD 79 nM
4A	42 nm AuNPs	12.4 nm thick PSS/PAH layers	NP-4-Py	EF of MEF 7.9; EF of SOG 10.6
4B	133 nm length, 45 nm width AuNRs	12.6 nm thick PSS/PAH layers	Eosin Y	EF of MEF 110; EF of SOG 21

Table 7.2. Best SERS substrates presented in this thesis.

Chapter Number	Substrate	Best composition	Reaction temperature	Work highlight
5A	Ag-Cu alloy (SERS)	90% Ag, 10% Cu	350 °C	Single molecule SERS of R6G
5B	Ag-Cu alloy (SERRS)	90% Ag, 10% Cu	350 °C	Femto molar detection of MTO
6	Ag-Au-Cu (SERS)	TM 73 (90% Ag, 7% Au and 3% Cu)	350 °C	Nano molar detection of L-Cys and Pico molar detection of Aromatic thiols

- The dependence of size of AuNPs on MEF was studied and the best MEF sensor was used for selective detection of picric acid.
- The role of isotropic and anisotropic MNP and spacer distance was carefully optimized for simultaneous MEF and MESOG effects for useful PDT applications.
- Bimetallic MFs of various compositions of Ag and Cu was engineered carefully for achieving better enhancement factors and used for Zeptomolar level detection of R 6G.
- SERS and SERRS on Ag-Au and Ag-Cu MF substrates was studied and used for detection of femtomolar level detection of Mitoxantrone and for multiplexed sensing of MTO and DOX both in water and mouse blood plasma.
- Trimetallic MFs of various surface compositions were fabricated and used for detection of low Raman cross section thiols and their multiplexed sensing.

Future perspectives

- The synthesized nano hybrids (MNP-AIEgen) can be further studied using two photon photodynamic therapy.
- GNR-Ey hybrid PS can be used for exploring the image guided Photodynamic therapy.
- Synthesized GNR hybrids can be loaded inside thermosensitive vesicles and photothermal therapy can be explored.
- Synthesized bimetallic and trimetallic films can be explored for plasmonic catalysis in liquid phase and also graphene plasmonics on Ag-Cu MFs can be studied further for useful catalytic applications.
- The role of semiconductor materials such as TiO_2, ITO can be explored by synthesizing MFs on those matrices.

Bibliography

Chapter 1

(1) Jang, Y. J.; Chung, K.; Lee, J. S.; Choi, C. H.; Lim, J. W.; Kim, D. H. ACS Photonics 2018, 5 (12), 4711–4723.

(2) Ghobadi, A.; Hajian, H.; Butun, B.; Ozbay, E. ACS Photonics 2018, 5 (11), 4203–4221.

(3) Höppener, C.; Novotny, L. Q. Rev. Biophys. 2012, 45 (2), 209–255.

(4) Petryayeva, E.; Krull, U. J. Anal. Chim. Acta 2011, 706 (1), 8–24.

(5) Zhang, Y.; McKelvie, I. D.; Cattrall, R. W.; Kolev, S. D. Talanta 2016, 152, 410–422.

(6) Bousiakou, L. G.; Gebavi, H.; Mikac, L.; Karapetis, S.; Ivanda, M. Croat. Chem. Acta 2019, 92 (4), 479–494.

(7) Hilger, I.; Hergt, R. IEEE Proc. nanobiotechnology 2005, 152 (6), 207–211.

(8) Ghosh Chaudhuri, R.; Paria, S. Chem. Rev. 2012, 112 (4), 2373–2433.

(9) Fulmore, J. S.; Geiger, B. F.; Werner, K. A.; Talbott, L. L.; Jones, D. C. J. Phys. Chem. B 2003, 107, 668–677.

(10) Jain, P. K.; Lee, K. S.; El-Sayed, I. H.; El-Sayed, M. A.. J. Phys. Chem. B 2006, 110 (14), 7238–7248.

(11) Katyal, J.; Soni, R. K. J. Mod. Opt. 2013, 60 (20), 1717–1728.

(12) González, A. L.; Noguez, C.; Beránek, J.; Barnard, A. S. J. Phys. Chem. C 2014, 118 (17), 9128–9136.

(13) Liu, L.; Zhong, H.; Bai, Z.; Zhang, T.; Fu, W.; Shi, L.; Xie, H.; Deng, L.; Zou, B. Chem. Mater. 2013, 25 (23), 4828–4834.

(14) Zhu, J. J. Phys. Chem. C 2009, 113 (8), 3164–3167.

(15) Amendola, V.; Scaramuzza, S.; Agnoli, S.; Polizzi, S.; Meneghetti, M. Nanoscale 2014, 6 (3), 1423–1433.

(16) Hao, E.; Schatz, G. C. J. Chem. Phys. 2004, 120 (1), 357–366.

(17) Geddes, C. D.; Lakowicz, J. R. J. Fluoresc. 2002, 12, 121–129.

(18) Aslan, K.; Gryczynski, I.; Malicka, J.; Matveeva, E.; Lakowicz, J. R.; Geddes, C. D. Curr. Opin. Biotechnol. 2005, 16, 55–62.

(19) Jeong, Y.; Kook, Y. M.; Lee, K.; Koh, W. G. Biosens. Bioelectron. 2018, 111 (January), 102–116.

(20) Aslam, U.; Chavez, S.; Linic, S. Nat. Nanotechnol. 2017, 12 (10), 1000–1005.

(21) Xin, Y.; Yu, K.; Zhang, L.; Yang, Y.; Yuan, H.; Li, H.; Wang, L.; Zeng, J. Adv. Mater. 2021, 33 (32), 1–26.

(22) Cortés, E.; Besteiro, L. V.; Alabastri, A.; Baldi, A.; Tagliabue, G.; Demetriadou, A.; Narang, P. ACS Nano 2020, 14 (12), 16202–16219.

(23) Stiles, P. L.; Dieringer, J. A.; Shah, N. C.; Van Duyne, R. P. Annu. Rev. Anal. Chem. 2008, 1 (1), 601–626.

(24) Schlücker, S. Angew. Chemie - Int. Ed. 2014, 53 (19), 4756–4795.
(25) Moskovits, M. J. Raman Spectrosc. 2005, 36 (6–7), 485–496.
(26) Mejía-Salazar, J. R.; Oliveira, O. N. Chem. Rev. 2018, 118 (20), 10617–10625.
(27) Shao, L.; Ruan, Q. F.; Jiang, R. B.; Wang, J. F. Small 2014, 10, 802–811.
(28) Akbari, A.; Derakhshesh, M.; Abrishami, M. E. Inorg. Chem. Commun. 2018, 98, 159–164.
(29) Qian, X. M.; Nie, S. M. Chem. Soc. Rev. 2008, 37 (5), 912–920.
(30) Cao, Y. W. C.; Jin, R.; Mirkin, C. A. Science (80-.). 2002, 297 (5586), 1536–1540.
(31) Aslan, K.; Wu, M.; Lakowicz, J. R.; Geddes, C. D. J. Am. Chem. Soc. 2007, 129 (6), 1524–1525.
(32) Chen, Y.; Munechika, K.; Ginger, D. S. Nano Lett. 2007, 7 (3), 690–696.
(33) Willets, K. A.; Wilson, A. J.; Sundaresan, V.; Joshi, P. B. Chem. Rev. 2017, 117 (11), 7538–7582.
(34) Badshah, M. A.; Koh, N. Y.; Zia, A. W.; Abbas, N.; Zahra, Z.; Saleem, M. W.. Nanomaterials 2020, 10 (9), 1–22.
(35) Gontero, D.; Veglia, A. V.; Boudreau, D.; Bracamonte, A. G. J. Nanophotonics 2017, 12 (1), 012505.
(36) Vendrell, M.; Maiti, K. K.; Dhaliwal, K.; Chang, Y. T. Trends Biotechnol. 2013, 31 (4), 249–257.
(37) Fales, A. M.; Yuan, H.; Vo-Dinh, T.. Langmuir 2011, 27 (19), 12186–12190.
(38) Zhang, Y.; Aslan, K.; Previte, M. J. R.; Geddes, C. D. Proc. Natl. Acad. Sci. U. S. A. 2008, 105 (6), 1798–1802.
(39) Pawar, S.; Bhattacharya, A.; Nag, A. ACS Omega 2019, 4 (3), 5983–5990.
(40) Nakamura, T.; Hayashi, S.. Japanese J. Appl. Physics, 2005, 44 (9 A), 6833–6837.
(41) Aslan, K.; Lakowicz, J. R.; Geddes, C. D. J. Phys. Chem. B 2005, 109, 3157–3162.
(42) Aslan, K.; Lakowicz, J. R.; Geddes, C. D. J. Phys. Chem. B 2005, 109 (13), 6247–6251.
(43) Bardhan, R.; Grady, N. K.; Cole, J. R.; Joshi, A.; Halas, N. J. ACS Nano 2009, 3 (3), 744–752.
(44) Sun, B.; Wang, C.; Han, S.; Hu, Y.; Zhang, L. RSC Adv. 2016, 6 (66), 61109–61118.
(45) Pang, J.; Theodorou, I. G.; Centeno, A.; Petrov, P. K.; Alford, N. M.; Ryan, M. P.; Xie, F. J. Mater. Chem. C 2017, 5 (4), 917–925.
(46) Abel, B.; Coskun, S.; Mohammed, M.; Williams, R.; Unalan, H. E.; Aslan, K. J. Phys. Chem. C 2015, 119 (1), 675–684.
(47) Theodorou, I. G.; Jawad, Z. A. R.; Jiang, Q.; Aboagye, E. O.; Porter, A. E.; Ryan, M. P.; Xie, F. Chem. Mater. 2017, 29 (16), 6916–6926.
(48) Zhang, L.; Song, Y.; Fujita, T.; Zhang, Y.; Chen, M.; Wang, T. H. Adv. Mater. 2014, 26 (8), 1289–1294.
(49) Ray, K.; Lakowicz, J. R. J. Phys. Chem. C 2013, 117 (30), 15790–15797.

(50) Chen, J.; Qiao, Y.; Li, Y.; Liu, T.; Zhang, X. D. AIP Adv. 2020, 10 (12).
(51) Loiseau, A.; Asila, V.; Boitel-Aullen, G.; Lam, M.; Salmain, M.; Boujday, S.. Biosensors 2019, 9 (2).
(52) Dragan, A. I.; Bishop, E. S.; Casas-Finet, J. R.; Strouse, R. J.; McGivney, J.; Schenerman, M. A.; Geddes, C. D.. Plasmonics 2012, 7 (4), 739–744.
(53) Zhou, Z.; Huang, H.; Chen, Y.; Liu, F.; Huang, C. Z.; Li, N. Biosens. Bioelectron. 2014, 52, 367–373.
(54) Akbay, N.; Lakowicz, J. R.; Ray, K. J. Phys. Chem. C 2012, 116 (19), 10766–10773.
(55) Ray, K.; Badugu, R.; Lakowicz, J. R. Chem. Mater. 2007, 19 (24), 5902–5909.
(56) Tang, F.; Ma, N.; Tong, L.; He, F.; Li, L. Langmuir 2012, 28 (1), 883–888.
(57) Choi, J. H.; Ha, T.; Shin, M.; Lee, S. N.; Choi, J. W. Biomedicines 2021, 9 (8).
(58) Geddes, C. D. Metal-Enhanced Fluorescence. Phys. Chem. Chem. Phys. 2013, 15 (45), 19537.
(59) Deng, W.; Xie, F.; Baltar, H. T. M. C. M.; Goldys, E. M. Phys. Chem. Chem. Phys. 2013, 15 (38), 15695–15708.
(60) da Silva, A. G. M.; Rodrigues, T. S.; Wang, J.; Camargo, P. H. C. Chem. Commun. 2022, 58 (13), 2055–2074.
(61) Lin, S.; Wang, Z.; Zhang, Y.; Huang, Y.; Yuan, R.; Xiang, W.; Zhou, Y. J. Alloys Compd. 2017, 700, 75–82.
(62) Lim, W. Q.; Gao, Z. Nano Today 2016, 11 (2), 168–188.
(63) Zhou, X.; Pu, H.; Sun, D. W. Crit. Rev. Food Sci. Nutr. 2021, 61 (14), 2277–2296.
(64) Tian, L.; Li, Y.; Ren, T.; Tong, Y.; Yang, B.; Li, Y. Talanta 2017, 170 (March), 530–539.
(65) Heidi Abrahamse Hamblin, M. R. Anti cancer agents Med. Chem. 2021, 21, 123–136.
(66) Felsher, D. W.. Nat. Rev. Cancer 2003, 3 (5), 375–380.
(67) Zhou, N.; López-Puente, V.; Wang, Q.; Polavarapu, L.; Pastoriza-Santos, I.; Xu, Q. H. RSC Adv. 2015, 5 (37), 29076–29097.
(68) Chen, C. W.; Chan, Y. C.; Hsiao, M.; Liu, R. S. ACS Appl. Mater. Interfaces 2016, 8 (47), 32108–32119.
(69) Li, Y.; Wen, T.; Zhao, R.; Liu, X.; Ji, T.; Wang, H.; Shi, X.; Shi, J.; Wei, J.; Zhao, Y.; Wu, X.; Nie, G. ACS Nano 2014, 8 (11), 11529–11542.
(70) Amirjani, A.; Shokrani, P.; Sharif, S. A.; Moheb, H.; Ahmadi, H.; Ahmadiani, Z. S.; Paroushi, M. S. J. Mater. Chem. B 2023, 3537–3566.
(71) Calzavara-Pinton, P. G.; Venturini, M.; Sala, R. J. Eur. Acad. Dermatology Venereol. 2007, 21 (3), 293–302.
(72) Wang, Y. Y.; Liu, Y. C.; Sun, H.; Guo, D. S. Coord. Chem. Rev. 2019, 395, 46–62.
(73) Konan, Y. N.; Gurny, R.; Allémann, E. J. Photochem. Photobiol. B Biol. 2002, 66 (2), 89–106.

(74) Hasrat, K.; Wang, X.; Li, Y.; Qi, Z. Sensors Actuators B Chem. 2023, 392 (February), 134053.
(75) Dai, J.; Wu, X.; Ding, S.; Lou, X.; Xia, F.; Wang, S.; Hong, Y. J. Med. Chem. 2020, 63 (5), 1996–2012.
(76) Tavakkoli Yaraki, M.; Pan, Y.; Hu, F.; Yu, Y.; Liu, B.; Tan, Y. N.. Mater. Chem. Front. 2020, 4 (10), 3074–3085.
(77) Mooi, S. M.; Heyne, B. Photochem. Photobiol. 2014, 90 (1), 85–91.
(78) Planas, O.; Macia, N.; Agut, M.; Nonell, S.; Heyne, B. J. Am. Chem. Soc. 2016, 138 (8), 2762–2768.
(79) MacIa, N.; Bresoli-Obach, R.; Nonell, S.; Heyne, B. J. Am. Chem. Soc. 2019, 141 (1), 684–692.
(80) Macia, N.; Kabanov, V.; Côté-Cyr, M.; Heyne, B. J. Phys. Chem. Lett. 2019, 10 (13), 3654–3660.
(81) Zhang, Y.; Aslan, K.; Previte, M. J. R.; Geddes, C. D. J. Fluoresc. 2007, 17 (4), 345–349.
(82) DeRosa, M. C.; Crutchley, R. J. Coord. Chem. Rev. 2002, 233–234, 351–371.
(83) George, B. P.; Chota, A.; Sarbadhikary, P.; Abrahamse, H. Front. Chem. 2022, 10 (July), 1–14.
(84) Wang, H.; Jiang, S.; Chen, S.; Li, D.; Zhang, X.; Shao, W.; Sun, X.; Xie, J.; Zhao, Z.; Zhang, Q.; Tian, Y.; Xie, Y. Adv. Mater. 2016, 28 (32), 6940–6945.
(85) Raman, C. V.; Krishnan, K. S. Nature 1928, 121 (3048), 501–502.
(86) Ball, D. W. Spectrosc. (Santa Monica) 2001, 16 (11), 32–34.
(87) Banwel.Pdf. New age international 2006 book.
(88) Kauffmann, T. H.; Kokanyan, N.; Fontana, M. D. J. Raman Spectrosc. 2019, 50 (3), 418–424.
(89) (a) McCaman, D. W.; Kukura, P.; Yoon, S.; Mathies, A.R.; Rev. Sci. Instrum. 2004, 75, 4971-4980. (b) Efremov, E. V.; Ariese, F.; & Gooijer, C.; Anal. Chim. Acta., 2008, 606(2), 119-134. (c) Harvey, A.B.; Anal. Chem. 1978, 50, 9, 905A–912A. (d) Zhang, Z.; Sheng, S.; Wang, R.; Sun, M,; Anal. Chem., 2016, 88, 19, 9328-9346.
(90) (a) M. Fleishmann, P. J. H. and A. J. M. Chem. Phys. Lett. 1974, 26 (2), 163–166. (b) Jeanmaire, D. L.; Duyne, R. P. VAN. J. Electroanal Chem. 1977, 84, 1–20.
(91) Albrecht, M. G.; Creighton, J. A. J. Am. Chem. Soc. 1977, 99 (15), 5215–5217.
(92) Hildebrandt, P.; Stockhurger, M. J. Phys. Chem. 1984, 88 (24), 5935–5944.
(93) Sharma, B.; Fernanda Cardinal, M.; Kleinman, S. L.; Greeneltch, N. G.; Frontiera, R. R.; Blaber, M. G.; Schatz, G. C.; Van Duyne, R. P. MRS Bull. 2013, 38 (8), 615–624.
(94) Zhao, Y.; Zhang, Y. J.; Meng, J. H.; Chen, S.; Panneerselvam, R.; Li, C. Y.; Jamali, S. B.; Li, X.; Yang, Z. L.; Li, J. F.; Tian, Z. Q. J. Raman Spectrosc. 2016, 47 (6), 662–667.

(95) Chaffin, E.; O'Connor, R. T.; Barr, J.; Huang, X.; Wang, Y. J. Chem. Phys. 2016, 145 (5).
(96) Guo, P.; Sikdar, D.; Huang, X.; Si, K. J.; Xiong, W.; Gong, S.; Yap, L. W.; Premaratne, M.; Cheng, W. Nanoscale 2015, 7 (7), 2862–2868.
(97) Stranahan, S. M.; Titus, E. J.; Willets, K. A. ACS Nano 2012, 6 (2), 1806–1813.
(98) Silaghi, S. D.; Scholz, R.; Salvan, G.; Suzuki, Y. J.; Friedrich, M.; Kampen, T. U.; Zahn, D. R. T. Appl. Surf. Sci. 2004, 234 (1–4), 113–119.
(99) Tang, X.; Zhao, X.; Wen, J.; Liu, J.; Zhang, F.; Guo, X.; Zhang, K.; Zhang, J.; Wang, A.; Gao, R.; Wang, Y.; Zhang, Y. J. Mater. Chem. C 2022, 10 (39), 14549–14559.
(100) Yan, X.; Li, P.; Yang, L.; Liu, J. Analyst 2016, 141 (17), 5189–5194.
(101) Meyer, S. A.; Le Ru, E. C.; Etchegoin, P. G. AIP Conf. Proc. 2010, 1267, 204–205.
(102) Guo, Z.; Chen, P.; Yosri, N.; Chen, Q.; Elseedi, H. R.; Zou, X.; Yang, H.. Food Rev. Int. 2023, 39 (3), 1440–1461.
(103) Wu, J.; Zhang, L.; Huang, F.; Ji, X.; Dai, H.; Wu, W. J. Hazard. Mater. 2020, 387, 121714.
(104) Pilot, R. J. Raman Spectrosc. 2018, 49 (6), 954–981.
(105) Wei, H.; Hossein Abtahi, S. M.; Vikesland, P. J.. Environ. Sci. Nano 2015, 2 (2), 120–135.
(106) Pang, S.; Yang, T.; He, L. TrAC - Trends Anal. Chem. 2016, 85, 73–82.
(107) Chao, J.; Cao, W.; Su, S.; Weng, L.; Song, S.; Fan, C.; Wang, L. J. Mater. Chem. B 2016, 4 (10), 1757–1769.
(108) Eskandari, V.; Sahbafar, H.; Zeinalizad, L.; Sabzian-Molaei, F.; Abbas, M. H.; Hadi, A. J. Mol. Struct. 2023, 1274, 134497.
(109) Ngo, H. T.; Wang, H. N.; Fales, A. M.; Vo-Dinh, T. Anal. Bioanal. Chem. 2016, 408 (7), 1773–1781.
(110) De Oliveira Penido, C. A. F.; Pacheco, M. T. T.; Lednev, I. K.; Silveira, L. J. Raman Spectrosc. 2016, 47 (1), 28–38.
(111) Liu, Y.; Lu, F. Rev. Anal. Chem. 2017, 36 (3), 1–14.
(112) Beeram, R.; Vepa, K. R.; Soma, V. R. Biosensors 2023, 13 (3).
(113) Kao, Y. C.; Han, X.; Lee, Y. H.; Lee, H. K.; Phan-Quang, G. C.; Lay, C. L.; Sim, H. Y. F.; Phua, V. J. X.; Ng, L. S.; Ku, C. W.; Tan, T. C.; Phang, I. Y.; Tan, N. S.; Ling, X. Y.. ACS Nano 2020, 14 (2), 2542–2552.
(114) Muehlethaler, C.; Leona, M.; Lombardi, J. R.. Anal. Chem. 2016, 88 (1), 152–169.

Chapter 2

(1) Ziegler, C.; Eychmüller, A. *J. Phys. Chem. C* **2011**, *115* (11), 4502–4506.
(2) Frens, G.; *Nat. Phys. Sci.* **1973**, *241*, 20.
(3) Demirörs, A. F.; Van Blaaderen, A.; Imhof, A. *Langmuir* **2010**, *26* (12), 9297–9303.

(4) Li, C.; Zhu, Y.; Zhang, X.; Yang, X.; Li, C. *RSC Adv.* **2012**, *2* (5), 1765–1768.
(5) Rainville, L.; Dorais, M. C.; Boudreau, D. *RSC Adv.* **2013**, *3* (33), 13953–13960.
(6) Liang, J.; Li, K.; Gurzadyan, G. G.; Lu, X.; Liu, B. *Langmuir* **2012**, *28* (31), 11302–11309.
(7) Kim, J. K.; Jang, D. J.; *J. Mater. Chem. C* **2017**, *5* (24), 6037–6046.
(8) Ramalingam, V.; Varunkumar, K.; Ravikumar, V.; Rajaram, R. *Sci. Rep.* **2018**, *8* (1), 1–12.
(9) Labala, S.; Mandapalli, P. K.; Kurumaddali, A.; Venuganti, V. V. K. *Mol. Pharm.* **2015**, *12* (3), 878–888.
(10) Wu, Z.; Liang, J.; Ji, X.; Yang, W. *Colloids Surfaces A Physicochem. Eng. Asp.* **2011**, *392* (1), 220–224.
(11) Arantes, T. M.; Pinto, A. H.; Leite, E. R.; Longo, E.; Camargo, E. R. *Colloids Surfaces A Physicochem. Eng. Asp.* **2012**, *415*, 209–217.
(12) Damera, D. P.; Nag, A. *J. Mol. Liq.* **2021**, *340*, 117110.
(13) Picciolini, S.; Mehn, D.; Ojea-Jiménez, I.; Gramatica, F.; Morasso, C. *J. Vis. Exp.* **2016**, *2016* (114), 1–7.
(14) Wang, B.; Wang, J. H.; Liu, Q.; Huang, H.; Chen, M.; Li, K.; Li, C.; Yu, X. F.; Chu, P. K. *Biomaterials* **2014**, *35* (6), 1954–1966.
(15) Shafqat, S. S.; Khan, A. A.; Zafar, M. N.; Alhaji, M. H.; Sanaullah, K.; Shafqat, S. R.; Murtaza, S.; Pang, S. C. *J. Mater. Res. Technol.* **2019**, *8* (1), 385–395. \
(16) Mettela, G.; Siddhanta, S.; Narayana, C.; Kulkarni, G. U. *Nanoscale* **2014**, *6* (13), 7480–7488.
(17) Pawar, S.; Teja, B. R.; Nagarjuna, R.; Ganesan, R.; Nag, A. *Colloids Surfaces A Physicochem. Eng. Asp.* **2019**, *578*.
(18) Kaja, S.; Nag, A. *Langmuir* **2021**, *37* (44), 13027–13037.
(19) Mukherjee, A.; Chakravarty, M. *New J. Chem.* **2020**, *44* (16), 6173–6181.
(20) Macia, N.; Kabanov, V.; Côté-Cyr, M.; Heyne, B. *J. Phys. Chem. Lett.* **2019**, *10* (13), 3654–3660.
(21) Bregnhøj, M.; Rodal-Cedeira, S.; Pastoriza-Santos, I.; Ogilby, P. R. *J. Phys. Chem. C* **2018**, *122* (27), 15625–15634.
(22) Mishra, H.; Mali, B. L.; Karolin, J.; Dragan, A. I.; Geddes, C. D. *Phys. Chem. Chem. Phys.* **2013**, *15* (45), 19538–19544.
(23) Windt, D. L.; Cash, W. C.; Scott, M.; Arendt, P.; Newnam, B.; Fisher, R. F.; Swartzlander, A. B. *Appl. Opt.* **1988**, *27* (2), 246.
(24) Rioux, D.; Vallières, S.; Besner, S.; Muñoz, P.; Mazur, E.; Meunier, M. *Adv. Opt. Mater.* **2014**, *2* (2), 176–182.
(25) ASM Handbook W Volume 22A Fundamentals of Modeling for Metals Processing. **2009**, *22* (05215G), 603.

Chapter 3

(1) Peng, Y.; Zhang, A.-J.; Dong, M.; Wang, Y.-W. *Chem. Commun.* **2011**, *47* (15), 4505.

(2) Hou, X. G.; Wu, Y.; Cao, H. T.; Sun, H. Z.; Li, H. Bin; Shan, G. G.; Su, Z. M. *Chem. Commun.* **2014**, *50* (45), 6031–6034.

(3) Akhavan, J. *The Chemistry of Explosives*; Royal Society of Chemistry, 2011.

(4) *Picric acid - National Library of Medicine HSDB Database*. https://toxnet.nlm.nih.gov/cgi-bin/sis/search/a?dbs+hsdb:@term+@DOCNO+2040 (accessed 2019-06-14).

(5) Sadhanala, H. K.; Nanda, K. K. *J. Phys. Chem. C* **2015**, *119*, 13138–13143..

(6) Satya Bharati, M. S.; Chandu, B.; Rao, S. V. *RSC Adv.* **2019**, *9* (3), 1517–1525..

(7) Wang, T.; Zhang, N.; Bai, R.; Bao, Y. *J. Mater. Chem. c* **2018**, *6*, 266–270..

(8) Sarkar, S.; Dutta, S.; Chakrabarti, S.; Bairi, P.; Pal, T. *ACS Appl. Mater. Interfaces* **2014**, *6*, 6308–6316.

(9) Li, A.; Li, L.; Lin, Z.; Song, L.; Wang, Z.; Chen, Q.; Yang, T. *New J. Chem.* **2015**, *39*, 2289–2295.

(10) Xiao, J. D.; Qiu, L. G.; Ke, F.; Yuan, Y. P.; Xu, G. S.; Wang, Y. M.; Jiang, X. *J. Mater. Chem. A* **2013**, *1* (31), 8745–8752.

(11) Qi, X.; Jin, Y.; Li, N.; Wang, Z.; Wang, K.; Zhang, Q. *Chem. Commun.* **2017**, *53*, 10318–10321.

(12) Rachuri, Y.; Parmar, B.; Bisht, K. K.; Suresh, E. *Dalt. Trans.* **2016**, *45*, 7881–7892.

(13) Kumar, S.; Venkatramaiah, N.; Patil, S. *J. Phys. Chem. C* **2013**, *117*, 7236–7245.

(14) Maity, S.; Shyamal, M.; Das, D.; Mazumdar, P.; Sahoo, G. P.; Misra, A. *Sensors Actuators B. Chem.* **2017**, *248*, 223–233.

(15) Gu, P.; Wang, C.; Nie, L.; Long, G.; Zhang, Q. *RSC Adv.* **2016**, *6*, 37929–37932.

(16) Mahendran, V.; Shanmugam, S. *RSC Adv.* **2015**, *5*, 92473–92479.

(17) Mazumdar, P.; Maity, S.; Shyamal, M.; Das, D. *Phys.Chem.Chem.Phys.,* **2016**, *18*, 7055–7067.

(18) Hariharan, P. S.; Pitchaimani, J.; Madhu, V.; Anthony, S. P. *J. Fluoresc.* **2016**, *26* (2), 395–401.

(19) Roy, B.; Bar, A. K.; Gole, B.; Mukherjee, P. S. *J. Org. Chem.* **2013**, *78*, 1306–1310.

(20) Kaleeswaran, D.; Murugavel, R. *J. Chem. Sci.* **2018**, *130*, 1–14.

(21) Mahendran, V.; Pasumpon, K.; Thimmarayaperumal, S.; Thilagar, P.; Shanmugam, S. *J. Org. Chem.* **2016**, *81*, 3597–3602.

(22) Luggar, R. D.; Farquharson, M. J.; Horrocks, J. A.; Lacey, R. J. *X-Ray Spectrom.* **1998**, *27*, 87–94.

(23) Gaft, M.; Nagli, L. *Opt. Mater. (Amst).* **2008**, *30* (11), 1739–1746.

(24) Krull, I. S.; Davis, E. A.; Santasania, C.; Kraus, S.; Basch, A.; Bamberger, Y. *Anal. Lett.* **1981**, *14*, 1363–1376.

(25) Gogoi, B.; Sen Sarma, N. *ACS Appl. Mater. Interfaces* **2015**, *7*, 11195–11202.
(26) Geddes, C. D.; Lakowicz, J. R. Editorial. *J. Fluoresc.* **2002**, *12*, 121–129.
(27) Aslan, K.; Gryczynski, I.; Malicka, J.; Matveeva, E.; Lakowicz, J. R.; Geddes, C. D. *Curr. Opin. Biotechnol.* **2005**, *16*, 55–62.
(28) Pompa, P. P.; Martiradonna, L.; Torre, A. Della; Sala, F. Della; Manna, L.; De Vittorio, M.; Calabi, F.; Cingolani, R.; Rinaldi, R. *Nat. Nanotechnol.* **2006**, *1*, 126–130.
(29) Jian Zhang; Yi Fu; Mustafa H. Chowdhury, A.; Lakowicz, J. R. *ACS nano Lett.* **2007**, *7*, 2101–2107.
(30) Lakowicz, J. R.; Ray, K.; Chowdhury, M.; Szmacinski, H.; Fu, Y.; Zhang, J.; Nowaczyk, K. *Analyst* **2008**, *133*, 1308.
(31) Deng, W.; Goldys, E. M. *Langmuir* **2012**, *28*, 10152–10163.
(32) Park, M.; Hwang, C. S. H.; Jeong, K.-H. *ACS Appl. Mater. Interfaces* **2018**, *10*, 290–295.
(33) Aslan, K.; Wu, M.; Lakowicz, J. R.; Geddes, C. D. *J. Fluoresc.* **2007**, *17* (2), 127–131.
(34) Tam, F.; Goodrich, G. P.; Johnson, B. R.; Halas, N. J. *Nano Lett.* **2007**, *7* (2), 496–501.
(35) Ayala-Orozco, C.; Liu, J. G.; Knight, M. W.; Wang, Y.; Day, J. K.; Nordlander, P.; Halas, N. J. *Nano Lett.* **2014**, *14* (5), 2926–2933.
(36) Kim, J. K.; Jang, D. J. *J. Mater. Chem. C* **2017**, *5* (24), 6037–6046.
(37) Gan, W.; Tserkezis, C.; Cai, Q.; Falin, A.; Mateti, S.; Nguyen, M.; Aharonovich, I.; Watanabe, K.; Taniguchi, T.; Huang, F.; Song, L.; Kong, L.; Chen, Y.; Li, L. H. *ACS Nano* **2019**, *13* (10), 12184–12191.
(38) Chen, B.; Yang, M.; Zhang, L.; Han, Z.; Zeng, H.; Chen, C.; Tao, C. *Opt. Express,* **2017**, *25* (9), 9901–9910.
(39) Feng, A. L.; You, M. L.; Tian, L.; Singamaneni, S.; Liu, M.; Duan, Z.; Lu, T. J.; Xu, F.; Lin, M. *Sci. Reports 2015 5* **2015**, *5*, 7779.
(40) Camposeo, A.; Persano, L.; Manco, R.; Wang, Y.; Del Carro, P.; Zhang, C.; Li, Z. Y.; Pisignano, D.; Xia, *ACS Nano* **2015**, *9* (10), 10047–10054.
(41) Pawar, S.; Bhattacharya, A.; Nag, A. *ACS Omega* **2019**, *4* (3), 5983–5990.
(42) Gontero, D.; Veglia, A. V; Bracamonte, A. G.; Boudreau, D. *RSC advances*, **2017,** 7, 10252.
(43) Ngo, V. K. T.; Nguyen, H. P. U.; Huynh, T. P.; Tran, N. N. P.; Lam, Q. V.; Huynh, T. D. *Adv. Nat. Sci. Nanosci. Nanotechnol.* **2015**, *6* (3).
(44) Zou, Y.; Chen, H.; Li, Y.; Yuan, X.; Zhao, X.; Chen, W.; Cao, F.; Cai, N.; Huang, X.; Yang, F.; Liu, W. *J. Saudi Chem. Soc.* **2019**, *23* (3), 378–383.
(45) Li, H.; Zheng, H.; Tong, W.; Gao, C. *J. Colloid Interface Sci.* **2017**, *496*, 228–234.
(46) Hwang, E.; Smolyaninov, I. I.; Davis, C. C.. *Nano Lett.* **2010**, *10*, 813–820.

(47) Ray, K.; Badugu, R.; Lakowicz, J. R.. *Langmuir* **2006**, *22*, 8374–8378.
(48) Anger, P.; Bharadwaj, P.; Novotny, L. *Phys. Rev. Lett.* **2006**, *96*, 113002.
(49) Brown, L. O.; Doom, S. K. *Langmuir* **2008**, *24* (5), 2178–2185.
(50) Švanda, J.; Kalachyova, Y.; Slepička, P.; Švorčík, V.; Lyutakov, O. *ACS Appl. Mater. Interfaces* **2016**, *8* (1), 225–231.
(51) C.F. Bohren, D. Huffman, MieCalc. Freely Configurable Program for Light Scattering Calculations (Mie Theory); John Wiley: New York, 1983; Homepage: http://www.lightscattering.de/MieCalc/ eindex.html.
(52) McMahon, J. M.; Schatz, G. C.; Gray, S. K. *Phys. Chem. Chem. Phys.* **2013**, *15* (15), 5415–5423.
(53) Majee, P.; Singha, D. K.; Mondal, S. K.; Mahata, P.. *ChemistrySelect* **2018**, *3*, 683–689.
(54) Mondal, T. K.; Dinda, D.; Saha, S. K. *Sensors Actuators, B Chem.* **2018**, *257*, 586–593.
(55) Ma, H.; Li, F.; Yao, L.; Feng, Y.; Zhang, Z.; Zhang, M. *Sensors Actuators, B Chem.* **2018**, *259*, 380–386.
(56) Ponnuvel, K.; Banuppriya, G.; Padmini, V. *Sensors Actuators, B Chem.* **2016**, *234*, 34–45.
(57) Wei, W.; Lu, R.; Tang, S.; Liu, X. *J. Mater. Chem. A* **2015**, *3* (8), 4604–4611.
(58) Sivaraman, G.; Vidya, B.; Chellappa, D. *RSC Adv.* **2014**, *4* (58), 30828–30831.
(59) Chopra, R.; Kaur, P.; Singh, K. *Anal. Chim. Acta* **2015**, *864*, 55–63.
(60) Hussain, S.; Malik, A. H.; Afroz, M. A.; Iyer, P. K. *Chem. Commun.* **2015**, *51* (33), 7207–7210.
(61) Baig, M. Z. K.; Sahu, P. K.; Sarkar, M.; Chakravarty, M. *J. Org. Chem.* **2017**, *82*, 13359–13367.
(62) Li, D.; Liu, J.; Kwok, R. T. K.; Liang, Z.; Tang, B. Z.; Yu, J. *Chem. Commun.* **2012**, *48*, 7167–7169.
(63) D. Zaho.; Swager, T. M. *Macromolecules* **2005**, *38*, 9377–9384.

Chapter 4A

(1) Li, X.; Lee, S.; Yoon, J. *Chem. Soc. Rev.* **2019**, *47* (4), 1174–1188.
(2) Yun, S. H.; Kwok, S. J. J. *Nat. Biomed. Eng. 2017 11* **2017**, *1* (1), 1–16.
(3) Feng, L.; Li, C.; Liu, L.; Wang, Z.; Chen, Z.; Yu, J.; Ji, W.; Jiang, G.; Zhang, P.; Wang, J.; Tang, B. Z. *ACS Nano* **2022**, *16*, 4162–4174.
(4) Gao, S.; Wang, G.; Qin, Z.; Wang, X.; Zhao, G.; Ma, Q.; Zhu, L.. *Biomaterials* **2017**, *112*, 324–335.
(5) Li, X.; Kwon, N.; Guo, T.; Liu, Z.; Yoon, J. *Angew. Chemie Int. Ed.* **2018**, *57* (36), 11522–11531.
(6) Maas, A. L.; Carter, S. L.; Wiley, E. P.; Miller, J.; Yuan, M.; Yu, G.; Durham, A. C.; Busch, T. M. *Cancer Res.* **2012**, *72* (8), 2079–2088.

(7) Fan, W.; Huang, P.; Chen, X. *Chem. Soc. Rev.* **2016**, *45* (23), 6488–6519.
(8) Zhao, X.; Liu, J.; Fan, J.; Chao, H.; Peng, X.. *Chem. Soc. Rev.* **2021**, *50* (6), 4185–4219.
(9) Hong, Y.; Lam, J. W. Y.; Tang, B. Z. *Chem. Soc. Rev.* **2011**, *40* (11), 5361–5388.
(10) Peng, Q.; Shuai, Z. *Aggregate* **2021**, *2* (5), 91.
(11) Ma, S.; Du, S.; Pan, G.; Dai, S.; Xu, B.; Tian, W. *Aggregate* **2021**, *2* (4), 96.
(12) Han, T.; Wang, X.; Wang, D.; Tang, B. Z. *Top. Curr. Chem.* **2022**, *379* (7), 287–333.
(13) Prusti, B.; Chakravarty, M. *Analyst* **2020**, *145* (5), 1687–1694.
(14) Mukherjee, A.; Chakravarty, M. *New J. Chem.* **2020**, *44* (16), 6173–6181.
(15) Chen, J.; Chen, X.; Wang, P.; Liu, S.; Chi, Z. *J. Hazard. Mater.* **2021**, *413*, 125306.
(16) Wu, W.; Li, Z. *Mater. Chem. Front.* **2021**, *5* (2), 603–626.
(17) Lu, H.; Zheng, Y.; Zhao, X.; Wang, L.; Ma, S.; Han, X.; Xu, B.; Tian, W.; Gao, H. *Angew. Chemie Int. Ed.* **2016**, *55* (1), 155–159.
(18) Khan, I. M.; Niazi, S.; Iqbal Khan, M. K.; Pasha, I.; Mohsin, A.; Haider, J.; Iqbal, M. W.; Rehman, A.; Yue, L.; Wang, Z. *TrAC Trends Anal. Chem.* **2019**, *119*, 115637.
(19) Ma, H.; Zhao, C.; Meng, H.; Li, R.; Mao, L.; Hu, D.; Tian, M.; Yuan, J.; Wei, Y.. *ACS Appl. Mater. Interfaces* **2021**, *13* (7), 7987–7996.
(20) Feng, X.; Tong, B.; Shi, J.; Zhao, C.; Cai, Z.; Dong, Y. *Mater. Chem. Front.* **2021**, *5* (3), 1164–1184.
(21) Fothergill, S. M.; Joyce, C.; Xie, F. *Nanoscale* **2018**, *10* (45), 20914–20929.
(22) Tavakkoli Yaraki, M.; Hu, F.; Daqiqeh Rezaei, S.; Liu, B.; Tan, Y. N. *Nanoscale Adv.* **2020**, *2* (7), 2859–2869.
(23) Tavakkoli Yaraki, M.; Pan, Y.; Hu, F.; Yu, Y.; Liu, B.; Tan, Y. N. *Mater. Chem. Front.* **2020**, *4* (10), 3074–3085.
(24) MacIa, N.; Bresoli-Obach, R.; Nonell, S.; Heyne, B. *J. Am. Chem. Soc.* **2019**, *141* (1), 684–692.
(25) Planas, O.; Macia, N.; Agut, M.; Nonell, S.; Heyne, B. *J. Am. Chem. Soc.* **2016**, *138* (8), 2762–2768.
(26) Macia, N.; Kabanov, V.; Côté-Cyr, M.; Heyne, B. *J. Phys. Chem. Lett.* **2019**, *10* (13), 3654–3660.
(27) Hou, J. Q.; Kang, H. S.; Kim, K. W.; Hahn, J. R. *J. Chem. Phys.* **2008**, *128* (13), 134707.
(28) Rainville, L.; Dorais, M. C.; Boudreau, D. *RSC Adv.* **2013**, *3* (33), 13953–13960.
(29) Liang, J.; Li, K.; Gurzadyan, G. G.; Lu, X.; Liu, B. *Langmuir* **2012**, *28* (31), 11302–11309.
(30) Kaja, S.; Damera, D. P.; Nag, A. *Anal. Chim. Acta* **2020**, *1129*, 12–23.
(31) Aslan, K.; Wu, M.; Lakowicz, J. R. Geddes, C. D. *J. Fluoresc.* **2007**, *17* (2), 127–131.
(32) Kobayashi, Y.; Katakami, H.; Mine, E.; Nagao, D.; Konno, M.; Liz-Marzán, L. M.

d. *J. Colloid Interface Sci.* **2005**, *283* (2), 392–396.
(33) Pawar, S.; Bhattacharya, A.; Nag, A.. *ACS Omega* **2019**, *4* (3), 5983–5990.
(34) Kim, J. K.; Jang, D. J. *J. Mater. Chem. C* **2017**, *5* (24), 6037–6046.
(35) Ke, X.; Wang, D.; Chen, C.; Yang, A.; Han, Y.; Ren, L.; Li, D.; Wang, H. *Nanoscale Res. Lett.* **2014**, *9* (1), 1–8.
(36) Li, S.; Shen, X.; Xu, Q. H.; Cao, Y.. *Nanoscale* **2019**, *11* (41), 19551–19560.
(37) Praneeth, N. V. S.; Paria, S. *CrystEngComm* **2018**, *20* (30), 4297–4304.
(38) Ghosh, S. K.; Pal, T. *Phys. Chem. Chem. Phys.* **2009**, *11* (20), 3831–3844.
(39) Freitas, L. F. de. *Photodyn. Ther. - From Basic Sci. to Clin. Res.* **2020**.
(40) Damera, D. P.; Nag, A. *J. Mol. Liq.* **2021**, *340*, 117110.
(41) Damera, D. P.; Venuganti, V. V. K.; Nag, A. *ChemistrySelect* **2018**, *3* (14), 3930–3938.

Chapter 4B

(1) D. W. Felsher, Nat. Rev. Cancer, 2003, 3, 375–380.
(2) McDonald I. J. and Dougherty T. J., J. Porphyr. Phthalocyanines, 2001, 5, 105–129.
(3) H. Zheng, Technol. Cancer Res. Treat., 2005, 4, 283–293.
(4) S. Li, F. Yang, Y. Wang, T. Du and X. Hou, Chem. Eng. J., 2023, 451, 138621.
(5) W. Bäumler, J. Regensburger, A. Knak, A. Felgenträger and T. Maisch, Photochem. Photobiol. Sci., 2012, 11, 107–117.
(6) J. M. Fernandez, M. D. Bilgin and L. I. Grossweiner, J. Photochem. Photobiol. B Biol., 1997, 37, 131–140.
(7) M. A. Liebert, D. Ph, N. D. Kumar, D. Ph, C. Zhao, D. Ph, P. N. Prasad and D. Ph, J. Clin. Laser Med. Surg., 1997, 15, 201–204.
(8) V. Giannini, A. I. Fernández-Domínguez, S. C. Heck and S. A. Maier, Chem. Rev., 2011, 111, 3888–3912.
(9) N. Kongsuwan, A. Demetriadou, M. Horton, R. Chikkaraddy, J. J. Baumberg and O. Hess, ACS Photonics, 2020, 7, 463–471.
(10) B. Gallinet and O. J. F. Martin, Opt. Express, 2011, 19, 22167.
(11) C. D. Geddes and J. R. Lakowicz, J. Fluoresc., 2002, 12, 121–129.
(12) K. Aslan, I. Gryczynski, J. Malicka, E. Matveeva, J. R. Lakowicz and C. D. Geddes, Curr. Opin. Biotechnol., 2005, 16, 55–62.
(13) N. MacIa, R. Bresoli-Obach, S. Nonell and B. Heyne, J. Am. Chem. Soc., 2019, 141, 684–692.
(14) M. Bregnhøj, S. Rodal-Cedeira, I. Pastoriza-Santos and P. R. Ogilby, J. Phys. Chem. C, 2018, 122, 15625–15634.
(15) N. Macia, V. Kabanov, M. Côté-Cyr and B. Heyne, J. Phys. Chem. Lett., 2019, 10, 3654–3660.

(16) O. Planas, N. Macia, M. Agut, S. Nonell and B. Heyne, J. Am. Chem. Soc., 2016, 138, 2762–2768.
(17) S. Kaja, A. Mukherjee, M. Chakravarty and A. Nag, Colloids Surfaces A Physicochem. Eng. Asp., 2022, 649, 129448.
(18) N. S. Abadeer, M. R. Brennan, W. L. Wilson and C. J. Murphy, ACS Nano, 2014, 8, 8392–8406.
(19) R. Bardhan, N. K. Grady, J. R. Cole, A. Joshi and N. J. Halas, ACS Nano, 2009, 3, 744–752.
(20) H. Chen, L. Shao, Q. Li and J. Wang, Chem. Soc. Rev., 2013, 42, 2679–2724.
(21) J. Zheng, X. Cheng, H. Zhang, X. Bai, R. Ai, L. Shao and J. Wang, Chem. Rev., 2021, 121, 13342–13453.
(22) W. Xiong, D. Sikdar, L. W. Yap, P. Guo, M. Premaratne, X. Li and W. Cheng, Nano Res., 2016, 9, 415–423.
(23) P. Priecel, H. A. Salami, R. H. Padilla, Z. Zhong and J. A. Lopez-Sanchez, Cuihua Xuebao/Chinese J. Catal., 2016, 37, 1619–1650.
(24) S. Chang, Q. Li, X. Xiao, K. Y. Wong and T. Chen, Energy Environ. Sci., 2012, 5, 9444–9448.
(25) X. Huang, I. H. El-Sayed, W. Qian and M. A. El-Sayed, J. Am. Chem. Soc., 2006, 128, 2115–2120.
(26) W. Il Choi, J. Y. Kim, C. Kang, C. C. Byeon, Y. H. Kim and G. Tae, ACS Nano, 2011, 5, 1995–2003.
(27) R. Mooney, L. Roma, D. Zhao, D. Van Haute, E. Garcia, S. U. Kim, A. J. Annala, K. S. Aboody and J. M. Berlin, ACS Nano, 2014, 8, 12450–12460.
(28) T. Zhao, L. Li, S. Li, X. F. Jiang, C. Jiang, N. Zhou, N. Gao and Q. H. Xu, J. Mater. Chem. C, 2019, 7, 14693–14700.
(29) K. Imura, T. Nagahara and H. Okamoto, J. Phys. Chem. B, 2005, 109, 13214–13220.
(30) W. S. Kuo, C. N. Chang, Y. T. Chang, M. H. Yang, Y. H. Chien, S. J. Chen and C. S. Yeh, Angew. Chemie - Int. Ed., 2010, 49, 2711–2715.
(31) R. Vankayala, Y. K. Huang, P. Kalluru, C. S. Chiang and K. C. Hwang, Small, 2014, 10, 1612–1622.
(32) E. L. L. Yeo, J. U. J. Cheah, D. J. H. Neo, W. I. Goh, P. Kanchanawong, K. C. Soo, P. S. P. Thong and J. C. Y. Kah, J. Mater. Chem. B, 2017, 5, 254–268.
(33) L. Luo, W. Sun, Y. Feng, R. Qin, J. Zhang, D. Ding, T. Shi, X. Liu, X. Chen and H. Chen, ACS Appl. Mater. Interfaces, 2020, 12, 12591–12599.
(34) B. Huang, J. Tian, D. Jiang, Y. Gao and W. Zhang, Biomacromolecules, 2019, 20, 3873–3883.
(35) X. Huang, X. J. Tian, W. L. Yang, B. Ehrenberg and J. Y. Chen, Phys. Chem. Chem. Phys., 2013, 15, 15727–15733.

(36) X. Ke, D. Wang, C. Chen, A. Yang, Y. Han, L. Ren, D. Li and H. Wang, Nanoscale Res. Lett., 2014, 9, 1–8.
(37) E. D. Novikova, Y. A. Vorotnikov, N. A. Nikolaev, A. R. Tsygankova, M. A. Shestopalov and O. A. Efremova, Chem. Commun., 2021, 57, 7770–7773.
(38) T. Mthethwa and T. Nyokong, J. Lumin., 2015, 157, 207–214.
(39) X. Zhou, X. He, S. Wei, K. Jia and X. Liu, J. Colloid Interface Sci., 2016, 482, 252–259.
(40) C. Liang, J. Luan, Z. Wang, Q. Jiang, R. Gupta, S. Cao, K. K. Liu, J. J. Morrissey, E. D. Kharasch, R. R. Naik and S. Singamaneni, ACS Appl. Mater. Interfaces, 2021, 13, 11414–11423.
(41) J. Liang, K. Li, G. G. Gurzadyan, X. Lu and B. Liu, Langmuir, 2012, 28, 11302–11309.
(42) Z. Wei, D. Chen, Z. Guo, P. Jia and H. Xing, Inorg. Chem., 2020, 59, 5386–5393.
(43) M. Tavakkoli Yaraki, F. Hu, S. Daqiqeh Rezaei, B. Liu and Y. N. Tan, Nanoscale Adv., 2020, 2, 2859–2869.
(44) D. P. Damera, V. Krishna, V. V. K. Venuganti and A. Nag, J. Photochem. Photobiol. B Biol., 2021, 225, 112335.

Chapter 5A

(1) Stiles, P. L.; Dieringer, J. A.; Shah, N. C.; Duyne, R. P. Van. *annurev.anchem* **2008**, *1* (1), 601–626.
(2) Schlücker, S. *Angew. Chemie Int. Ed.* **2014**, *53* (19), 4756–4795.
(3) Cialla, D.; März, A.; Böhme, R.; Theil, F.; Weber, K.; Schmitt, M.; Popp, J. *Anal. Bioanal. Chem.* **2012**, *403* (1), 27–54.
(4) Vo-Dinh, T. *TrAC Trends Anal. Chem.* **1998**, *17* (8–9), 557–582.
(5) J. Banholzer, M.; E. Millstone, J.; Lidong Qin; A. Mirkin, C. *Chem. Soc. Rev.* **2008**, *37* (5), 885–897.
(6) Zong, C.; Xu, M.; Xu, L.-J.; Wei, T.; Ma, X.; Zheng, X.-S.; Hu, R.; Ren, B. *Chem. Rev.* **2018**, *118* (10), 4946–4980.
(7) Fikiet, M. A.; Khandasammy, S. R.; Mistek, E.; Ahmed, Y.; Halámková, L.; Bueno, J.; Lednev, I. K. *Acta Part A Mol. Biomol. Spectrosc.* **2018**, *197*, 255–260.
(8) Muehlethaler, C.; Leona, M.; Lombardi, J. R. *Anal. Chem.* **2015**, *88* (1), 152–169.
(9) Craig, A. P.; Franca, A. S.; Irudayaraj, J. *annurev-food* **2013**, *4* (1), 369–380.
(10) Zheng, J.; He, L. *Compr. Rev. Food Sci. Food Saf.* **2014**, *13* (3), 317–328.
(11) Tang, H.; Zhu, C.; Meng, G.; Wu, N. *J. Electrochem. Soc.* **2018**, *165* (8), B3098.
(12) Gao, S.; Zhang, Z.; He, L. *Int. J. Environ. Anal. Chem.* **2016**, *96* (15), 1495–1506.
(13) Min, J.; Shenmiao, L.; Liguo, Z.; Xiaonan, L.; Hongyan, Z. *Nanomater. (Basel, Switzerland)* **2018**, *8* (9), 730.
(14) Guerrini, L.; Alvarez-Puebla, R. A. *Cancers 2019, Vol. 11, Page 748* **2019**, *11* (6),

748.
(15) Xu, X.; Hu, X.; Fu, F.; Liu, L.; Liu, X. *ACS Sustain. Chem. Eng.* **2021**, *9* (14), 5217–5229.
(16) Zhai, W.; You, T.; Ouyang, X.; Wang, M. *Compr. Rev. Food Sci. Food Saf.* **2021**, *20* (2), 1887–1909.
(17) Ong, T. T. X.; Blanch, E. W.; Jones, O. A. H. *Sci. Total Environ.* **2020**, *720*, 137601.
(18) Li, D.-W.; Zhai, W.-L.; Li, Y.-T.; Long, Y.-T. *Microchim. acta* **2014**, *181*, 23–43.
(19) Guerrini, L.; Alvarez-Puebla, R. A. *ACS Omega* **2021**, *6* (2), 1054–1063.
(20) Kneipp, K.; Wang, Y.; Kneipp, H.; Perelman, L. T.; Itzkan, I.; Dasari, R. R.; Feld, M. S. *Phys. Rev. Lett.* **1997**, *78* (9), 1667.
(21) Blackie, E. J.; Ru, E. C. Le; Etchegoin, P. G. *J. Am. Chem. Soc.* **2009**, *131* (40), 14466–14472.
(22) Lasse Jensen; M. Aikens, C.; C. Schatz, G. *Chem. Soc. Rev.* **2008**, *37* (5), 1061–1073.
(23) Banik, M.; Nag, A.; El-Khoury, P. Z.; Perez, A. R.; Guarrotxena, N.; Bazan, G. C.; Apkarian, V. A. *J. Phys. Chem. C* **2012**, *116* (18), 10415–10423.
(24) Kumar, G. V. P. *J. Nanophotonics* **2012**, *6* (1), 064503.
(25) Pawar, S.; Teja, B. R.; Nagarjuna, R.; Ganesan, R.; Nag, A. *Colloids & Surfaces A Physicochem. Eng. Asp.* **2019**, *578*, 123638.
(26) Yong Yang, ; Shigemasa Matsubara; Liangming Xiong; Tomokatsu Hayakawa, and; Nogami, M. *J. Phys. Chem. C* **2007**, *111* (26), 9095–9104.
(27) Pergolese, B.; Bonifacio, A.; Bigotto, A. *Phys. Chem. Chem. Phys.* **2005**, *7* (20), 3610–3613.
(28) Fu, G.; Sun, D. W.; Pu, H.; Wei, Q. *Talanta* **2019**, *195*, 841–849.
(29) Cheng, Z.-Q.; Li, Z.-W.; Xu, J.-H.; Yao, R.; Li, Z.-L.; Liang, S.; Cheng, G.-L.; Zhou, Y.-H.; Luo, X.; Zhong, J. *Nanoscale Res. Lett.* **2019**, *14* (89), 1–7.
(30) Pham, T. B.; Hoang, T. H. C.; Pham, V. H.; Nguyen, V. C.; Nguyen, T. Van; Vu, D. C.; Pham, V. H.; Bui, H. *Sci. Reports* **2019**, *9* (1), 1–10.
(31) Focsan, M.; Craciun, A. M.; Potara, M.; Leordean, C.; Vulpoi, A.; Maniu, D.; Astilean, S. *Sci. Reports* **2017**, *7* (1), 1–11.
(32) Liu, Y.; Wu, S. H.; Du, X. Y.; Sun, J. J. *Sensors Actuators B Chem.* **2021**, *338*, 129854.
(33) Xiang, S.; Lu, L.; Zhong, H.; Lu, M.; Mao, H. *Biomater. Sci.* **2021**, *9* (14), 5035–5044.
(34) Harder, R. A.; Wijenayaka, L. A.; Phan, H. T.; Haes, A. J. *J. Raman Spectrosc.* **2021**, *52* (2), 497–505.
(35) Patel, A. S.; Juneja, S.; Kanaujia, P. K.; Maurya, V.; Prakash, G. V.; Chakraborti, A.; Bhattacharya, J. *Nano-Structures & Nano-Objects* **2017**, *249*, 329–336.
(36) Qiu, H.; Wang, M.; Jiang, S.; Zhang, L.; Yang, Z.; Li, L.; Li, J.; Cao, M.; Huang, J.

Sensors Actuators B Chem. **2017**, *249*, 439–450.
(37) Zhang, M.; Zhao, A.; Sun, H.; Guo, H.; Wang, D.; Li, D.; Gan, Z.; Tao, W. *J. Mater. Chem.* **2011**, *21* (46), 18817–18824.
(38) Liao, J.; Zhan, Y.; Liu, Q.; Hong, R.; Tao, C.; Wang, Q.; Lin, H.; Han, Z.; Zhang, D. *Appl. Surf. Sci.* **2021**, *540*, 148397.
(39) Hoeven, J. E. S. van der; Deng, T.-S.; Albrecht, W.; Olthof, L. A.; Huis, M. A. van; Jongh, P. E. de; Blaaderen, A. *ACS Omega* **2021**, *6* (10), 7034–7046.
(40) Jian-Feng Li; Zhi-Lin Yang; Bin Ren; Guo-Kun Liu; Ping-Ping Fang; Yu-Xiong Jiang; De-Yin Wu, and; Tian, Z.-Q. *Langmuir* **2006**, *22* (25), 10372–10379.
(41) SS, L.; P, S.; AJ, W.; JJ, F. *J. Colloid Interface Sci.* **2016**, *482*, 73–80.
(42) Chen, T.; Rodionov, V. O. *ACS Catal.* **2016**, *6* (6), 4025–4033.
(43) Da Li; Jingquan Liu; Hongbin Wang; J. Barrow, C.; Wenrong Yang. *Chem. Commun.* **2016**, *52* (73), 10968–10971.
(44) Sravan Thota; Yongchen Wang; Jing Zhao. *Mater. Chem. Front.* **2018**, *2* (6), 1074–1089.
(45) Rycenga, M.; Cobley, C. M.; Zeng, J.; Li, W.; Moran, C. H.; Zhang, Q.; Qin, D.; Xia, Y. *Chem. Rev.* **2011**, *111* (6), 3669–3712.
(46) Zhang, B.; Xu, P.; Xie, X.; Wei, H.; Li, Z.; Mack, N. H.;Wang, H. L. *J. Mat. Chem.* **2011**, 21(8), 2495-2501.
(47) Li, S.; Miao, P.; Zhang, Y.; Wu, J.; Zhang, B.; Du, Y.; Han, X.; Sun, J.; Xu, P. *Advanced Materials* **2021**, 33(6), 2000086.
(48) Liang, C.; Lu, Z.A.; Wu, J.; Chen, M.X.; Zhang, Y.; Zhang, B.; Gao, G.L.; Li, S.; Xu, P.; *ACS Appl. Mater. Interfaces,* **2020**, 12 (49), 54266–54284
(49) Kim, N. R.; Shin, K.; Jung, I.; Shim, M.; Lee, H. M. *J. Phys. Chem. C* **2014**, *118* (45), 26324–26331.
(50) Chen, X.; Cui, C.-H.; Guo, Z.; Liu, J.-H.; Huang, X.-J.; Yu, S.-H. *Small* **2011**, *7* (7), 858–863.
(51) Lee, J.-P.; Chen, D.; Li, X.; Yoo, S.; Bottomley, L. A.; El-Sayed, M. A.; Park, S.; Liu, M. *Nanoscale* **2013**, *5* (23), 11620–11624.
(52) Zhang, D.; Liu, X. *J. Mol. Struct*. **2013**, *1035*, 471-475.
(53) Pal, A. K.; Bharathi Mohan, D. *J. Alloys Compd.* **2017**, *698*, 460–468.
(54) Rao, V. K.; Ghildiyal, P.; Radhakrishnan, T. P. *J. Phys. Chem. C* **2017**, *121* (2), 1339–1348.
(55) Nandhagopal, P.; Pal, A. K.; Bharathi Mohan, D. *Opt. Mater. (Amst)*. **2019**, *97* (3), 109381.
(56) Bharati, M. S. S.; Chandu, B.; Rao, S. V. *RSC Adv.* **2019**, *9* (3), 1517–1525.
(57) Tran, T. H.; Nguyen, M. H.; Nguyen, T. H. T.; Dao, V. P. T.; Nguyen, Q. H.; Sai, C. D.; Pham, N. H.; Bach, T. C.; Ngac, A. B.; Nguyen, T. T. *Appl. Surf. Sci.* **2020**, *509*, 145325.

(58) Rivera-Rangel, R. D.; Navarro-Segura, M. E.; Arizmendi-Morquecho, A.; Sánchez-Domínguez, M. *Nanotechnology* **2020**, *31* (46), 465605.
(59) Dubkov, S. V.; Savitskiy, A. I.; Trifonov, A. Y.; Yeritsyan, G. S.; Shaman, Y. P.; Kitsyuk, E. P.; Tarasov, A.; Shtyka, O.; Ciesielski, R.; Gromov, D. G. *Opt. Mater. X* **2020**, *7*, 100055.
(60) Dubkov, S.; Savitskiy, A.; Tarasov, A.; Novikov, D.; Mineeva, N.; Bazarova, M.; Overchenko, A.; Gromov, D. *IOP Conf. Ser. Mater. Sci. Eng.* **2021**, *1093* (1), 012005.
(61) Mettela, G.; Siddhanta, S.; Narayana, C.; Kulkarni, G. U. *Nanoscale* **2014**, *6* (13), 7480–7488.
(62) Choi, E.; Lee, S.; Piao, Y. *CrystEngComm* **2015**, *17* (31), 5940–5946.
(63) Gójska, A. M.; Kozioł, K.; Miśta-Jakubowska, E. A.; Diduszko, R. *Nucl. Instruments Methods Phys. Res. Sect. B Beam Interact. with Mater. Atoms* **2020**, *468*, 65–70.
(64) Tsuji, M.; Hikino, S.; Tanabe, R.; Matsunaga, M.; Sano, Y. *CrystEngComm* **2010**, *12* (11), 3900–3908.
(65) Rao, V. K.; & Radhakrishnan, T. P. *ACS Appl. Mater. Interfaces,* **2015**, 7, 23, 12767–12773.
(66) Kaja, S.; Damera, D. P.; & Nag, A. *Analytica Chimica Acta*, **2020**, 1129, 12-23
(67) Nie, S.; Emory, S.R. *Science* **1997**, *275* (5303), 1102–1106.
(68) Majoube, M.; Henry, M. *Spectrochim. Acta Part A Mol. Spectrosc.* **1991**, *47* (9–10), 1459–1466.
(69) Banik, M.; Nag, A.;Bazan, G. C.; Apkarian, V. A. *ACS Nano* **2012**, *6* (11), 10353-10354.

Chapter 5B

(1) Salvagno, L.; Contu, A.; Bianco, A.; Endrizzi, L.; Schintu, G. M.; Olmeo, N.; Aversa, S. M. L.; Chiarion-sileni, V.; Sorarú, M.; Fiorentino, M. V. *Ann. Oncol.* **1992**, *3* (10), 833–837.
(2) Amadori, S.; Arcese, W.; Isacchi, G.; Meloni, G.; Petti, M. C.; Monarca, B.; Testi, A. M.; Mandelli, F. *J. Clin. Oncol.* **1991**, *9* (7), 1210–1214.
(3) Neidhart, J. A.; Gochnour, D.; Roach, R.; Hoth, D.; Young, D. *J. Clin. Oncol.* **1986**, *4* (5), 672–677.
(4) Nicoletto, M. O.; Padrini, R.; Galeotti, F.; Ferrazzi, E.; Cartei, G.; Riddi, F.; Palumbo, M.; De Paoli, M.; Corsini, *Cancer Chemother. Pharmacol.* **2000**, *45* (6), 457–462.
(5) Neuhaus, O.; Kieseier, B. C.; Hartung, H. P. *Pharmacol. Ther.* **2006**, *109* (1–2), 198–209.
(6) Posner, L. E.; Dukart, G.; Goldberg, J.; Bernstein, T.; Cartwright, K. *Invest. New*

Drugs **1985**, *3* (2), 123–132.
(7) Liu, Y.; Wei, M.; Hu, Y.; Zhu, L.; Du, J. *Sensors Actuators B Chem.* **2018**, *255*, 544–551.
(8) Hong, B.; Cheng, Q. *Adv. Chem. Eng. Sci.* **2012**, *02* (04), 453–460.
(9) Rentsch, K. M.; Schwendener, R. A.; Hänseler, E. *J. Chromatogr. B Biomed. Sci. Appl.* **1996**, *679* (1–2), 185–192.
(10) Nicolau, G.; Szucs-Myers, V.; McWilliams, W.; Morrison, J.; Lanzilotti,. *Invest. New Drugs* **1985**, *3* (1), 51–56.
(11) Kika, F. S.; Zacharis, C. K.; Theodoridis, G. A.; Voulgaropoulos, A. N. *Anal. Lett.* **2009**, *42* (6), 842–855.
(12) Liu, S.; Wang, F.; Liu, Z.; Hu, X.; Yi, A.; Duan, H. *Anal. Chim. Acta* **2007**, *601* (1), 101–107.
(13) Xue, L.; Zhang, M.; Li, G.; Cao, J.; Yao, H. *green Chem. Lett. Rev.* **2021**, *14* (2), 393–401.
(14) Jagirani, M. S.; Mahesar, S. A.; Uddin, S.; Sherazi, S. T. H.; Kori, A. H.; Lakho, S. A.; Kalwar, N. H.; Memon, S. S. *J. Clust. Sci.* **2022**, *33* (1), 241–247.
(15) Wei, J. R.; Chen, H. Y.; Zhang, W.; Pan, J. X.; Dang, F. Q.; Zhang, Z. Q.; Zhang, J. e. *Sensors Actuators B Chem.* **2017**, *244*, 31–37.
(16) Ponlamuangdee, K.; Hornyak, G. L.; Bora, T.; Bamrungsap, S. *New J. Chem.* **2020**, *44* (33), 14087–14094.
(17) Dougan, J. A.; Faulds, K. *Analyst* **2012**, *137* (3), 545–554.
(18) Banik, M.; Nag, A.; El-Khoury, P. Z.; Rodriguez Perez, A.; Guarrotxena, N.; Bazan, G. C.; Apkarian, V. A. *J. Phys. Chem. C* **2012**, *116* (18), 10415–10423.
(19) Mettela, G.; Siddhanta, S.; Narayana, C.; Kulkarni, G. U.. *Nanoscale* **2014**, *6* (13), 7480–7488.
(20) Hameed, M. K.; Parambath, J. B. M.; Gul, M. T.; Khan, A. A.; Park, Y.; Han, C.; Mohamed, A. A. *Appl. Surf. Sci.* **2022**, *583*, 152504.
(21) Dendisová, M.; Dendisová-Vyškovsk, D.; Vyškovská, V.; Prokopec, V.; Clupek, M.; Matějka, P.; Matějka, M. *J. Raman Spectrosc.* **2012**, *43* (2), 181–186.
(22) Pawar, S.; Teja, B. R.; Nagarjuna, R.; Ganesan, R.; Nag, A. *Colloids Surfaces A Physicochem. Eng. Asp.* **2019**, *578*, 123638.
(23) Singh, M. K.; Chettri, P.; Basu, J.; Tripathi, A.; Mukherjee, B.; Tiwari, A.; Mandal, R. K. *Mater. Res. Express* **2020**, *7* (1), 015052.
(24) Kaja, S.; Nag, A. *Langmuir* **2021**, *37* (44), 13027–13037.
(25) Xie, Y.; Wu, D. Y.; Liu, G. K.; Huang, Z. F.; Ren, B.; Yan, J. W.; Yang, Z. L.; Tian, Z. Q. *J. Electroanal. Chem.* **2003**, *554–555* (1), 417–425.
(26) Lombardi, J. R.; Birke, R. L. *J. Chem. Phys.* **2012**, *136* (14), 144704.
(27) Hildebrandt, P.; Stockhurger, M. *J. Phys. Chem.* **1984**, *88* (24), 5935–5944.
(28) McNay, G.; Eustace, D.; Smith, W. E.; Faulds, K.; Graham, D. *Appl. Spectrosc.*

2011, *65* (8), 825–837.
(29) McLaughlin, C.; MacMillan, D.; McCardle, C.; Smith, W. E. *Anal. Chem.* **2002**, *74* (13), 3160–3167.
(30) Ackermann, K. R.; Henkel, T.; Popp, J. *ChemPhysChem* **2007**, *8* (18), 2665–2670.
(31) Wu, H. Y.; Cunningham, B. T. *Nanoscale* **2014**, *6* (10), 5162–5171.
(32) Wallace, R. A.; Charlton, J. J.; Kirchner, T. B.; Lavrik, N. V.; Datskos, P. G.; Sepaniak, M. J. *Anal. Chem.* **2014**, *86* (23), 11819–11825.
(33) McLintock, A.; Cunha-Matos, C. A.; Zagnoni, M.; Millington, O. R.; Wark, A. W. *ACS Nano* **2014**, *8* (8), 8600–8609.
(34) Lee, B. S.; Dutta, P. K. *J. Phys. Chem.* **1989**, *93* (15), 5665–5672.
(35) Saljooqi, A.; Shamspur, T.; Mostafavi, A. *Sensors* **2019**, *19* (12), 4364–4368.
(36) Manjunatha, J. G. *J. Surf. Sci. Technol* **2018**, *34*, 970–1893.
(37) Alizadeh, M.; Azar, P. A.; Mozaffari, S. A.; Karimi-Maleh, H.; Tamaddon, A. M. An Experimental/Docking Investigation. *Front. Chem.* **2020**, *8* (814), 1–10.
(38) Hasanzadeh, M.; Khalilzadeh, B.; Shadjou, N. *Nanocomposites.* **2016**, *2* (2), 76–83.
(39) Jiang, X.; Feng, D. Q.; Liu, G.; Fan, D.; Wang, W. *Sensors Actuators B Chem.* **2016**, *232*, 276–282.
(40) Lian, X.; Zhang, Y.; Wang, J.; Yan, B. *Inorg. Chem.* **2020**, *59* (14), 10304–10310.
(41) Mohammadinejad, A.; Es'haghi, Z.; Abnous, K.; Mohajeri, S. A. Tandem *J. Lumin.* **2017**, *190*, 254–260.
(42) Chaffin, E.; O'Connor, R. T.; Barr, J.; Huang, X.; Wang, Y. *J. Chem. Phys.* **2016**, 145 (5), 054706.
(43) Saini, R. K.; Sharma, A. K.; Agarwal, A.; Prajesh, R. *Mater. Chem. Phys.* **2022**, *287*, 126288.
(44) Sakir, M.; Pekdemir, S.; Karatay, A.; Küçüköz, B.; Ipekci, H. H.; Elmali, A.; Demirel, G.; Onses, M. S. *ACS Appl. Mater. Interfaces*. **2017**, 9 (45), 39795–39803.

Chapter 6:

(1) Paul, B. D.; Sbodio, J. I.; Snyder, S. H. *Trends Pharmacol. Sci.* **2018**, *39* (5), 513–524.
(2) Clemente Plaza, N.; Reig García-Galbis, M.; Martínez-Espinosa, R. M. *Molecules* **2018**, *23* (3), 1–13.
(3) Robert C . Fahey. *Adv Exp Med Biol.* **1977**, *86*, 1–30.
(4) Bin, P.; Huang, R.; Zhou, X. *Biomed Res. Int.* **2017**, 9584932.
(5) K., S. D. *Essential Amino Acids: Chart, Abbreviations and Structure | Technology Networks*. Applied Sciences. https://www.technologynetworks.com/applied-sciences/articles/essential-amino-acids-chart-abbreviations-and-structure-

324357.
(6) Amrolia, P.; Sullivan, S. G.; Stern, A.; Munday, R. *J. Appl. Toxicol.* **1989**, *9* (2), 113–118.
(7) Yang, N.; Song, H.; Wan, X.; Fan, X.; Su, Y.; Lv, Y. *Analyst* **2015**, *140* (8), 2656–2663.
(8) Lai, Y. T.; Ganguly, A.; Chen, L. C.; Chen, K. H. *Biosens. Bioelectron.* **2010**, *26* (4), 1688–1691.
(9) Rani, B. K.; John, S. A. *Biosens. Bioelectron.* **2016**, *83*, 237–242.
(10) Wang, Y.; Wang, W.; Wang, S.; Chu, W.; Wei, T.; Tao, H.; Zhang, C.; Sun, Y. *Sensors Actuators, B Chem.* **2016**, *232*, 448–453.
(11) Huang, K.; Bulik, I. W.; Martí, A. A. *Chem. Commun.* **2012**, *48* (96), 11760–11762.
(12) Chwatko, G.; Kuźniak, E.; Kubalczyk, P.; Borowczyk, K.; Wyszczelska-Rokiel, M.; Głowacki, R. *Anal. Methods* **2014**, *6* (19), 8039–8044.
(13) Cao, F.; Huang, Y.; Wang, F.; Kwak, D.; Dong, Q.; Song, D.; Zeng, J.; Lei, Y. *Anal. Chim. Acta* **2018**, *1019*, 103–110.
(14) Guselnikova, O.; Elashnikov, R.; Svorcik, V.; Kartau, M.; Gilroy, C.; Gadegaard, N.; Kadodwala, M.; Karimullah, A. S.; Lyutakov, O. *Nanoscale Horizons* **2023**, 499–508.
(15) Ganesan, S.; Venkatakrishnan, K.; Tan, B. *Biosens. Bioelectron.* **2020**, *151*, 111967.
(16) Pei, J., Sun, Y., Yu, X., Tian, Z., Zhang, S., Wei, S. & Boukherroub, R. *J. Colloid Interface Sci.* **2022**, *626*, 608–618.
(17) Fu, H. Y.; Lang, X. Y.; Hou, C.; Wen, Z.; Zhu, Y. F.; Zhao, M.; Li, J. C.; Zheng, W. T.; Liu, Y. B.; Jiang, Q. *J. Mater. Chem. C* **2014**, *2* (35), 7216–7222.
(18) Jeanmaire, D. L.; Van Duyne, R. P. *J. Electroanal. Chem.* **1977**, *84* (1), 1–20.
(19) Albrecht, M. G.; Creighton, J. A. *J. Am. Chem. Soc.* **1977**, *99* (15), 5215–5217.
(20) Yang, Y.; O'Riordan, A.; Lovera, P. *Sensors Actuators B Chem.* **2022**, *364*, 131851.
(21) Mahar, N.; Haroon, M.; Saleh, T. A.; Al-Saadi, A. A. *Surfaces and Interfaces* **2022**, *31*, 102059.
(22) Xu, D.; Zhang, Y.; Zhang, S.; Yang, W.; Wang, Z.; Li, J. *Opt. Laser Technol.* **2022**, *145*, 107502.
(23) Wang, D.; Shi, F.; Jose, J.; Hu, Y.; Zhang, C.; Zhu, A.; Grzeschik, R.; Schlücker, S.; Xie, W. *J. Am. Chem. Soc.* **2022**, *144* (11), 5003–5009.
(24) Tian, S.; Neumann, O.; McClain, M. J.; Yang, X.; Zhou, L.; Zhang, C.; Nordlander, P.; Halas, N. J. *Nano Lett.* **2017**, *17* (8), 5071–5077.
(25) Wu, Y.; Dang, H.; Park, S. G.; Chen, L.; Choo, J. *Biosens. Bioelectron.* **2022**, *197*, 113736.
(26) Skwierczyńska, M.; Woźny, P.; Runowski, M.; Kulpiński, P.; Lis, S. *Carbohydr. Polym.* **2022**, *279*, 119010.
(27) Hameed, M. K.; Parambath, J. B. M.; Gul, M. T.; Khan, A. A.; Park, Y.; Han, C.;

Mohamed, A. A. *Appl. Surf. Sci.* **2022**, *583*, 152504.
(28) Sun, M.; Guo, W.; Tian, J.; Chen, X.; Zhang, Q. *Colloids Surfaces A Physicochem. Eng. Asp.* **2022**, *642*, 128590.
(29) Chen, S.; Li, Q.; Tian, D.; Ke, P.; Yang, X.; Wu, Q.; Chen, J.; Hu, C.; Ji, H. *Spectrochim. Acta - Part A Mol. Biomol. Spectrosc.* **2022**, *273*, 121030.
(30) Pham, T. B.; Hoang, T. H. C.; Pham, V. H.; Nguyen, V. C.; Nguyen, T. Van; Vu, D. C.; Pham, V. H.; Bui, H. *Sci. Rep.* **2019**, *9* (1), 1–10.
(31) Pawar, S.; Teja, B. R.; Nagarjuna, R.; Ganesan, R.; Nag, A. *Colloids Surfaces A Physicochem. Eng. Asp.* **2019**, *578*, 123638.
(32) Kaja, S.; Nag, A. *Langmuir* **2021**, *37* (44), 13027–13037.
(33) Chang, K.; Chung, H. *RSC Adv.* **2016**, *6* (79), 75943–75950.
(34) Karthikeyan, B.; Loganathan, B. *Nanostructures* **2013**, *49*, 105–110.
(35) Loganathan, B.; Karthikeyan, B. *Colloids Surfaces A Physicochem. Eng. Asp.* **2013**, *436*, 944–952.
(36) Kang, S. W.; Lee, Y. W.; Park, Y.; Choi, B. S.; Hong, J. W.; Park, K. H.; Han, S. W. *ACS Nano* **2013**, *7* (9), 7945–7955.
(37) Zhang, Z.; Ahn, J.; Kim, J.; Wu, Z.; Qin, D. *Nanoscale* **2018**, *10* (18), 8642–8649.
(38) Huang, Q.; Xi, Z.; Wei, W. *J. Alloys Compd.* **2020**, *843*, 155971.
(39) Bich Quyen, T. T.; Su, W. N.; Chen, C. H.; Rick, J.; Liu, J. Y.; Hwang, B. J. *J. Mater. Chem. B* **2014**, *2* (34), 5550–5557.
(40) Li, T.; Vongehr, S.; Tang, S.; Dai, Y.; Huang, X.; Meng, X.. *Sci. Rep.* **2016**, *6*, 1–11.
(41) Ryu, H. J.; Shin, H.; Oh, S.; Joo, J. H.; Choi, Y.; Lee, J. S. *ACS Appl. Mater. Interfaces* **2020**, *12* (2), 2842–2853.
(42) Guselnikova, O.; Nugraha, A. S.; Na, J.; Postnikov, P.; Kim, H. J.; Plotnikov, E.; Yamauchi, Y. *ACS Appl. Mater. Interfaces* **2022**, *14* (36), 41629–41639.
(43) Berthou, M.; Clarot, I.; Gouyon, J.; Steyer, D.; Monat, M. A.; Boudier, A.; Pallotta, A. *Microchem. J.* **2022**, *183* (September), 107994.
(44) Wu, X. Q.; Wu, X. W.; Shen, J. S.; Zhang, H. W. *RSC Adv.* **2014**, *4* (90), 49287–49294.
(45) Hashimoto, Y.; Seniutinas, G.; Balcytis, A.; Juodkazis, S.; Nishijima, Y. *Sci. Rep.* **2016**, *6*, 1–9.
(46) Gójska, A. M.; Kozioł, K.; Miśta-Jakubowska, E. A.; Diduszko, R. *Nucl. Instruments Methods Phys. Res. Sect. B Beam Interact. with Mater. Atoms* **2020**, *468*, 65–70.
(47) Li, T.; Vongehr, S.; Tang, S.; Dai, Y.; Huang, X.; Meng, & X. *Sci. Rep.* **2016**, *6*, 37092.
(48) Zhang, Z.; Ahn, J.; Kim, J.; Wu, Z.; Qin, D. *Nanoscale* **2018**, *10* (18), 8642–8649.
(49) Carlini, L.; Fasolato, C.; Postorino, P.; Fratoddi, I.; Venditti, I.; Testa, G.; Battocchio, C.. *Colloids Surfaces A Physicochem. Eng. Asp.* **2017**, *532*, 183–188.

(50) Joseph, Y.; Besnard, I.; Rosenberger, M.; Guse, B.; Nothofer, H.; Wessels, J. M.; Wild, U.; Knop-gericke, A.; Su, D.; Schlo, R.,. *J. Phys. Chem. B* **2003**, *107*, 7406–7413.
(51) Choi, E.; Lee, S.; Piao, Y. *CrystEngComm* **2015**, *17* (31), 5940–5946.
(52) Pal, A. K.; Bharathi Mohan, D. *J. Alloys Compd.* **2017**, *698*, 460–468.
(53) Chen, L.; Zhang, D.; Chen, J.; Zhou, H.; Wan, H. *Mater. Sci. Eng. A* **2006**, *415* (1–2), 156–161.
(54) Aryal, S.; Remant, B. K. C.; Dharmaraj, N.; Bhattarai, N.; Kim, C. H.; Kim, H. Y. *Spectrochim. Acta - Part A Mol. Biomol. Spectrosc.* **2006**, *63* (1), 160–163.
(55) López-Tobar, E.; Hernández, B.; Ghomi, M.; Sanchez-Cortes, S. *J. Phys. Chem. C* **2013**, *117* (3), 1531–1537.
(56) Fleming, G. D.; Finnerty, J. J.; Campos-Vallette, M.; Celis, F.; Aliaga, A. E.; Fredes, C.; Koch, R. *J. Raman Spectrosc.* **2009**, *40* (6), 632–638..
(57) Yao, G.; Huang, Q. *J. Phys. Chem. C* **2018**, *122* (27), 15241–15251.
(58) Jing, C.; Fang, Y. *Chem. Phys.* **2007**, *332* (1), 27–32.
(59) Rodríguez-Zamora, P.; Cordero-Silis, C. A.; Fabila, J.; Luque-Ceballos, J. C.; Buendiá, F.; Heredia-Barbero, A.; Garzón, I. L. *Langmuir* **2022**, *38* (18), 5418–5427.
(60) R. L. Aggarwal, L. W. Farrar, E. D. D. and D. L. P. *J. Raman Spectrosc.* **2009**, *40*, 1331–1333.
(61) Graff, M.; Bukowska, J. *J. Phys. Chem. B* **2005**, *109* (19), 9567–9574.
(62) Ray, C.; Dutta, S.; Sarkar, S.; Sahoo, R.; Roy, A.; Pal, T. *J. Mater. Chem. B* **2014**, *2* (36), 6097–6105.
(63) Shen, J. S.; Li, D. H.; Zhang, M. B.; Zhou, J.; Zhang, H.; Jiang, Y. B. *Langmuir* **2011**, *27* (1), 481–486.
(64) Zhang, L.; Zhang, W.; Nie, Y.; Wang, Y.; Zhang, P. *J. Colloid Interface Sci.* **2023**, *636*, 568–576.
(65) Heydari, S.; Hosseinpour Zaryabi, M. *Opt. Mater.* **2023**, *135*, 113376.
(66) Singh, G.; Chowdhary, K.; Singh, A.; Satija, P.; Mohit; Pawan; Soni, S.; Raghav, N.; Sharma, R. *Inorganica Chim. Acta* **2023**, *545*, 121232.
(67) Li, C. F.; Wu, Y. Y.; Chen, L. S.; Liu, Z. B.; Gan, S. Y.; Han, D. X.; Niu, L.; Qin, D. D.; Tao, C. L. *ACS Appl. Nano Mater.* **2022**, *6*, 1009-1018
(68) Ayaz Ahmed, K. B.; Sengan, M.; Suresh Kumar, P. *Sensors Actuators, B Chem.* **2016**, *233*, 431–437.
(69) Lian, J.; Liu, P.; Jin, C.; Liu, Q. Y.; Zhang, X.; Zhang, X. *ACS Sustain. Chem. Eng.* **2020**, *8 (47)*, 17540–17550.
(70) Hou, J.; Jia, P.; Yang, K.; Bu, T.; Sun, X.; Wang, L. *Sensors Actuators, B Chem.* **2021**, *344*, 130266.
(71) Zhang, D.; Zhang, F.; Wang, S.; Hu, S.; Liao, Y.; Wang, F.; Liu, H. *Spectrochim.*

Acta - Part A Mol. Biomol. Spectrosc. **2023**, *290*, 122285.
(72) Mohammadnavaz, A.; Beitollahi, H.; Modiri, S. *Inorganica Chim. Acta* **2023**, *548*, 121340.
(73) Jia, D.; Zhang, Y.; Xie, Y.; Zhang, X.; Pan, H.; Chen, Z. *Sensors Actuators B Chem.* **2023**, *377*, 133095.
(74) Bai, Y. H.; Xu, J. J.; Chen, H. Y. *Biosens. Bioelectron.* **2009**, *24* (10), 2985–2990.
(75) Khamcharoen, W.; Henry, C. S.; Siangproh, W. *Talanta* **2022**, *237*, 122983.
(76) Li, H.; Xu, T.; Zhang, Z.; Chen, J.; She, M.; Ji, Y.; Zheng, B.; Yang, Z.; Zhang, S.; Li, *Chem. Eng. J.* **2023**, *453*, 139722.
(77) Li, H.; Han, B.; Ma, H.; Li, R.; Hou, X.; Zhang, Y.; Wang, J. J. *Microchim. Acta* **2023**, *190* (2).
(78) An, S.; Lin, Y.; Wang, J.; Ye, T.; Mao, Y.; Zhang, J.; Guo, L.; Li, L.; Qian, Z.; Liu, H. *Sensors Actuators B Chem.* **2023**, *374*, 132799.
(79) Li, L. K.; Liu, Q.; Cai, R.; Ma, Q.; Mao, G.; Zhu, N.; Liu, S. *Microchem. J.* **2023**, *187*, 108449.
(80) Zhao, Q.; Qin, J.; Kong, F.; Wang, D.; Guo, Y.; Li, Y. *J. Photochem. Photobiol. A Chem.* **2023**, *436*, 114383.
(81) Dong, J.; Wang, Y.; Fan, C.; Tu, Y.; Pu, S. *Dye. Pigment.* **2023**, *210*, 110994.
(82) Yang, X.; Wang, J.; Zhang, Z.; Zhang, B.; Du, X.; Zhang, J.; Wang, J. *Food Chem.* **2023**, *416*, 135730.
(83) Sun, T.; Fan, R.; Xiao, R.; Xing, T.; Qin, M.; Liu, Y.; Hao, S.; Chen, W.; Yang, Y. *J. Mater. Chem. A* **2020**, *8* (11), 5587–5594.
(84) Lin, Z.; Zeng, Q.; Deng, Q.; Yao, W.; Deng, H.; Lin, X.; Chen, W. *Sensors Actuators B Chem.* **2022**, *359*, 131563.
(85) Yin, G. X.; Niu, T. T.; Gan, Y. B.; Yu, T.; Yin, P.; Chen, H. M.; Zhang, Y. Y.; Li, H. T.; Yao, S. Z. *Angew. Chemie - Int. Ed.* **2018**, *57* (18), 4991–4994.
(86) Anantha Lakshmi, B.; Sangubotla, R.; Kim, J.; Kim, Y. J. *Spectrochim. Acta - Part A Mol. Biomol. Spectrosc.* **2022**, *282*, 121685.
(87) Qi, X.; Kan, W.; Zhao, B.; Du, J.; Ding, L.; Wang, L.; Song, B. *Inorganica Chim. Acta* **2023**, *549*, 121393.
(88) Yu, Q. Y.; Wei, C. W.; Wang, X. J.; Gao, S. Q.; Tong, X. Y.; Lin, Y. W. *J. Biol. Inorg. Chem.* **2023**, *28* (2), 205–211.
(89) Hu, Y.; Lu, L.; Guo, S.; Wu, X.; Zhang, J.; Zhou, C.; Fu, H.; She, Y. *Sensors Actuators B Chem.* **2023**, *382*, 133534.
(90) Xu, Y.; Ma, H.; Su, X.; He, L.; Wang, E.; Wang, F.; Ren, J. *Sensors Actuators B Chem.* **2023**, *382*, 133564.
(91) Zhou, B.; Wang, B.; Bai, M.; Dong, M.; Tang, X. *Spectrochim. Acta - Part A Mol. Biomol. Spectrosc.* **2023**, *294*, 122523.
(92) Rohilla, D.; Chaudhary, S.; Kaur, N.; Shanavas, A. *Mater. Sci. Eng. C* **2020**, *110*,

110724.
(93) Wang, G. L.; Dong, Y. M.; Yang, H. X.; Li, Z. J. *Talanta* **2011**, *83* (3), 943–947.
(94) Anand, T.; Kumar, A. S. K.; Sahoo, S. K. *Photochem. Photobiol. Sci.* **2018**, *17* (4), 414–422. htt
(95) He, L.; Yang, X.; Xu, K.; Kong, X.; Lin, W. *Chem. Sci.* **2017**, *8* (9), 6257–6265.
(96) Zhang, P.; Xiao, Y.; Zhang, Q.; Zhang, Z.; Yu, H.; Ding, C. *New J. Chem.* **2019**, *43* (20), 7620–7627.
(97) Feng, Y. C.; Cai, Z. Bin; Li, S. L.; Chen, L. J.; Ye, Q.; Tian, Y. P. *Dye. Pigment.* **2023**, *210*, 111021.
(98) Shiraishi, Y.; Yamamoto, K.; Sumiya, S.; Hirai, T. *Phys. Chem. Chem. Phys.* **2014**, *16* (24), 12137–12142.
(99) Kand, D.; Mishra, P. K.; Saha, T.; Lahiri, M.; Talukdar, P. *Analyst* **2012**, *137* (17), 3921–3924.
(100) Shiraishi, Y.; Yamamoto, K.; Sumiya, S.; Hirai, T. *Chem. Commun.* **2013**, *49* (99), 11680–11682.
(101) Hong, Y.; Wang, R.; Jiang, Z.; Cong, Z.; Song, H. *Int. J. Anal. Chem.* **2020**, *2020*.
(102) Abdelsalam, M. E. *Cent. Eur. J. Chem.* **2009**, *7* (3), 446–453.
(103) Guselnikova, O.; Nugraha, A. S.; Na, J.; Postnikov, P.; Kim, H. J.; Plotnikov, E.; Yamauchi, Y. *ACS Appl. Mater. Interfaces* **2022**, *14* (36), 41629–41639..
(104) Xu, Y.; Ma, H.; Su, X.; He, L.; Wang, E.; Wang, F.; Ren, J. *Sensors Actuators B Chem.* **2023**, *382*, 133564.
(105) Hu, Y.; Lu, L.; Guo, S.; Wu, X.; Zhang, J.; Zhou, C.; Fu, H.; She, Y. *Sensors Actuators B Chem.* **2023**, *382*, 133534.
(106) Li, L. K.; Liu, Q.; Cai, R.; Ma, Q.; Mao, G.; Zhu, N.; Liu, S. *Microchem. J.* **2023**, *187*, 108449.
(107) Huang, G. G.; Hossain, M. K.; Han, X. X.; Ozaki, Y.. *Analyst* **2009**, *134* (12), 2468–2474.
(108) Krimm, S.; Qian, W. Vibrational Analysis of Glutathione. *Biopolymers* **1994**, *34*, 18.
https://doi.org/10.1002/bip.360341009
(109) Stewart, S.; Fredericks, P. M. *Spectrochim. Acta - Part A Mol. Biomol. Spectrosc.* **1999**, *55* (7–8), 1615–1640.

List of Publications

1. **Kaja, S.;** Mathews, A. V.; Venuganti V. V. K.; and Nag, A.* “Bimetallic Ag–Cu Alloy SERS Substrates as Label-Free Biomedical Sensors: Femtomolar Detection of Anticancer Drug Mitoxantrone with Multiplexing” Langmuir, 2023, 39, 5591-5601.
2. **Kaja, S.;** Mukherjee, A.; Chakravarty, M.; and Nag, A.* “Identifying high performance photosensitizer with simultaneous enhancement in fluorescence and singlet oxygen generation, from ‘(Ag/Au)-aggregation-induced emission-active fluorogen’ theranostic nanoparticles” Colloids and surfaces A: Physicochemical and Engineering Aspects, 2022, 649, 129448.
3. **Kaja, S.;** and Nag, A.* “Bimetallic Ag–Cu Alloy Microflowers as SERS Substrates with Single-Molecule Detection Limit” Langmuir, 2021, 37, 13027-13037.
4. **Kaja, S.;** Damera, D. P.; and Nag, A.*. "A metal-enhanced fluorescence sensing platform for selective detection of picric acid in aqueous medium" Analytica Chimica Acta, 2020, 1129, 12- 23.
5. **Kaja, S**.; and Nag, A.* “Bimetallic SERS substrates for the detection of trace levels of analytes: A mini-review” Asian journal of physics, 2022, 31, 9-10.
6. **Kaja, S**.; and Nag, A.* “Ag-Au-Cu Trimetallic Alloy Microflower: A Highly Sensitive SERS Substrate for Detection of Low Raman Scattering Cross-Section Thiols.” (Manuscript Just accepted in Langmuir)
7. **Kaja, S.;** Mathews, A. V.; and Nag, A.* “Polymer Coated Gold Nanorod Cores Adsorbed with Eosin Y: Engineered Plasmon-Enhanced Nano-Photosensitizers” (Manuscript submitted)
8. Lazarus, R.; Kothari, R; **Kaja, S.;** Venuganti, V.V.K.; and Nag, A.* “Designing a Nanothermometer using Gel-to-Liquid Phase Transition Property of Hybrid Niosome.” Analyst, 2023, 148, 3169-3173.
9. Sharma, P.; Naithani,; S.; Layek, S.; Kumar, A.; Rawat, R.; **Kaja, S.;** Nag, A.; Kumar, S.;* and Goswami, T.* “Highly sensitive fluorescence “turn-on” sensing of Hg 2+ ions using copper nanocluster” Spectrochimica Acta, Part A: Molecular and Biomolecular Spectroscopy, 2023, 297, 122697.

10. Goswami, T.; Bheemaraju, A.; Kataria, A.; Nag, A.; **Kaja, S**.; Mishra, S.; Mishra, K. A.; “Highly fluorescent water-soluble PTCA incorporated silver nano-cluster for sensing of dopamine” Materials Chemistry and Physics, 2021, 259, 124086.
11. Pawar, S.; **Kaja, S**.; and Nag, A*. " Red-Emitting Carbon Dots as a Dual Sensor for In3+ and Pd2+ in Water" ACS Omega, 2020, 5, 8362-8372.
12. Damera, D. P.; **Kaja, S.;** Janardhanam, L. S. L.; Alim, S.; Venuganti, V. K. and Nag, A*. "Synthesis, detailed characterization and dual drug delivery application of BSA loaded Aquasomes" ACS Applied Bio Materials, 2019, 2, 4471 - 4484.

List of Conferences

1. **S. Kaja** and A. Nag; Poster: “Trimetallic Ag:Au:Cu alloy Microflowers as SERS substrates for L-Cysteine sensing.” in Convergence of Chemistry & Materials CCM-2, a National Symposium in Chemistry held at BITS Pilani Hyderabad Campus in January 2023.
2. **S. Kaja** and A. Nag; Poster: “Trimetallic Ag:Au:Cu alloy Microflowers as SERS substrates for L-Cysteine sensing.” At IX international conference on perspectives of vibrational spectroscopy (ICOVPS) held at Devi Ahilya Vishwavidyalaya in coordination with UGC-CSR DAE, Indore in December 2022.
3. **S. Kaja** and A. Nag; Oral Presentation: " Bimetallic Ag-Cu alloy SERS substrates as label-free biomedical sensor" at two-day international seminar on current trends and futuristic challenges in chemical sciences, held at university college of science, Osmania university, Hyderabad in July 2022.
4. **S. Kaja** and A. Nag; Oral Presentation: "Unprecedented SERS efficiency of bimetallic Ag-Cu alloy microflowers leading to single molecule detection" at 7th International Conference on Advanced Nanomaterials and Nanotechnology organized by IIT Guwahati, held online during December 14th -17th, 2021.
5. A. Nag and **S. Kaja**; Oral Presentation: "Single molecule detection using Ag-Cu bimetallic Microflowers for single molecule detection" at the Frontiers in Optics and Photonics 2021 (FOP-21), IIT Delhi, held online during September 24-27, 2021.
6. S. Pawar, **S. Kaja**, and A. Nag; poster: "Nitrogen-doped hydrothermal synthesis of red-emitting carbon dots and its application in dual Pd2+and In3+ sensing in the water" at National Symposium on Convergence of Chemistry & Materials (CCM 2019), held at BITS-Pilani Hyderabad Campus, Hyderabad in December, 2019.
7. **S. Kaja,** D. P. Damera and A. Nag Invited Talk: "Gold nanoparticle-based plasmon enhanced fluorescence of polyallylamine hydrochloride: An efficient and selective sensor for picric acid in aqueous media" at 258th ACS National

Meeting & exposition, held at San Diego, CA, United States, August 25-29, 019 (2019), PHYS-0003 .

8. **S. Kaja** and A. Nag; poster: "Metal enhanced fluorescence of chitosan carbon dots adsorbed on to Au@SiO2 core shell nano particles" at 24th CRSI National Symposium in Chemistry (CRSI-NSC-24, 2019), held at The Central Leather Research Institute (CRSI-CLR), Chennai in February, 2019.

Biography of Ms. Sravani Kaja

Ms. Sravani Kaja was born in Kothagudem, Telangana. She completed her Bachelor of Science with Chemistry from Priyadarshini Degree and PG college under Kakatiya University and Master of Science in Chemistry (Organic chemistry specialization) from Telangana Mahila University (TMV), formerly known as University college for Women, located in Koti, Hyderabad. She joined the department of chemistry, BITS-Pilani, Hyderabad campus for her doctoral research under the supervision of Prof. Amit Nag in 2018. During her doctoral study she received fellowship from BITS-Pilani, Hyderabad campus. During her research work she explored plasmon enhanced spectroscopy and used it for sensing various important analytes and theranostic applications. She has published twelve scientific publications in well-renowned international journals and presented papers at various national and international conferences.

Biography of Prof. Amit Nag

Dr. Amit Nag is a Professor in Chemistry at BITS-Pilani Hyderabad Campus. He received his Ph.D. in 2009 from the Indian Institute of Technology, Kanpur under the supervision of Professor Debabrata Goswami on femtosecond laser chemistry. From 2009-2011 he worked as a Post-doctoral fellow at the University of California, Irvine, U.S.A with Professor V. Ara Apkarian on scan-probe microscopy. During 2011-2012 he has worked as a postdoctoral fellow at the Department Chemie und CeNS, Ludwig-Maximilians-University, Munich, Germany with Professor Achim Hartschuh in the area of plasmonics and Tip- Enhanced Raman Spectroscopy. Also, he has visited Germany in 2013 for 3 months under the International Collaborative Exchange Programme by INSA, New Delhi, India. He has successfully completed two sponsored projects funded by BITS-Pilani and by DST- SERB under a young scientist scheme. Currently he has two ongoing projects, one of them is funded by BITS-RMIT (a joint collaborative research project with RMIT, Australia) and other one is DST-PURSE. His research interests include Nonlinear laser spectroscopy, Scanning-probe microscopy of nanomaterials, Fluorescence Spectroscopy, Metal Enhanced Fluorescence (MEF), Surface enhanced Raman spectroscopy (SERS), metal enahnced photodynamic therapy, Carbon Dots, Nanocarrier mediated drug entrapment and delivery.